Cláudia Brito da Costa
Licenciada em Química Aplicada - Ramo Materiais Plásticos

Printed electronics for ubiquitous computing applications

Dissertação para obtenção do Grau de Doutor em
Química

Orientador: António Câmara, Professor Catedrático, Faculdade
de Ciências e Tecnologia – Universidade Nova de Lisboa
Orientador Empresarial: Inês Henriques, CEO, Ynvisible
Co-orientador: César A. T. Laia, Investigador Auxiliar, Faculdade
de Ciências e Tecnologia – Universidade Nova de Lisboa

Júri:

Presidente: Rodrigo Martins, Professor Catedrático, Faculdade de Ciências e Tecnologia - Universidade Nova de Lisboa
Arguente: Aline Rougier, Directeur de Recherche – CNRS e Directeur Adjoint de ICMCB, Institut de Chimie de la Matière Condensée de Bordeaux
Arguente: António Vieira, CEO, WeProductise
Vogal: Alda Simões, Professor associado com Agregação, Instituto Superior Técnico – Universidade Técnica de Lisboa
Vogal: António Câmara, Professor Catedrático, Faculdade de Ciências e Tecnologia – Universidade Nova de Lisboa
Vogal: César A. T. Laia, Investigador Auxiliar, Faculdade de Ciências e Tecnologia – Universidade Nova de Lisboa

FCt **FACULDADE DE
CIÊNCIAS E TECNOLOGIA**
UNIVERSIDADE NOVA DE LISBOA

Fevereiro 2013

Cláudia Brito da Costa
Licenciada em Química Aplicada - Ramo Materiais Plásticos

Printed electronics for ubiquitous computing applications

Dissertação para obtenção do Grau de Doutor em
Química

Orientador: António Câmara, Professor Catedrático, Faculdade
de Ciências e Tecnologia – Universidade Nova de Lisboa
Orientador Empresarial: Inês Henriques, CEO, Ynvisible
Co-orientador: César A. T. Laia, Investigador Auxiliar, Faculdade
de Ciências e Tecnologia – Universidade Nova de Lisboa

Júri:

Presidente:	Rodrigo Martins, Professor Catedrático, Faculdade de Ciências e Tecnologia - Universidade Nova de Lisboa
Arguente:	Aline Rougier, Directeur de Recherche – CNRS e Directeur Adjoint de ICMCB, Institut de Chimie de la Matière Condensée de Bordeaux
Arguente:	António Vieira, CEO, WeProductise
Vogal:	Alda Simões, Professor associado com Agregação, Instituto Superior Técnico – Universidade Técnica de Lisboa
Vogal:	António Câmara, Professor Catedrático, Faculdade de Ciências e Tecnologia – Universidade Nova de Lisboa
Vogal:	César A. T. Laia, Investigador Auxiliar, Faculdade de Ciências e Tecnologia – Universidade Nova de Lisboa

Fevereiro 2013

Printed electronics for ubiquitous computing applications

Table of Contents

Resumo

Este projecto de Doutoramento foca-se principalmente na síntese de materiais funcionais inorgânicos, na sua transformação em tintas e na sua deposição usando impressão por jacto de tinta em substratos não convencionais, como papel, com o objective de contribuir para o avanço do estado da arte na área dos ecrãs electrocrómicos impressos. Outros materiais, tintas, técnicas e substratos foram também explorados.

Para obter um dispositivo electrocrómico impresso, primeiro é necessário sintetizar os materiais funcionais necessários para as diferentes camadas que compõem o dispositivo; esta parte do trabalho foi focada unicamente em materiais electrocrómicos inorgânicos (óxido de tungsténio e óxido de vanádio) e em óxidos condutores transparentes (TCO). ATO (óxido de estanho dopado com antimónio) foi sintetizado usando o método de Pechini e os resultados obtidos foram promissores.

Nanopartículas de óxido de tungsténio e óxido de vanádio foram sintetizadas também por uma via de sol-gel. Medidas de FTIR, Raman e difração de raios-X mostraram que as nanopartículas de óxido de tungsténio sintetizadas por via de sol-gel são principalmente amorfas com alguns domínios cristalinos (hexagonais) e permitiram analisar a extensão de hidratação das nanopartículas. O gel de óxido de vanádio sintetizado no âmbito deste trabalho é parecido com outros previamente descritos na literatura, consistindo em $V_2O_5 \cdot 6H_2O$, com microestruturas semelhantes a V_2O_5 ortorômbico e as medições Raman também mostram a presença de domínios amorfos. O tamanho das nanopartículas foi medido combinando técnicas como difração dinâmica de luz (DLS), sedimentação e técnicas microscópicas (AFM e TEM), tendo os resultados mostrado que o diâmetro das nanopartículas de óxido de tungsténio se situa entre 160 e 200nm, e as de óxido de vanádio têm um tamanho médio de cerca de 60nm.

As nanopartículas foram usadas para produzir tintas para impressão por jacto de tinta. Para além de óxido de tungsténio e óxido de vanádio, outros materiais electrocrómicos foram impressos. Esta parte do trabalho analisa a possibilidade de imprimir vários materiais electrocrómicos orgânicos (politiofenos) e inorgânicos (óxidos metálicos e hexacianometalatos de metais) e também avalia o funcionamento destes materiais electrocrómicos depois de impressos. Poli(3,4-etilenodioxitiofeno) poli(estirenosulfonato), poli(3-hexiltiofeno), óxido de tungsténio, óxido de vanádio e azul da Prússia foram impressos por jacto de tinta em substratos flexíveis como plástico ou papel.

Foram construídos dispositivos electrocrómicos de estado sólido à temperatura ambiente em plástico e em papel, sem sinterização dos filmes impressos, mostrando, em alguns casos, um contraste excelente entre os estados ligado e desligado. Os dispositivos de óxido de tungsténio e óxido de vanádio foram caracterizados usando espectroelectroquímica com espectroscopia de absorção no Vis/NIR. O óxido de tungsténio mostra uma resposta dupla dependendo do potencial aplicado e o óxido de vanádio mostra vários passos redox, que dão origem a uma variedade de cores em função também do potencial aplicado. Todos os dispositivos foram avaliados em termos de transições electrocrómicas usando uma

análise de cor, monitorização do contraste de cor e testes de durabilidade em função do número de ciclos redox do dispositivo, assim como através de técnicas de voltametria cíclica.

Várias deposições diferentes de TCO foram também estudadas, sendo que, em condições de deposição óptimas usando pulverização catódica DC e um alvo de IZO cerâmico, foram obtidos filmes finos de IZO com uma resistência folha de 20 Ω/sq e uma transmitância óptica de 80% na parte visível do espectro solar, assim como uma estabilidade superior a 8 meses.

Globalmente, este trabalho contribui para avançar o estado da arte na área dos dispositivos electrocrómicos impressos, focando-se não só em desenvolvimentos fundamentais a nível da síntese e impressão de materiais funcionais, como também numa vertente de aplicação desses mesmos materiais em dispositivos com desempenho adequado para aplicações comerciais.

Palavras-chave: electrocromismo, dispositivos, jacto de tinta, tintas, materiais funcionais, sol-gel.

Abstract

This Ph.D. project is focused on the synthesis of functional inorganic materials, their formulation into inks and their deposition using inkjet printing on non-conventional substrates, such as paper, with the ultimate goal of advancing the state-of-the-art in the area of printed electrochromic displays. Other materials, inks, techniques and substrates were also explored.

The first step in building a printed electrochromic display is to synthesize the functional materials necessary for the different layers of the device; this part of the work focused on inorganic electrochromic materials (tungsten oxide and vanadium oxide) and on transparent conductive oxides (TCO). ATO (antimony tin oxide) was synthesized using the Pechini method and the results obtained were promising.

Tungsten oxide and vanadium oxide nanoparticles were also synthesized via a sol-gel route. FTIR, Raman and X-ray diffraction spectroscopic measurements showed that tungsten oxide nanoparticles synthesized via sol-gel are mainly in an amorphous state, with hexagonal crystalline domains, and allowed the analysis of the hydration extent of those nanoparticles. Vanadium oxide gel synthesized in this work is similar to those previously described in the literature, consisting of $V_2O_5.6H_2O$, with microstructures similar to orthorhombic V_2O_5, while Raman spectroscopy also showed the presence of amorphous domains. The nanoparticle sizes were measured combining Dynamic Light Scattering, sedimentation and microscopic techniques (AFM and TEM). Tungsten oxide particles presented an average nanoparticle size between 160 and 200 nm, and vanadium oxide of 60 nm.

The nanoparticles were used to produce ink formulations for application in inkjet printing. In addition to tungsten oxide and vanadium oxide, other electrochromic materials were printed. This part of the work examined the possibility of inkjet printing several organic (poly(thiophene)s) and inorganic electrochromic materials (metal oxides and metal hexacyanometallates) and also evaluated the performance of the resulting electrochromic devices. Poly(3,4-ethylenedioxythiophene) poly(styrenesulfonate), poly(3-hexylthiophene), tungsten oxide, vanadium oxide and Prussian blue were inkjet printed on flexible substrates, such as plastic and paper.

Solid-state electrochromic devices were assembled at room temperature on plastic and on paper substrates, without sintering the printed films, showing, in some cases, excellent contrast between the *on* and *off* state. The tungsten oxide and vanadium oxide devices were then tested through spectroelectrochemistry by Visible/NIR absorption spectroscopy. Tungsten oxide showed a dual spectroscopic response depending on the applied voltage and vanadium oxide presented several redox steps, which give rise to a variety of color transitions, also as a function of the applied voltage. Color space analysis was used to characterize the electrochromic transitions; monitorization of the color contrast and cycling tests, as well as techniques such as cyclic voltammetry, were also used to characterize device performance.

Several different TCO depositions were studied; using DC sputtering and a IZO ceramic target, thin films with a sheet resistance as low as 20 Ω/sq., with an optical transmittance of ca. 80% in the visible spectrum range, and stability above 8 months, were obtained.

Overall, this work contributes to advancing the state-of-the-art in the area of printed electrochromic devices, and focuses not only on fundamental developments in terms of synthesis and printing of functional materials, but also on the application of those materials on solid-state devices with adequate performances for commercial applications.

Keywords: electrochromism, devices, inkjet, inks, functional materials, sol-gel.

Abbreviature List

a	Length of contacts
A	Ampere
a*	CIELAB coordinate relative to the redness-greenness of the color
a.u.	Arbitrary units
Abs	Absorbance
AC	Alternating current
ADI	Agência de Inovação
AFM	Atomic force microscopy
Ar	Argon
AZO	Antimony-doped zinc oxide
b*	CIELAB coordinate relative to the yellowness-blueness of the color
C	Coulomb
CE	Coloration efficiency
CeO_2	Cerium oxide
CF_4	Tetrafluoromethane
CIE	Comission international de l'Éclairage
CIJ	Continuous inkjet
cm	Centimeter
Co	Cobalt
cP	Centipoise
Cr	Chromium
CT	Charge transfer
CTAB	Cetyl trimethylammonium bromide
d	Film thickness
D	Diffusion coefficient
d	Particle diameter
D_0	Diffusion coefficient at infinite dilution
D65	Standard illuminant defined by CIE
DC	Direct current
DG	Diethylene glycol
DLS	Dynamic light scattering
DMP	Dimatix materials printer
DOD	Drop-on-demand
DSC	Differential scanning calorimetry

E (V)	Electric potential (Volt)
E (eV)	Energy (electron Volt)
E (kJ.mol^{-1})	Energy (kilo Joule per mole)
e-	Electron
EB	Electron beam
ECD	Electrochromic device
ECM	Electrochromic material
EGMBE	Ethylene glycol monobutyl ether
Ei	Coefficient of the Standard Illuminant CIE
emf	Electromotive force
E_p^a	Oxidation peak potential
E_p^c	Reduction peak potential
eV	Electron Volt
Fe	Iron
FTIR	Fourier transform infrared spectroscopy
FTO	Fluorine-doped tin oxide
g	Gravity acceleration constant
Hz	Hertz
I	Electric current
I	Intensity of the transmitted light
I_0	Light intensity from a light source
ICI	Imperial chemical industries
ICP-MS	Inductively coupled plasma mass spectrometry
I_p^a	Oxidation peak of current consumption
I_p^c	Reduction peak of current consumption
Ir	Iridium
IR	Ohmic potential
ITO	Tin-doped indium oxide
IZO	Indium oxide doped with zinc oxide
J	Joule
JCPDS	Joint Committee on Powder Diffraction Standards
K_B	Boltzmann constant
L*a*b*	L*a*b* tristimuli CIE color space
LCD	Liquid crystal display
Li	Lithium
Li+	Lithium cation

LiClO$_4$	Lithium perchlorate
M	Molar
M	Metal
M+	Metal cation
mm	Millimeter
Mn	Manganese
Mo	Molybdenum
N	Newton
N$_2$	Nitrogen
NaOH	Sodium hydroxide
Nb	Niobium
Ni	Nickel
NIR	Near infrared region radiation
nm	Nanometer
O$_2$	Oxygen
OLED	Organic light emitting diodes
P3HT	Poly(3-hexylthiophene)
Pa	Pascal
PAA	Polyacrylic acid
PB	Prussian Blue
PDDA	Poly(diallyldimethylamonium chloride)
PEDOT	Poly(3,4-ethylenedioxythiophene)
PEN	Polyethylene naphthalate
PEO	Polyethylene oxide
PET	Polyethylene terephthalate
PIXE	Particle-induced X-ray emission
pl	Picoliter
PLD	Pulsed laser deposition
PML	Polymer multi-layer
PMMA	Poly(methyl methacrylate)
PPG	Polypropylene glycol
PPO	Polypropylene oxide
PSS	Poly(styrenesulfonate)
PVA	Polyvinyl alcohol
PvOH	Polyvinyl alcohol
PVP	Polyvinylpyrrolidone

Q	Charge consumption
Q_b	Charge consumption for the bleaching process
Q_c	Charge consumption for the coloration process
R	Electric resistance
Rsq	Electric sheet resistance
r	Radial position
R&D	Research and development
RBS	Rutherford backscattering spectrometry
RF	Radio-frequency
RGB	Red, green and blue additive color system
Rh	Rhodium
S	Siemens
s	Second
sccm	Standard cubic centimeters per minute
SCE	Saturated calomel electrode
SDS	Sodium dodecyl sulfate
sq	Square
t	Time
T	Transmittance
T	Absolute temperature
Ta	Tantalum
TCO	Transparent conductive oxide
TEM	Transmission electron microscopy
TFT	Thin-film transistor
TGA	Thermogravimetric analysis
Ti	Titanium
T_i	Optical transmittance at a specific wavelength
TiO_2	Titanium oxide
TX-100	Triton X 100
u	Sedimentation velocity
u_{calc}^g	Calculated sedimentation velocity for earth gravity
u_{exp}^g	Experimental sedimentation velocity for earth gravity
UNL	Universidade Nova de Lisboa
UV	Ultraviolet
V	Volt
v/v	Volume/volume

V_2O_5	Vanadium oxide
Vis	Visible region radiation
Voff	Resting voltage
W	Tungsten
W	Watt
w/v	Weight/volume
w/w	Weight/weight
WO_3	Tungsten oxide
X^-	Anion species
X, Y, Z	Theoretical tristimuli values
x_i	Coefficient of the tristimulus value
X_n, Y_n, Z_n	White color values for the illuminant used
XRD	X-ray diffraction
XRF	X-ray fluorescence
ΔA	Absorbance variation
Δa^*	Variation of the CIELAB coordinate relative to the redness-greenness of the color
Δb^*	Variation of the CIELAB coordinate relative to the yellowness-blueness of the color
ΔE	Color contrast
ΔL^*	Variation of the CIELAB coordinate relative to the luminance of the color
ΔT	Transmittance variation
2φ	2-theta angle
α	Virial coefficient
$\Delta \rho$	Density difference between particles and solvent
η	Viscosity
λ	Wavelength
μm	Micrometer
μs	Microsecond
v	Wavenumber
υ	Frequency
ρ	Density
ρ	Resistivity
τ_b	Time for bleaching
τ_c	Time for coloration
ϕ	Volume fraction
ω	Angular velocity
Ω	Ohm

Figures Index

xxiii

Tables Index

Preface

This work is a contribution to the ubiquitous computing area. The term ubiquitous computing refers to the acquisition, processing and visualization of information through components like sensors, actuators, processors, screens or projectors embedded into everyday objects, such as walls, furniture, clothing, books, advertising displays, etc. The father of ubiquitous computing, Mark Weiser, once wrote: "The most profound technologies are those that disappear. They weave themselves into the fabric of everyday life until they are indistinguishable from it. (…) Such a disappearance is a fundamental consequence not of technology, but of human psychology. (…) Ubiquitous computing will help overcome the problem of information overload. There will be more information available at our fingertips during a walk in the woods than in any computer system, yet people find a walk among trees relaxing and computers frustrating. Machines that fit the human environment, instead of forcing humans to enter theirs, will make using a computer as refreshing as taking a walk in the woods."[1] Following this inspiring vision, António Câmara, of YDreams, started the "Reality Computing" initiative in 2006 with the objective of developing smart and interactive objects based on simple technologies of physical and/or chemical nature bridging the gap between "paper and pen" communication and state-of-the-art conventional computing.

YDreams was created in 2000 as a spin-off of Universidade Nova de Lisboa's (UNL) research programs in multimedia, virtual reality, geographic information systems and mobile computing. The first three years of operations were dedicated mostly to intensive R&D initiatives in order to develop advanced technologies and prepare YDreams to achieve a leadership position in projects, services and products. YDreams also invested strongly into building a solid intellectual property portfolio based on the company's core proprietary technologies. YDreams and UNL started a joint research initiative involving a multi-disciplinary team drawn from YDreams' YLabs and from UNL's Photochemistry and Supramolecular Chemistry Group and CENIMAT (Centre for Materials Research). Each project member brought to the group its own expertise, namely in Interactivity and Interface Design (YDreams), electrochromic technology (Photochemistry Group), and metal oxides' processing (CENIMAT).

In mid-2006, the initiative was extended with the signing of three separate R&D contracts between YDreams/UNL and three industrial partners. These projects were sponsored by the Portuguese Government's Agência de Inovação (ADI), and their purpose was to study the viability of assembling electrochromic displays using as substrates the materials manufactured or transformed by each of the industrial partners: paper company Renova S.A., textile company Fábrica de Malhas Filobranca S.A., and visual communication products manufacturer Bi-silque S.A.

Each of these projects lasted around 18 months, having finished at the end of June 2008. This Ph.D. work started within the context of these projects. The results achieved during the projects led to a continued R&D effort in this technological area and contributed to motivate YDreams to create a spin-out company focused on this new technology and its commercialization. Ynvisible was formally created in

January 2010.

Ynvisible is dedicated to the development and commercialization of innovative technologies that bring new interactive properties and functionalities to existing substrates and products (see examples in Figure 1). The company´s vision is to bring everyday objects and surfaces to life, making them more useful and enjoyable to people. Ynvisible adapts functionalities familiar to consumers from on-line / digital experiences and applies these to physical (printed) objects. Ynvisible sees advertising and marketing applications offering the first opportunities to opening a market for interactive solutions in everyday items. Global advertising media spend in 2010 was 450 billion USD and roughly ¼ of this value was spent by the top 100 advertisers – most of them producers of physical goods.

Figure 1: Examples of new conceptual interactive products: A) Greeting cards, B) Fast food tray papers, C) Advertising panels, D) Board games.

The present Ph.D. dissertation is the result of a cooperative work executed in the last years as a combined Ph.D. between UNL's Chemistry Department and YDreams, and was co-funded by YDreams and Fundação para a Ciência e a Tecnologia through a BDE scholarship (Bolsa de Doutoramento em Empresa).

The main objective of this PhD work is to meet the R&D objectives of both YDreams and Ynvisible, by developing simple interactive devices based on chemical reactions, such as electrochromic devices, using several types of substrates, like paper, cork, fabric, glass, leather, ceramics, plastic, concrete or wood, in a way that new interactive applications can emerge for already existing products, using cost-effective, industrial printing technologies. Printing technologies have been referred to as the

future of electronics: "printed electronics". The use of common substrates and the choice of cost-effective printing and converting techniques will allow high volume production of quasi-disposable devices.

More specifically, this thesis is focused on the synthesis of functional inorganic materials, their transformation into inks and their deposition using inkjet printing on non-conventional substrates, like flexible plastics and paper. However, other materials, inks, techniques and substrates were also explored. Chapter 1 is an introduction to all the concepts, techniques and materials studied in this work, including also a review of the state-of-the-art for all the different topics. Chapter 2 is the main section of this dissertation and presents the experimental work conducted during the Ph.D. and the main results achieved. This chapter was divided according to the different areas explored during this project and discusses the results that were obtained in the context of the state-of-the-art and existing literature.

To obtain a printed electrochromic device, first, the functional materials must be synthesized; this part of the work was focused on inorganic electrochromic materials (tungsten oxide and vanadium oxide) and on transparent conductive oxides (TCO). With these functional materials, inks must be developed and printed; a description of the formulation and printing of several electrochromic materials (PEDOT:PSS, P3HT, PB, vanadium oxide and tungsten oxide) can also be found in Chapter 2. Finally the devices are built with these printed materials; this sub-chapter presents the results obtained for different device architectures on different substrates and with different inks, as well as a more specific study of the spectroelectrochemistry behavior obtained for vanadium oxide and tungsten oxide. During this Ph.D. work, a constant need to find ways to make conductive surfaces on different substrates led to a separate section of complementary work (Chapter 3). A description of several approaches that were tested can be found in Chapter 3. Conclusions and future work are presented at the end of this document, as well as the description of some products created by Ynvisible and an assessment of Ynvisible's technological competitiveness and differentiating factors, followed by the list of publications and bibliography.

Special thanks also to my colleagues from Ynvisible for the great work environment created in these years. I like to think of this Ph.D. work also as a result of teamwork; I hope to reflect, in this thesis, our self-learning, determination and will power to always achieve better in a quasi-new field in Portugal.

Thank you also to Prof. Elvira Fortunato and Prof. Rodrigo Martins for their contribution in the beginning of this project.

Finally, I would like to thank my family for their unconditional support and affection.

---

[1] Weiser,M. SIGMOBILE Mob. Comput. Commun. Rev.3, 3 (1999) 3-11.

1 General Introduction

1.1 Electronic displays

In the last ten years, a new display technology was developed called electronic paper or e-paper. This is the common name given to new flexible displays based on optical contrast, which use photographic paper, plastic or metal foils as substrates. There are, nowadays, several technologies used to produce e-paper that differ from each other in the choice of active materials (electrophoretic inks, electrochromic and/or conductive polymers, etc.), substrates (paper, plastic or metal) and production methods.

There are several applications in the market for electronic paper, from high-resolution displays used in electronic e-book readers to configurable advertising panels[2,3,4,5,6,7].

The main mass product that uses e-paper technology is the "e-reader". E-readers are electronic devices that have some paper attributes (like definition and contrast) but are not based on cellulose. In addition to e-readers, the main e-paper applications are: smart labeling systems, advertising panels, smart packaging, smart cards, cellphone displays and other devices (Figure 2)[8,9,10,11].

Figure 2: Some examples of e-paper applications.

The most broadly used e-paper technology is based on a change of contrast from white to black, created by electrophoretic inks (Figure 3) and developed by E-Ink®. Electrophoretic inks consist of white and black particles suspended in a fluid in a microcapsules form: when a positive potential is applied, the white particles migrate through the fluid to the surface of the microcapsule; if the applied potential is negative, the black particles are attracted to the microcapsule surface. Therefore, a change in color can be seen depending on the applied potential at the surface of the device (Figure 3). It is also possible to add color filters that allow other colors, in addition to black and white, to be observed[12,13].
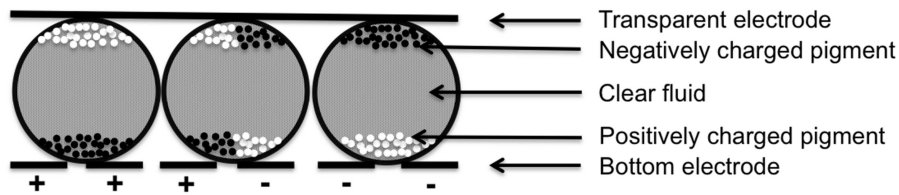
Figure 3: The working principle of E-ink's electrophoretic inks.

Comparing electrophoretic technology with electrochromic devices, some advantages can be pointed out for electrochromic devices:

- The production method through printing techniques is simpler, more efficient and less expensive than the production methods associated with electrophoretic displays.
- Electrochromic devices are produced in solid-state, while electrophoretic technology always needs a fluid, leading to more demanding encapsulation technologies.
- Electrochromic devices can be fully transparent, while electrophoretic always have a back color.

1.2   Electrochromic Devices

An electrochromic device (ECD) is a multi-layer electrochemical system containing functional materials (electrochromes) that change color (through a reversible redox process), when a potential is applied. To obtain such effect, a device with two electrodes separated by an electrolyte must be built. The electrochromic layers are in direct contact with the electrodes to allow for the electron exchange process that leads to color change to occur.

There are several possible applications for materials that have the ability to change color reversibly under the application of a low potential, the most important ones being:

- Information displays: the device consists of an electrochromic film deposited on a white pigment surface that can be patterned. They present an excellent contrast and a reading angle higher than liquid crystals.

- Variable reflectance mirrors: this device is the most commercially successful product using electrochromics. They are used in rearview mirrors in the automobile industry. The electrochromic material is deposited on top of a material with a specular reflection. "Schott", in Germany, developed this technology.[14]

- Smart windows: the working principle is to build an electrochromic device with variable transmittance that allows the control of the light intensity that passes through the window. The term "smart window" was first introduced by Svensson and Granqvist[15,16].

- Variable emittance surfaces: these devices are based on a special architecture with a crystalline WO_3 film deposited on the exposed to solar light side. The intercalation and deintercalation of cations causes infrared radiation to be absorbed or reflected, resulting in a lower or higher thermal emission, respectively[17].

State-of-the-art electrochromic devices are used mostly in smart windows and rearview mirrors (Figure 4). Two different electrochromic materials with complementary properties are used in the electrode and counter-electrode. When the first electrochromic material is reduced (at the cathode) and changes from colorless to colored, the complementary electrochromic material also changes in the same manner, and vice-versa (during the oxidation at the anode), meaning that the two electrochromic materials reach bleached and colored states at the same time and this fact will enhance the contrast between these two states. This technology is already used on substrates like glass or plastic[18,19,20,21].

Figure 4: Examples of commercially available products based on electrochromics.

There are already a few companies that merged together the concept of e-paper and electrochromism. Figure 5 shows some devices produced by [®]ACREO. The substrate used is photographic paper, a coated paper. The structure exploited is a parallel structure where the electrochromic material and the counter electrode are the same material and are deposited at the same level, physically separated by a solid electrolyte. The planar structure of the device implies that part of the coloration is always visible; the design never has a transparent state (see Figure 146, in section "products and competitiveness study")[22],[23]. The production method used is a roll-to-roll printing process.

Figure 5: Electrochromic devices created by ACREO®.

®NTERA is another company that explores the e-paper vision with electrochromic materials (Figure 6). In this case, the substrate used is plastic and the back of the device is white because the electrochromic material is adsorbed onto inorganic nanoparticles (titanium oxide (TiO_2)). Those nanoparticles are deposited on top of a reflector film to enhance the contrast (see Figure 147 in section "products and competitiveness study)[24,25].

Figure 6: Electrochromic devices created by NTERA®.

1.2.1   Electrochromism

Electrochromism is the phenomenon exhibited by some materials that change color when an electric potential is applied. To see such change, a cell composed by two electrodes separated by an electrolyte (in the case of solid-state devices) must be prepared (Figure 7) or two electrodes must be immersed in a liquid electrolyte. The optically active material can be an organic or inorganic substance that is able to convert between two or more color states upon oxidation or reduction. In a solid-state device, each electrode is composed of a substrate (at least one of them must be transparent or translucide) coated with a transparent conductive material (at least one of them must be transparent or translucide). On top of the conductive material layer, an electrochromic material is deposited (on one electrode) and on the other electrode a counter-electrode is needed. The electrolyte is responsible for the ionic current inside the cell between the two electrodes.
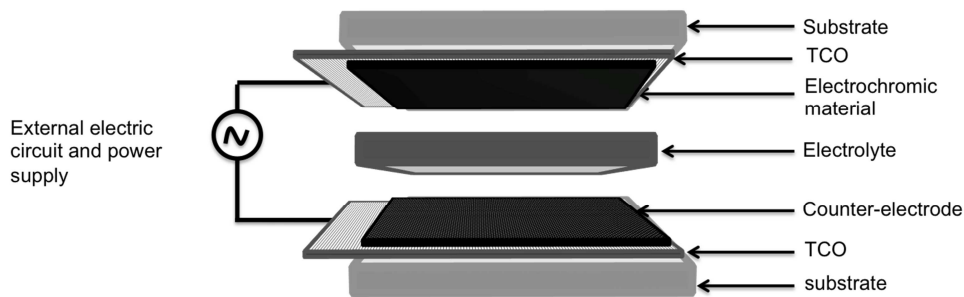
Figure 7: Architecture scheme of a solid-state electrochromic device.

In this work, it was decided to use the same electrochromic material at both electrodes, thereby producing symmetric devices. To see the color transitions, the devices had to be pattern in such a way that the two electrochromic materials were not overlapping (Figure 8). Using this scheme, it is possible to have interesting color and pattern animations, by taking advantage of different design effects. This characteristic is an innovation in terms of design capability, animations and transition speed between electrodes, when compared with already existing technologies.
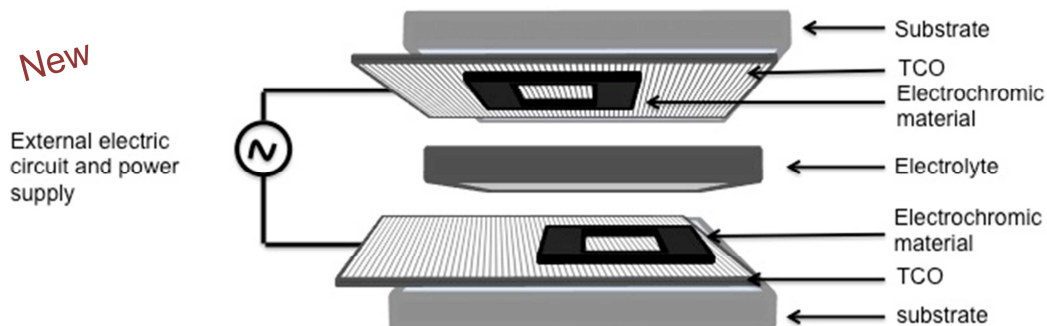
Figure 8: Scheme of the solid-state electrochromic device architecture used in this work. The substrate used was PET coated with ITO, or paper coated with IZO.

1.2.2 Electrochromic materials

Electrochromic materials can be divided into four main groups: metal oxides, organic molecules (such as viologens), conjugated semiconductor polymers, and metal coordination complexes. In this work, only metal oxides were synthesized (Chapter 2), but, in addition to metal oxides, two conjugated semiconductor polymers (PEDOT:PSS (Poly(3,4-ethylenedioxythiophene):poly(styrenesulfonate)) and P3HT (poly(3-hexylthiophene))), and one metal coordination complex (PB (Prussian Blue)), for which the chemical structure is shown in Figure 9, were formulated as inks, printed and assembled into electrochromic devices. However, metal oxides were the main focus of this work, so, the present section focuses mostly on these electrochromic materials.

7
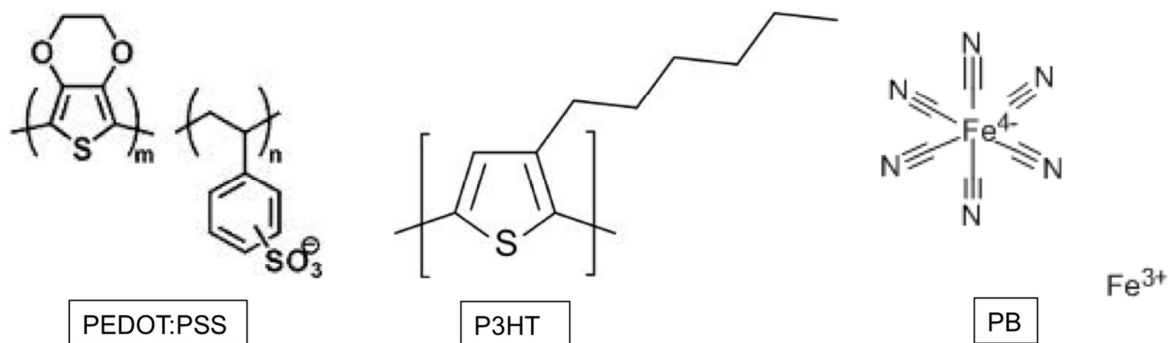
Figure 9: Chemical structure of PEDOT:PSS, P3HT and PB.

Some History…

In 1704, Diesbach discovered the optical effects of Prussian blue[26]. In 1815, Berzelius described that a change in color is seen when hydrogen passes through slightly heated WO_3[27]. In 1824, Wohler noticed a change in color of WO_3 with sodium[28]. In 1930, the electrochemical reduction of WO_3 was studied by Kobosew and Nekrassow, who described that WO_3 can change its color to blue using electrochemical reduction in an acidic solution, concluding that the hydrogen atom was responsible for the reduction of WO_3[29]. In 1942, the first step to electrochromic devices happened with Tamley's study about films coloration of molybdenum and tungsten oxide particles associated with their electrochemical reduction[30]. In 1951, Brimm talked about the reversibility of tungsten oxide[31] and, in 1953, Kraus wrote an unpublished laboratory report about tungsten oxide electrochromism[32]. In 1960, Imperial Chemical Industries (ICI) in England and Philips (Dutch division) are the first companies interested in commercializing electrochromic products. The first devices are composed by aqueous Viologens[33],[34],[35]. In 1961, Platt introduces the term "electrochromism"[36]. In 1969, Deb published two scientific papers about WO_3 electrochromism that mark the beginning of the general interest for electrochromism and are still cited today[37],[38]. In 1978, Mohapatra described, for the first time, the redox mechanism for WO_3 with lithium[39] as:

$$WO_3\ (s)\ +\ xLi^+\ (aq)\ +\ e^-\ \rightleftarrows\ Li_xWO_3\ (s)$$
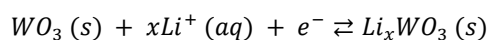
Electrochromism of metal oxides is found in the elements of the periodic table belonging to the transition metals group. These metals are presented in Figure 10. Elements shown in black present a cathodic coloration (Ti, Nb, Mo, Ta and W) and those with anodic coloration are represented in gray (Cr, Mn, Fe, Co, Ni, Rh and Ir). Vanadium is an exception among transition metals, since vanadium pentoxide has both cathodic and anodic coloration.

Figure 10: Periodic table elements that can form electrochromic oxides. Black: cathodic coloration and gray: anodic coloration.

Only Ti, Ni, Nb, Mo, Ta, W and Ir oxides present a completely transparent state in the visible region of the spectrum. There are also binary or ternary combinations of these oxides. Some colorations obtained with several of those metal oxides are presented in Table 1.[40,41]

Table 1: Oxidized and reduced form obtained for some electrochromic metal oxides.

Metal	Oxidized form / color	Reduced form / color
Cobalt	$LiCoO_2$ / pale yellow	M_xLiCoO_2 (M≠Li) / dark brown
Iridium	$IrO_2.H_2O$ / blue-gray	$Ir(OH)_3$ / colorless
Iron	Fe_2O_3 /brown	$M_xFe_2O_3$ / black
Manganese	MnO_2 / brown	M_xMnO_2 / yellow
Molybdenum	MoO_3 / colorless	M_xMoO_3 / intense blue
Nickel	$Ni^{II}_{(1-x)}Ni^{III}_{(1-y)}H_{(z-x)}$ / black	$Ni^{II}O_{(1-y)}H_z$ / colorless
Niobium	Nb_2O_5 / colorless	$M_xNb_2O_5$ / blue
Rhodium	Rh_2O_3 / yellow	RhO_2 / dark green
Tantalum	Ta_2O_5 / colorless	TaO_2 / pale blue
Titanium	TiO_2 / colorless	M_xTiO_2 / blue-grey
Tungsten	WO_3 / pale yellow-transparent	M_xWO_3 / intense blue
Vanadium	V_2O_5 / Brown-yellow	$M_xV_2O_5$ / pale blue

Table 2 resumes the techniques normally used to deposit electrochromic metal oxides. These techniques are divided in three main groups: physical, electrochemical and chemical methods. In physical methods, techniques such as evaporation and sputtering can be found. In electrochemical methods, electrodeposition and anodization are highlighted, and, as chemical methods, techniques such as spray pyrolysis, decomposition reactions and thermal oxidation are emphasized. Some of these techniques have variations that are also pointed out.

Table 2: Techniques used to deposit electrochromic metal oxides and possible variations.

Category	Technique/Method	Variations
Physical	Evaporation	Vacuum
		Reactive (O_2 / N_2 / H_2O)
		Ion assisted
	Sputtering	Non-reactive (Ar)
		Reactive (Ar / O_2)
		"Chemical" (O_2 / CF_4)
Electrochemical	Electrodeposition	-----------
	Anodization	-----------
Chemical	Vapor deposition	Atmospheric pressure
		Low pressure
		Plasma enhanced
	Sol-gel	Dipping
		Spin-coating
		Spraying
	Spray pyrolysis	------------
	Decomposition reaction	------------
	Thermal oxidation	------------

To deposit metal oxides using a printing technique, an ink must be developed. This ink must preserve all the properties of the functional material. Sol-gel materials appear to be a promising way to achieve this goal[53, 54]. It can be noticed, from the techniques or methods presented in Table 2, that sol-gel is the only one that can give the final product during the reaction step and not only when deposited onto the substrate. It is then possible to produce the functional material nanoparticles to use afterwards as the main component of the ink for inkjet printing. There are other methods to produce nanoparticles such as milling processes, but sol-gel appears to be the simplest and most cost-effective method. This approach produces selected, more complex structures from atoms or molecules as well as better controlled sizes and shapes.

1.2.3   Electrically conductive materials

As explained above, to build an electrochromic device, at least one electrode must be transparent. In this project, since the main idea was to build electrochromic devices on different substrates, it would be interesting to have both electrodes transparent: one to allow the bottom substrate to be seen and the other to allow the observation of the displayed message. For this reason, only methods to obtain transparent electrodes were considered. Commercially, only glass and plastic can be found with a transparent conductive coating.

Materials can be divided into three groups regarding their electric conductivity (or resistivity). They can be conductors, semiconductors or insulators (Figure 11). For electrochromic device applications, the materials must be conductors (or semiconductors, in the limit to conductors).

Conductors	Semiconductors	Insulators
⇩	⇩	⇩

Conductivity	$> 10^3$ S/cm	10^3 S/cm – 10^{-8} S/cm	$< 10^{-8}$ S/cm
Resistivity	$< 10^{-4}$ Ω.cm	10^{-4} Ω.cm – 10^7 Ω.cm	$> 10^7$ Ω.cm
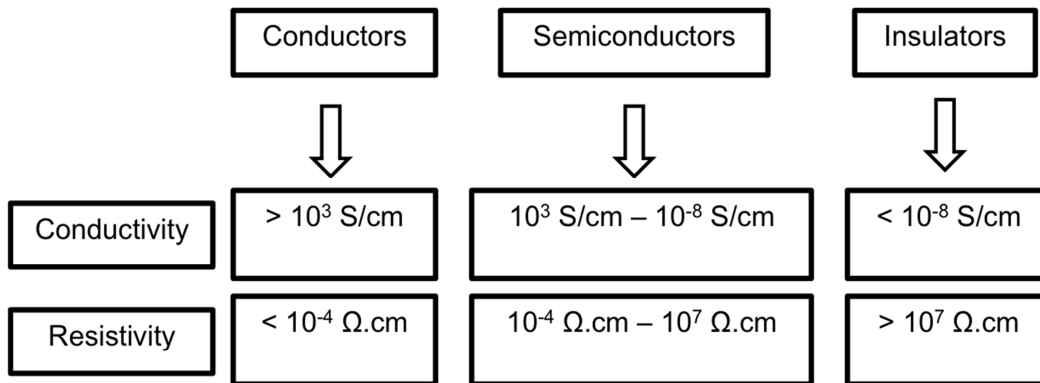
Figure 11: Classification of materials regarding their conductivity and resistivity.

There are several approaches to make a substrate electrically conductive: metals (thin films or meshes), semiconductor polymers (thin films), carbon based materials (thin films or meshes) and transparent conductive oxides (thin films).

<u>Metals</u>

Metals are conductors by definition. In printed electronics the metals most commonly used are copper, silver, gold or platinum. Creating a transparent electrode based on metals is a challenge because metals are opaque and shiny by nature. The strategy to obtain these materials as transparent electrodes is to deposit thin films or meshes with very fine lines. To produce thin films, methods such as thermal evaporation, pulsed laser deposition or sputtering are normally used. To build meshes, printing methods can be used (using nanoparticles of these metals). Several conductive inks based on metals are commercially available. From several contacts with producers of those metals at printed electronics conferences, we learned that the problem with metals is that they are not electrochemically stable, so their use in electrochromic devices is rather limited.

<u>Carbon based materials</u>

Materials such as graphite, graphene or carbon nanotubes are used. Like metals, these materials are also opaque, so, the same strategy is needed to obtained transparent electrodes: thin films or meshes. In the last few years, an effort has been made to create conductive inks (for printing methods) and products with carbon because, unlike metals, they are electrochemically stable. Also from contacts made in

conferences, we understood that these carbon-based conducting films are being strongly developed in the industry (and in academia) but they are still difficult to obtain commercially and very expensive, since there aren't optimized industrial methods for their production.

Semiconductor polymers

The interest in semiconductor polymers increased in the last years due to the possibility of combining electrical conductivity and plastic characteristics. Some examples of conductive polymers are: polyacetylene, polythiophene, polyaniline, polyphenylene, polypyrrole and derivatives. PEDOT (polythiophene), synthesized by Bayer laboratories, has been extensively studied and is commercialized by H.C. Starck and Agfa. These materials have strong colors, so their application as transparent conductors must be as thin films using techniques such as spin coating or printing. It is also possible to use physical techniques such as plasma polymerization.

In a near future, depending on the final application and on the production method chosen, the choice of the most adequate conductive material will diverge. For electronic devices in general, such as cell phones, TVs, etc., it is likely that the best choice will be carbon based materials (probably graphene). This material still presents serious technological challenges, such as the difficulty to deposit one single layer of material with no defaults, to allow a perfect electric conductivity close to metals with a high transparency. These materials also present a significant limitation, which is the impossibility to use printing techniques, therefore increasing the production cost. Due to their lack of electrochemical stability, and although some research groups are already trying to encapsulate them to increase their stability, metals do not seem to be a viable choice in the near future. Conductive polymers are now an attractive option because they can be deposited using printing techniques, but their electric conductivity and transparency is limited. In electrochromic devices applications, the use of most of these materials is also limited because they are chemically and/or electrochemically unstable. However, conductive polymers can be used simultaneously as electrochromic materials, which has been Acreo$^{®}$'s approach. TCO's seem to be the most viable choice in the short/medium term as the electrodes for ECDs. It will be necessary to substitute Indium, but this topic is already being extensively studied. The use of TCO's with printing techniques is also being developed using sol-gel approaches. For the sinterization step, some alternatives to temperature are also emerging, allowing their use on flexible and heat sensitive substrates. Therefore, it seems that the fastest and most lucrative development in this field will be to obtain a TCO in ink form, that can be used with different printing techniques, and replace the sinterization step using temperature by a high energy light pulse, allowing its deposition on flexible and heat sensitive substrates.

In this work, some of these alternatives to create transparent conductive materials were tested, but the focus was put on TCO's (transparent conductive oxides). Over the last years, the field of TCO's became a

hot topic and a vast amount of work has been reported describing new materials, new deposition techniques and new approaches. This intense activity in the field occurred because these materials meet the requirements for printed electronics, concerning both conductivity and transparency.

The most common choice among TCO's is indium-tin oxide (ITO), but there are other possibilities like Al-doped zinc oxide (AZO), Zn-doped indium oxide (IZO) or F-doped tin oxide (FTO). These materials have good electric conductivities and high transparency in the visible region. Commercially, only conductive glass and plastic (with TCO) may be found.

Some history[42]…

1907 - Badecker produced for the first time a TCO using cadmium deposited by sputtering.
1947 – ATO was deposited for the first time by Mochel using spray pyrolysis[43].
1947 – ITO was used as TCO by Zunick[44].
1993 – Sato described for the first time a p-type TCO (NiO).
1995 – IZO was deposited using sputtering by Manami.

TCO's can be of two types: n-type or p-type. Figure 12 illustrates these two possibilities for a silicon semiconductor. n-type TCO's have more negative charge carriers than positive holes. Elements such as phosphorus, with 5 valence electrons, are used as doping agents. p-type TCO's have more positive holes than negative charge carriers. Elements such as boron or aluminum, with 3 valence electrons, are used as doping agents.
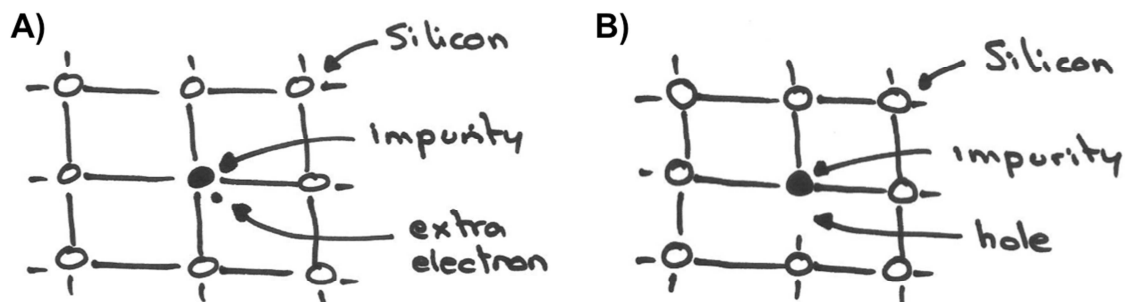
Figure 12: types of TCO: A) n-type and B) p-type.

TCO's are normally deposited by physical techniques, such as thermal evaporation, sputtering, vapor deposition and pulsed laser. Sol-gel methods are also a possibility to produce these materials; sol-gel produced TCO's are deposited by spin coating, dip coating or spray on the substrate. They need to be sintered at high temperatures to make them conductive and, because of that, only glass can be used. Printing methods are also referred to as a possible technique to deposit TCO's and some results have already been reported using inkjet and gravure printing[45, 46, 47, 48,49]. Table 3 resumes the best results from the literature in terms of resistivity obtained for TCO's, as well as the method used for deposition.

Table 3: Best results in terms of resistivity obtained for TCO and method used for deposition[42].

Composition	Method	ρ ($\times 10^{-4}$ Ω cm)
Al:ZnO	PLD	0.85
Al:ZnO	Sputtering	1.39
ITO	PLD	0.95
ITO	RF magnetron sputtering	1.2
Mo:In_2O_3	Sputtering	1.6
ITO	Spray	0.77
ITO	Nanowires	0.629
Mo:In_2O_3	RF magnetron sputtering	1.5

The TCO commonly used in optoelectronics, in devices such as TFTs, OLEDs, solar cells (Figure 13) or electrochromic devices, is ITO, but there are several other possibilities for these applications. They are n-type, as mentioned above, only because p-type TCO's appeared for the first time in 1993 and they are not yet optimized to be used in such applications. See Table 4 for a list of TCO materials described in the literature[50].

Table 4: TCO materials most often described in the literature and dopants used.

Material	Dopant
SnO_2	Sb, F, As, Nb, Ta
In_2O_3	Sn, Ge, Mo, F, Ti, Zr, Hf, Nb, Ta, W, Te
ZnO	Al, Ga, B, In, Y, Sc, F, V, Si, Ge, Ti, Zr, Hf
CdO	In, Sn
ZnO-SnO_2	
ZnO-In_2O_3	

$In_2O_3\text{-}SnO_2$	
$CdO\text{-}SnO_2$	
$CdO\text{-}In_2O_3$	
$GaInO_3$, $(Ga, In)_2O_3$	Sn, Ge
$CdSb_2O_6$	Y
$ZnO\text{-}In_2O_3\text{-}SnO_2$	
$CdO\text{-}In_2O_3\text{-}SnO_2$	
$ZnO\text{-}CdO\text{-}In_2O_3\text{-}SnO_2$	
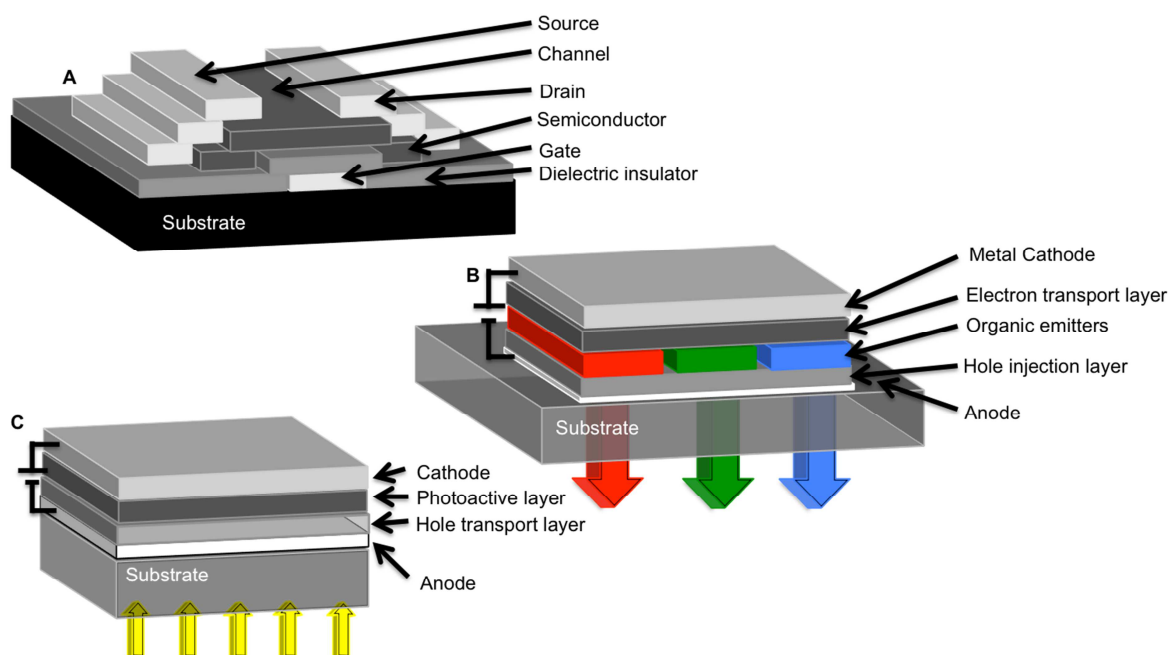
Figure 13: Optoelectronic Devices and possible configurations: A) TFT B) OLED C) Solar cell.

For electrochromic device applications, TCO's need to have a fast charge transfer and sheet resistance between 1 and 100 Ω/sq. ITO and FTO are the TCO materials most commonly applied. ITO is a very expensive material, normally deposited using sputtering. FTO is more accessible in terms of price and is deposited preferably by spray pyrolysis[40,41].

1.2.4 Electrolytes

In electrochromic devices, the electrolyte is responsible for the ionic current inside the cell between the two electrodes. During the coloration and bleaching (for electroneutrality) it supplies the mobile ions that enter and leave the facing electrochrome layers. In other words, it is an ionic conductive material but it must be also electronically insulator. It can be as simple as a salt dissolved in a solvent such as water, but scientific and industrial development has been focused on gel and solid electrolytes. The main advantage

of gel or solid electrolytes when compared to liquid electrolytes is that they are easier to confine between the two electrodes. They can also work as laminators holding the two electrodes together and they minimize the pressure that can cause substrate deformation and leakage problems[41].

Liquid electrolytes can be either aqueous or polar organic solvents such as nitriles, dimethylformamide or propylene carbonate with an ionic salt dissolved in it such as lithium perchlorate ($LiClO_4$), Trifluoromethanesulfonic acid (CF_3SO_3H) or Phosphoric acid (H_3PO_4). The majority of solid-state electrochromic devices use inorganic solids or organic polymers, the last one being flexible and resistant to mechanical stress. As inorganic solids, materials such as $LiAlF_4$, TiO_2, ZrO_2 or Ta_2O_5 can be pointed out. As organic polymers Nafion, PMMA or PEO can be highlighted. The viscosity of such polymer electrolytes can be adjusted using different molecular weight. Increasing molecular weights will increase the viscosity, so, it is possible to have liquid polymer electrolytes or others that behave as rigid solids. Another interesting approach is to use UV curable electrolytes. In this case, it is possible to have a liquid material to deposit using printing techniques for example, and then to cure the deposited film having, in the end, a solid-electrolyte with all the advantages related to it.

In this Ph.D. work, the electrolyte layer was not developed or studied. The materials used for this layer were developed by Ynvisible team and have been used as received. Three different electrolytes were used: a polymer gel (1st generation electrolyte) and two UV curable (3rd and 4th generation electrolytes) described in the experimental section.

1.3 Functional Inks

To produce the functional inks reported in this work, the same approach was used for all of them; first, the functional material was synthesized using sol-gel techniques to obtained the powder (or nanoparticles), then the powder was redispersed in solvents to form the ink and finally this ink was printed on the substrate and sintered when needed. The synthesis methods of each one of the functional materials tested are better described in the experimental section (2.4). The solvents used were always the most "green" as possible and water was always preferred to organic solvents.

1.3.1 Sol-gel method

Sol-gel is a methodology of materials preparation, starting with molecular precursors in which an oxide net is obtained via inorganic polymerization. These reactions occur in solution. Sol-gel processes have gain interest in the last decades because the obtained materials have high purities, homogeneity and low processing temperatures when comparing with traditional methods like vapor deposition techniques, evaporation or sputtering. One important characteristic of sol-gel is the possibility to control all the steps from molecular precursors to the final product, allowing a better control of all the process and the possibility to obtain materials with different properties (Figure 14).[52]

There are two possible sol-gel routes: alkoxide precursors in organic solvents or inorganic precursors in aqueous solutions. These two routes involved always two steps: hydrolysis and condensation.
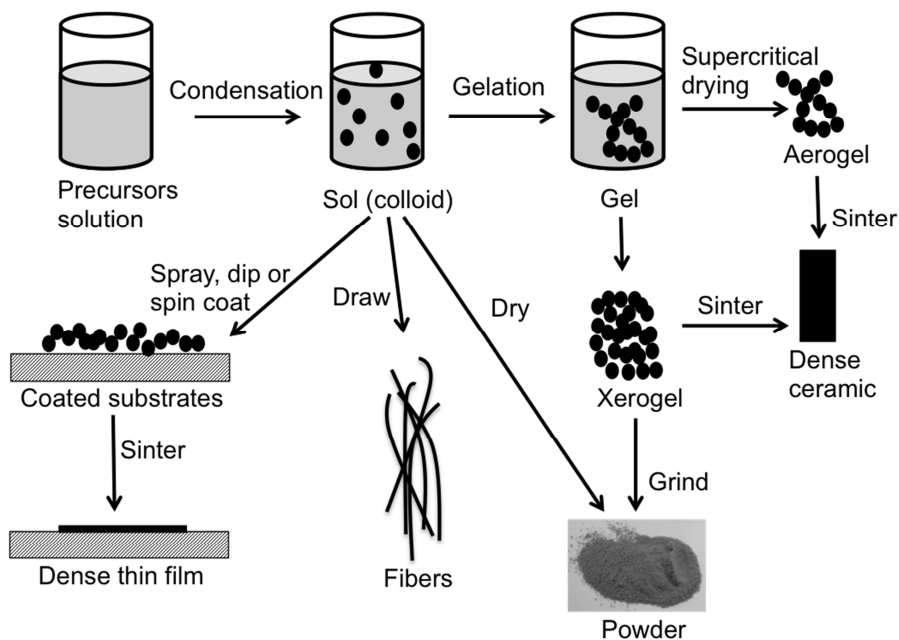
Figure 14: Products that can be obtained by Sol-gel.

Alkoxide precursors in organic solvents:

The precursors used in this type of synthesis are metal alkoxides, $M(OR)_z$ (R = methyl, ethyl, etc.) where z is the metal oxidation state. Currently, metal alkoxides are commercially available.

The metal alkoxide in the presence of water will promote hydrolysis, but the precursor must be dissolved in a co-solvent (alcohol) prior to hydrolysis because it is insoluble in water. The high electronegativity of alkoxi group (OR) will promote a nucleophilic attack from water molecules to the metallic atom. The hydrolysis step will form a hydroxide group (M-OH), so, the hydrolysis reaction can be described as:

$$M - OR + H_2O \Rightarrow M - OH + ROH$$
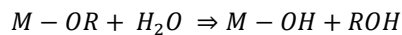
the second step is the condensation of M-OH species, leading to –M-O-M- bonds that will result, after several condensation steps, in a net M-O$_n$.[51, 52, 53, 54] Condensation reactions can be described as follow:

$$M - OH + RO - M \Rightarrow M - O - M + ROH$$
$$\text{or}$$
$$M - OH + HO - M \Rightarrow M - O - M + H_2O$$
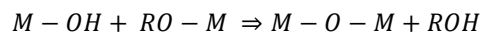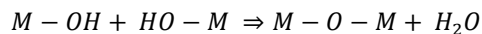
Inorganic precursors in aqueous solution:

The hydrolysis of transition metals cations consists of their solvation by water molecules giving $[M(OH_2)_n]^{z+}$ species followed by a deprotonation:

$$(M(OH_2)_n)^{z+} + hH_2O \Rightarrow (M(OH)_h(OH_2)_{n-h})^{(z-h)+} + hH_3O^+$$
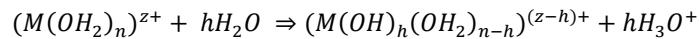
Two possible mechanisms are responsible for the condensation, olation and oxilation described as follow:

$$olation: \quad M - OH + H_2O - M \Rightarrow M - OH - M + H_2O$$
$$oxilation: \quad M - OH + HO - M \Rightarrow M - O - M + H_2O$$
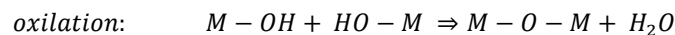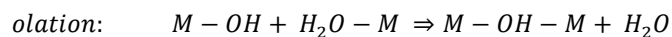
Olation occurs preferably when the metallic cation as an oxidation state less than four and oxilation occurs for oxidation states higher than four.

Since the main objective of this work is to use heat sensitive substrates as electrodes, the sinterization step is a problem. To eliminate or reduce the temperature of the sinterization step, a small change was done to the method usually employed (Figure 15). The temperature needed to the conversion of the material into the final product is applied before the deposition step. A powder or nanoparticles are produced with this approach. The powder is then dispersed in solvents to produce the ink and only afterwards the deposition onto the substrate is performed.
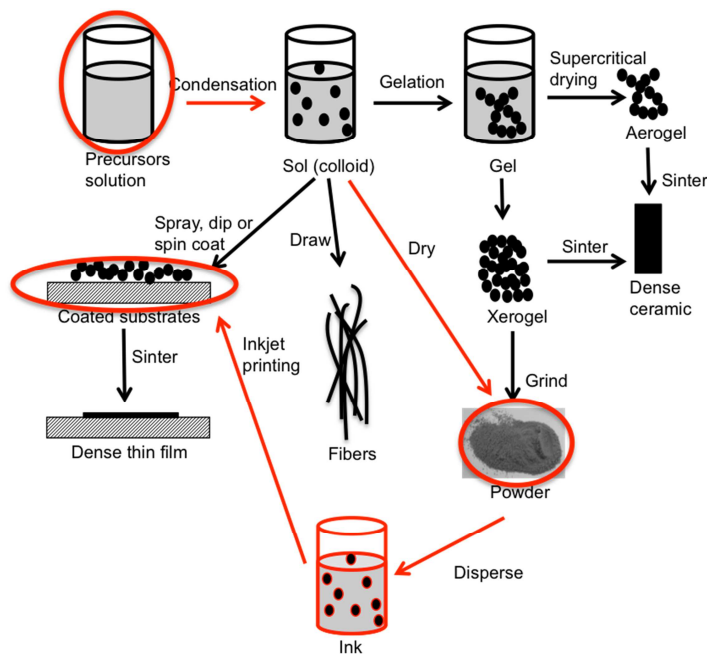
Figure 15: Scheme of the process followed from precursor's solution to the printed film using sol-gel technology.

For electrochromic materials, this approach will completely eliminate the sinterization step. The electrochromic layer does not need to be dense or continuous to perform properly. Actually, some porosity could be beneficial for an easiest intercalation of cations into the material.

In TCO case, a sinterization step will always be needed because the particles must be in contact with each other for electric conductivity. This is not only a question of conversion between the material and the final product but also a physical transformation: the particles must be melted.

In the literature, the best result obtained, in terms of resistivity, for a sintered TCO (600ºC) was a thin film with $1,8 \times 10^{-4}$ Ω.cm. There is an increasing interest on finding alternatives for the sinterization step using temperature. Some possibilities have been published recently. The most common one is the use of excimer laser (but still, the TCO must be heat at 200ºC previously to the laser exposure), the material used is ATO but the sheet resistance presented is still very high (200 kΩ/sq, 1000 Ω/sq, 20 kΩ/sq)[55, 56].

Puetz and Aegerter developed ITO nanoparticles. With these nanoparticles, they prepared UV curable ink for gravure printing. Before curing, the film presented 1500 Ω/sq sheet resistance. After the UV cure, the film was sintered at 130ºC presenting a 300 Ω/sq sheet resistance. Both will degrade if kept in air. In 2005, Tahar described an electrical sinterization of an AZO thin film deposited using dip coating, but the resistivity is still too high (10^3 Ω.cm) [57]. Some of these authors claim that the use of dispersed nanoparticle instead of the sol would drastically decrease the temperature sinterization or would allow the use of

19

sinterization techniques other than temperature.[48,58,59,60] The substrates mentioned until now are glass, PET or PEN.

As alternative to these approaches, two companies have emerged in printed electronics area with some solutions to sinter materials without heating the substrate. Those companies are [®]NovaCentrix and [®]Xenon. Both of them use a powerful lamp enclosing a large interval of wavelength. A pulse of light from these lamps will heat the surface of the substrate but not the substrate itself. Typically, the thin film deposited on top of the substrate will suffer a high temperature heating for a fraction of second, but this high temperature will not reach the substrate.

1.3.2   Ink formulation

Some wide format inkjet printers use aqueous inks, but the majority, in professional use, employ a much wider range of inks, most of which require piezo inkjet heads and extensive maintenance.

Inks can be based on water, solvents (alcohols, glycols, lactates), oils (long molecules glycols/hydrocarbonates), phase change (waxes and long organic molecules) or UV cured (monomers, oligomers and photoinitiators) and they are composed by:

- Liquid transport (water, solvent, oil),
- Binders (polymers used to increase viscosity),
- Functional material (pigment, dye, metals, oxides),
- Additives (surfactants, defoaming agents, etc.)

The most critical materials are binders and functional materials because of their influence in jet performance, process reliability and stability, as well as in the final application. There are several parameters to be monitored when developing inks, such as reagents compatibility, nozzles architecture, interaction between binder and functional material, chemical structure of reagents, molecular weight of the polymer and viscoelasticity, interfacial energy between the ink and the nozzles material, rheology of the ink and wettability of the ink on the substrate. The principal parameters to be measured in inks are: viscosity, surface tension, pH, particles size, evaporation temperature and reliability.

The optimal ink physical properties for the printer DMP-2800 are: surface tension between 28–33 mN/m, viscosity between 3–12 cp, density above 1 g/cm^3 and pH between 4 - 8. Those ink physical properties are important to achieve an optimal printing performance, but they are not limitative. It is possible to print inks even if those values are outside the optimal ranges but the reliability and drop formation maybe affected.

1.4 Printing methods

There are several printing methods available to customize images into different substrates. The choice of the ideal printing method depends on the final application, printing quality required, the production number and the substrate. Some printing methods are highlighted in this chapter: offset, flexography, screen-printing, gravure and inkjet. In this Ph.D. work, screen-printing and inkjet were used, but the focus was put in inkjet. All the inks were developed for inkjet printing and only commercially available PEDOT:PSS was used with screen-printing. Figure 16 shows a diagram of the different printing techniques used depending on the viscosity of inks, particles size and concentration of functional material (pigment). It can be seen that inkjet printing is used for inks with viscosity close to water and screen-printing inks must have a honey-like viscosity[61].
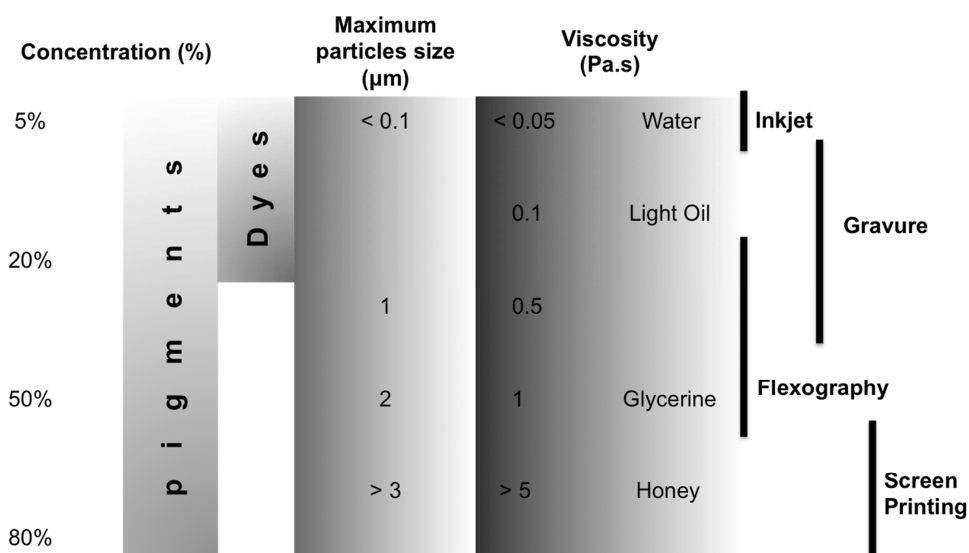
Figure 16: Diagram of the different printing techniques used depending on the viscosity of inks, particles size and concentration of functional material (pigment).

1.4.1 Flexography

Flexography is a contact technique that uses plates on polymer or on rubber material to transfer the ink to the substrate. These plates are created using analog or digital processes and are assembled to the plate cylinder (Figure 17). The ink is kept inside a tank in which the ink roll is partially immersed, then, the ink is transferred to the anilox roll whose texture retains a certain amount of ink and a doctor blade removes the excess. This exact amount of ink is transferred to the plate cylinder with a uniform thickness and finally is

printed on the substrate that is pressed between the plate cylinder and the impression cylinder. The substrate with the printed image passes through a dryer or a UV lamp depending on the type of ink used. Flexography major advantage is that a wide range of different types of ink can be used and it is a technique to print on a variety of different materials like plastic, foil, acetate film, brown paper, and other materials used in packaging. Flexographic inks generally have a low viscosity allowing a faster drying and, as a result, faster production, which results in lower costs. Printing speeds of up to 600 m/min. are now achievable[62].
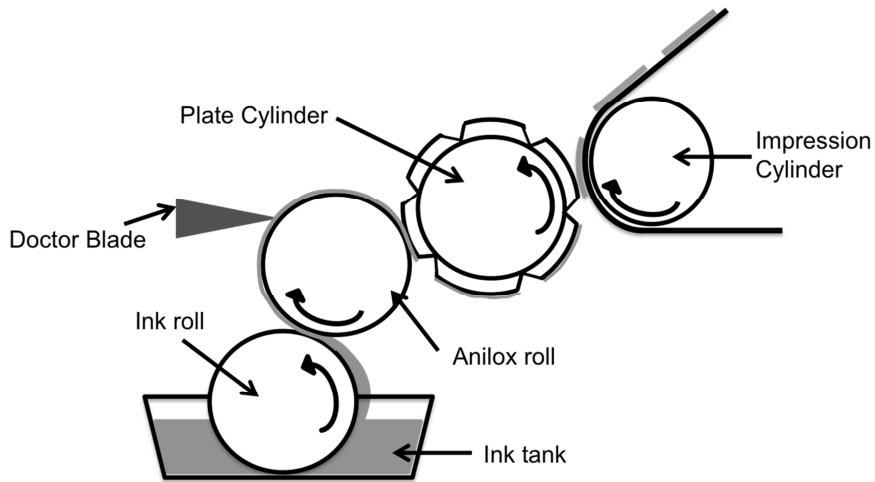
Figure 17: Scheme of flexography working principle.

1.4.2 Screen Printing

Screen-printing is a printing technique that uses an interlaced mesh with open areas and closed areas to define the pattern to be printed onto the substrate surface. The ink will be pushed through the open areas of the mesh using a squeegee (figure 18).
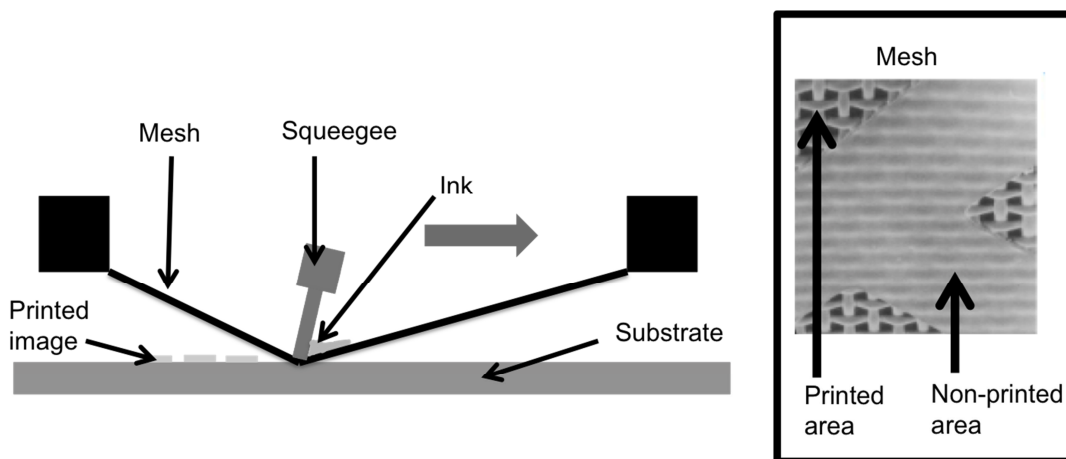
Figure 18: Scheme of screen-printing working principle.

A screen is made of a piece of porous woven fabric (mesh) stretched over a frame of aluminum or wood. The screen is placed on top of a substrate such as paper or fabric and ink is placed on top of the screen, a fill bar is used to fill the mesh openings with ink. The ink that is in the mesh opening is squeezed by capillary action to the substrate in a controlled amount; the ink deposited is proportional to the thickness of the mesh. As the squeegee moves toward the rear of the screen the tension of the mesh pulls the mesh up away from the substrate (called snap-off) leaving the ink upon the substrate surface. The screen can be re-used after cleaning. The surface of substrates does not have to be planar. Substrates such as textiles, ceramics, wood, paper, glass, metal and plastic can be used allowing this technique to be used in many different industries[63].

1.4.3   Offset

Offset printing is an indirect printing technique based on the water-oil repulsion that requires the use of plates (Figure 19). I
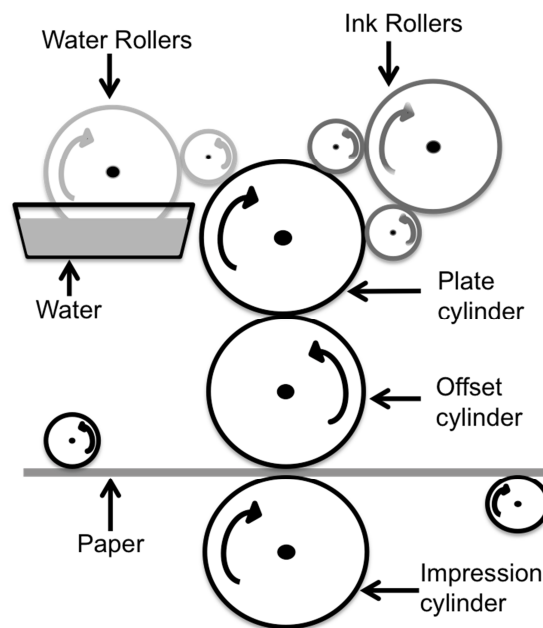
Figure 19: Scheme of Offset working principle.

It is a printing technique in which the inked image is transferred from a plate to a rubber blanket, then to the printing surface. When used in combination with the lithographic process, which is based on the repulsion of oil and water, the offset technique employs a flat image carrier on which the image to be

printed obtains ink from ink rollers, while the non-printing area attracts a water-based film keeping the non-printing areas ink-free. Compared to other printing methods, offset printing is more appropriate for economically produce large volumes of high quality prints that require little maintenance such as newspapers, magazines, brochures and books. The main advantages of offset when comparing to other printing techniques are: consistent high image quality, quick and easy production of printing plates and cost[64].

1.4.4 Gravure

In gravure printing, the image is engraved onto a cylinder because, such as offset printing and flexography, it uses a rotary printing press. The first step of Gravure is to create the cylinder with the engraved image; the engraving process will create cells that will contain the ink on the cylinder surface. The amount of ink contained in the cells corresponds to different color intensities on the paper (deeper cells will produce more intensive colors). In a typical gravure printing process, the engraved cylinder is partially immersed in the ink fountain, filling the recessed cells. As the cylinder rotates, it draws ink out of the fountain with it. A doctor blade scrapes the cylinder before it enters in contact with the paper, removing excess ink from the non-printing areas and leaving in the cells the right amount of ink required. Next, the paper gets sandwiched between the impression roller and the gravure cylinder (Figure 20). Then the paper goes through a dryer because it must be completely dry before going through the next color unit. Since the gravure printing process requires the creation of one cylinder for each color of the final image, being very expensive, it is suitable for high volume printing[65].
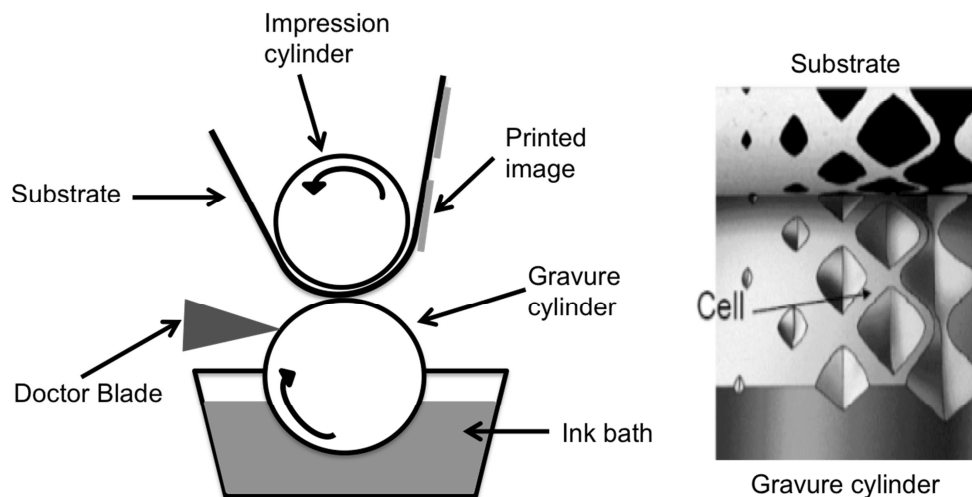
Figure 20: Scheme of Gravure working principle.

1.4.5 Inkjet

Inkjet printing is a technique that allows printing graphical images by firing small drops of ink into a substrate. Inkjet printers are the most commonly used type of printer and range from small inexpensive consumer models to very large professional machines that can cost tens of thousands of dollars.

Inkjet printing technology was first extensively developed in the early 1950s. In the late 1970s, inkjet printers that could reproduce digital images generated by computers were developed, mainly by Epson, Hewlett-Packard, and Canon. There are four main inkjet printers producer worldwide: Canon, HP, Epson, and Lexmark.

In Inkjet printing, there are several ways to produce and control the droplets, two main technologies can be pointed out: continuous (CIJ) and Drop-on-Demand (DOD) (figure 21)[66,67].
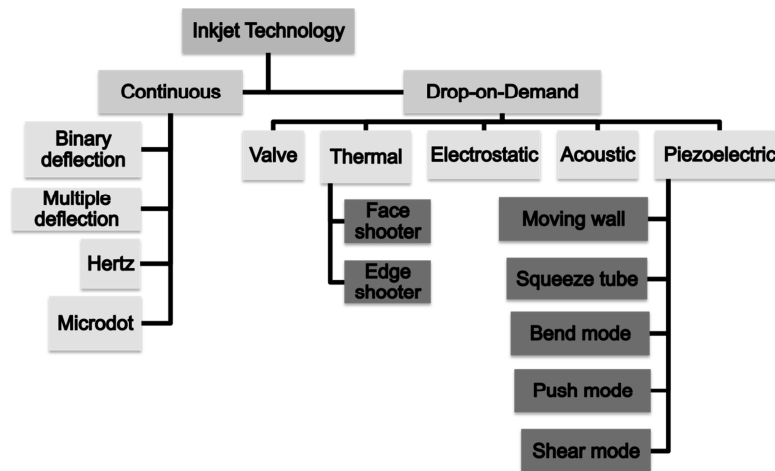
Figure 21: Inkjet printing categories classification in terms of printheads technology.

In continuous inkjet technology, a high-pressure pump directs the ink from a reservoir through the nozzle of the printhead, creating a continuous stream of ink droplets based on the Plateau-Rayleigh instability theory. Only a small fraction of the droplets is used to print, the majority being recycled. The major advantages are the high velocity (~50 m/s) of the ink droplets, which allows a very high drop ejection frequency and the low nozzle clogging as the jet is always in use, therefore allowing more volatile solvents.

Drop-on-demand technology only ejects the droplets required for the execution of a pattern, so there is no waste of ink. It is an increasingly attractive tool to print materials with high accuracy because of the precise control of dispensed volume per drop, it also allows changing patterns very easily and being a non-contact technique with no heat associated, it is possible to print on any substrate wanted (Figure 22).
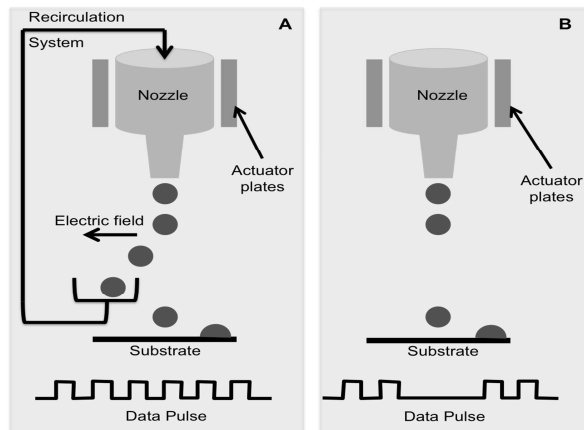
Figure 22: A) Scheme of continuous Inkjet printing working principle; B) Scheme of Drop-on-demand Inkjet printing working principle.

DOD is divided in two principal categories: thermal DOD and piezoelectric DOD among others. DOD thermal inkjet creates droplets inside the nozzles using thermal plates. These thermal plates are triggered by a pulse of current causing a rapid vaporization of the ink in the nozzle to form a bubble, which causes a large pressure increase, propelling a droplet of ink onto the paper. The inks used must have a volatile component to form the vapor bubble, otherwise droplet ejection cannot occur.

In DOD piezoelectric inkjet, each droplet is also created inside a nozzle, were a voltage pulse is applied to a piezoelectric crystal, creating a change in shape and size of the nozzle and, in consequence, creating a pressure pulse in the ink allowing a drop to be release from the nozzle. It allows a wider variety of inks than thermal inkjet as there is no requirement for a volatile component, but the printheads are more expensive to manufacture due to the use of piezoelectric material (usually zirconium titanate) (Figure 23).
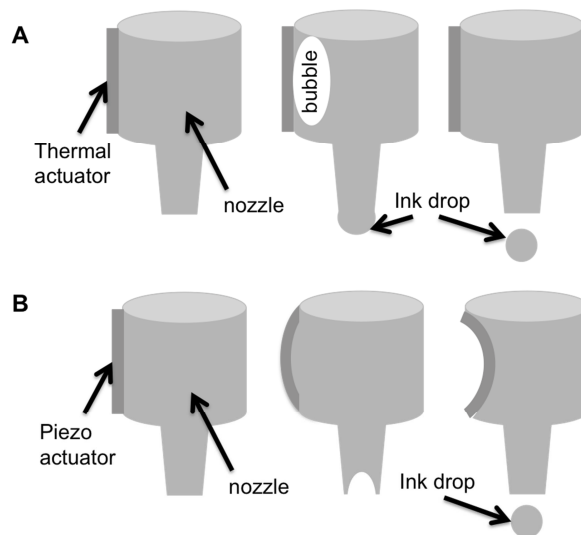
Figure 23: Working principle of Drop-on-demand printheads A) Thermal e B) Piezoelectric.

Piezo inkjet technology is often used on production lines to mark products, for instance the "use-before" date is often applied to products with this technique; in this application the head is stationary and the product moves past. Most of inkjet printing applications use moving printheads and the substrate can also move or not. These moving printheads can lead to another kind of problems related to the wrong location of drops on paper due to turbulence (Figure 24).
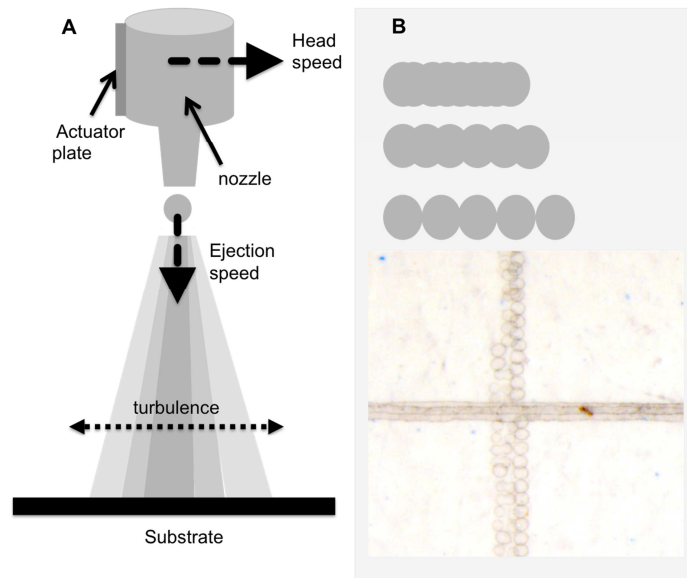
Figure 24: A) Accuracy problems with inkjet printing e B) inkjet printing resolution.

The primary cause of inkjet printing problems is due to ink drying on the printhead, clogging the nozzles. To combat this drying, nearly all inkjet printers include a mechanism to reapply moisture to the printhead. Typically there is no separate supply of pure ink-free solvent available to do this job, so instead; the ink itself is used to remoisten the printhead. Some printers use a supplemental air-suction pump, that forces the ink to come out the nozzles using this air pressure and then the nozzles surface are cleaned in a cleaning pad were the excess of ink is kept.

Inkjet printers are used in the production of many microscopic items such as conductive traces for circuits, and color filters in LCD and plasma displays.

Models produced by Dimatix (now part of Fujifilm), Xennia Technology and Pixdro, are used in many labs around the world for developing alternative deposition methods that reduce consumption of expensive, rare, or problematic materials. These printers have been used in the printing of polymer, macromolecular, quantum dot, metallic nanoparticles, carbon nanotubes etc. The applications of such printing methods include organic thin-film transistors, organic light emitting diodes, organic solar cells, sensors, etc. Inkjet technology is also used in the emerging field of bio printing.[68]

This deposition market uses typically printheads using piezoelectric crystals, to deposit materials directly on substrates. For the electrochromism technology presented in this work, inkjet printing was also identified as the most promising printing technology available. It is a technique with several advantages when compared with others:

- Possibility to change patterns easily without the need of plates, meshes or photolytes to transfer the pattern.

- The printing speed is evolving, being for now possible to print at a maximum speed of 100m/min for singles passes. Once it is a very recent printing technology when compared with the others mentioned above, the evolution of the method is in high growth.

- Because inkjet printing is a non-contact technique, a high diversity of rigid or flexible substrates with different smoothness can be used and it is possible to print directly on 3D objects.

- There is no waste of material; this is a very important fact when talking about expensive functional materials such as gold or indium nanoparticles.

- Since the structure of the electrochromic devices here presented is a layered structure, the use of one printer machine with several printheads (for different inks) can be used, allowing simplifying all the printing process.

In this work, a Drop-on-demand piezo lab-scale Dimatix® materials printer (DMP-2800) was used to print all the inks tested.

1.5   Problems and issues

When building electrochromic devices, some outcomes have to be considered. There are some technical problems or limitations that have to be studied in order to build electrochromic device with the performance wanted.

1.5.1   Terminal effect

Terminal effect is the non-uniform appearance of the color when the electrode is electrically stimulated. The color appears from the edge of the devices (starting from the electric contacts) to the center gradually (Figure 25).
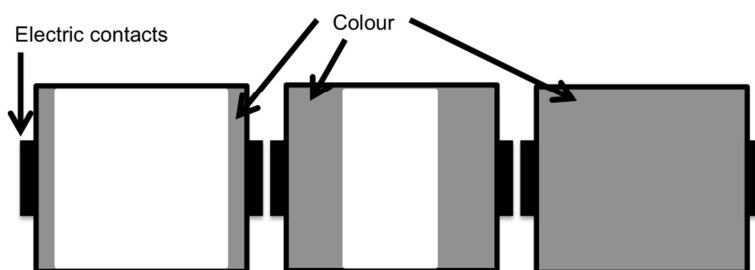
Figure 25: Terminal effect.

Due to the resistivity of the conductive material, a gradient of potential is formed across the electrode, where the potential near to the external electric contacts is higher than elsewhere, so the coloration is formed at different speeds across the electrode. With less conductive electrodes, this effect will be enhanced. It also depends on the response time of the electrochromic material; slowest electrochromic materials will enhance the terminal effect. To have more uniform color appearance with the same electrochromic material, more conductive TCO can be used (or more electrically conductive materials), conductive tape can be placed around all the device in contact with the TCO layer (but not in contact with the electrolyte layer) to promote a fastest diffusion of electrons to all the device almost at the same time (visually).

1.5.2   Short circuits

Short circuits happened when the two electrical materials (TCO) are in contact with each other. This problem can occur for different reasons such as the electrolyte not being present in all the area of the device, working as insulator between the two TCO. When a short circuit is present, the color transition can be much slower or completely halted, depending on the extension of the short circuit and also depending on the electrochromic material used. In the case of PEDOT:PSS, when a short circuit happens some

electrons are still able to go to the electrochromic layer because this electrochromic material is also a semi conductive material, but the color transition is very slow. When the sort circuit happened with electrochromic materials such as WO_3, which is much less conductive than PEDOT:PSS, all the electrons passes through the short circuit, so no color transition is seen. Figure 26 illustrates these two distinct behaviors.
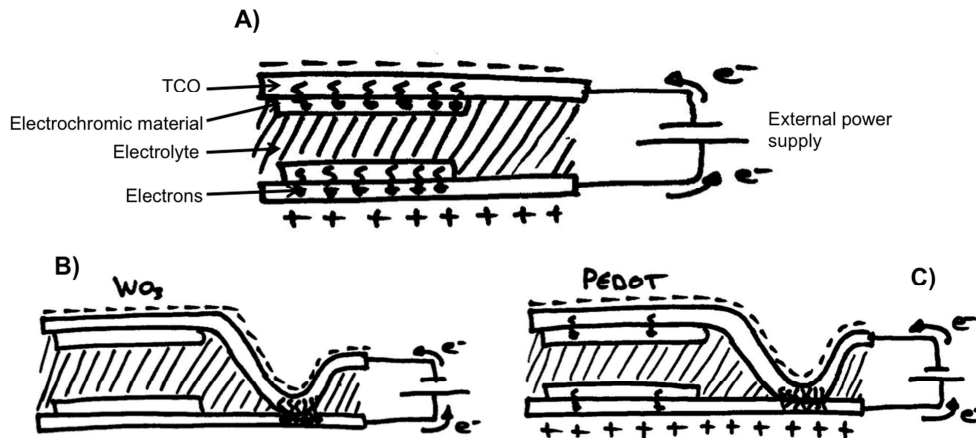
Figure 26: Electrochromic devices with short circuits. A) Normal functioning of an electrochromic device B) short circuit with no color transition C) short circuit with a slow color transition.

1.5.3 Design influence

Figure 27 is a PEDOT:PSS device with a flame in each electrode; when one flame appears, the other one disappears and vice-versa. It is possible to see that with this design, for example, some areas present a faster color transition than others. It is possible to conclude that areas that are "surrounded" by electrochromic material in the opposite electrode are faster than those that are isolated in comparison again with the back electrode.

The different sizes of images (or concentration of electrochromic material) in the two electrodes are also an important factor, the image with less ink, or less electrochromic material will be faster than the image with more electrochromic material. These facts are due to the speed migration and concentration of ions in the transition from one electrode to the other. The size of the entire device will also influence its performance; big devices are slower than smaller ones and in this case, terminal effect will also affect the performance.
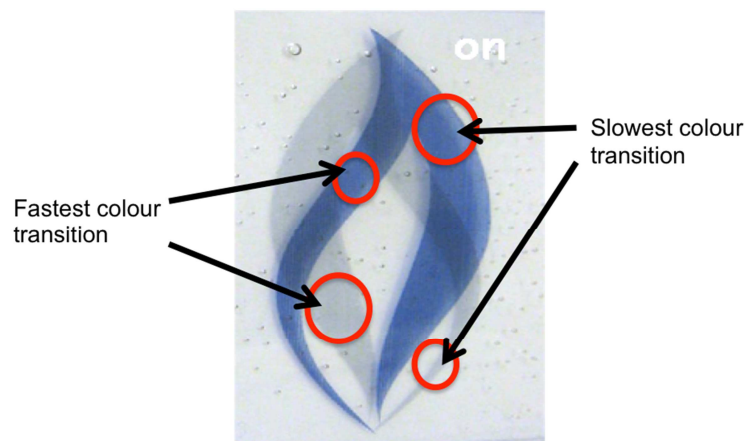
Figure 27: PEDOT:PSS symmetric device with the areas that present a fastest and a lowest color transition.

1.5.4   Device encapsulation

The device encapsulation is crucial to the lifetime of an electrochromic device and represents a challenge often as big as the device development itself, especially when the objective is to bring the device to commercial viability. When a solid electrolyte is used, the encapsulation is important to prevent degradation with air or moisture and it needs to be chemically stable. When the electrolyte is a liquid or a gel, the encapsulation is even harder mostly because it has also to prevent leakage problems. There is also the spacing problem needed between the two electrodes, but in this case some spacers can be used. In the literature, the sealant used is rarely revealed but there are some authors that described the use of elastomeric polymers such as PPG (Polypropylene glycol), acetate silicon or a thermoplastic tape (DuPont, Surly)[41].

1.6 Devices characterization

To evaluate the performance of an electrochromic device, some parameters have to be studied, such as: optical contrast, response time, stability (cycling tests), electrochromic memory, power consumption and coloration efficiency[41]. This section is a description of these parameters and it describes the theory behind the techniques used to characterize them.

1.6.1 Optical contrast

The optical contrast is defined as the difference in color observed between the reduced and oxidized states of an electrochromic device. It can be determined using either spectroelectrochemical measurements or color coordinates (see experimental section). Using spectroelectrochemical measurements, the optical contrast is defined by the variation of absorption spectra (ΔA) or the variation of the transmittance spectra ($\Delta\%T$) between the reduced and the oxidized states of an electrochromic device, measured at one specific wavelength. Absorbance is defined as:

$$A_\lambda = ln(I_0/I_1) \tag{1}$$

where I_1 is the intensity of light at a specific wavelength λ that passes through a sample (transmitted light intensity) and I_0 is the light intensity before it interferes with the sample, or incident light intensity. Therefore, absorbance is the fraction of incident light (or electromagnetic radiation) at a specific wavelength that is retained by the sample. Transmittance is the fraction of electromagnetic radiation at a specific wavelength that passes through a sample. Transmittance (T) is defined as:

$$A_\lambda = -lnT_\lambda \tag{2}$$

The absorption spectra and the variation of absorbance (ΔA) are used mostly to show molecular interactions and reactions, as well as to calculate the concentration of the sample. $\Delta\%T$ gives a better perception of the optical contrast obtained, since it mimics the light that reaches the eye.

To calculate the optical contrast of electrochromic films or devices, an experimental setup built as explained in the experimental section, using a spectrophotometer and a potentiostat, is needed. The potentiostat is used to apply the potential to the electrochromic film or device using a square waveform (Figure 28), while the spectrophotometer monitors the absorption or the transmittance at a certain wavelength during the redox cycles.
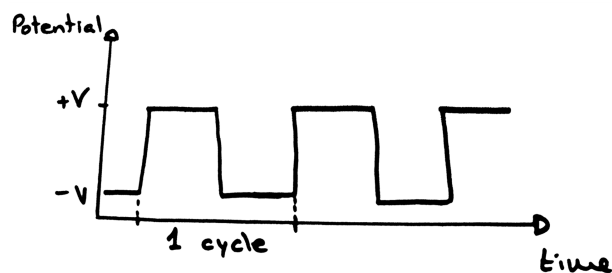
Figure 28: Square waveform applied by the potentiostat in spectroelectrochemical measurements.

The information used to calculate the optical contrast is the data collected from the spectrophotometer (Figure 29), where the maximum and minimum values of absorbance (or transmittance) are subtracted to give the optical contrast as ΔA or $\Delta\%T$.
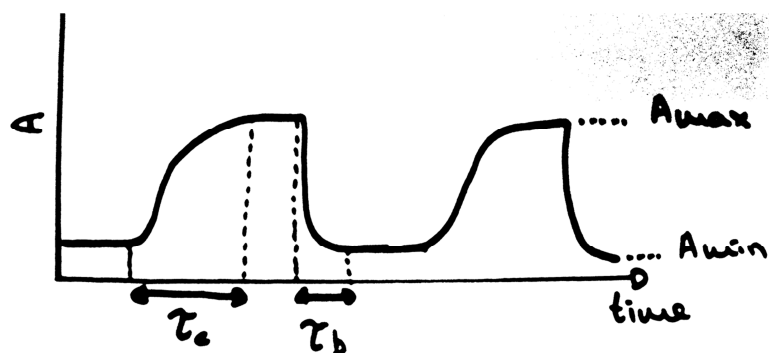
Figure 29: Data obtained from the spectrophotometer in spectroelectrochemistry measurements.

An alternative for calculating optical contrast of electrochromic materials is to use color coordinates (color contrast).

"Color is the general name for all sensations arising from the activity of the retina of the eye and its attached nervous mechanisms, this activity being, in nearly every case in the normal individual, a specific response to radiant energy of certain wavelengths and intensities". (T.L. Troland, Report of O.S.A. Committee on Colorimetry for 1920-1921).

Electromagnetic radiation is characterized by its wavelength (or frequency) and its intensity. The visible spectrum is the range of wavelengths between 390 nm and 750 nm.

Light sources emit light at different wavelengths and a source's spectrum is a distribution giving its intensity at each wavelength. The spectrum of light arriving at the eye from a given direction determines the color sensation in that direction. Table 5 shows approximate frequencies and wavelengths for various pure spectral colors, as well as wavenumbers and energies.

Table 5: Frequencies (ν), wavelengths (λ), wavenumbers (νb) and energies (E) for various pure spectral colors.

Color	λ(nm)	ν(THz)	$\nu_b(\mu m^{-1})$	E(eV)	E(kJ mol^{-1})
Red	700	428	1.43	1.77	171
Orange	620	484	1.61	2.00	193
Yellow	580	517	1.72	2.14	206
Green	530	566	1.89	2.34	226
Blue	470	638	2.13	2.64	254
Violet	420	714	2.38	2.95	285

The light interaction with bulk matter can result in reflection, scattering, absorption and transmission of light (Figure 30). Depending on the light and the nature of the object, several of these phenomena can happen at the same time[69].
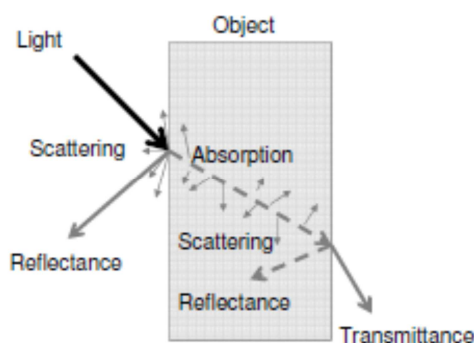
Figure 30: Light interaction with matter; reflectance, scattering, absorption and transmittance phenomena.

The spectrum of the light reflected from or transmitted by an object which gives the overall color perception, depends on the spectrum of the incident light on the object and on the reflection/transmission characteristics of the object.

The origin of color can be explained by different physical and chemical mechanisms[70]. In the case of electrochromic devices, the origin of color is mostly due to electron activity. It is a result from the partial absorption of the visible electromagnetic radiation, resulting from the interactions between light and electrons. In metal-oxides electrochromic systems, the source of color is usually an optical charge-transfer (CT) transition between two atoms of the same element[41]. In a CT system, when a photon is absorbed, an electron is optically excited from an orbital on the donor atom in the ground state to a vacant electronic orbital on an adjacent atom, producing an excited state. In the case of tungsten oxide, for example, the

blue color is caused by the absorption of red light that promotes the transition between adjacent tungsten centers. The resulting atoms that are in an excited state lose the energy acquired from the photon by thermal dissipation to the involving system.

Under normal lighting conditions and assuming a "standard" vision: the eye has 3 receptors (cones) that respond differently to photons at different wavelengths within the visible light spectrum. The brain then interprets the signals from the 3 receptors to give the perception of color. Two different light spectra, which excite the receptors in the eye to the same degree, will be perceived as the same color. These receptors have peak sensitivities at 420 nm (violet), 564 nm (yellow-green) and 534 nm (green), as represented in Figure 31.
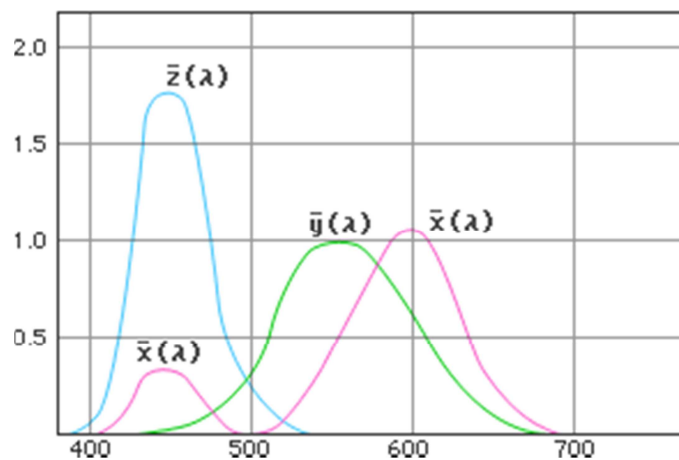
Figure 31: Spectral sensitivity curves corresponding to the human eye, according to the CIE definition of the 1931 Standard Observer.

It was found that two light sources with different mixtures of wavelengths but with the same tristimuli values have the same apparent color to an observer, meaning that those tristimuli values are reliable to describe a color. To have a component that describes the perceived brightness, completely theoretical components were calculated. These theoretical tristimuli values are given in the CIE (Commission Internationale de l'Éclairage) 1931 color space, in which they are denoted X, Y, and Z. Any specific method for associating tristimuli values with each color is called a color space.

This system consists of describing a color using three characteristics: 1) hue: identifies a color by its location in the spectral sequence, i.e. the wavelength associated with the color; 2) saturation: associated with the levels of black and white; 3) luminance: the brightness of the color, gives information about the transparency of the sample. This approach allows the definition of a color numerically. There are several different scales of color developed through the years; in this work, the CIE L*a*b* was used because it is the system that is usually used to define the color in paint industries. CIE L*a*b* is a uniform color space

developed in 1976. L* measures the lightness; +a* relates to the red direction; –a* is the green direction; +b* is the yellow direction and –b* is the blue direction (Figure 32).
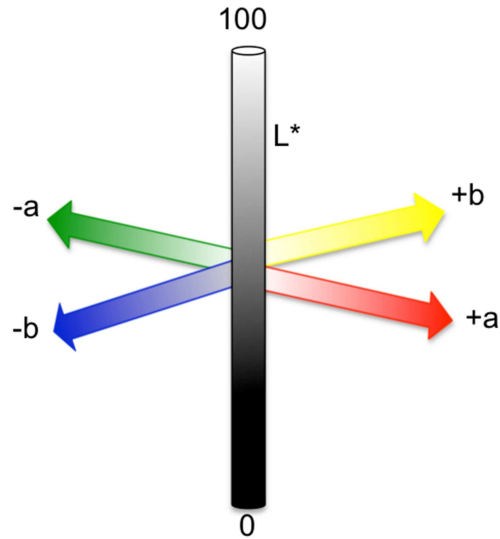
Figure 32: Diagram representative of L*a*b* coordinates color directions.

To calculate the color coordinates during the electrochromic transition of a solid-state cell, a setup with a digital camera under diffuse light inside a room was used (see experimental section). Afterwards, the images were analyzed by calibrating with a ColorChecker®, in order to calculate L^*, a^* and b^*.

Since absorption spectra (or transmittance) are directly connected to color, it is also possible to calculate color coordinates using the spectra obtained from a spectrophotometer in the visible range. In this work, the Standard Illuminant CIE D65 was used to calculate the trichromatic individual coordinates X, Y and Z:[71,72]

$$X = \sum E_i x_i T_i \tag{3}$$

where E_i is the coefficient of the Standard Illuminant CIE, x_i is the coefficient of the tristimulus value and T_i is the optical transmittance, all for a given wavelength λ_i (the same type of calculation is done for Y and Z). X, Y and Z values can then be converted to L*a*b* color coordinates using the following equations:

$$L^* = 116 \left(\frac{Y}{Y_n}\right)^{1/3} - 16 \tag{4}$$

$$a^* = 500 \left[\left(\frac{X}{X_n}\right)^{1/3} - \left(\frac{Y}{Y_n}\right)^{1/3}\right] \tag{5}$$

36

$$b^* = 200 \left[\left(\frac{Y}{Y_n} \right)^{1/3} - \left(\frac{Z}{Z_n} \right)^{1/3} \right] \tag{6}$$

where X_n, Y_n and Z_n are the white color values with the illuminant used. These equations are valid as long as the quotients X/X_n, Y/Y_n and Z/Z_n are greater than 0.008856 (which is normally the case).

To determine the color contrast (ΔE) of electrochromic materials using L*a*b* coordinates, the following equations were used[73]:

$$\Delta E = \sqrt{((\Delta L^*)^2 + (\Delta a^*)^2 + (\Delta b^*)^2)} \tag{7}$$

Where:

$$\Delta L^* = |\,L\ \text{reduction} - L\ \text{oxidation}\,| \tag{8}$$

$$\Delta a^* = |\,a\ \text{reduction} - a\ \text{oxidation}\,| \tag{9}$$

$$\Delta b^* = |\,b\ \text{reduction} - b\ \text{oxidation}\,| \tag{10}$$

In the case of vanadium oxide, equations 8, 9 and 10 were slightly modified because this electrochromic material has no transparent state. Therefore, the oxidized state (1.5 V) was used as reference.

$$\Delta L^* = |L^*_{ox} - L^*(t)| \tag{11}$$

$$\Delta a^* = |a^*_{ox} - a^*(t)| \tag{12}$$

$$\Delta b^* = |b^*_{ox} - b^*(t)| \tag{13}$$

1.6.2   Response time

Response time is defined as the time (τ) required for an electrochromic material to change from its bleached to its colored state and vice-versa. Usually, $\tau_{bleached}$ is different from $\tau_{colored}$. In this work, the response time was defined as the time needed until 90% of the fully colored state was reached or until 90% of the bleached state was achieved. This parameter is calculated from the data obtained with the spectrophotometer (Figure 29). It is also possible to calculate response times using L*a*b* coordinates, by monitoring color contrast (ΔE) with time.

37

1.6.3 Stability (cycling tests)

This parameter gives information about the durability of the device in terms of cycling. It indicates how many cycles the device can perform with a certain applied voltage and cycle duration before significant degradation has occurred. Stability measurements using cycling tests can be evaluated using spectroelectrochemical measurements or L*a*b* coordinates. In both cases, it consists of monitoring the optical contrast (ΔA or Δ%T) at one wavelength (Figure 29) or the color contrast (ΔE), with time. The associated degradation is calculated using the difference between the contrast in the first cycles and the contrast after a number of cycles.

Full switch, between the bleached and the colored states, is measured at the beginning of the cycling experiment at a specified wavelength (ΔA_i). A double potential step is applied to the device in order to operate a full cycle (full switch): write-erase (coloration-bleaching) and vice versa. The comparison of the maximum optical variation (100% of full switch) after the operation of n cycles (ΔA_n) and ΔA_i allows calculating the loss of color variation (when working in transmittance or color contrast, ΔA is substituted by Δ%T or ΔE, respectively):

$$\% \, degradation \, (\lambda, nm) = 100 - (\Delta A_n \, x \, 100 / \Delta A_i) \tag{14}$$

1.6.4 Memory effect

Memory effect of an electrochromic device is the capacity of the device to retain one redox state after the electric stimulus is removed. It is defined as the time that the electrochromic material takes to lose its color after the electric stimulus is disconnected. The memory effect can also be evaluated using spectroelectrochemical measurements or L*a*b* coordinates. Again, it consists of monitoring the optical (ΔA or Δ%T) (Figure 29) or the color contrast (ΔE) with time after the removal of the power supply. This parameter was not characterized in this work.

1.6.5 Power consumption

This parameter is calculated using spectroelectrochemical measurements. As explained above, the device is connected to a potentiostat that applies a potential in a square waveform (Figure 28). The data obtained from the potentiostat are represented in Figure 33.
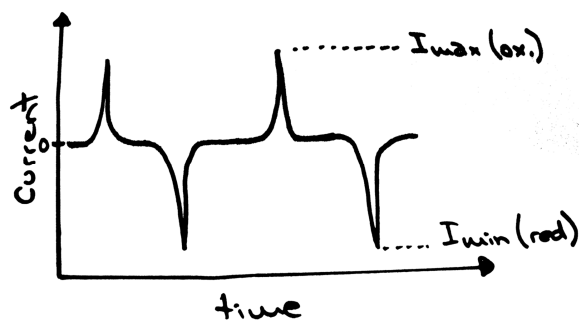
Figure 33: Data obtained from the potentiostat in spectroelectrochemistry measurements.

This graph represents the current variation with time, when a potential in a square waveform is applied to the device. Power consumption can be calculated for both the coloration and bleaching processes using the equation:

$$E = \Delta V \int_{t_o}^{t_f} I(t)\, dt \qquad (15)$$

where ΔV is the amount of electrical potential applied to the ECD and I(t) is the current spent during the cycle, i.e. the current used to achieve one redox state.

1.6.6   Coloration efficiency

For electrochromic materials, the coloration efficiency (CE) is defined as the change in the optical contrast per unit of inserted charge. In the literature, some authors[73] emphasize that the methods chosen for measurement of coloration efficiencies often vary between research groups, which causes difficulty in comparing values for different electrochromes. A general method for effectively and consistently measuring composite coloration efficiencies (CCEs) was proposed. The CCE of an electrochromic system is defined by Reynolds[73] using equation 16:

$$CCE = \Delta A / \Delta Q' \qquad (16)$$

where Q' is the inserted charge that promoted the (ΔA) change.
To determine the CCE, the data obtained from spectroelectrochemistry measurements, both from the spectrophotometer and the potentiostat, are used (Figure 29 and 33).

2 Results and Discussion

2.1 Conductive materials

Several sol-gel formulations were studied with the aim to identify which method would be more adequate for the final purpose of this work: to obtain a viable method for industrial implementation and to have a final product with optimal stability, electrical and optical properties. For this purpose, two different methods were studied: an approach using metallic chlorides and the Pechini method. The intention is to use a sol-gel method to obtain a sol or a dispersion of nanoparticles with a good conductivity and transmittance when deposited as a thin film using inkjet printing followed by a sinterization step.

Once such material is developed, technologies industrialized by companies such as ®NovaCentrix or ®Xenon (mentioned in Introduction chapter, in section 1.2.4) would be tested to sinter the thin film material. Both of these companies use a powerful lamp enclosing a large interval of wavelength that heats the surface of the substrate but not the substrate itself. The details of these equipments are intellectual property of those companies[74,75].

2.1.1 Metallic chloride method

This method consists in mixing a metal chloride precursor in ethanol (or other alcohols) and allowing it to react and to dry. For a typical conductive oxide doped with only one different type of elements (such as ATO, ITO or FTO), two different precursors will be needed. Then, the obtained precursor powders are mixed together in ethanol and allowed to react[76,77]. The detailed descriptions of the syntheses are given in section 2.4.

Some promising results were obtained with this method:

- Spin coated FTO with a transmittance of 50% and a sheet resistance of 250 Ω/sq (Figure 34).
- Spin-coated ATO with 85% of transmittance but a high sheet resistance (5 kΩ/sq) (Figure 35).
- Inkjet printed ITO with a sheet resistance of 15 Ω/sq, but with a low transmittance (7%) (Figure 36).
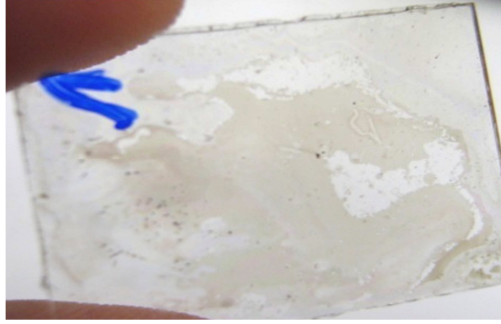
Figure 34: Deposition of FTO via sol-gel on glass using spin coating.
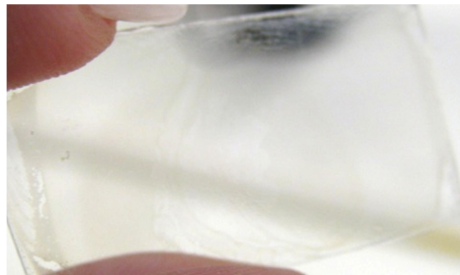
Figure 35: Deposition of ATO via sol-gel on glass using spin coating.

Figure 36: Deposition of ITO via sol-gel on glass using inkjet printing.

Despite this method being promising, the results obtained were very difficult to reproduce. It is very sensitive to moisture and temperature, therefore difficult to implement in an industrial environment. Because of this issue, it was decided to study other synthesis methods such as the Pechini method.

2.1.2   Pechini method

The Pechini method consists on producing metal oxides using polymeric precursors and metallic salts (chlorides or citrates), ethylene glycol and citric acid[52,78,79,80,81]. This method allows the metallic cations to be mixed at a molecular level achieving the stoichiometric composition wanted using citric acid as

chelating agent. There are two possible final products when using this method: thin films obtained from the precursor's solution or metallic oxide nanoparticles. Thin films will be obtained from the polymeric precursor when it presents a viscosity between 4 and 8 cp, deposited using, e.g., inkjet printing on glass and then sinterization at 500ºC for two hours to remove the organic material. The nanoparticles will be obtained heating the same polymeric precursor at 300ºC, grounding the resulting powder and then sintering it at 500ºC to remove the carbon still present. It is then possible to disperse these nanoparticles into an appropriate solvent and deposit the dispersion also using, e.g., inkjet printing. It will be necessary to sinter the film again, but this time with a much lower temperature because the nanoparticles do not have organic material in their composition.

The percentage of ethylene glycol, citric acid and dopant metal is obviously determinant to achieve the conductivity and the transparency wanted. Several combinations were tested and the most promising results obtained are described below.

For comparison, commercial ATO nanoparticles (with 20 nm average diameter) were also tested dispersing this powder in solvents to produce a dispersion followed by spin-coating on glass and sinterization. This study allowed us to understand some of the problems that appeared with the synthesized particles.

Synthesized ATO

Antimony tin oxide (ATO) was selected to implement this method for several reasons[42,82,83]:

- It is a less expensive material than others containing indium, such as ITO.
- It is referred to as a promising material in the thin film technology for electronics area.
- Antimony atoms are easily incorporated in tin oxide nets.
- Tin oxide is a very stable material in corrosive atmospheres.

Figure 37 shows a scheme of the protocol used for this method following several parameters that were changed to produce the polymeric solution and the nanoparticles. Parameters A, B and C are:

A: The reaction can proceed with or without water.
B: Citrates or chlorides (of antimony and tin) can be used as precursors. The precursor for antimony can also be antimony oxide (SbO_3).
C: The solvents used for the dispersion were water and/or ethanol, and a mixture of water, citric acid and ethylene glycol.
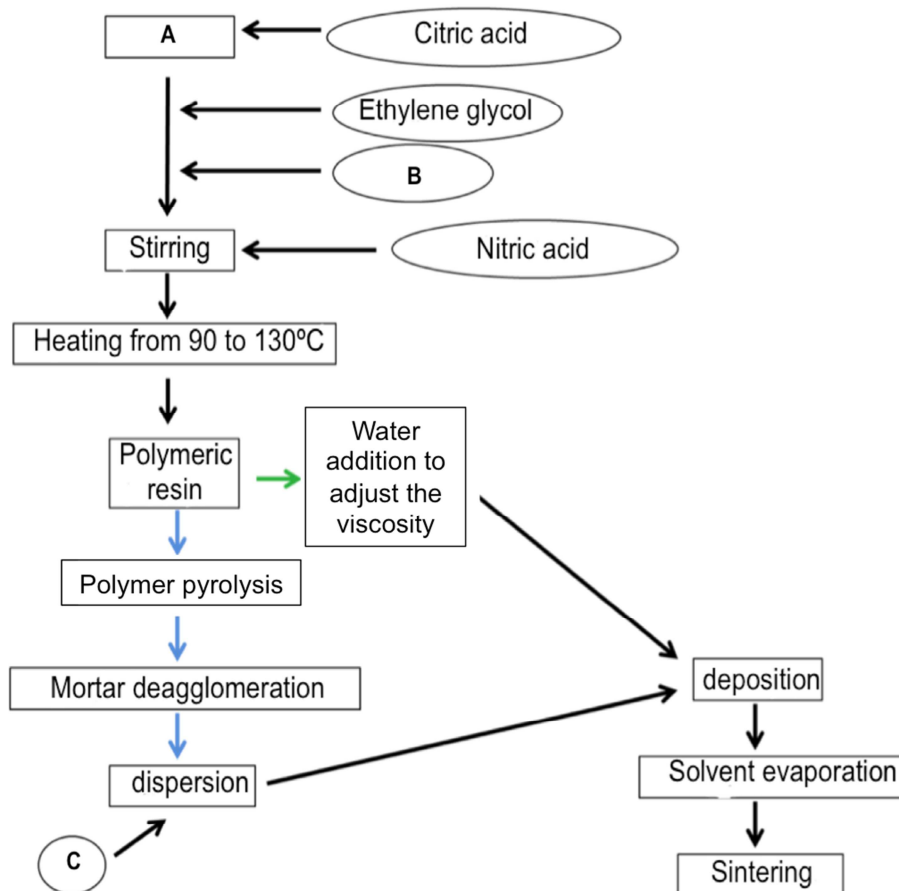
Figure 37: Scheme of the protocol used for the Pechini method with several parameters that were changed to produce the polymeric solution and the nanoparticles (see text).

Three different syntheses were achieved: ATO 1, ATO 2 and ATO 3, the details are given in the experimental section.

Characterization

Table 6 shows some interesting results obtained with the Pechini method. Those results will be compared with those obtained with the commercial sample. The most promising results, for this set of experiments, are obtained for the sol-gel and not for the nanoparticles approach. This result might indicate that the thin films made from the nanoparticles approach are not being done properly. The major problem seems to be the size of the particles. According to some preliminary sedimentation experiments, the particles have around 2 µm, being that way very difficult to deposit using spin coating and impossible to use inkjet printing. The thin films deposited with these particles are discontinuous; the particles are not percolating.

Table 6: Results obtained for Pechini method synthesis in terms of sheet resistance and appearance of the thin films deposited on glass and sintered at 550ºC.

Sample	Reagents	Deposition technique	Sheet resistance (Ω/sq)	Film appearance
ATO 1 (Sol-gel)	**A**-Water **B**-Metallic chlorides	Inkjet	6k	Bluish, translucide, not uniform
ATO 1 (Powder)		Spin-coating	a)	Transparent
ATO 2 (Powder)	**A**-no water **B**-Metallic citrates		a)	Bluish, poor adhesion
ATO 2 (Sol-gel)			2M	Transparent, not uniform
ATO 3 (Powder)	**A**-Water **B**-Metallic citrates		a)	Bluish, poor adhesion

a) No conductivity was found.

To ensure the composition of the products obtained with the tree different synthesis, and to compare them with the commercial ATO, elemental analysis, XRD and DSC were performed.

In XRD results, all the synthesized powders show the same morphology (Figure 38). This experiment revealed the presence of synthetic cassiterite (SnO_2) (JCPDS card 41-1445), for all the synthesized samples and also for the commercial ATO.
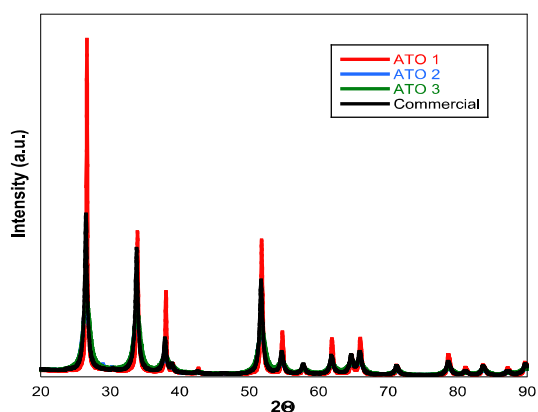
Figure 38: XRD analysis of the ATO powders tested.

For DSC analysis (Figure 39), the difractograms of the different powders are very similar. It was found that all of them have an endothermic peak from water evaporation that occurs before 100ºC. Since the powders are previously sintered at 550 ºC, it is possibly water from moisture contamination and not water entrapped inside the structure of the material or from its composition. No other peaks were found.
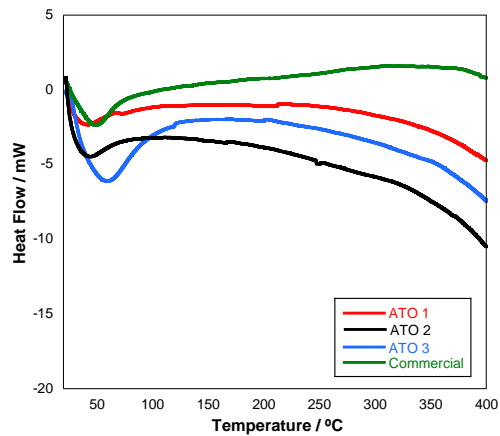
Figure 39: DSC analysis of the ATO powders tested.

Elemental analysis (table 7) shows that all samples have a residual amount of carbon in their composition, certainly prevenient from the synthesis method or from some adsorbed carbon dioxide. Hydrogen is also found in sample ATO 3 and commercial, in accordance with DSC results. For ATO 1 and ATO 2, hydrogen was not found possibly because these two samples were kept inside a desiccator before this experiment.

Table 7: Elemental analysis of all powders*.*

	Carbon (%)	Hydrogen (%)
ATO 1	0.02	0.00
ATO 2	0.05	0.00
ATO 3	0.04	0.12
Commercial	0.04	0.11

The color is another parameter that was evaluated. It can be seen that the 4 powders have different colors (Figure 40). This result might be due to the particles size variation and/or presence of water in the composition. Another explanation could be the difference of the bandgap of the samples. In that case, the darkest powder should have the smaller bandgap meaning that probably it is the most intrinsically conductive material. In semiconductors, the bandgap is the energy difference between the top of the valence band and the bottom of the conduction band, it is the energy needed to trigger the transition of electrons between this two energy levels. The smallest the bandgap, more conductive is the material. For transitions with small bandgap, the associated energy is high, absorbing the wavelengths in the visible range (low wavelengths) giving the black color.

45
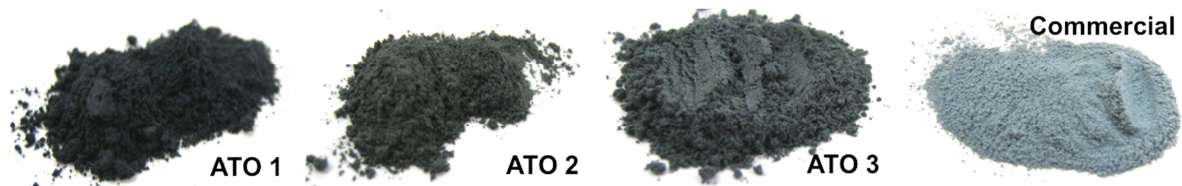
Figure 40: Colors of the powders obtained with Pechini method in comparison with the commercial sample.

ATO1, ATO 2, ATO 3 and the commercial sample were dispersed in a solution with citric acid and ethylene glycol. Those dispersions were then deposited using spin coating. The dispersion made with the commercial ATO was very stable when compared with the other dispersions, probably because of the size of the particles, once small particles formed more stable suspensions. Thin films deposited from the synthesized powders are not uniform; they are not percolating. Figure 41 shows a typical film deposited by spin coating using these powders.
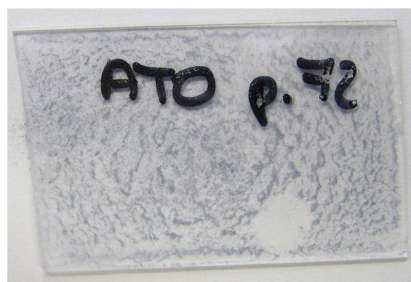
Figure 41: Typical thin film obtained from the synthesized powders using spin coating.

When the commercial particles are spin-coated on glass, the result is clearly different from that shown in Figure 42. A continuous film is obtained, meaning that they are much smaller than the synthesized powders. However, in this case, the doping level cannot be changed, so the conductivity obtained cannot be improved using the commercial powder. Figure 42 shows the films obtained after one and three spin coating depositions.
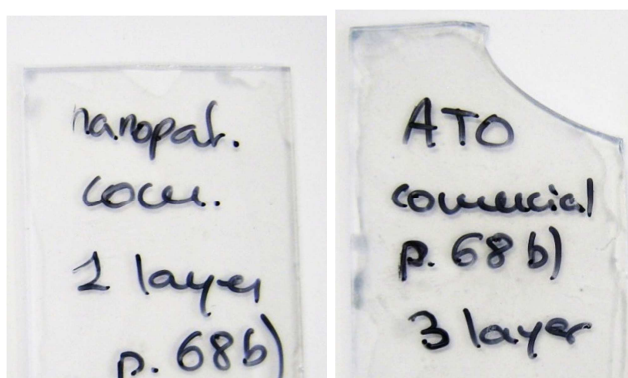
Figure 42: Thin films obtained after one and three spin coating depositions of the commercial ATO.

Figure 43 shows the transmittance spectra of the thin films for one, two and three consecutive depositions of the commercial ATO. The transmittance decreases with the number of depositions but the sheet resistance also decreases, as expected (table 8). Since the objective of this work is to have a good compromise between transmittance and sheet resistance, it was decided not to deposit another layer because of the transmittance value, which is already too low. To improve the sheet resistance and the transmittance of the thin film, it would be necessary to use a powder with a different doping level.
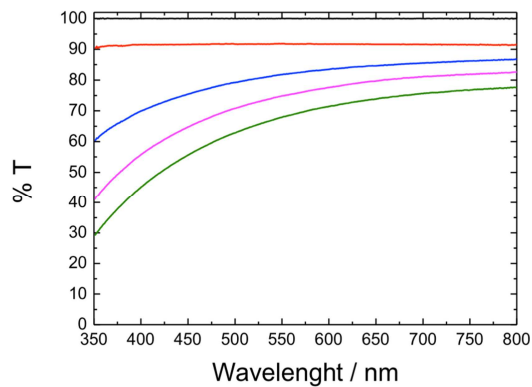
Figure 43: Transmittance spectra obtained for several consecutive spin coating depositions of commercial ATO. Red line is for glass, Blue line is for 1 deposition, pink line is for 2 depositions and green line is for 3 depositions.

Table 8: Sheet resistance obtained for the three different layers of spin coated commercial ATO on glass.

	Sheet resistance (Ohm/square)
Layer 1	0.4M
Layer 2	25k
Layer 3	13k

Some conclusions:

As explained above, the study with commercial ATO was performed to confirm that Pechini method was correctly been used to obtain ATO particles and to compare these synthesized powders with a "reference" material. In the case of the commercial ATO, it is obviously not possible to change the doping level, so the conductivity achieved was limited from the start.

It was possible to conclude that the synthesized particles were very similar to the commercial ones in terms of composition and structure but completely different it terms of size; the commercial ones are much smaller (20 nm). Because of the size of the synthesized powders, the deposition technique used was limited to spin coating, once inkjet printing requires particles smaller than 1μm. Even with spin coating, differences could be observed on the deposited thin films: the bigger particles lead to non-uniform and non-conducting films.

The doping level could not be detected or measured with these experiments; in fact, it is very difficult to see antimony atoms inside a tin oxide net. This is due to antimony and tin being very similar atoms in terms of size and because antimony is inserted perfectly in tin oxide nets. Such similarities turn the final doping undetectable to some techniques. However, there are some techniques that would allow this kind of detection such as RBS, PIXE or ICP-MS.

To continue this study, it is imperative to obtain nanoparticles. This can be achieved grinding the already obtained particles (mechanically, e.g. with a planetary ball mill), changing some parameters of the synthesis such as the temperature and heating time used or even change the synthesis method completely.

2.2   Electrochromic Materials

2.2.1   Functional material

2.2.1.1   Tungsten oxide

Figure 44: WO_3 powder and dispersion synthesized in this work.

WO_3 is, perhaps, one of the most well-known electrochromic substances. Its application is well reviewed in several books and papers[40,84,85,86] and, along with viologens, it has been commercially explored on electrochromic applications such as "smart windows".[53,87,88,89] WO_3 popularity stems from its strong color contrast with a relatively low production cost. WO_3 has transitions both in the near infrared and visible region of the light spectrum, filtering thus an important part of the solar light and potentially reducing air-conditioning costs in buildings. The usual deposition method for WO_3 is sputtering or thermal evaporation, and   much   of   the   literature   and   technological   applications   apply   this technique.[84,90,91,92,93,94,95,96,97,98,99,100,101,102,103,104,105]

To use other methods, such as inkjet printing, it is important to synthesize the compound as nanoparticles, which can be achieved using a sol-gel method,[51,52,53,106,107,108,109,110,111,112,113,114,115,116,117,118,119] since larger particles may damage the printer nozzles. Normally, in this case, amorphous tungsten oxide nanoparticles are obtained.[45,85,105,110,111,112,113,114]

There are several sol-gel methods to produce WO_3 nanoparticles: Tungsten ethoxide ($W(OEt)_6$) solutions stabilized by acetic acid were used to form WO_3 layers, but this method is expensive and their high sensitivity toward water limits their use in commercial production[120].

Chloro-alkoxides seem to be more convenient precursors, since they dissolve well in alcohol solvents forming stable solutions of oxychloroalkoxides. This process is inexpensive and precursor solutions remain stable for several months[107,120,121,122]:

$$WOCl_4 + xROH \Rightarrow WOCl_{4-x}(OR)_x + xHCl$$
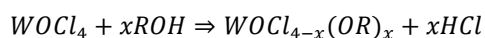
In the literature it is also described the formation of WO_3 sols from aqueous solutions. Such sols can be easily prepared via the acidification of sodium tungstate (Na_2WO_4) aqueous solutions. These aqueous sols are not stable. At room temperature precipitation occurs within a few days or even hours depending on concentration, constituting a drawback of these otherwise promising methods. A possible solution for this problem is to use complexing agents such as hydrogen peroxide to stabilize aqueous solutions of tungsten (VI) precursors[123, 124]. Stable solutions of peroxotungstic acid can be obtained via the reaction of tungsten, tungsten carbide or even tungsten oxide with a hydrogen peroxide aqueous solution. A peroxotungstic acid is formed in which two OH groups are replaced by one peroxo anion that behaves as a chelating ligand preventing further condensation and precipitation.

The method here described is a sol-gel method to obtain WO_3 nanoparticles from the peroxotungstic acid route. In 1986, Kudo described this route[123,124] and it is referred by some authors to be the best way to stabilize aqueous sols[53,125,126,127]. This method consists in mixing metallic tungsten with hydrogen peroxide and then, removing the hydrogen peroxide with a platinum foil. The solvent is partially dried under a stream of air at room temperature and then a polar solvent is added where the previous mixture is soluble, this solution is used for deposition. The obtained films were heated at 120ºC for 1 hour. Some authors used this method with some changes like P. K. Biswas[127] or B. Pecquenard[128]. In 1996, J. P. Cronin described a variant of this method to produce WO_3 sols. This process includes long time reactions, refluxes, filtrations and drying steps using vacuum and reduces pressure techniques, where the principal change is the addition of a carboxylic acid to improve the electrochromic performance of the film[129]. Since then, other authors like C. O. Avellaneda[130], D. He[131], S. A. Agnihotry[116], M. A. Aegerter[132] and others used Cronin method. There are of course other approaches to produce WO_3 sols that follow other sol-gel routes like those described by K. D. Lee[109] that used tungsten alkoxides as precursor, Y. Djaoued[133], S. Badilescu[134] and Ozkan[111], that used tungsten hexachloride as precursor, but all of them are complicate procedures or require sinterization after the film deposition. In the literature, authors generally refer or describe a sinterization/drying step that can vary from 60ºC to 600ºC during few minutes to several hours[85,87,89,92,93,94,95,96].In 2001, Bessiére described a deposition on flexible PET/ITO using spin-coating with a sol based on tungsten chloride in alcohol, but also with a drying step of 12h at 80ºC[135].

It is known that sol-gel synthesized particles normally lead to the formation of amorphous material (as mentioned above), which may be submitted to annealing after deposition to make crystalline particles. The strategy of this work consisted in analyzing four different tungsten oxide powders in order to make a comparison.

In addition to the synthesized powder (A) (Figure 44) obtained as explained in section 2.4 and the commercially available tungsten oxide (B), two more powders were obtained: one in which A was sintered at 550ºC for 1 hour (C) and another powder by dispersing A in water, followed by 1 week of ageing and lyophilisation, in order to obtain the "dry" powder D.

XRD and elemental analysis

The tungsten oxide powder was characterized using the experimental techniques described below, confirming the presence of tungsten oxide nanoparticles. The composition of the powder was studied using XRF and Elemental analysis techniques. Two XRF spectra were made, one for the synthesized powder and another using commercially available tungsten oxide powder. The two spectra aligned perfectly, showing that there was no other element (heavier than oxygen) in the composition of the two powders.

In elemental analysis, again, a comparison with commercially available WO_3 powder was performed to determine differences in terms of percentage of carbon and hydrogen elements. The carbon percentage was practically the same (0.22% (w/w) for the sol-gel powder and 0.24% (w/w) for the commercial powder) in both samples. In the sol-gel powder, however, hydrogen was also detected (0.64% (w/w)), while it was undetectable on the commercial powder.

DLS (dynamic light scattering) and dispersion analysis

DLS measurements of the sol-gel tungsten oxide particles dispersions of powder (A) were done in water/ethanol mixtures 1:1 (v/v). Table 9 summarizes the values of diffusion coefficient for infinite dilutions D_0, the virial coefficient α, and the average particle diameter d obtained from these experiments. The data shows that α is close to zero, meaning that repulsive and attractive interaction forces in this system are well balanced, cancelling each other. The average particle diameters were in the range 160-225 nm, depending on the filtration used. As expected, the average diameters decrease slightly after filtration through a 200 nm filter.

Table 9: Values for the diffusion coefficient for infinite dilutions D_0, the virial coefficient α, and the average particle diameter d, obtained by DLS.

	$D_0/cm^2.s^{-1}$	α	d /nm
Filtration: 1 μm	$(9.7\pm0.1)\times10^{-9}$	0 ± 0.1	230 ± 10
Filtration: 200 nm	$(1.6\pm0.1)\times10^{-8}$	0 ± 0.1	160 ± 10

Dispersion analysis was used to calculate also the particles size and the value obtained was 160nm average diameter, filtered at 1 μm (Figure 45). This experimental value can then be compared with those

calculated using the particle diameter obtained in DLS experiments, taking into account the solvent viscosity of each sample.

Powder B (commercial) and C (sintered) have a particle size higher than 1 μm because it was not possible to filter them with this pore size, while powder D (lyophilized) seem to have a particles size smaller than powder (A), around 120 nm.
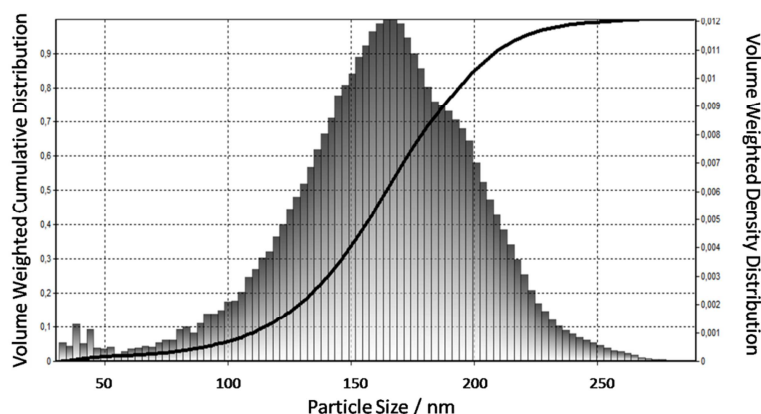
Figure 45: Particles size distribution of the tungsten oxide ink (powder A).

Thermal and Calorimetric measurements

Figure 46 shows differential scanning calorimetry (DSC) and thermogravimetry analysis (TGA) of the synthesized sol-gel tungsten oxide nanoparticles (A). From the DSC results, a small exothermic crystallization peak is observed at 550ºC. Some other endothermic processes, around 100ºC and from 250ºC to 350ºC, seem also to take place, but their intensity is rather small. TGA analysis shows material loss in this region, thus these processes are most likely linked to solvent evaporation. An intense endothermic peak above 1200ºC is detected, without any significant mass change in TGA data, indicating a phase transition at this region (most probably the melting point, although for pure tungsten oxide it is reported to be 1473ºC). Such discrepancy could be due to the composition of the nanoparticles (see below). DSC measurements of other tungsten oxide materials discussed in this work are shown in Figure 47. Powders B and C show the same behavior, as expected, with no peaks in the studied temperature range. Samples A and D show the same peaks but during the evaporation phase, around 100ºC, sample D show two sharp peaks instead of one large peak (sample A).

53
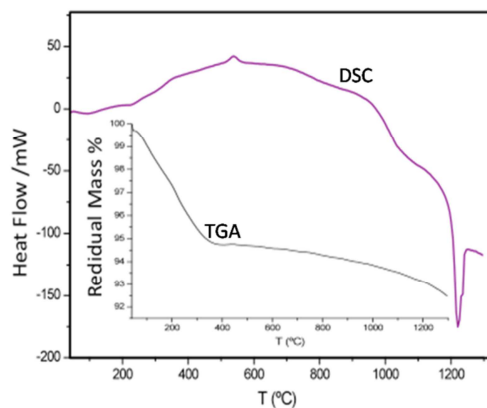
Figure 46: DSC and TGA analysis of the tungsten oxide synthesized nanoparticles (powder A) (scan rate equal to 10ºC/min).
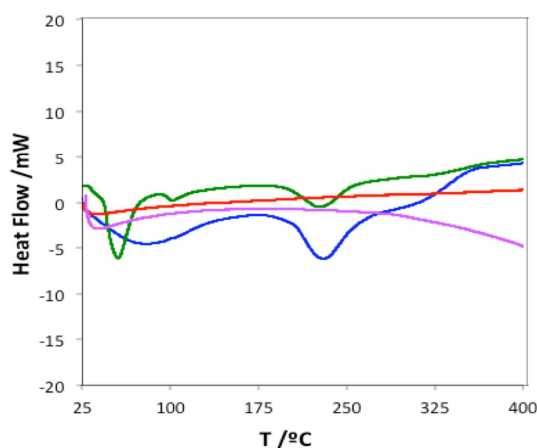
Figure 47: DSC measurements of all the tungsten oxide powders tested. Green line is the Lyophilized sample, Blue line is the synthesized powder (A), Red line is the commercially available powder and the pink line is the sintered sample.

<u>X-Ray diffraction (XRD), FTIR and Raman spectroscopy</u>

XRD, FTIR and Raman spectroscopy were employed with the aim of characterizing the crystallinity of the powders. The DSC measurement clearly shows presence of solvent molecules (mainly water) and an exothermic crystallization peak at 550ºC. Therefore with powder C we are able to characterize the crystallization process at 550ºC, while with powder D the main objective was to check if dispersion and ageing had an effect on the crystallinity of powder A. One must be aware, however, that the lyophilisation treatment also can lead to changes in crystallinity, which will be further discussed below.

The XRD spectra (Figure 48) show well-defined diffraction peaks for all samples. However each sample displays different crystallinity. A (the synthesized particles) show peaks consistent with a hexagonal

structure (JCPDS card 35-1001, hexagonal phase of $WO_3 \cdot 0.33H_2O$) that indeed has some water molecules incorporated. As expected from the specifications of the supplier, B shows a cubic structure (JCPDS card 46-1096, cubic phase of WO_3) without presence of water molecules. C has a tetragonal structure (JCPDS card 53-0434, tetragonal phase of WO_3), different from B, but also without water molecules. This result confirms that at 550ºC, the solvent is removed and the particles change their crystallinity. Powder D displays an orthorhombic structure (JCPDS card 43-0679, orthorhombic phase of $WO_3 \cdot H_2O$). Finally XRD peaks of A and D suggest that probably an amorphous phase co-exists with the crystalline phase (more broad and with less intensity peaks are obtained).
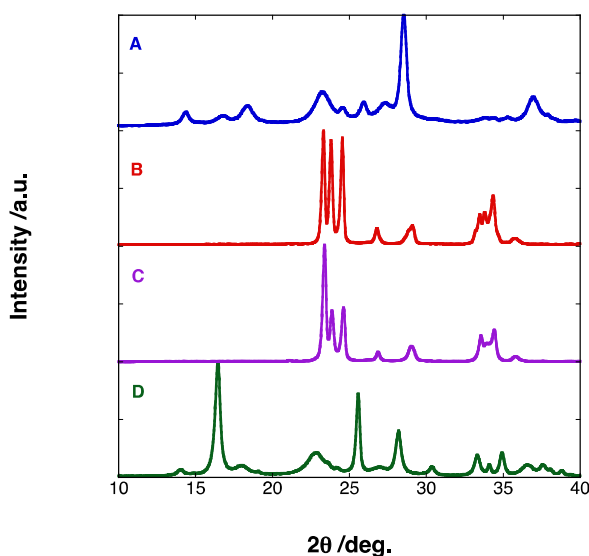
Figure 48: XRD spectra of synthesized powder (A), commercially available WO_3 (B), synthesized powder sintered at 550ºC for 1 hour (C) and synthesized powder dispersed in water, followed by 1 week ageing and lyophilisation (D).

FTIR and Raman spectra can provide a more conclusive answer for the presence of an amorphous phase and/or hydration of tungsten oxide. Several revealing features are observed in this set of spectra (see Figure 49). At 3400 cm^{-1} and 1615 cm^{-1} intense absorption IR peaks are observed on powders A and D. These results were expected since they correspond to vibrational modes of water molecules. These peaks are almost absent on powders B and C. Powders A and D also display a transition at 946 cm^{-1}, with small intensity in FTIR spectra but more evident in the Raman spectra, which is attributed to W=O or terminal W-O in amorphous compounds.[117,136,137] Around 820 cm^{-1} every sample displays a transition which relative intensity depends on the powder. These transitions are attributed to the W-O stretching mode, which is shifted to lower wavenumbers when the material is in amorphous state rather than in crystalline state.[112] This stretching mode also appears on samples B and C around 710 cm^{-1} (more clear in the Raman spectra). A broad peak appears at 636 cm^{-1} for powder A only, which is related with O-W-O

bending mode for a hydrated sample. This bending mode appears at 328 cm^{-1} and 274 cm^{-1} for samples B and C, but in this case without the presence of water molecules. For powder D, the results seem to be between the other samples and are difficult to interpret. All peaks below 200 cm^{-1} observed in powders B and C are attributed to lattice modes of WO_3 crystalline particles.[117] The lattice modes are absent in A and D.
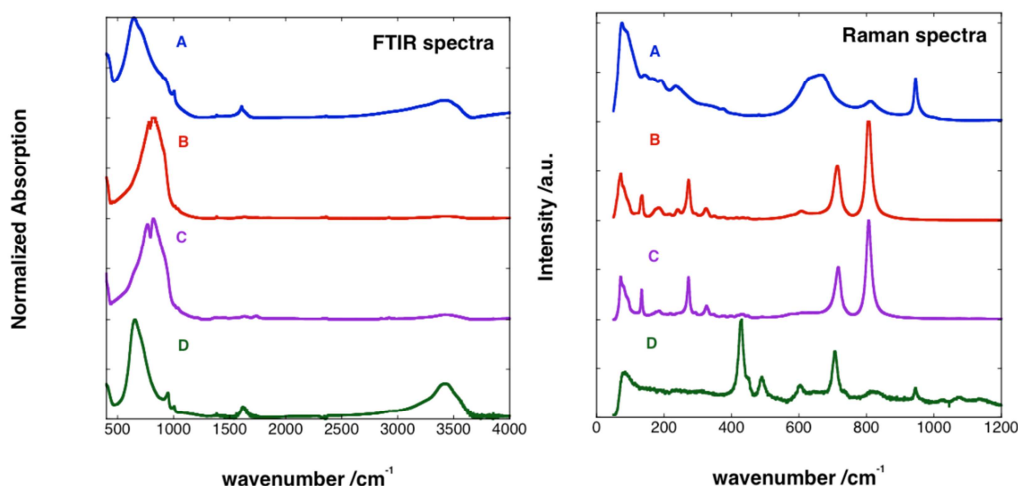
Figure 49: FTIR and Raman Spectra of synthesized powder (A), commercially available WO_3 (B), synthesized powder sintered at 550ºC for 1 hour (C) and synthesized powder dispersed in water, followed by 1 week ageing and lyophilisation in order to obtain (D).

In summary:

XRD, FTIR and Raman measurements indicates that powder A has an hydrated hexagonal structure with some amorphous phase, powder B shows a cubic structure, C has a tetragonal structure and powder D displays an hydrated (more hydrated than powder A) orthorhombic structure also with some amorphous phase.

   The coexistence of crystalline/amorphous domains on powders A and D is a result already discussed in the literature.[95] The amount of crystalline/amorphous domains depends of the reaction conditions, such as temperature, pH and concentration. The tungsten oxide produced is also called polycrystalline (a name which can be often misleading due to the presence of an amorphous fraction, see discussion on ref. 95), however such tungsten oxide usually has large fractions of crystalline domains (e.g., 70%, see also ref. 95) which does not seem to be the present case since Raman spectra shows mainly amorphous tungsten oxide. Using tungstate acid precursors, Livage et. al. studied in great detail the growth mechanism arriving

to the conclusion that at high temperatures the water dielectric constant is sufficiently low to increase electrostatic repulsions between W(VI) ions, thus leading to hexagonal phases similar to the one observed in this work, with a more open structure.[108] Although the precursor is different, it seems the same mechanism is occurring in this work. The mechanism that leads to orthorhombic structure on powder D is, however, less clear. Probably low temperatures (-30ºC) and/or water sublimation triggers the transition from hexagonal to orthorhombic phase. Also, from the intensity of the W=O Raman peak, it seems the powder D has a larger fraction of crystalline structure, but tungsten oxide is still present in the form of nanoparticles with 200 nm of diameter for this powder.

2.2.1.2 Vanadium oxide
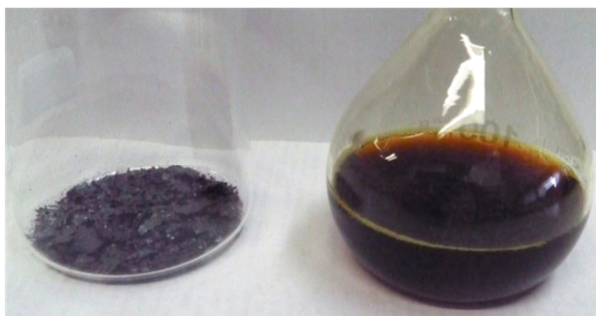
Figure 50: V_2O_5 powder and dispersion synthesized in this work.

Vanadium oxide structure is very complex due to vanadium multivalence and also due to the fact that this material can support a high level of defects in its structure. It has been used mostly as catalyzer[138, 139], gas sensor[140], solar cells[141] and batteries[142]. Vanadium oxide is also used in electrochromic devices[143] as a secondary electrochrome, in counter-electrode use, because of the poor color contrast and low coloration efficiency usually reported[144,145]. Sol-gel synthesis was studied and developed greatly in the last decade, leading to new open structures (gels) formed from aqueous precursors that favor the diffusion of small ionic or molecular species[146].

Using sol-gel methods, it is possible to produce vanadium pentoxide with very interesting properties. The films produced by sol-gel are usually hydrated. These products have been studied during the last century and the literature is vast. Livage wrote some reviews about this subject[147,148,149,150,151,152,153].

Four different sol-gel techniques are mostly described:

- Dissolution in water of amorphous V_2O_5.
- Vanadates protonation in aqueous solution: prepared from the acidification of vanadates aqueous solutions, but the sols are not stable.
- Vanadium alkoxides hydrolysis: vanadium alkoxides are very sensitive to hydrolysis; to make the reaction more comfortable, vanadium isopropoxides $(VO(OPr^i)_3)$ or vanadium tertio-amyl $(VO(OAm^t)_3$ are used.
- Reactions with hydrogen peroxide: gels or vanadium oxide sols can be obtained through the reaction of hydrogen peroxide with V_2O_5 or metallic vanadium. Vanadium peroxo-complexes are formed but they are not as stable as Tungsten ones.

This work shows that this metal oxide can also be formulated for inkjet applications, displaying electrochromic activity with excellent contrast. Colors obtained are gray, blue, green and yellow. The powder synthesis is described in section 2.4.

<u>Elemental analysis</u>

The composition of the powder was studied using Elemental analysis. A comparison with the commercially available vanadium oxide powder (used in the synthesis) was performed to determine differences in terms of percentage of carbon and hydrogen elements. The commercially available powder, carbon or hydrogen was not found. For the synthesized powder, 0.05% of carbon and 1.34% of hydrogen was detected.

<u>XRD, FTIR and Raman spectroscopy</u>

XRD, FTIR and Raman spectroscopy were employed with the aim of characterizing the crystallinity of the synthesized vanadium oxide powder (A). For comparison, the commercially available powder (B, see experimental section) was also characterized.

Figure 51 shows the XRD spectra with well-defined peaks for both samples. Nevertheless the crystallinity state is clearly different. Whereas powder B shows diffraction peaks characteristic of orthorhombic V_2O_5 (JCPDS card 41-1426), powder A is typical of a vanadium oxide gel (JCPDS card 40-1296). According to the literature, the vanadium oxide gel with this XRD pattern is an ionic compound with layers of $V_2O_5.6H_2O$ and microstructures similar to orthorhombic V_2O_5.[154] It can be described as a nanocomposite build with water molecules entrapped in the V_2O_5 net. Usually this kind of gel presents a ribbon like structure made with a double layer of VO_5 (like pyramids) facing each other.[150,154] Powder A was sintered at 400ºC and the same orthorhombic V_2O_5 was obtained (JCPDS card 41-1426).
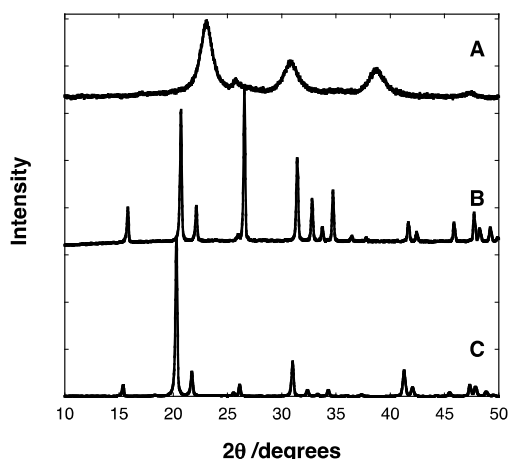
Figure 51: XRD spectra of the synthesized vanadium oxide powder (A, vanadium oxide gel) and commercially available V_2O_5 (B, orthorhombic V_2O_5). The synthesized powder was sintered at 400ºC, with XRD spectrum shown as well (C, orthorhombic V_2O_5).

FTIR and Raman spectra can provide insights for the presence of an amorphous phase and/or hydration of vanadium oxide. Several revealing features are observed in this set of spectra (see Figure 52). At 3400 cm^{-1} and 1615 cm^{-1} intense absorption IR peaks are observed on powder A. These results were expected since they correspond to vibrational modes of water molecules. For powder B, these peaks are weak. In the region around 1000 cm^{-1} peaks relative to the V=O terminal oxygen stretching mode are seen in both FTIR and Raman spectra.[155] For powder A, these Raman peaks are split to one weak peak at 1023 cm^{-1} and another strong peak at 892 cm^{-1}. The commercial sample shows a single strong peak at 969 cm^{-1}, in accordance with published results for crystalline V_2O_5.[155] Around 750 cm^{-1} (FTIR) a peak corresponding to a V-O-V asymmetric stretching mode [156] is seen in both powders, but it is shifted to lower wavenumbers in powder, A which may indicate the presence of amorphous material in those particles. The Raman spectra show this vibrational mode at 682 cm^{-1} for the commercial sample (characteristic from corner shared oxygen common to 2 pyramids), but it is split into two peaks (706 and 650 cm^{-1}) for the synthesized powder. The appearance of two peaks was already observed earlier for amorphous vanadium oxide, and thus it can result from the mix of amorphous and crystalline portions in A powder.[157] The same authors also observed two peaks on the 900 – 1000 cm^{-1} region, concluding that a peak at 932 cm^{-1} is due to V(IV)=O stretching that appears due to oxygen deficiency.[157] If the same reasoning applies to the 892 cm^{-1} peak, that would imply the presence of V(IV) on powder A. At 516 cm^{-1} in FTIR spectra a V-O-V symmetric stretching mode is found. In Raman spectra, peaks at around 530 cm^{-1} corresponding to V_3O stretching mode from edge shared oxygen common to 3 pyramids are found in the two samples.
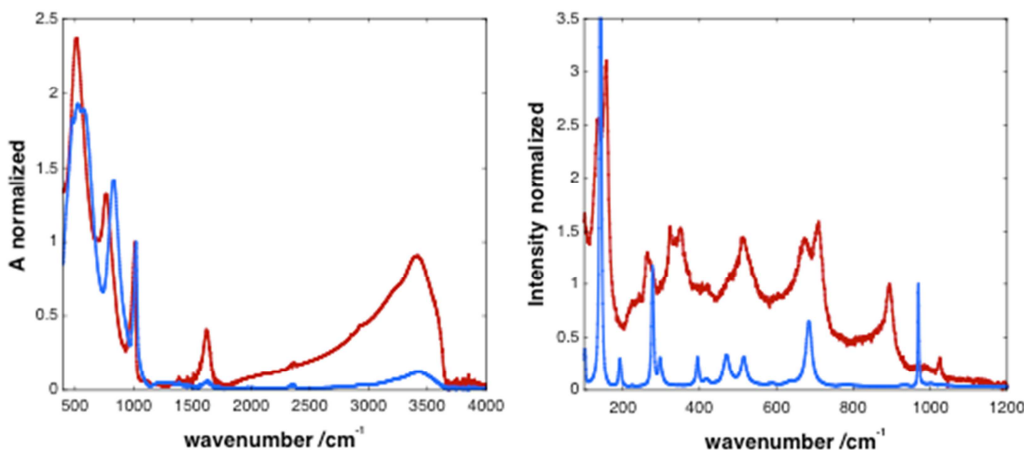
Figure 52: FTIR (left) and Raman (right) spectra of synthesized powder (red) and commercially available V_2O_5 (blue).

For lower frequencies, one observes mainly bending modes.[155,157,158] At 483, 405, 283 and 303 cm^{-1} peaks of V-O-V bending mode, V=O bending modes and V_3O bending mode respectively are found in the commercial sample that are equivalent to the peaks found for the synthesized sample at 450 to 200 cm^{-1}

but for disordered framework. Finally peaks found above 200 cm^{-1} are typical for lattice modes and it can be notice that those peaks are much less intense in the synthesized sample due to the lack of long-range order.

Thermal and Calorimetric measurements

Figure 53 DSC and TGA of the vanadium oxide powder A and the commercially available V_2O_5 powder B (only DSC in this case). Powder B DSC analysis does not show any transition in the available temperature range (between 25 and 500 ºC), as expected since no solvent evaporation or phase transition occurs for this powder within the temperature range. Powder A, however, shows a large endothermic process from room temperature until 140ºC attributed to free water evaporation, confirmed by the loss of mass in this temperature range on the TGA graph (Fig. 3B). At 311ºC a sharp second endothermic transition is observed, followed by an exothermic transition at 337 ºC. The first process is linked to release of water entrapped within the vanadium oxide structure, see also TGA graphic. This process triggers the exothermic transition due to change of the vanadium oxide crystalline state to orthorhombic, as can be seen on Figure 53 (JCPDS card 41-1426, V_2O_5).[159,160] Without the water molecules, the crystalline structure becomes metastable and evolves to anhydrous crystalline phase.
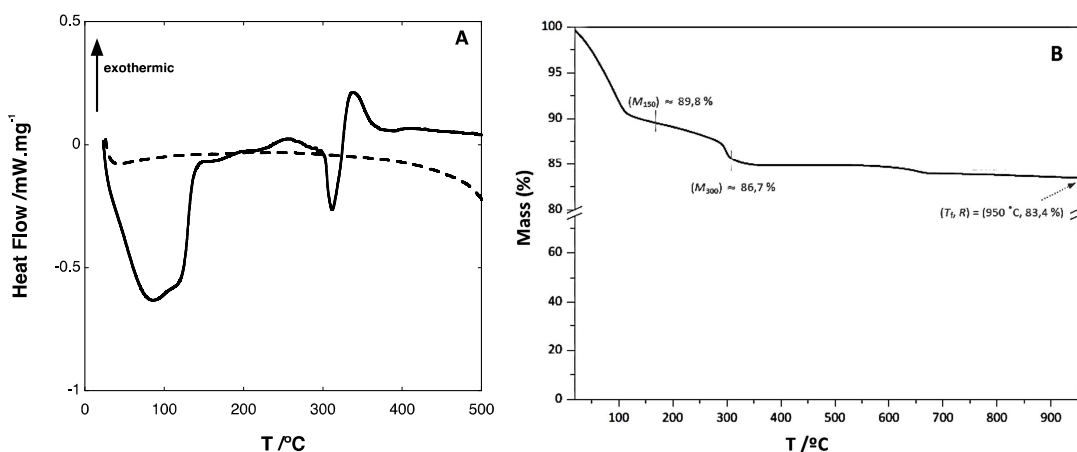
Figure 53: A - DSC analysis of the vanadium oxide synthesized gel (full line) and of the commercial vanadium oxide (dashed line). Scan rate equal to 10ºC/min. B – TGA of the vanadium oxide synthesized gel.

As described above, sol-gel vanadium oxide normally exists in the form of ribbons[150]. However our synthesis product is the powder of the vanadium oxide gel, which leads to other structures as can be seen

on TEM images (Figure 54). Instead, thin sheets of material are synthesized with sizes clearly above 200 nm. AFM images of the powder (Figure 55) also show features in accordance with TEM images. Sahana et al reported similar results for vanadium oxide gels deposited as thin films deposited by spin coating followed by baking at 100/350ºC (however on this case a sinterization step at 450ºC was performed)[159].
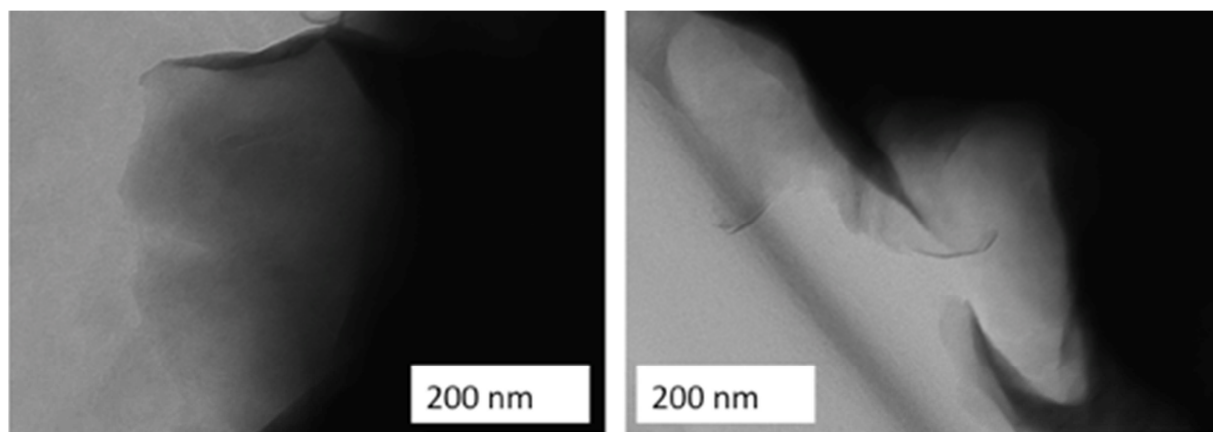
Figure 54: TEM images of the synthesized vanadium oxide powder.
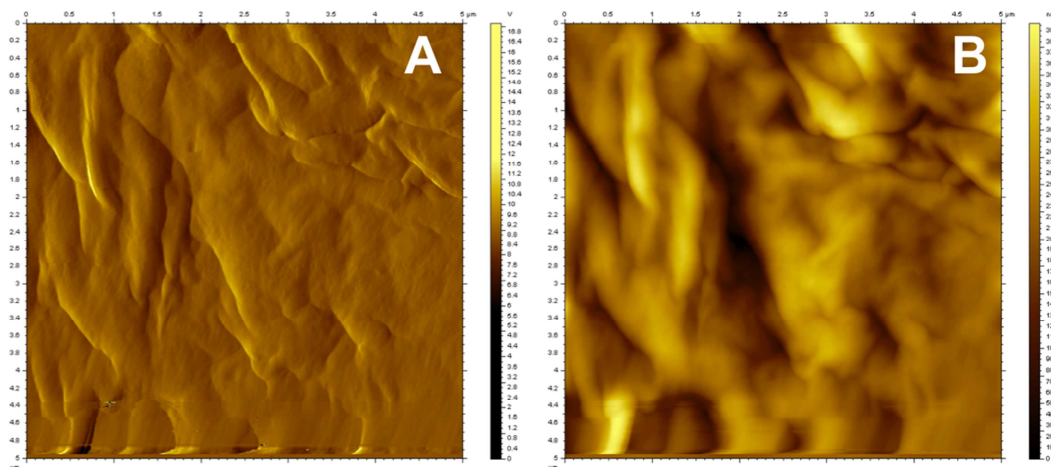
Figure 55: AFM images of the synthesized V2O5 gel A) deflection image, B) topographic image.

The results here presented are therefore in line with those obtained earlier for vanadium oxide gels using the reaction of V_2O_5 as precursor with hydrogen peroxide. As described earlier, the evolution of this mixture evolves initially the formation of water-soluble peroxo species that later decompose to vanadate species. This solution evolves to decavanadic acid that finally polymerizes to $V_2O_5.nH_2O$ gels[150,161,162].

These pseudo-crystalline phases contain both amorphous and crystalline portions, as seen here. 2-dimensional sheets are observed in the powder, with very large sizes, but as can be seen in the next section, its re-suspension in water leads to very stable colloidal particles that can be used in inkjet printing.

2.2.2   Ink formulation and inkjet printing.

This work focused on the electrochromic material of the electrochromic devices. A study was performed to evaluate the possibility of inkjet printing several different and well-known electrochromic materials. As organic electrochromic materials, poly(3,4-ethylenedioxythiophene)–polystyrene sulfonic acid (PEDOT: PSS) and poly-3-hexylthiophene (P3HT), that are poly(thiophene)s, were tested and as inorganic materials, Prussian Blue (PB) (metal hexacyanomettalate) (see structures in Figure 9), tungsten trioxide and vanadium pentoxide (metal oxides) were chosen.

Metal oxides are widely studied mostly because of their photochemical stability in comparison with organic electrochromic materials, but they can be unstable chemically in the presence of moisture, they are brittle by nature and it is also known that organic materials has more available colors and more contrast between the oxidized or reduced states[163]. Tungsten oxide and PB are very interesting materials because one of the redox states is transparent. PEDOT is one of the most studied electrochromic materials and present as advantages, commercial products already available, environmental stability and ease of processability[41]. PEDOT: PSS has already been inkjet printed for other applications then electrochromic device[164]. These three materials present blue colors, so, to have different colors then blue, vanadium oxide (blue/yellow) and P3HT (blue/red) were tested.

Tables 10 to 12 give an overview of the results obtained in this section allowing a direct comparison between inks. These tables will be mentioned again during this section. Table 10 shows the composition of the inks. Table 11 presents the physical parameters of the inks. For comparison, the optimal values for the use of a given ink formulation on an inkjet printer are also shown[171]. The sedimentation velocity and the printer parameters used to print those inks are also shown in table 11. Table 12 shows the reliability (see experimental section) of the inks.

.

Table 10: Inkjet printing inks composition of the electrochromic materials studied.

Ink	Composition
Pedot	Water (50,2%w/w), Pedot:PSS solution (47,8% w/w), NaOH 1M (2%w/w), Triton-x (1%w/w)
P3HT	Tetrahydrofuran (46.1% w/w), chlorobenzene (52.5% w/w), P3HT (1.4% w/w)
WO$_3$	Water, WO$_3$ nanoparticles (0,4% w/w)
V$_2$O$_5$	Water, V$_2$O$_5$ powder (1% w/w)
PB	Water, PB nanoparticles (1,1% w/w)

Table 11: Values of surface tension, density, viscosity and pH for all the electrochromic inks and optimal values for the DMP-2800. Number of layers printed, applied potential and pulse duration of the printer. Sedimentation velocity.

Ink	Density (g/ml)	Viscosity (cp)	Surface tension (dyn/cm)	pH	Number layers	Potential (V)	Pulse duration (µs)	Sedimen-tation (mm/day)
Pedot	0.99	14	31.3	6	5	19	41	0
P3HT	1.04	1.77	29.2	3	5	11	15	0
WO_3	1.00	2	65.4	3.5	20	14	32	5.8
V_2O_5	1.00	2.2	60	2.5	13	26	32	0.018
PB	0.97	2	57.2	6	3	12	32	0.014
Optimal values DMP-2800	≥ 1	3-12	28-33	3-8				

The inks were printed on PET/ITO and on paper to evaluate the print quality on both substrates using a drop-on-demand piezo (DOD piezo) inkjet lab-scale Dimatix® materials printer (DMP-2800). The drops were small (volume equal to 10 pL, around 10 µm of radius) and spherical as required. PET/ITO electrodes with the printed inks were characterized using cyclic voltammetry and spectroelectrochemistry in liquid state. An independent work was done on PEDOT:PSS and tungsten oxide in collaboration with ®Xennia. These inks were formulated to achieve optimum rheological properties with the objective to use them in industrial printers. Those optimizations are described ahead in this section

Table 12: Reliability of the inks, measured after 5 minutes of continuous printing and after 1 minute of pause.

Ink	Reliability	
	5 minutes printing	1 minute pause
Pedot	100%	100%
WO_3	70%	70%
PB	90%	90%
V_2O_5	100%	100%
P3HT	100%	100%

2.2.2.1 Tungsten oxide

The obtained tungsten oxide nanoparticles (powder A) were dispersed in water (see experimental section), giving a stable colloidal suspension characterized by sedimentation techniques. The ink dispersion used has a tungsten oxide concentration equal to 1.7 g/dm^3 in water.

However, additives, dispersants, surfactants and binders were introduced in order to optimize the dispersion stability. Several different dispersions were prepared and the function was tested, Table 13 resumes the obtained results. The goal was to obtain dispersions with optimal rheological properties that could be used as inkjet inks, therefore viscosity, pH and surface tension had to be measured and adjusted according to the different supporting substrates used without interfering with the ink function[165, 166,167,168, 169]. From the results obtained, it can be seen that much of the reagents used inhibits the electrochromic response of the materials, probably due to nanoparticles encapsulation or to redox competition. In the case of alcohols, it was found that the performance seems to be maintained at the beginning, but cycling tests shown that it degrades much faster than devices built only with aqueous inks (see table 29 in section 2.2.3.1).

Table 13: Reagents (additives, dispersants, surfactants and binders) that were added to dispersions of water and tungsten oxide nanoparticles in order to optimize the rheological characteristics of the inks.

Reagents	Effect detected on the ink / electrochromic performance
Ethanol	Decrease drastically the number of cycles
Methanol	
1-butanol	
2-propanol	
Hexanol	Limited solubility in water
PVA	Partial or complete inhibition of electrochromism
Dextran	
Triton-X	
Glycerol	
Oxalic acid	
PEO-PPO	
PVP	
PDDA	
SDS	
PAA	
1,3-propanediol	
Diethylene glycol	
PSS	Nanoparticles precipitation
CTAB	
Propyl lactate	
1-methyl-2-pyrrolidinone	Surface tension decrease
Ethyl L-lactate	
Ethylene glycol	Viscosity increase

Experimental and calculated (using the DLS results in section 2.2.1.1) sedimentation velocities obtained for different tungsten oxide ink formulations for earth gravity are presented in table 14 where experimental values were compared with calculated values. In less polar solvents, smaller sedimentation velocities are observed and filtration, as expected, decreases the sedimentation velocities. One would expect that inclusion of $LiClO_4$ salt could improve the electrochromic performance of the devices[170]. However, the presence of salt leads to particles with sizes well above 1 μm. This is not recommended for inkjet formulations due to the nozzle sizes of these printers (a nozzle size is typically around 20μm for a 10pl drop), the recommended maximum particles size to avoid nozzle damages is 1μm [171] (Figure 56). Nanoparticles concentration affects the stability of the ink; lower concentration makes the ink less stable. But the larger effect is the aging of the particles. Indeed after 1 day the sedimentation velocity decreases to about half the initial value, becoming stable afterwards (Figure 57). This important result shows that aging improves the colloidal stability of the system (table 14). Finally, additives like diethylene glycol also reduce the sedimentation velocities. The most stable formulation found has a 0.8 mm/day sedimentation velocity; however the addition of surfactants such as triton-X 100 or diethylene glycol is not appropriate because electrochromism effect is lost, as referred above.

Several observations can be discussed. Inks with $LiClO_4$ salt leads to particles with sizes above 1 μm, meaning that there was particle aggregation. This result shows that WO_3 nanoparticles are negatively charged: when salt is added the electrostatic repulsion is cancelled and the forces balance is shifted to attractive interactions. The addition of methanol and ethanol leads to smaller sedimentation velocities meaning that in less polar solvents (i.e., lower dielectric constants) the electrostatic repulsion should be enhanced. However this trend is not completely clear, since viscosity also increases. Probably both effects play a role in water/solvent mixtures. Surprisingly, nanoparticles lower concentration makes the ink less stable, again, probably due to repulsive attraction between particles. The aging of the particles is the most affecting parameter tested, showing that aging improves the colloidal stability of the system also because of the repulsive attraction between particles. In fact, when the dispersion is allowed to age, the nanoparticles in the dispersion should slowly disaggregate due to these repulsive forces, meaning that the initial powder is constituted by small particles aggregations. As expected, additives like diethylene glycol or triton-X improves the dispersion stability, however this addition of surfactants is not appropriate because electrochromism effect is lost. This behavior could be explained by an encapsulation of the nanoparticles by the surfactants, but this encapsulation is preventing the ion exchange during the oxidation-reduction process.

Table 14: Sedimentation velocity for Earth gravity with different ink formulations (estimated error of 0.1mm/day).

Solvent	ϕ (%)	Filtration	Age /days	Additives (% w/v)	u_{exp}^{g} (mm/day)	u_{calc}^{g} (mm/day)[1(a)]
Water	0.07	—	0	—	13.8	16.2
Water	0.07	—	1	—	7.4	16.2
Water	0.07	1 μm	7		5.8	16.2
Water	0.07	1 μm	0	—	8.5	16.2
Water	0.047	—	0	—	12.0	16.2
Water	0.035	—	0	—	15.6	16.2
Water	0.07	—	0	2% TX-100	12.0	12.2
Water	0.07	—	0	2% DG	11.2	13.3
Water/ethanol (1:1 v/v)	0.07	—	1	—	5.7	7.3
Water/methanol (1:1 v/v)	0.07	—	1	—	5.9	9.8
Water	0.07	—	0	Commercial WO_3	21.6	—
Water	0.07	—	0	Lyophilized WO_3	9.6	—
Water/ethanol (1:1 v/v)	0.07	1 μm	7	2% DG	0.8	5.05

(a) Calculated using eq. 18 (Section 2.3.1), using d obtained in DLS experiments.

(b) Viscosity was measured experimentally, except for samples with $LiClO_4$ (values taken from literature[172])
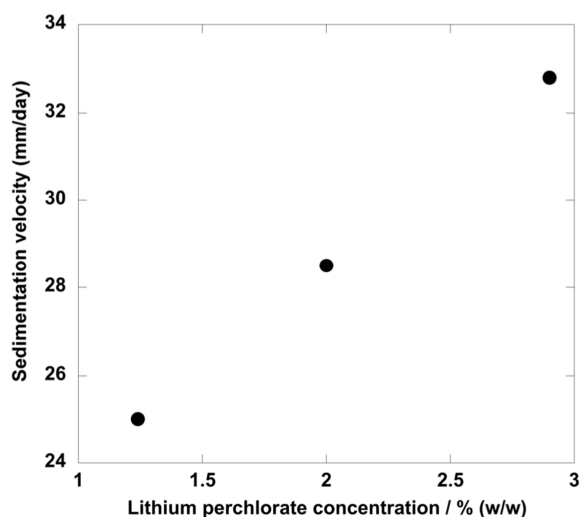
Figure 56: Effect of lithium perchlorate concentration on the sedimentation velocity of tungsten oxide ink (estimated error of 0.1mm/day).
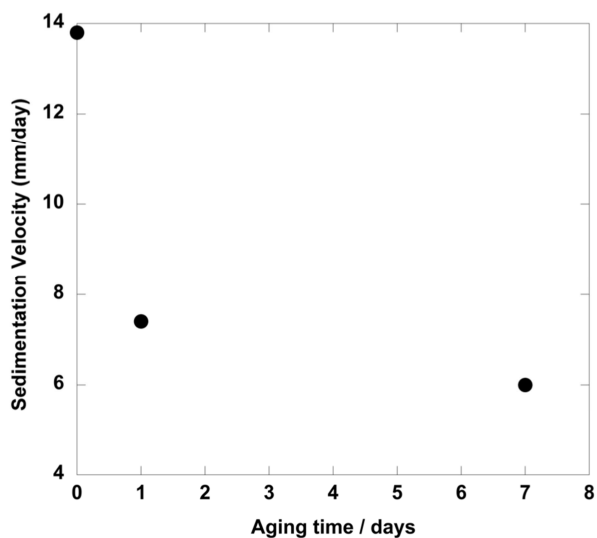
Figure 57: Aging time effect on the sedimentation velocity of tungsten oxide ink (estimated error of 0.1mm/day).

Table 11 shows the results obtained for viscosity, surface tension, density and pH measurements for the formulation of tungsten oxide with water only. Although this formulation is not completely within the manufacturer specifications, the tests performed in several substrates were satisfactory, both in terms of ink deposition and patterning. It is demonstrated in section 2.2.3.1 that the ink that has a better behavior in terms of electrochromism is the formulation with only water. The nanoparticles sizes were also determined with sedimentation technique and the value obtained was 200 nm average diameter.

Inkjet printing

The ink was printed using a waveform with an applied voltage of 14V (Table 11) and a firing drop frequency of 6 kHz. Two different drop spacing were compared, 10 and 20 µm, the amount of ink was maintained in both cases so the comparison could be effective. 20 passes were done to obtain the final film.

The waveform has 5 segments as shown in Figure 58 and the total pulse time is 32 µs. Each segment has three properties: duration, level (of voltage) and slew rate. After the last segment (segment 5) the nozzle is ready for another pulse. The applied voltage is related to the extension to which the chamber membrane is being bended, the slew rate is how fast it is being bended and the duration is how long it stays in that position. Before beginning the pulse, the piezo is in the standby position (V off), which is a percentage of the defined potential; in this position the chamber is slightly depressed. Segments 1 and 2 will bring the piezo to a relaxed position with the chamber at its maximum volume (0 volts), in this stage, the ink is pulled into the chamber. Segment 3 is responsible for the ejection of the drop, where the

chamber is compressed at 100% of the programmed voltage. Segments 4 and 5 are the recovery phases where the piezo is brought back to the standby position[171]. The amplitude (voltage), the second and third segments have the most impact on the jetting process, this three variables can change drop formation drastically.

Figure 58: Waveform used to print the WO_3 layer using a lab-scale Dimatix® materials printer (DMP-2800).

Figure 59 shows the sequential drop formation of the WO_3 ink using the waveform shown before, where the drops are small and without defects like satellites or tails. Reliability (measured by determination of the percentage of nozzles that are still working after a certain time) is an important parameter to define the cleaning cycles of a printing process. It will directly influence the production speed. All inkjet processes have cleaning cycles associated, but if the interval between those cycles is larger, the printing process will be faster.

The reliability of the ink is still not perfect (table 12), which in this case is attributed to the ink composition (constituted only by nanoparticles and water without other solvents or surfactants), but the reliability is still 70% of working nozzles after 5 minutes of continuous printing with a frequency of 6 kHz. To eliminate the reliability problems during printing, cleaning cycles were programmed from time to time to recover all the possible non-working nozzles. This indicates that the cleaning cycle must be set in shorter intervals than 5 minutes. Figure 59 shows also the printing quality for a pattern of WO_3 ink. Since the printed ink is almost transparent, it is very difficult to see it with naked eye, the printed films were put under a UV light to reveal the printed images. The print quality on paper and on plastic is satisfactory for the applications wanted. Figure 60 shows printed films (seen with the Dimatix microscope) both printed with the same ink

70

formulation, ink volume and waveform shown in Figure 58 but with different drop spacing. The difference is that A) was printed with a drop spacing of 10µm and B) with a drop spacing of 20µm. To guarantee the exact same amount of ink in the two samples, 20 layers of 20 µm drop spacing were printed (B), and to obtain a 10 µm drop spacing (A), 10 layers of 20 µm drop spacing were printed and then another 10 layers of 20 µm drop spacing but with a 10 µm delay from the starting point. One can see that the differences between the two samples are quite evident, since A) has a larger covered area and less empty spaces, as well as bigger "islands" of ink then B).
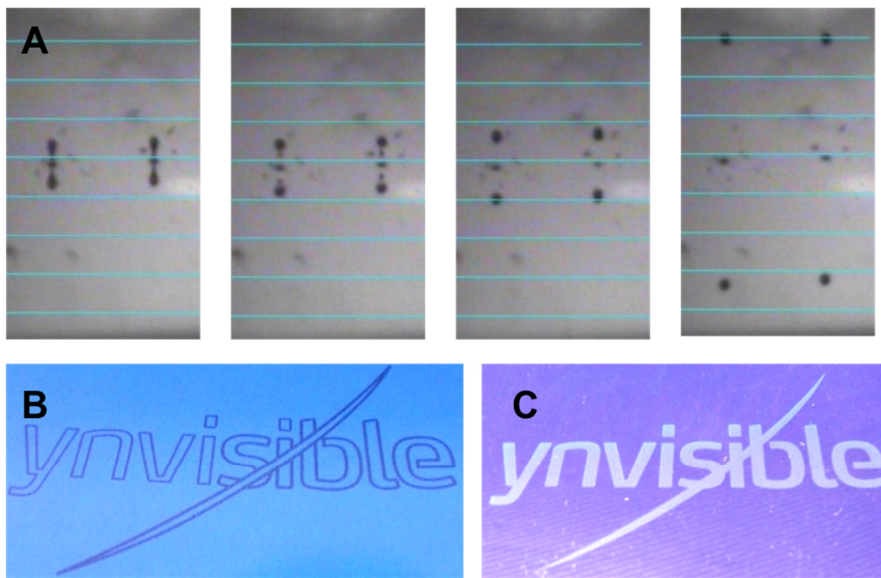
Figure 59: A) Sequential drop formation in a lab-scale Dimatix® materials printer (DMP-2800) printhead of a WO$_3$ inkjet ink B) the print quality on paper and C) the print quality on plastic.

If no droplet agglomeration took place, a continuous tungsten oxide film would be seen in these images. However tungsten oxide islands were observed, with a size of approximately 200 µm. The formation of these islands is related with two different factors: agglomeration of deposed droplets due to capillarity effects (the contact angle between the ink and PET/ITO is 40º), and drying of the droplets, which is not instantaneous.

71
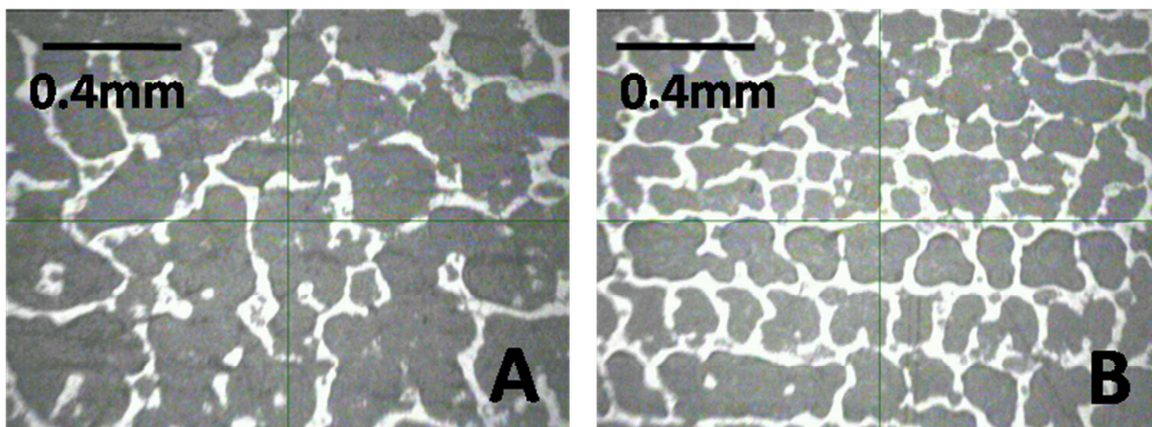
Figure 60: WO_3 ink printed on PET-ITO A) 10 µm drop spacing, B) 20 µm drop spacing.

Films characterization

AFM images displayed on Figure 61 show more details of the printed films. Tungsten oxide particles are clearly seen, with sizes ranging from 100 to 200 nm in accordance with DLS and sedimentation experiments. The rugosity of the film is also shown on Figure 61, with amplitude of 100 nm for the region investigated. The rugosity of PET/ITO without tungsten oxide particles is much smaller than this (around 5 nm, Figure 62) showing that this rugosity comes only from the tungsten oxide coating. This is an important aspect for electrochromism, since a higher rugosity leads to a larger interfacial area with the electrolyte layer, thus facilitating Li^+ insertion in the electrochromic material.
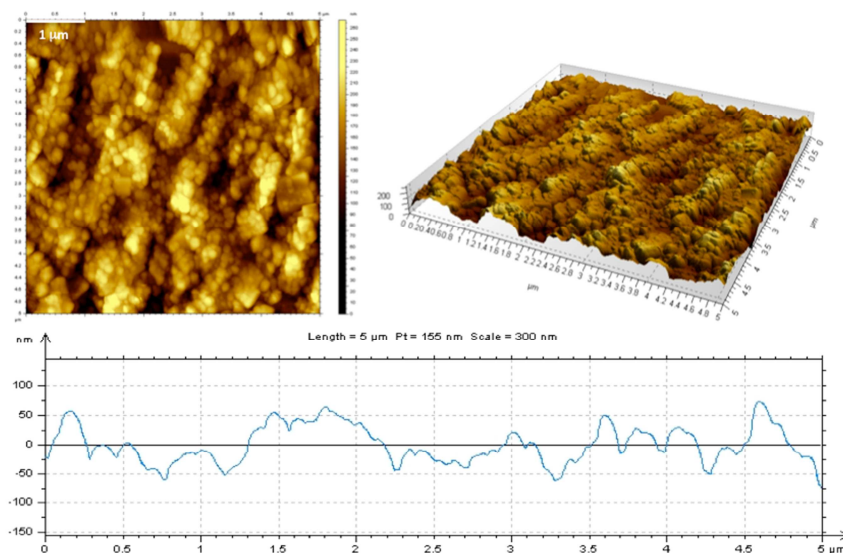
Figure 61: AFM images and rugosity measurements of tungsten oxide printed films on PET/ITO substrates.
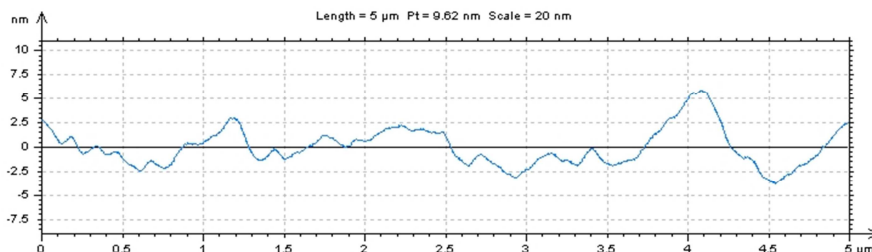
Figure 62: Rugosity measurements of PET/ITO substrates.

Attempts were made to print powders B and C. However, dispersions with these crystalline powders resulted into particles with sizes too large to pass the filter and, therefore, could not be deposited by inkjet. Such limitation was not observed with D, which could also be deposited by inkjet.

The electrochemistry and spectroelectrochemistry study of tungsten oxide printed films is presented in section 2.2.3.

Collaboration with [®]Xennia

Tungsten oxide inks were developed and optimized to be printed with high reliability at a 10kHz frequency using semi-industrial and industrial systems. All the rheological properties were adjusted to reach the optimal ranges for industrial exploitation. The ink used before had a concentration of 1% (w/w) and 15 printed layers were necessary for a good color contrast. This study started with a more concentrated dispersion of tungsten oxide particles in water (13.3% (w/w)) so the number of layers could be reduced.

pH
To adjust the pH of the ink to 6, three different reagents were tested separately: lithium carbonate solution, sodium bicarbonate in water and ammonia carbonate in water.
The average particles size of the dispersion was slightly affected but is still under 200 nm (measured by Xennia with a sedimentation technique), meaning that all three solutions were adequate. Since the electrochromic displays contains lithium ions, the dispersion neutralized with lithium carbonate was chosen for further development.

Surface Tension
The dispersion neutralized with lithium carbonate had a surface tension of 69 dynes/cm. Inks used in industrial printheads should have a surface tension in the range of 24-36 dynes/cm. The surface tension was reduced by adding the solvents named in table 15 with a concentration of 10% (w/w). The particles

size for all the formulations was again measured to ensure that these reagents did not affect this important parameter (table 15).

Table 15: Solvents tested to reduce the surface tension (10% w/w), value of surface tension of the new ink and particle size*.*

Solvent	Surface tension (dynes/cm)	Particles size (nm)
Ethylene glycol monobutyl ether (EGMBE)	31	168.2
Diethylene glycol monobutyl ether	37	165.7
1,2-hexanediol	31	222.4
Dowanol PNP (Propylene Glycol n-Butyl Ether)	36	178.4
1-ethoxy-2-propanol	47	166.6

EGMBE and 1,2-hexanediol reduce the surface tension into the middle of the range acceptable to the printhead, but 1,2-hexanediol is expensive so EGMBE was used for further work.

Viscosity

The dispersion neutralized with lithium carbonate has a viscosity of 1.26 cP. The recommended viscosity for an industrial printhead is 8-20 cP, so the viscosity of the dispersion was raised to 10 cPs using the following quantities of solutions of commercial PVA (Mowiol and Alcotex) and again the particles size for all the formulations was measured (table 16).

Table 16: Solvents tested to increase the viscosity, value of surface tension of the new ink and particle size*.*

Solvent	Concentration (% on dispersion)	Particles size (nm)
25 % Mowiol 3-85 in water	47	274.2
25 % Mowiol 4-88 in water	43	217.1
25 % Mowiol 5-88 in water	30	217.9
35% Alcotex 864 in water	28	196.6

All the polymer solutions caused an increase in particle size. The solution of Mowiol 3-85 caused the greatest increase, therefore it was not used in further formulations. The three others were used for further development.

When 10% EGMBE is added to the neutralized dispersions with Mowiol 3-85, Mowiol 4-88 or Alcotex 864, the physical properties obtained are shown in table 17.

Table 17: Physical properties measured for the neutralized dispersions with 10% EGMBE and Mowiol 4-88, Mowiol 5.88 or Alcotex 864.

	Mowiol 4-88	Mowiol 5-88	Alcotex 864
WO_3 (% w/w)	6.93	7.61	7.75
Viscosity (cPs)	13	11.6	12.2
Surface tension (dynes/cm)	31	31	31
Particle size (nm)	230	230	209
pH	5.1	5.17	4.81

The three formulations prepared above were printed using a Xaar 760-GS8 printhead, it was noticed that the initial printed film color should be almost transparent (light yellow) but instead, a strong yellow coloration was seen. In the other hand, when the devices were closed and tested, no blue coloration appeared meaning that the electrochromism effect was lost. It was clear that the probable cause for this fact was the interference of the polymer with the nanoparticles, as seen before for other polymers. To solve these two problems, the tungsten oxide concentration was decreased and the polymers (Mowiol 3-85, Mowiol 4-88 or Alcotex 864) were removed from the formulations. Of course, the viscosity of this final formulation decreases to values outside the optimal range, but it was still possible to print with the chosen print head.

The final formulation was: - 4% Tungsten oxide powder

                                       - $LiCO_3$ (pH=6)

                                       - 10% of EGMBE and 1,2-hexanediol

New

The print quality was very good. The drop formation presented no tails or satellites. The devices displayed a good contrast and excellent transition speed with only two printed layers (Figure 63).
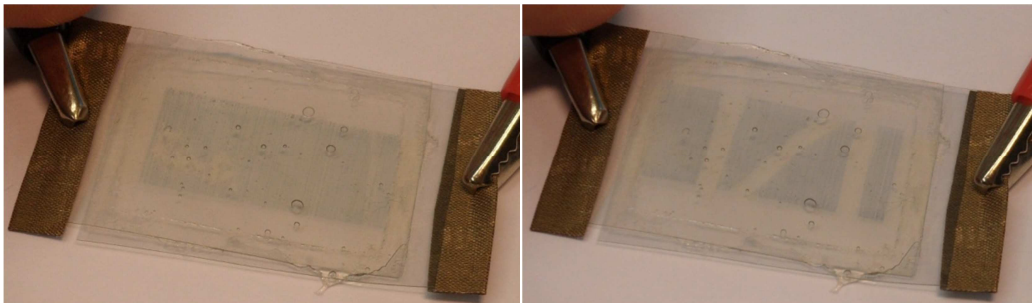
Figure 63: WO_3 printed device with only two printed layers.

2.2.2.2 Vanadium oxide

The synthesized vanadium oxide powder can be readily suspended on water (2.54 g/dm³) and filtered at 1µm, giving a very stable colloidal suspension (characterized by sedimentation techniques, see below), producing a formulation with the physical properties shown in table 11.

The experimental sedimentation velocity obtained of 0.018 mm/day indicates that the ink is very stable and appropriate for this kind of printing method. The nanoparticles average size determined using dynamic light scattering (DLS) measurements was 64 nm of radius, assuming a spherical shape for the particles.

The sedimentation and DLS results clearly are not in accordance with the results obtained for the vanadium oxide powder described above. Therefore one may conclude that the particles in solution do not have the same structure observed in the TEM images. Atomic Force Microscopy of the printed film sheds light about this issue (Figure 64). No spherical particles are observed. Instead, the film has a rugosity amplitude of about 30 nm, PET/ITO has an amplitude of 5 nm (Figure 62)) and the pattern of the film looks similar to threads. In fact it is known that vanadium oxide gels tend to form ribbons[150], and that type of structure is compatible with the AFM result. The rugosity of about 30 nm found in AFM measurements could be the average diameter of the ribbons and the result obtained from DLS (64 nm radius, assuming spherical particles) could reflect the length of these ribbons.
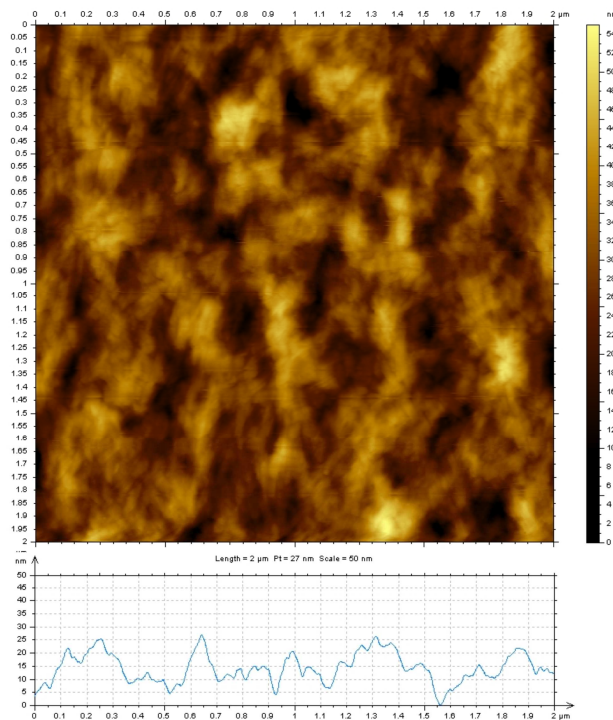
Figure 64: AFM images and rugosity measurements of vanadium oxide gel printed films on PET/ITO substrates.

76

<u>Inkjet Printing</u>

New

The ink was printed using the waveform presented in figure 65 with an applied voltage of 26V (Table 11) and a firing drop frequency of 6 kHz. 20 µm drop spacing was employed and 13 passes were done to obtain the final film.

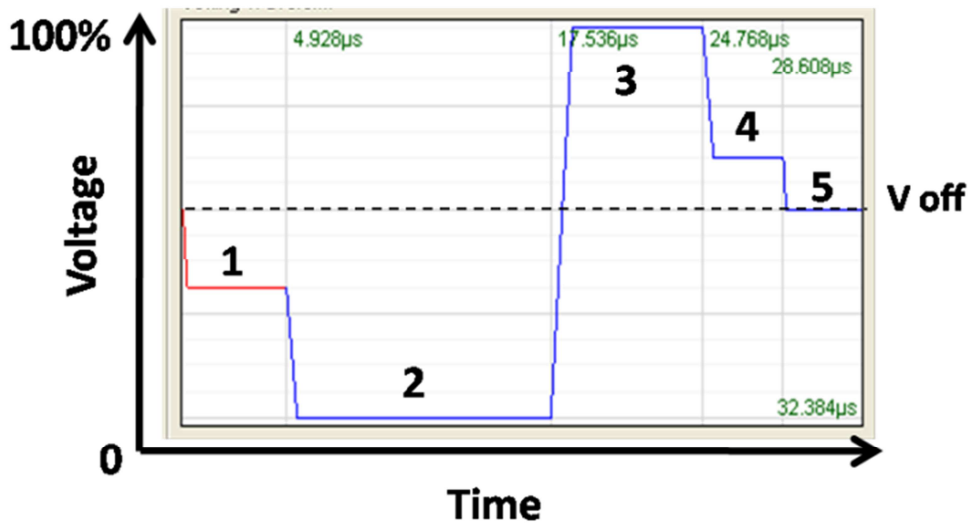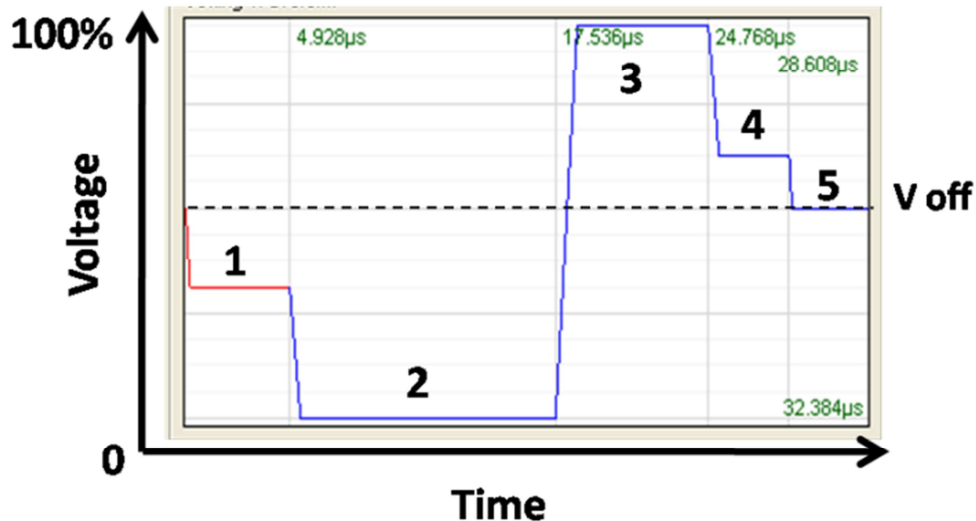**Figure 65:** Waveform used to print the V_2O_5 layer using a lab-scale Dimatix® materials printer (DMP-2800).

Figures 66 presents the formation of the drops when leaving the printhead and the print quality both on paper and on plastic. Although optimal rheological parameters are not reached, no defects were observed during the printing process. The image shows some non-matched velocities. It is a technical problem that can be solved by adjusting separately each 16 nozzles of the printhead. This is not because of the ink properties. However, because of the high surface tension of the ink, some deposits are observed around the nozzles. This is probably why such a high applied voltage (26 V) is needed to print this ink. The high surface tension also affects the print quality: instead of having a visually continuous film, as desired, the drops agglomerated to form large domains leading to a printed film with an observable drop pattern (Figure 67). Nevertheless the print quality on paper and on plastic is satisfactory for the applications wanted.

V_2O_5 present 100% reliability after 5 minutes of continuous printing and after 1 minute of pause. This indicates that the cleaning cycle can be set 5 in 5 minutes.

The spectroelectrochemistry study of vanadium oxide printed films is presented in section 2.2.3.

Figure 66: V_2O_5 ink: A) the formation of the drops when living the printhead, B) the print quality on paper and C) the print quality on plastic.
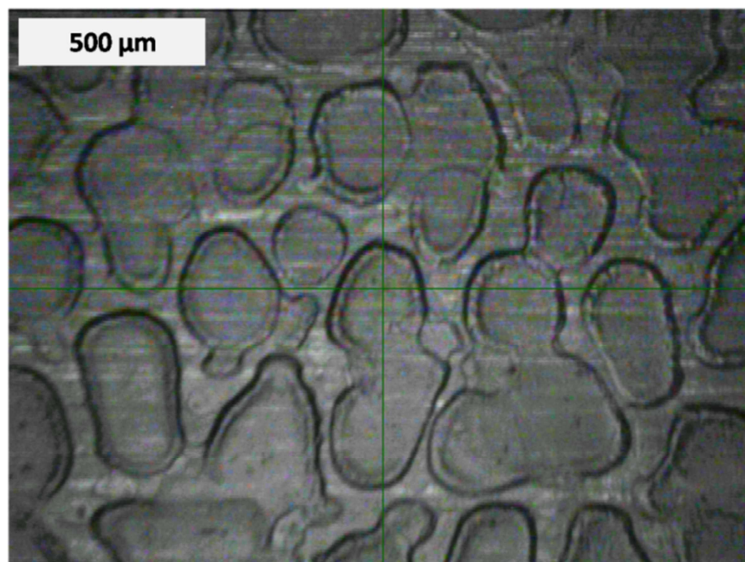
Figure 67: Printed film on PET-ITO substrate with 20 µm drop spacing and 13 passes.

2.2.2.3 Poly(3,4-ethylenedioxythiophene) poly(styrenesulfonate)

Some history:

In 1862, Henry Letheby reported for the first time the electrochemical and chemical oxidation products of aniline in acidic media, where the oxidized form was deep blue[173].

In 1954, researchers at Bell Labs reported organic charge transfer complexes with resistivities as low as 8 ohm.cm[174].

In 1963 Australians Bolto, DE Weiss, and coworkers reported iodine-doped oxidized polypyrrole blacks with resistivities as low as 1 ohm·cm[175]. This Australian group eventually claimed to reach resistivities as low as 0.03 ohm.cm with other conductive organic polymers. This resistivity is roughly equivalent to present-day efforts.

In 1977, Alan J. Heeger, Alan MacDiarmid and Hideki Shirakawa reported similar high conductivity in oxidized iodine-doped polyacetylene[176]. For this research, they were awarded the 2000 Nobel Prize in Chemistry "for the discovery and development of conductive polymers." Polyacetylene itself did not find practical applications, but drew the attention of scientists and encouraged the rapid growth of the field.[177] Since the late 1980s, organic light-emitting diodes (OLEDs) have emerged as an important application of conducting polymers.[178] PEDOT development starts also in the 1980s by ®Bayer AG[179,180,181,182]. Since then, one of the major applications for PEDOT:PSS is electrochromism. After Inganäs demonstrates that the cathodic deep blue color of PEDOT:PSS could be reverted to light blue using electrochemical methods at different potentials, several works in this area starts to emerge[183]. Namely, Reynolds[184] et al dedicates their study to the electrochromic properties of PEDOT:PSS and its derivatives.

PEDOT:PSS is a polymer mixture of two ionomers. In PSS, part of the sulfonyl groups are deprotonated and carry a negative charge. PEDOT is a conjugated polymer and carries positive charges (based on polythiophene). Together the charged macromolecules form a macromolecular salt.

It is used as a transparent, conductive polymer with high ductility in different applications. For example, ®AGFA coats 200 million photographic films per year with a thin, extensively-stretched layer of virtually transparent and colorless PEDOT:PSS as an antistatic agent to prevent electrostatic discharges during production and normal film use, independent of humidity conditions.

If high boiling solvents like methylpyrrolidone, dimethyl sulfoxide, sorbitol are added conductivity increases many orders of magnitude which makes it also suitable as a transparent electrode, for example in touchscreens, organic light-emitting diodes and electronic paper to replace the traditionally used indium tin oxide (conductivity up to 1000 S/cm are possible).

Water based PEDOT:PSS inks are mainly used in slot die coating, flexography, rotogravure, inkjet printing or screen-printing.

Commercially available PEDOT:PSS products are produced by [®]Heraeus with the trade name [®]Clevios and by [®]AGFA with the trade name [®]Orgacon.

The obtained PEDOT:PSS ink was formulated dissolving 47.8% (w/w) of the commercial solution of PEDOT:PSS (1.3% w/w in water) in water and adding 2% (w/w) of NaOH (1M in water) to neutralize the commercial PEDOT:PSS, and 1% (w/w) of triton-X. The final ink is a suspension very stable characterized by sedimentation techniques.

Inkjet printing

The ink was printed using the waveform presented in figure 68 with an applied potential of 19 V and a frequency of 6 kHz. This waveform is slightly different from the ones shown previously for tungsten oxide and vanadium oxide inks. The total pulse duration is longer and segment 3 is shorter. In table 11, the values of surface tension, density, viscosity and pH for this ink are also shown. This is the ink that is closer to the optimal parameters. 20 μm drop spacing was employed and 5 passes were done to obtain the final film.
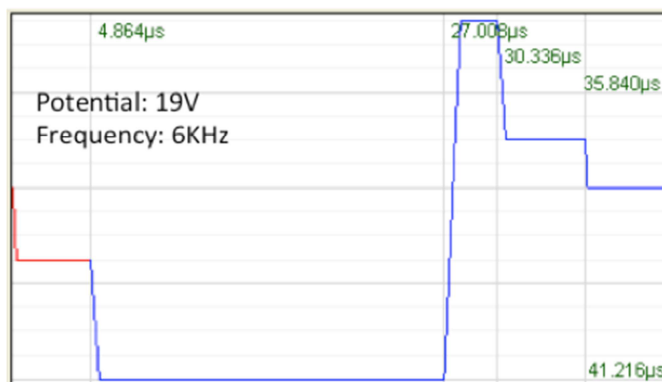
Figure 68: Waveform, applied potential and frequency used to print the PEDOT: PSS electrochromic ink.

Sedimentation measurements were performed to evaluate the stability of the ink and to estimate the particles size. The results show that PEDOT: PSS ink is very stable but the value of the sedimentation velocity and the average particle size could not be determined probably because the particles are very small and not detectable by the equipment. This experiments shows that the ink is perfect for inkjet printing use in terms of stability and particles size.

The ink was printed using the waveform and print parameters presented in Figure 68. Figure 69 presents A) the formation of the drops when leaving the printhead, B) the print quality on paper and C) the print quality on plastic. It is clear that there are no defaults like satellites, tails, or misdirected nozzles but the

image shows some non-matched velocities. Nevertheless, the print quality on paper and on plastic is satisfactory for the applications wanted.
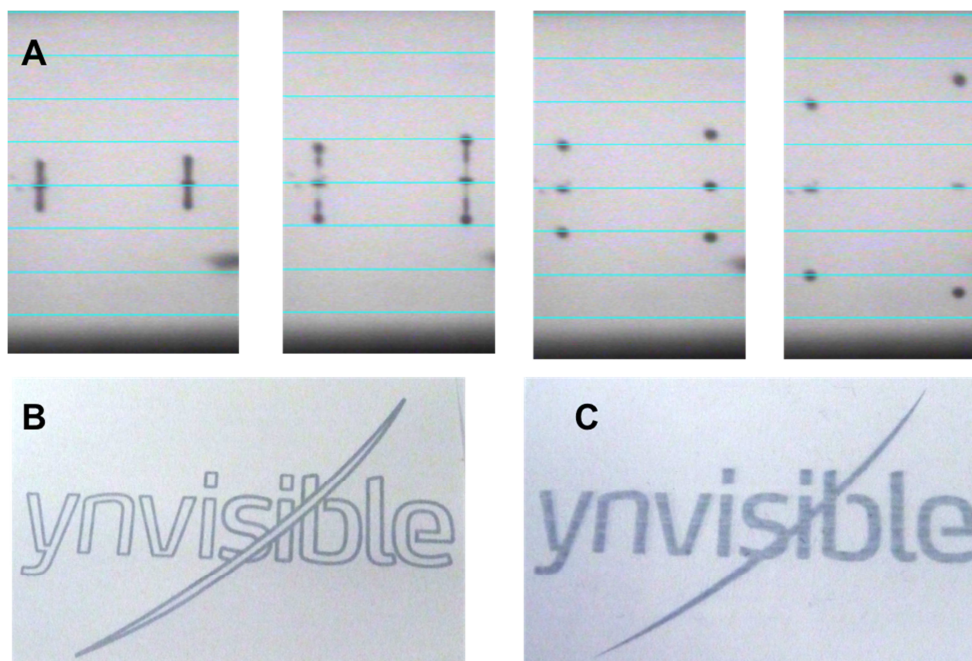
Figure 69: PEDOT: PSS ink: A) the formation of the drops when living the printhead, B) the print quality on paper and C) the print quality on plastic.

The reliability of ink was tested as explained in the experimental section, and PEDOT: PSS ink presents 100% reliability after 5 minutes of continuous printing and after 1 minute of pause (table 12). This indicated that the ink is very reliable and the cleaning cycles can be set from 5 to 5 minutes leading to a fast printing process.

Film characterization

Cyclic voltammetry was performed to determine the potential window of the electrochromic material. Figure 70 shows the voltammograms of PEDOT:PSS printed ink performed with a scan rate of 20 mV/s. It presents only one reduction peak (-0.15 V) and one oxidation peak (0.25 V), showing a simple oxidation-reduction reaction between two oxidation states of PEDOT:PSS. These results are very similar to those reported by Reynolds in the literature for PEDOT and its derivatives[185].
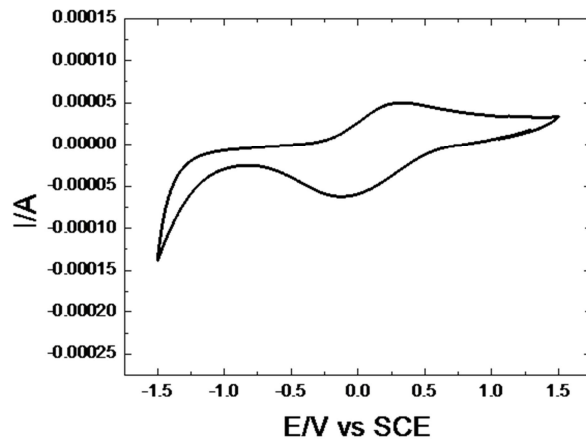
Figure 70: Cyclic voltammograms for PEDOT: PSS; one printed PET/ITO electrodes in liquid electrolyte (scan rate: 20 mV/s).

Spectroelectrochemical measurements were required (in liquid state) in order to optimize the electric potentials to maximize the optical contrast between the two states. Several potentials were tested (until the absorbance spectra stabilizes), for each tested potential, the absorbance was measured in the visible range (Figure 71 (left)), the arrow indicates the variation of the applied potential from 1 V to -1 V. The absorbance was plotted against the applied potential at the maximum wavelength variation to obtain the titulation curve (Figure 71 (right)). Table 18 shows the maximum wavelength variation and the potentials that affect the color of PEDOT:PSS printed films. Again, these results are in accordance with previous literature[185]. L*a*b* coordinates were also calculated in the reduced and oxidized states and shown in table 18.
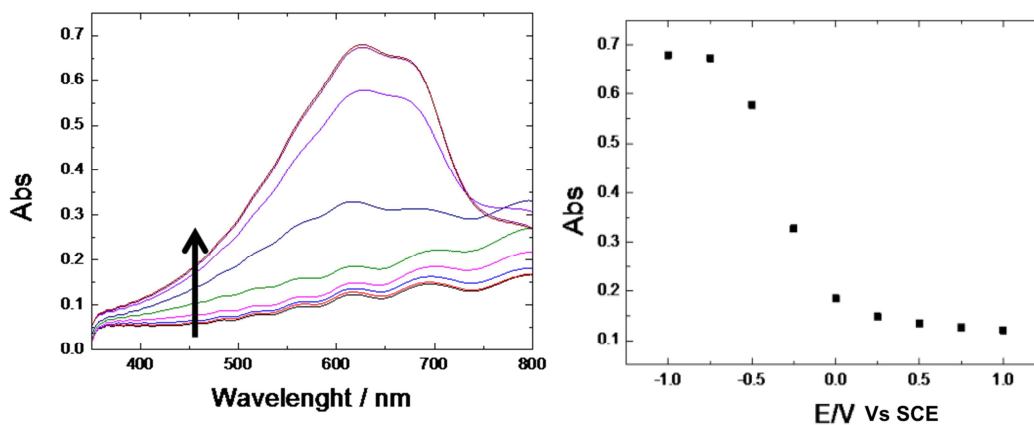
Figure 71: Spectroelectrochemistry measurements for PEDOT: PSS printed ink in liquid state; absorbance spectra for different potentials, the arrow indicate the decrease in potential from 1 V to -1 V (left). Absorbance plotted against applied potential at 628nm (right).

Table 18: Maximum wavelength variation, potentials that affect the color of the material and the color obtained for oxidized and reduced states, for all tested inks.

	Maximum wavelength variation (nm)	Minimum potential (V)	Maximum potential (V)	L*ab coordinates (reduced form)	L*ab coordinates (oxidized form)
PEDOT: PSS	628	-0.75	0.5	L*= 67.00 a*= -6.34 b*= -30.84	L*= 91.50 a*= -2.56 b*= -4.79

Collaboration with ®Xennia

PEDOT:PSS inks were developed and optimized to be printed with high reliability at a 10kHz frequency using semi-industrial and industrial systems. All the rheological properties were adjusted to reach the optimal ranges for industrial propose. The ink used until now had a concentration of 47.8% (of PEDOT:PSS solution in water (1.3% w/w)) and required 5 printed layers to achieve optimal contrast. Since the rheological properties of this ink are quite good, this formulation was first tested with a Xaar 760-GS8 printhead. The printed films presented a drying problem: the ink dries off too slowly, allowing the ink droplets to agglomerate on the substrate surface. To solve the drying problem, a wetting agent was added (®TEGO WET 270) with in a concentration of 0.8% (w/w). It was found that this last formulation produced very good continuous films and detailed patterns.

The next step followed the previous experience with tungsten oxide ink, replacing the sodium hydroxide with lithium carbonate to neutralize the PEDOT:PSS. The reason for this change is due to the fact that lithium ions help promotes the reaction of the PEDOT:PSS and increasing the speed of color transition. This new formulation and its physical properties are shown in table 19.

Table 19: PEDOT:PSS ink formulation and physical properties.

Reagents	Concentration (% w/w)	Viscosity (cP)	Surface Tension (dynes/cm)	pH
Deionized water	46			
1.3 % solution of PEDOT:PSS in water	47.5			
Triton X-100	1.00	8.00	28.0	6.76
lithium carbonate solution (1.3% w/w)	4.7			
Tego Wet 270	0.8			

This formulation was filtered at 1 μm. It was observed that the formulation tends to foam excessively during filtration. This foam then takes a long time to dissipate. An ink that has a strong tendency to foam can often demonstrate reduced printing reliability as dissolved gas within the ink can produce air bubbles in the printhead interfering with drop formation and causing nozzles to stop printing. To eliminate this foaming, the Triton X-100 was removed from the ink and replaced with the defoaming agent Tego Foamex 825 in combination with Tego Wet 270. The resulting ink demonstrated less foaming and any foam formed disappeared quickly.

The final formulation was:
- 46% Deionized water
- 47.5% PEDOT:PSS (1,3% in water)   *New*
- 4.7% lithium carbonate solution (1.3% w/w)
- 1% Tego Foamex 825
- 0.8% Tego Wet 270

The print quality was very good both on continuous films and on detailed patterns. The drop formation is good with no tails or satellites. The devices presented a good contrast and transition speed with only three printed layers (Figures 72 and 73).
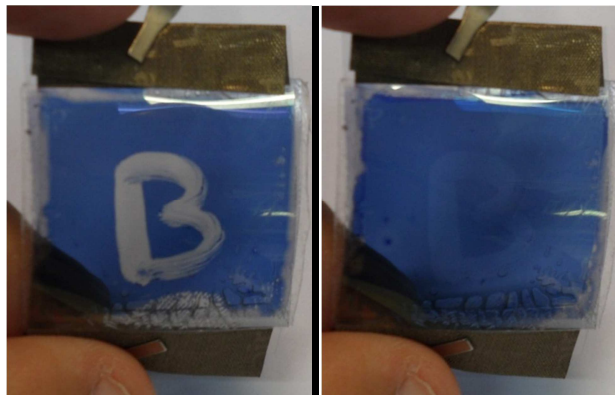
Figure 72: PEDOT:PSS printed device with only three printed layers of a continuous area.
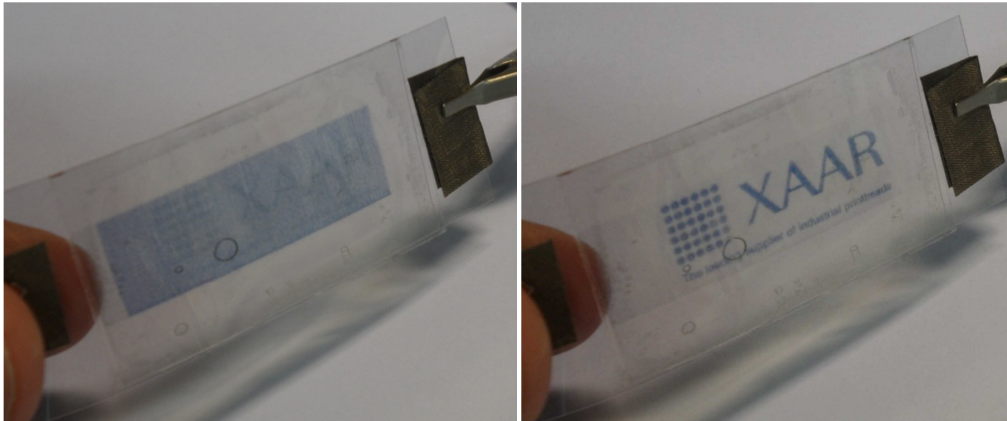
Figure 73: PEDOT:PSS printed device with only three printed layers of a detailed pattern.

2.2.2.4   Poly(3-hexylthiophene)

P3HT is a PEDOT derivative, therefore the history of their discovery and use are similar.

The obtained P3HT ink was formulated dissolving tetrahydrofuran (46.1% w/w), chlorobenzene (52.5% w/w) and P3HT (1.4% w/w) (see experimental section) with the physical properties presented in table 11. The final ink is a solution and not a dispersion, therefore the particles size is not an issue in this case. The solution is stable for several months.

Inkjet printing   *New*

The ink was printed using the waveform presented in figure 74 with an applied potential of 11 V and a frequency of 6 kHz. This waveform is different from the ones shown previously for tungsten oxide, vanadium oxide and PEDOT:PSS inks. The total pulse duration is shorter, there are only four segments and segment 3 is long when compared with the other segments. These main differences are due to a low surface tension conjugated with a very low viscosity of the ink. This combination is completely different from the other inks and as a result, this ink flow out the nozzles without a potential being applied. The challenge is this case was to retain the ink inside the nozzle and eject some ink only when required. In table 11, the values of surface tension, density, viscosity and pH for this ink are also shown in comparison with the other inks. 20 μm drop spacing was employed and 5 passes were done to obtain the final film.
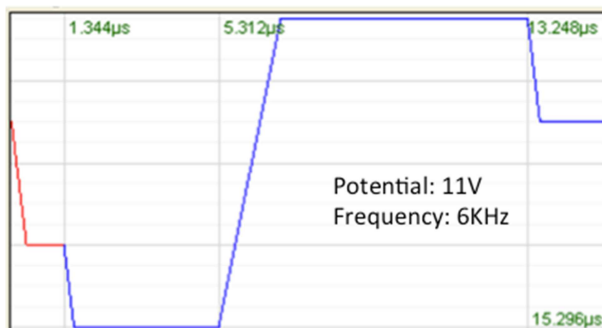
Figure 74: Waveform, applied potential and frequency used to print the P3HT electrochromic ink.

Figure 75 A) presents the formation of the drops when leaving the printhead, B) the print quality on paper and C) the print quality on plastic when the waveform presented in figure 74 is used. Some satellites are present after each drop, and tuning a little beat more the waveform can solve this problem. There is no tails, misdirected nozzles or non-matched velocities. The paper absorbs too much the ink (giving a blur effect to the image) and on plastic the ink is not drying fast enough, so some "ink islands" appears. This is directly related to the boiling point of the ink that is clearly too high. The solution to this problem is to adjust the percentage of each solvent to have a lower ebullition point of the ink.
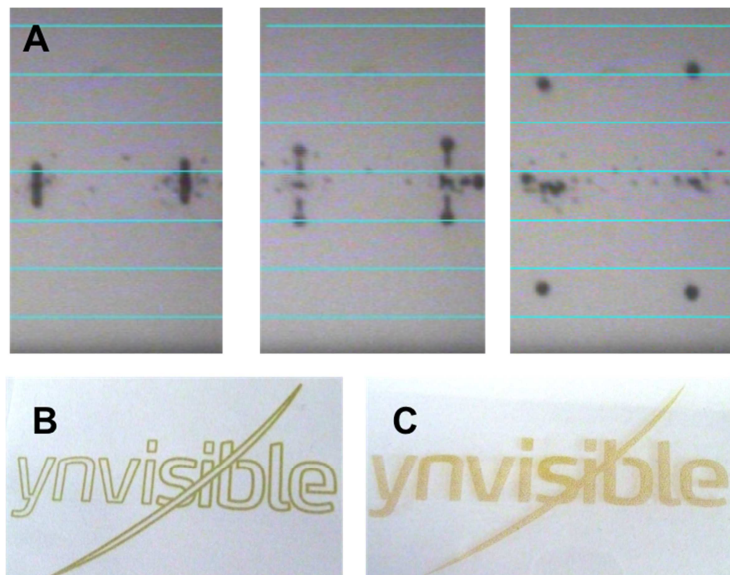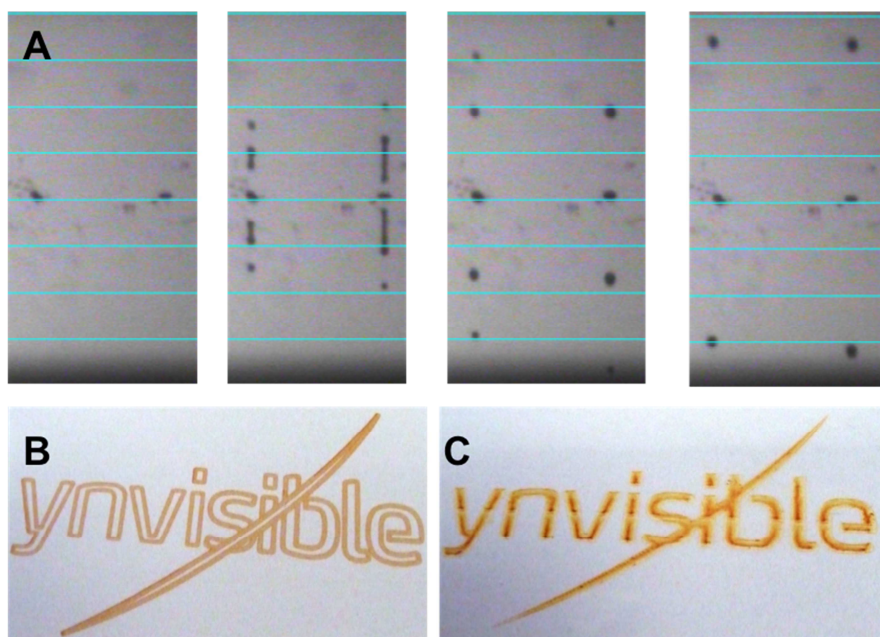
Figure 75: P3HT ink: A) the formation of the drops when living the printhead, B) the print quality on paper and C) the print quality on plastic.

The reliability of the ink was tested as explained in the experimental section, P3HT ink, such as PEDOT:PSS, presents 100% reliability after 5 minutes of continuous printing and after 1 minute of pause (table 12). This indicated that the ink is very reliable and the cleaning cycles can be set from 5 to 5 minutes leading to a fast printing process.

Film characterization

Cyclic voltammetry was performed to determine the potential window of the electrochromic material. Figure 76 shows the voltammograms of P3HT printed ink. It presents only one reduction peak (0.6 V) and one oxidation peak (1.25 V), showing a simple oxidation-reduction reaction between two oxidation states of P3HT similar to those reported in the literature[186]. The color obtained with the printed film merged in liquid electrolyte is shown in figure 77 (which is different from the colors seen in solid-state devices, see Figure 109).
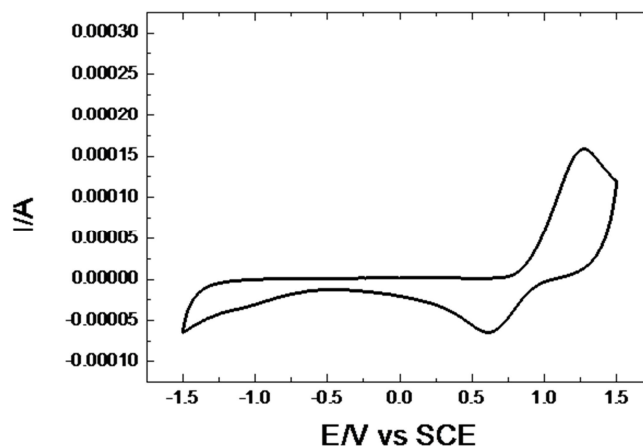
Figure 76: Cyclic voltammograms for P3HT printed film on PET/ITO electrode in liquid electrolyte.
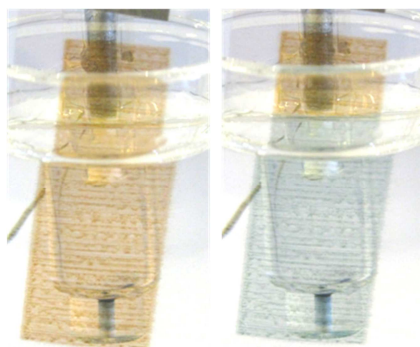
Figure 77: Colors obtained for P3HT printed ink in electrolyte solution.

Spectroelectrochemical measurements were required (in liquid state) in order to optimize the electric potentials to maximize the optical contrast between the two states. Several potentials were tested (until the absorbance spectra stabilizes), for each tested potential, the absorbance was measured in the visible range (Figure 78 (left)), the arrow indicates the variation of the applied potential from 1.5 V to -1.2 V. The absorbance was plotted against the applied potential at the maximum wavelength variation to obtain the titulation curve (Figure 78 (right)). Table 20 shows the maximum wavelength variation and the potentials that affect the color of P3HT printed films. L*a*b* coordinates were also calculated in the reduced and oxidized states and shown in table 20. These results are in accordance with those reported in the literature[187].
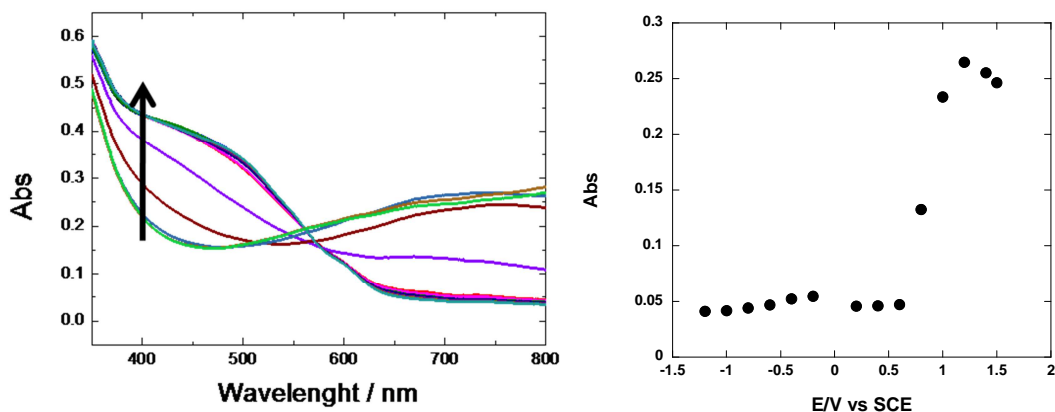
Figure 78: Spectroelectrochemistry measurements for P3HT ink; absorbance spectra for different potentials, the arrow indicate the decrease in potential from 1.5V to -1.2V (left). Absorbance plotted against applied potential at 700 nm (right).

In P3HT case, the blue coloration in anodic (oxidation) and not cathodic (reduction) as the electrochromic inks studied until now (tungsten oxide, vanadium oxide and PEDOT:PSS). Therefore, the plot of absorbance vs applied potential is inverted when compared with the others. The minimum absorbance is found for negative potentials.

Table 20: Maximum wavelength variation, potentials that affect the color of the material and the color obtained for oxidized and reduced states, for all tested inks.

	Maximum wavelength variation (nm)	Minimum potential (V)	Maximum potential (V)	L*a*b* coordinates (reduced form)	L*a*b* coordinates (oxidized form)
P3HT	700	0.4	1.2	L*= 82.47 a*= 11.61 b*= 21.85	L*= 84.32 a*= -3.67 b*= -3.57

2.2.2.5   Prussian blue

In 1704 Diesbach (a Berlin color maker) was preparing a red lake pigment based on potash and iron sulphate, when accidentally he obtained an intense blue pigment. The contamination present in the potash used by Diesbach produced the highly valuable Prussian blue pigment. The three main blue pigments used in this time were the Ultramarine produced from the very expensive lapis lazuli mineral; smalt, a cobalt blue glass which presents a weak covering power; and indigo extracted from a native Indian plant very susceptible to fading[188]. Prussian blue arrived as a winner substitute due to its great coloring power and good stability towards color fading and soon became commercially available. Diesbach obtained with this failed synthesis not only a valuable blue pigment, which had several social and historical consequences, but he became also the first man to synthetize a coordination polymer[189].

Prussian blue is a polynuclear transition-metal hexacyanometallates able to form coordinating polymer. The general formula of transition metal hexacyanometallates is $M'_m[M''(CN)_6]_n$ where M' and M'' are transition metals with different oxidation numbers and m and n are integral numbers.

Chemical synthesis of PB is performed by the mixture of $[Fe^{III}(CN)_6]^{3-}$ or $[Fe^{II}(CN)_6]^{2-}$ and Fe(II) or Fe(III), respectively. When a solution of $[Fe^{III}(CN)_6]^{3-}$ is poured into a flask containing Fe(II) solution a spectacular blue pigment is instantaneously precipitated. Addition of an excess of $[Fe^{III}(CN)_6]^{3-}$ will capp PB nanoparticles and make them dispersible in water (100 mg/ml) [190].

A Prussian blue dispersion in water (1.1%) such as tungsten oxide and vanadium pentoxide inks was used (see experimental section).

Inkjet printing   New

The ink was printed using the waveform presented in figure 79 with an applied potential of 12 V and a frequency of 6 kHz. This waveform is exactly the same as the ones shown for tungsten oxide and vanadium oxide. In table 11, the values of surface tension, density, viscosity and pH for this ink are also shown in comparison with the other inks. 20 μm drop spacing was employed and 3 passes were done to obtain the final film.
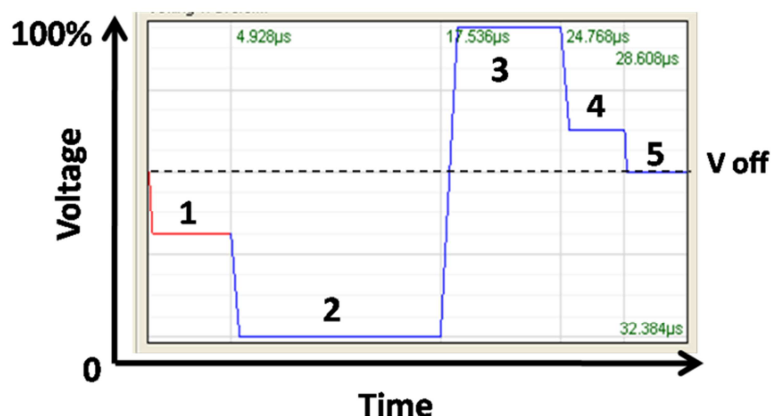
Figure 79: Waveform used to print the PB layer using a lab-scale Dimatix® materials printer (DMP-2800).

Sedimentation velocity was determined by analytical centrifugation (see experimental section). For this case, the experimentally obtained sedimentation velocity (0.014 mm/day) indicates that the ink is very stable and appropriate for this kind of printing method (very similar to vanadium pentoxide ink). The nanoparticles average diameter determined with this technique was 20 nm, with a typical Gaussian distribution as seen on Figure 80, assuming a spherical shape for the particles.
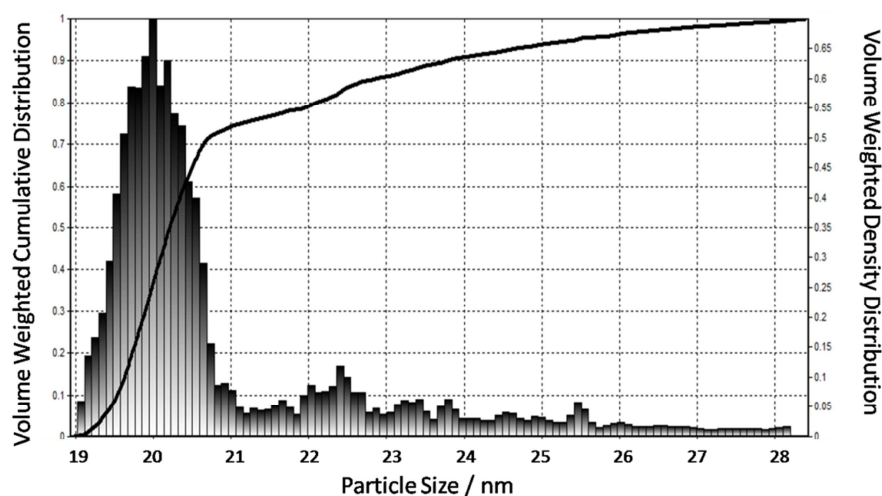
Figure 80: Particles size distribution of the PB ink.

PB ink was printed using the waveforms and print parameters presented above. Figure 81 A) shows the formation of the drops when living the printhead, B) the print quality on paper and C) the print quality on plastic. There are no defaults like satellites, tails, or misdirected nozzles but the image shows some non-matched velocities. As for PEDOT: PSS and V_2O_5 inks, it is a technical problem that can be solved by

adjusting separately each 16 nozzles of the printhead. Nevertheless the print quality on paper and on plastic is satisfactory for the applications wanted.
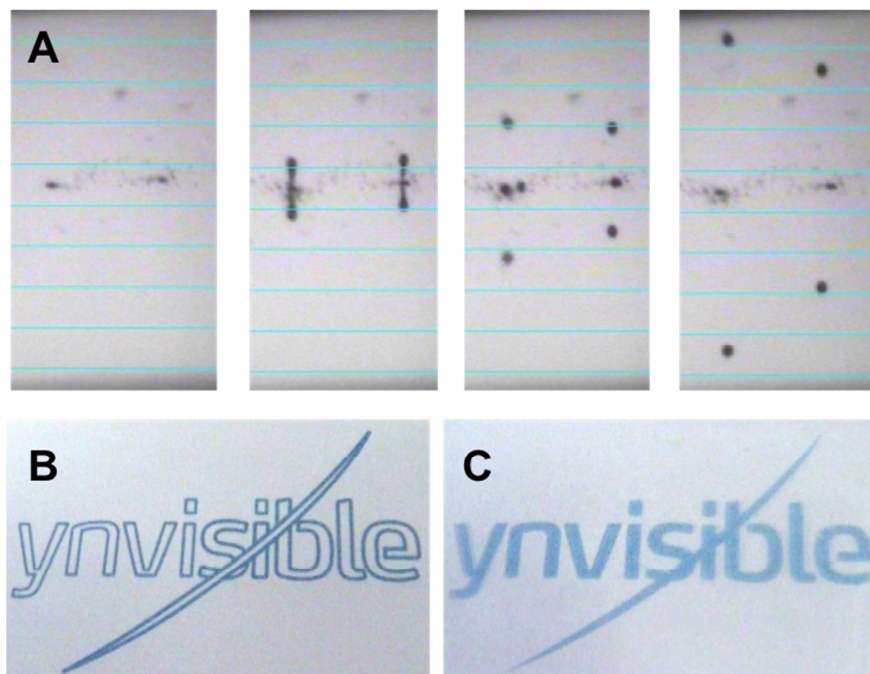
Figure 81: PB ink: A) the formation of the drops when living the printhead, B) the print quality on paper and C) the print quality on plastic.

PB ink presented 90% reliability after 5 minutes of continuous printing and after 1 minute of pause (table 12). This indicates that the cleaning cycle must be set shorter than 5 in 5 minutes, meaning that the printing process is slower than those for PEDOT:PSS and P3HT.

<u>Film characterization</u>

Cyclic voltammetry was performed to determine the potential window of the electrochromic material (scan rate used: 20 mV/s). Figure 82 shows the voltammograms of PB printed ink. It presents only one reduction peak (-0.05 V) and one oxidation peak (0.25 V), showing a simple oxidation-reduction reaction between two oxidation states of PB.[191]
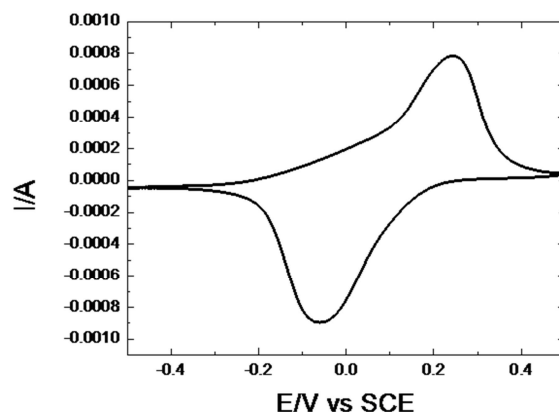
Figure 82: Cyclic voltammograms for PB printed film on PET/ITO electrode in liquid electrolyte.

Spectroelectrochemical measurements were required (in liquid state) in order to optimize the electric potentials to maximize the optical contrast between the two states. Several potentials were tested (until the absorbance spectra stabilizes), for each tested potential, the absorbance was measured in the visible range (Figure 83 (left)), the arrow indicates the variation of the applied potential from -0.5 V to 0.5 V. The absorbance was plotted against the applied potential at the maximum wavelength variation to obtain the titulation curve (Figure 83 (right)). Table 21 shows the maximum wavelength variation and the potentials that affect the color of PB printed films. L*a*b* coordinates were also calculated in the reduced and oxidized states and shown in table 21. These results are in accordance with those reported in the literature.[192]

In PB case, the blue coloration in also anodic (oxidation) as P3HT. Therefore the minimum absorbance is found for negative potentials.
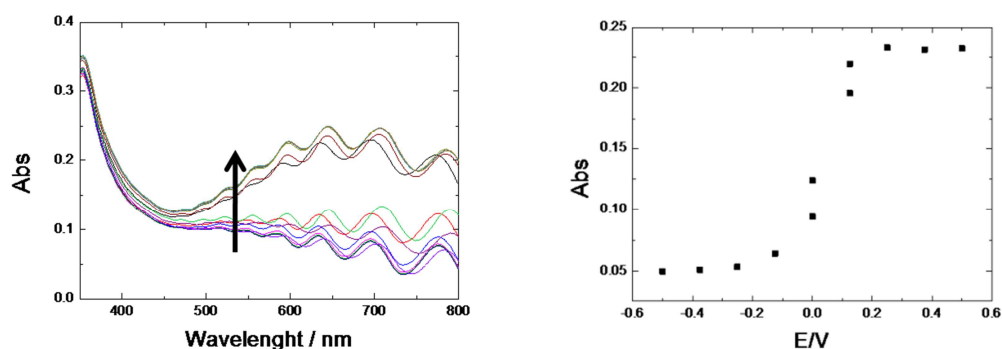
Figure 83: Spectroelectrochemistry measurements for PB ink; absorbance spectra for different potentials, the arrow indicate the increase in potential from -0.5V to 0.5V (left). Absorbance plotted against applied potential at 720nm (right).

Table 21: Maximum wavelength variation, potentials that affect the color of the material and the color obtained for oxidized and reduced states for PB printed films.

	Maximum wavelength variation (nm)	Minimum potential (V)	Maximum potential (V)	L*a*b* coordinates (reduced form)	L*a*b* coordinates (oxidized form)
PB	720	-0.25	0.25	L*= 91.07 a*= 0.77 b*= 1.80	L*= 85.25 a*= -4.67 b*= -6.01

Some conclusions:

The work done in collaboration with Xennia allowed the development of inks with the rheological and physical properties needed for industrial uses in inkjet printing specially for PEDOT:PSS. For tungsten oxide ink, the viscosity still needs to be improved. The inkjet printer parameters used for each ink are strongly dependent on the compromise viscosity/surface tension presented by the inks. PEDOT:PSS ink is the only one that presents viscosity and surface tension close to the optimal parameters of the inkjet printer. Vanadium oxide, tungsten oxide and PB inks are only based on water and the functional particles and the waveform used is exactly the same. Nevertheless, vanadium oxide needs a higher voltage to eject the droplets (26 V). This is due to the tendency of the ink to agglomerate around the nozzles and a higher pressure is needed to eject the droplets. P3HT ink is the only one that is not composed by water. In this case, the viscosity is too low and the surface tension is low when compared with the inorganic inks. This fact leads to ink that comes out from the nozzles without the application of the voltage. While the challenge for the other inks is to force the ejection the droplets out of the nozzles, in P3HT ink case the challenge is to retain the ink inside the nozzles and eject the droplets only when required. It seems that the pulse duration of the waveform is directly related with this compromise viscosity/surface tension.

2.2.3 Spectroelectrochemical study of inkjet printed tungsten oxide and vanadium oxide on PET/ITO electrodes.

2.2.3.1 Tungsten oxide

The tungsten oxide ink described in section 2.2.2 was inkjet printed on PET/ITO. The pattern used is represented in figure 84. The electrochromic material has an active area of 3 cm^2 and the devices built with these printed films had an area of around 5 cm^2. In this section, an electrochemical and spectroelectrochemical study was performed both in liquid and solid-state devices.
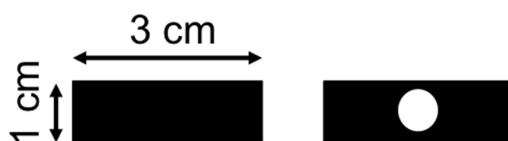
Figure 84: Pattern used to inkjet print the tungsten oxide ink.

Liquid-state

Cyclic Voltammetry

The PET/ITO substrates coated with tungsten oxide nanoparticles by inkjet printing were electrochemically characterized. On Figure 85, a cyclic voltammetry study of such coatings is shown. The results are in accordance with others previously published for tungsten oxide[111,193]. The oxidation wave shows a peak at -0.4 V, but the reduction wave does not show the corresponding reduction peak. This behavior was discussed previously and several explanations were put forward, from which two are described here [194, 195,196] (other explanations are in the review by Monk[95]):

A- Faughnan and Crandall model (potentiostatic coloration) [84, 197] – this model relies on two main assumptions: the rate limiting motion is the cation entering the tungsten oxide layer from the electrolyte layer, because a back emf is created at the interface. W(VI) is considered to be the only species existing in the film initially, meaning that cations are absent in the electrochromic layer. The back emf is particularly important in this model, because it explains the absence of a reduction peak.

B- Ingram, Duffy and Monk model (electronic percolation threshold) [198] – this model assumes that there is a percolation threshold where below it, the electron motion is the rate limiting step, instead of the cation insertion in model A. Above this threshold, models A and B are similar.

Both models A and B invoke a "characteristic time", which is proportional to the squared film thickness divided by the cation diffusion coefficient. Due to back emf, the response time will exceed this characteristic time. For usual scan rates (50 mV.s^{-1}) this implies the absence of the reduction peak, but at

smaller scan rates it can appear. In order to check this aspect, slower scan rates were investigated. Indeed, for 1 mV.s^{-1}, a reduction peak was found at -1.25V, at the expense of the oxidation peak (Figure 85). A slow scan rate enables Li$^+$ diffusion to take place, promoting the reduction of the electrochromic film, however the oxidation (accompanied by the exit of the cations from the electrochromic layer) is too fast in comparison with the reduction, so the very well defined oxidation peak is lost. Figure 85 also shows the decreasing intensity of the oxidation peak with a decreasing scan rate, accompanied by a shift of the peak.
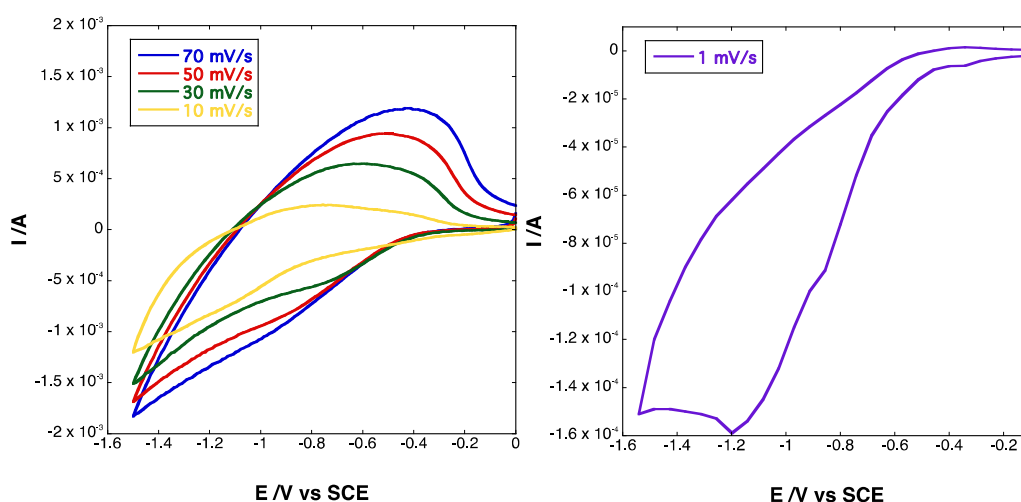
Figure 85: Cyclic voltammogram for the tungsten oxide synthesized nanoparticles measured at several scan rates (left) and cyclic voltammogram with 1 mV.s-1 scan rate measurement, showing the appearance of the reduction peak (right).

Spectroelectrochemistry

Spectroelectrochemical measurements in liquid-state were made, using a single PET/ITO electrode printed with tungsten oxide, to define the potentials that affect effectively the absorbance at the maximum wavelength variation in the visible range (Figure 86). Several potentials were tested and for each potential, the absorbance was measured in the visible range, the arrows indicates the variation of the applied potential from 0.2 V to -2 V. The absorbance was plotted against the applied potential at the maximum wavelength variation to obtain the titulation curve (Figure 86). Table 22 shows, the maximum wavelength variation, the potentials that affect the color of the material and the L*a*b* color coordinates obtained for oxidized and reduced states.
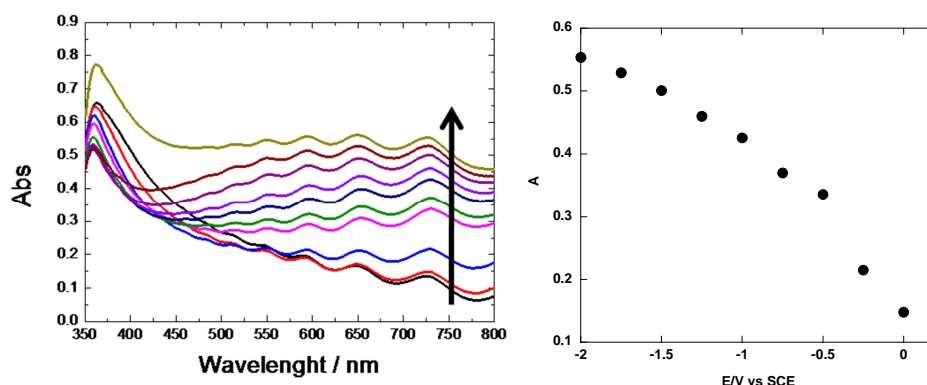
Figure 86: Spectroelectrochemistry measurements for tungsten oxide ink; absorption spectra for different potentials, the arrow indicate the change in potential from 0.2V to -2V (left). Absorbance plotted against applied potential at 725nm (right).

The absorbance is not stabilizing with the increase of the applied potential. This is certainly due to the phenomenon explained above in models A e B about Li^+ insertion. Even at -2V, the insertion of Li^+ is not complete and the reduction process is still happening during the time that the potential is applied. The absorbance will increase with the applied potential until one of the device layers starts to degrade and will, of course, affect the number of cycles performed.

Table 22: Maximum wavelength variation, potentials that affect the color of the material and the color obtained for oxidized and reduced states, for tungsten oxide ink.

Maximum wavelength variation (nm)	Minimum potential (V)	Maximum potential (V)	L*a*b* coordinates (reduced form)	L*a*b* coordinates (oxidized form)
725	-2	0.2	L*= 60.74 a*= -1.02 b*= -0.43	L*= 81.88 a*= 1.63 b*= 16.04

Solid-State

In this section, an independent study of electrochromic devices build using tungsten oxide electrochromic ink is described. Here, a description of the performance of 3 cm^2 devices is reported. The electrolyte used to build these electrochromic devices was a polymer gel electrolyte developed at Ynvisible's laboratory (1st generation electrolyte) described in the experimental section.

Vis-NIR spectroelectrochemistry

The optical properties of the tungsten oxide films were characterized by VIS-NIR spectroelectrochemistry in the wavelength range of 400 to 2500 nm and voltage range of -2 to 2 V. The measurements were made on a solid-state electrochromic cell, which contained all the components of the device, including the TCO and electrolyte layers. Figure 87 shows the change in absorbance (ΔA) when a voltage is applied on the device, between the on (i.e. negative voltage, reduced tungsten oxide) and the off (i.e. positive voltage, oxidized tungsten oxide) states. Even for low voltages such as -0.5 V, a change of absorbance between on and off states is observed. For voltages below-1.1 V, this response is only active in the NIR portion of the spectra and the absorption spectra peak is around 1900 nm, deep in the NIR region. An isosbestic point is observed at 550 nm, which is indicative of a conversion between two species (Figure 87 right).

Above 1.1 V, the peak position shifts to around 1400 nm as the voltage increases, and the visible portion of the spectra becomes active. The isosbestic point disappears, which indicates the presence of a third species (Figure 87 left).
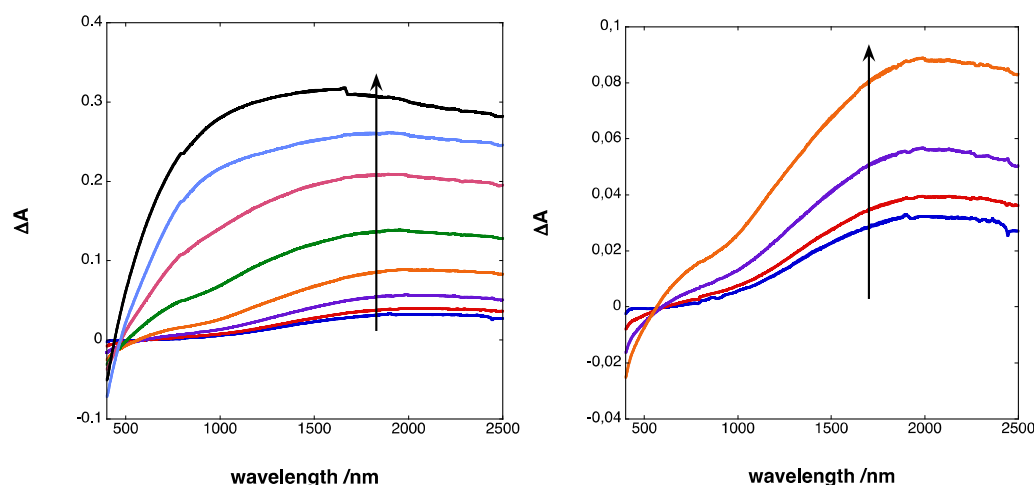
Figure 87: Visible-NIR spectra showing the change in absorbance when a voltage is applied on the device, between the on (i.e. negative voltage, reduced tungsten oxide) and the off (i.e. positive voltage, oxidized tungsten oxide) states at 0.5, 0.7, 0.9, 1.1, 1.3, 1.5, 1.7, and 1.9V (left) and zoom of the spectra obtained with lower voltages (right).

New

This shift is best viewed when the change of absorbance is normalized at the peak (Figure 88). Indeed, for low voltage the optical activity is observed for wavelengths above 1200 nm, while the second component appears with the concomitant shift of the absorption spectra at high voltages. If ΔA is plotted against the applied voltage, at 700 nm the signal only appears above -1.1 V, but at 1900 nm two regimes appear, one

above -1.1 V and a second one above -0.3 V (value obtained by extrapolation). The cyclic voltammogram with low scan rate indeed shows a wave at -1.2 V, but it also shows a very small peak around -0.3 V (see Figure 89). These results point out for two different species with different redox potentials and a different absorption spectroscopy.
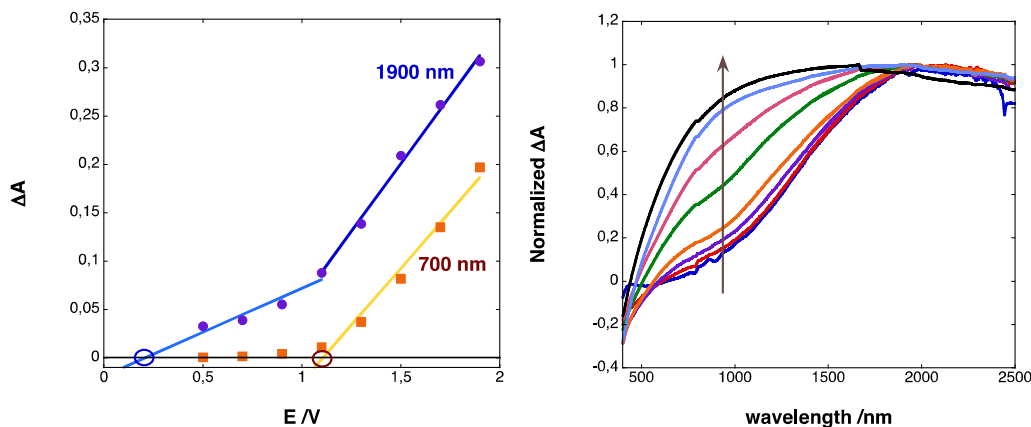
Figure 88: Change of Absorbance plotted against the applied voltage, at 700 and 1900 nm (left) and normalized change of absorbance for 0.5, 0.7, 0.9, 1.1, 1.3, 1.5, 1.7, and 1.9V (right).
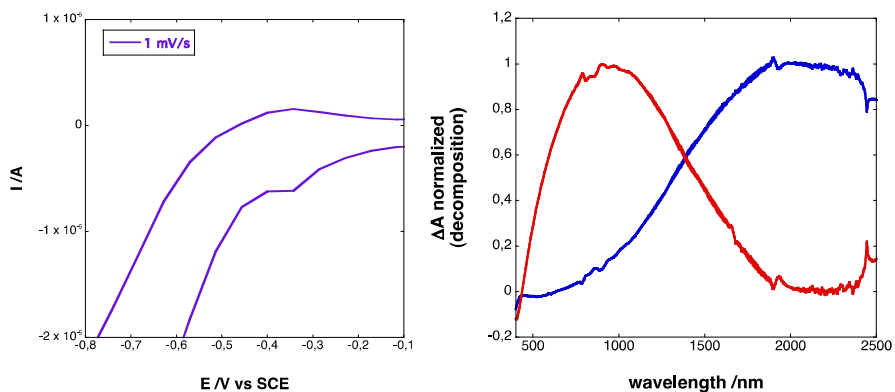
Figure 89: Cyclic voltammogram of 1 mV.s^{-1} scan rate measurement zoomed in order to evidence the appearance of a small reduction peak around -0.3V (left) and decomposition spectra from the normalized change in absorbance to obtain the two theoretical spectra of the two different species (right).

Different behaviors of the optical absorption for amorphous and polycrystalline WO_3 films were described earlier.[97,101,114,116,199,200,201] In the case of amorphous WO_3, it was found that the absorption peak is much more shifted into the blue, a result explained because the localization radius of the electron states is much smaller than in a crystalline phase.[200] Small-polaron absorption theory explains this result qualitatively, as described earlier.[88] Alternatively, a theory based on intervalence charge transfer absorption was given even earlier, in which the absorption spectra is caused by charge transfer

mechanisms between W(V) and W(VI).[40,90,95] In both cases, while amorphous films are optically active at higher energies (hence, visible range of the spectrum), crystalline states are active in NIR region. This interpretation is in accordance with the data obtained by Raman and XRD spectroscopy (see above), where both amorphous and crystalline (hexagonal) states are observed. So, for low voltage, the hexagonal portion of the WO_3 nanoparticles is being reduced, while higher voltages are required for the reduction of the amorphous portion of the nanoparticles.

Response time and cycling

These measurements were done only for inks with powder A and D, because the particles obtained with powder B and C are too large to be printed using inkjet. The device stability was tested by on/off cycling, by alternating between the two states of the device at a given voltage and monitoring the performance at 700 and 2100 nm (see Figure 90). The transmittance contrast for -0.9/+0.9 V cycles is rather small, but for -1.5/+1.5 V cycles the color stability can be measured and is very good after 1000 cycles in both spectral regions, with a slight increase of transmittance contrast after 1000 cycles. The contrast after 1000 cycles improves even more when -2.0/+2.0 V cycles are applied, although the transmittance decreases by about 5% at 700 nm (probably due to electrolyte layer degradation, which causes a yellowing of the device when many cycles are performed). The performance enhancement is much more evident for this case. The reason for this increase of performance in the first 1000 cycles is related with the assembly of the electrochromic cell. W(VI) is present in both electrodes when the device is assembled, and the first cycles establish the electrochemical difference between electrode and counter-electrode that gives rise to the color contrast. Only when W(V) is fully formed in one of the electrodes the device attains full contrast.
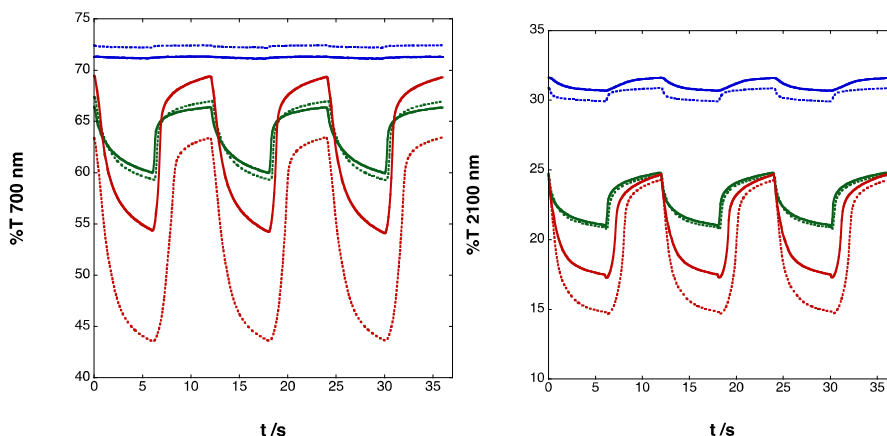
Figure 90: Cycling measurements of electrochromic devices measured at 700 nm (left) and at 2100 nm (right), built with the tungsten oxide printed films with powder A and tested at 0.9V (blue), 1.5V (green) and 2V (red), the straight lines show the initial cycles and the dot lines show the device performance after 1000 cycles.

Table 23 shows more details about the electrochromic performance of the device. The coloration time τ_c and bleaching time τ_b were measured, as well as the electric current and the so-called coloration efficiency CE. The coloration/bleaching times, however, are better in the visible region, probably because the amorphous component of the nanoparticles are more accessible for cation insertion. The total electric current Q_c and Q_b are similar for a given voltage, confirming the stability of the assembled devices. A comparison with results obtained for electrochromic devices using powder D is also shown. The performance is much smaller than powder A, as can also be seen on Figure 91. In terms of particle size, both powders are similar, so the main difference lies in the crystalline phase (hexagonal for powder A, orthorhombic for powder D). Therefore these results show that Li^+ insertion in the electrochromic layer is considerably delayed reducing contrast, color efficiency and also coloration and bleaching times, in both visible and NIR regions. Powder D is also more hydrated than powder A (see XRD results), which is also an additional factor that could influence the electrochromic performance. Nevertheless, samples with powder D show the same durability than samples with powder A. In conclusion, these results do not enable a detailed explanation to justify the differences here shown, but they clearly show that powder D is not suitable for this type of devices.

Table 23: Electric current, transition time between colored and bleached states, coloration efficiency, change in absorbance and in transmittance for 0.9, 1.5 and 2V at 700 and 2100nm of a flexible electrochromic device build with the tungsten oxide printed films on PET/ITO using powder A. For comparison proposes, results obtained with powder D are also shown.

Voltage /V	wavelength /nm	Q_c /mC.cm^{-2}	Q_b /mC.cm^{-2}	$\Delta\%T$	ΔA	CE /cm^2.C^{-1}	τ_c /s	τ_b /s
Powder A								
0.9	700	-0.30	0.27	0.7	0.008	29	—	—
1.5	700	-0.90	0.91	12.5	0.034	38	1.7	2.5
2.0	700	-3.0	3.1	26.0	0.090	27	2.0	1.7
0.9	2100	-0.30	0.27	3.9	0.040	133	> 6	> 6
1.5	2100	-1.00	1.00	12.5	0.092	88	> 6	> 6
2.0	2100	-2.9	3.1	16.6	0.161	55	2.5	2.4
Powder D								
2.0	700	-2.4	2.3	4.5	0.033	14	> 6	> 6
2.0	2100	-2.4	2.3	3.1	0.050	22	> 6	> 6
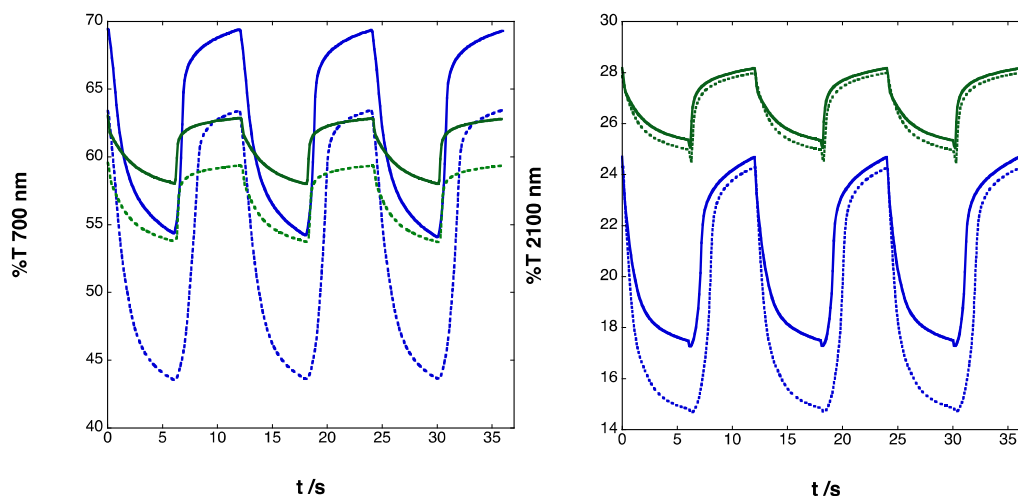
Figure 91: Cycling measurements of electrochromic devices measured at 700 nm (left) and at 2100 nm (right), built with the tungsten oxide printed films with powder A (blue) and powder D (green) and tested at 2V, the straight lines show the initial cycles and the dot lines show the device performance after 1000 cycles.

Several other parameters were tested in terms of response time and life cycling at two different wavelengths: 700 and 2100nm (Table 24 and 25). The response time and cycling monitored at the two wavelengths are very similar for the same sample tested in the same conditions. It can be seen that powder **A** shows a much better result in terms of ΔA when compared with powder **D** printed and tested in the exact same conditions. Possibly, a partially hexagonal structure favors the entrance and living of the ions, responsible for the electrochromic behavior[202] because this kind of structures results in hexagonal and trigonal tunnels where ions can be intercalated to form the reduced Li_xWO_3 where x can be as large as 3.4[119], a much higher x value that the one referred in the literature for other WO_3 structures[95]. Ethanol addition as co-solvent in the dispersion highly decreases the number of cycles before degradation showing that ethanol is interfering in the redox process. The print quality is another very important parameter. This work shows that a more porous printed film allows a much faster response than more dense films, resulting in a longer cycling life. This observation must be due to a higher contact area between the electrolyte and the electrochromic film in porous films, allowing a faster intercalation of the cations into the WO_3 printed film. The applied electric potential also has an impact on the electrochromic performance. Several voltages and response times were tested and results are conclusive regarding the best cycling conditions, in fact, the devices present a much higher cyclability and contrast using 2V with no more than 12s of cycle duration, probably also due to the partially amorphous /hexagonal structure (A), in which a higher voltage allows the ions to intercalate in some more internal hexagonal structures than

103

lower voltages[119]. The optimized parameters for stable devices with fast response time and good optical density are: nanoparticles with amorphous/hexagonal structure (powder A), avoiding ethanol in the dispersion, a 20 μm drop spacing and a 2V of applied potential with a cycle duration smaller than 12s. In these conditions, the devices are able to perform around 50000 cycles with 25% of degradation (Figure 92).

Table 24: Response time, cycling stability and ΔA for different parameters of WO_3 dispersions at 700nm.

Ink formulation	Drop Spacing (μm)	V	Cycle duration (s)	cycles	Initial ΔA	Final ΔA	Variation fraction of ΔA
Powder A+water	20	2	6	1090	0.1	0.134	+34%
"	"	"	12	1725	0.12	0.163	+36%
"	"	1.5	12	1650	0.04	0.05	+24%
"	"	"	20	900	0.1	0.083	-17%
"	10	2	12	1000	0.02	0.007	-65%
Powder A+water +ethanol	20	2	6	1300	0.06	0.056	- 6%
Powder D+water	"	"	12	700	0.03	0.04	+ 33%

Table 25: Response time, cycling stability and ΔA for different parameters of WO_3 dispersions at 2100nm.

Ink formulation	Drop Spacing (μm)	V	Cycle duration (s)	cycles	Initial ΔA	Final ΔA	Variation fraction of ΔA
Powder A+water	20	2	12	1725	0.12	0.17	+37%
"	"	1.5	12	1650	0.07	0.074	+6%
"	10	2	12	1000	0.09	0.03	-67%

Figure 92 shows photos of the device in on/off states, where the color contrast obtained is best viewed. The device is bendable, without any significant loss of optical activity, and almost completely transparent in the off state. 25% loss of absorbance contrast was obtained only after 50000 -2.0/+2.0 V cycles, with 6s of duration at any wavelength, with very good reproducibility.
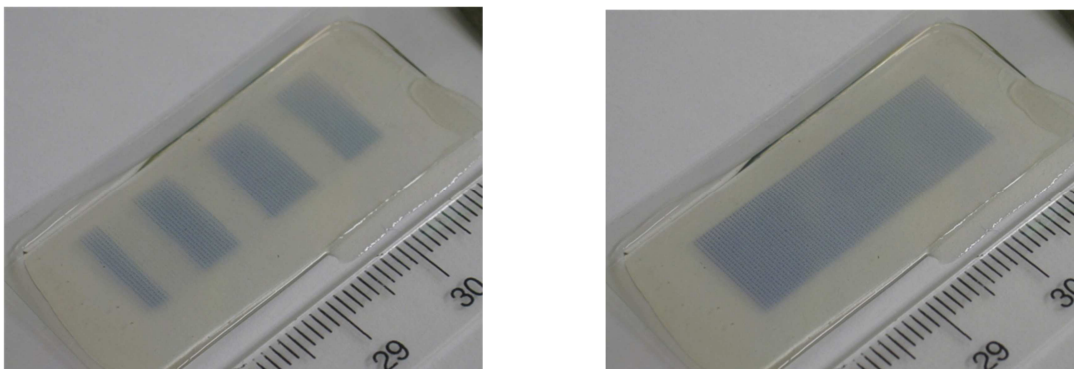
Figure 92: Photos of a flexible electrochromic device built with the tungsten oxide printed films on PET/ITO in on/off states.

Some conclusions:

Tungsten oxide nanoparticles sized 200 nm were synthesized via a sol-gel method. An inkjet formulation of these nanoparticles is proposed, which was deposited on the surface of flexible and heat sensitive PET/ITO electrode. The total absence of film sinterization is one of the most import achievements of this work. This fact could be explained because the printed material is already fully formed hydrated WO_3 nanoparticles and not a sol-gel solution. The sinterization step is used to change the crystallinity of films as well as the final deposited product composition. In this case, the printed material has already the crystallinity and composition wanted.

It is demonstrated that such tungsten oxide coatings have electrochromic activity with a good color contrast. Spectroelectrochemical measurements evidenced a dual response in the visible and the NIR part of the spectrum, depending on the applied voltage. Such behavior is connected to the presence of amorphous and crystalline states on the nanoparticles, and might be used in the future to construct devices in which light can be filtered on the NIR or NIR/Visible regions, by controlling the applied voltage, interesting behavior for applications such as electrochromic windows, which would allow the entrance of sun visible light while filtering the NIR part of the spectrum at low voltages. The application on flexible substrates can be useful too, in which NIR contrast might, for example, be used in the future for displaying hidden messages in augmented reality applications (sensors that would extend the user's visual range into infrared frequencies, not detectable by human).[203] Future synthesis efforts will be crucial for possible commercial applications of this technology, in order to obtain even better contrast at low voltage in the NIR region of the spectra.

2.2.3.2   Vanadium oxide

The vanadium oxide ink described in section 2.2.2 was inkjet printed on PET/ITO. The pattern used is represented in figure 84. The electrochromic material has an active area of 3 cm^2 and the devices built with these printed films had an area of around 5 cm^2. In this section, an electrochemical and spectroelectrochemical study was performed both in liquid and solid-state devices.

<u>Liquid-state</u>

Cyclic Voltammetry

The PET/ITO electrodes coated with vanadium oxide gel by inkjet printing were electrochemically characterized. Figure 93 shows a characteristic cyclic voltammogram made at 10 mV/s. The wave shows three pairs of oxidation/reduction peaks at -0.23/-0.8 V, 0.21/-0.4 V and 0.64/0.3 V. These peaks give rise to several color transitions: yellow/green, green/blue and blue/grey respectively (see insert in Figure 93), which is compatible with results described earlier by other authors. [204] One of those peaks disappears with the number of scans. It is known that the yellow color corresponds to V(V), blue color is V(IV) and violet color is V(II). V(III) has green color,[204] but given the sequence of colors, the green color seen here may arise from the mixture of yellow V(V) and blue V(IV).[41]

The origin of the peak that disappears with the number of scans is not completely clear, but probably it indicates a crystalline phase transition triggered by the oxidation/reduction cycles.[205] The synthesized vanadium oxide gel has at least one crystalline and one amorphous domain, as discussed from XRD and Raman spectra. During electrochemical cycles, Li$^+$ insertion could change this balance in the first scans, which would explain the disappearance of this peak. On the other hand, some change of morphology with the number of scans may put some sites responsible for such peak unreachable. Anaissi *et al* [205] had similar results with vanadium oxide gel films, in which a so-called "conditioning effect" is described. This effect arises from the intercalation of Li$^+$ during initial cycles, which in the final steady-state remain in interlamellar spaces of the vanadium oxide film, and also a more "homogeneous" film is formed. However, while this effect may indeed play a role, the peaks described here are relatively stable. Only one peak disappears after 10 scans. Therefore the presence of redox sites unreachable after some scans should play a role as well, implying a much more "heterogeneous film" than those described by Anaissi *et al* [205].
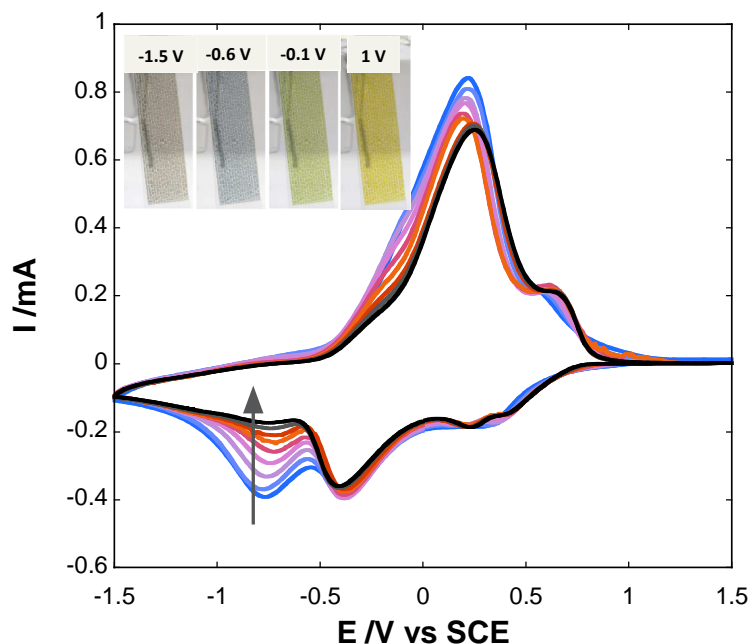
Figure 93: Cyclic voltammetry study for the vanadium oxide synthesized nanoparticles measured at 10 mV/s (10 scans). Insert shows color of the material at different potentials.

Spectroelectrochemistry

The analysis of the color transitions was performed by spectroelectrochemistry in the liquid state (see Figure 94 left). The absorption spectra on the visible region are very broad, except for the V(V) state where optical transparency is observed above 600 nm. Several isosbestic points are observed depending of the applied voltage; namely from 0.6 to 1.5 V, from -0.4 to 0.4 V and from -1.5 to -0.6 V. These ranges are comparable with those observed on the cyclic voltammogram. The physical interpretation of the experimental results should keep in mind that the processes here involved are linked with Li$^+$ insertion that leads to the formation of Li$_x$V$_2$O$_5$ species.[206,207] As discussed in the literature, the partial injection of Li$^+$ in the interval 0<x≤1 is responsible for the apparition of three distinct phases while for 1<x≤2, Li$^+$ cannot be entirely deintercalated.[207] This first insertion level (0<x≤1) gives rise to different crystalline states of the electrochromic material, reflecting the color changes observed. The formation of a broad band for higher wavelengths is indicative of the presence of V(IV), which through intervalence-transfer interactions with V(V) explains its appearance.[207] However, as seen before, even the synthesized powder has different crystalline states, explaining different Li$^+$ insertion processes[159,206,207,208,209]. Figure 94 (right) shows the absorption plotted against applied potential at 675 nm. It can be seen that the maximum reduced coloration is reached at -0.6 V. At 1.5 V, the maximum oxidized coloration is still not reached. L*a*b*

107

coordinates were also calculated for V_2O_5 printed thin film in the reduced and oxidized states. These values are listed in table 26.
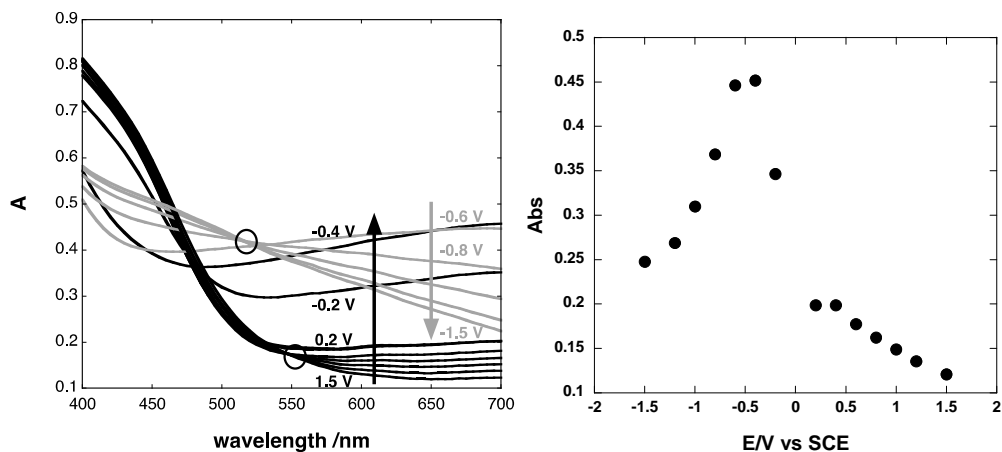
Figure 94: (Left) Spectroelectrochemistry in liquid state for the vanadium oxide inkjet printed film on a PET-ITO electrode. The applied potentials were between 1.5 V and -1.5 V (see arrows to see progression of the applied potentials). (Right) Absorption plotted against applied potential at 675 nm.

Table 26: Maximum wavelength variation, potentials that affect the color of the material and the color obtained for oxidized and reduced states, for all tested inks.

	Maximum wavelength variation (nm)	Minimum potential (V)	Maximum potential (V)	L*ab coordinates (-0.6 V)	L*ab coordinates (1.5 V)
V_2O_5	675	-0.6	1.5	L*= 66.39 a*= 0.02 b*= -0.35	L*= 83.35 a*= -7.12 b*= 36.79

Solid-state

Spectroelectrochemistry

The optical properties of the vanadium oxide gel films in a solid-state electrochromic cell were characterized by Vis-NIR spectroelectrochemistry in the wavelength range of 400 – 1500 nm and voltage range of -1.5 to 1.5 V. The solid-state electrochromic cell contains all components of the device, including the TCO and electrolyte layers, each one contributing for the light absorption. Figure 95A shows the

changes of the absorption spectra by applying voltage to the device. At all wavelengths the applied voltage induces optical changes. As in the liquid state, the more transparent state is reached when 1.5 V is applied, where significant light absorption exists only for wavelengths lower than 600 nm (and therefore explaining its yellow color corresponding to V(V)). As the material is reduced, light absorption gradually becomes significant at all wavelengths.

Figure 95B shows the differential absorption spectra using the most transparent state as reference (1.5 V). For applied voltages lower than 1.5 V, gradually a large absorption band appears raging from about 600 nm to wavelengths above 1500 nm. This broad band gives information in the NIR region not shown for liquid-state. Its band peak consistently shifts to lower wavelengths (or higher energies) when the applied voltage is more negative. However no isosbestic point is observed in the NIR region: instead the observed change of the absorption is gradually shifting. This results point out to a gradual Li$^+$ insertion on the optical layer, changing the relative fraction of V(IV) and V(V) species and probably the crystalline state of the vanadium oxide gel as well, which also depends of the number of scans but with changes much less evident than in the liquid cell (figure 96). The maximum electrochromic effect is seen at -0.9 V, where the blue color is more intense (see color space analysis below). Such processes are reflected on the transient measurement on Figure 97. The reduction leads to absorption increase at 750 nm on a time-scale of about 30 s with two distinct regimes, while the oxidation is slightly slower with no distinct regime. But at 488 nm the change of absorption with time is not monotonic, with a rather complex behavior. Again, Li$^+$ insertion coupled with different crystalline states seems to play here a major role. These results point out for a rather heterogeneous vanadium oxide layer, with different crystalline phases (probably those observed in the XRD experiments).
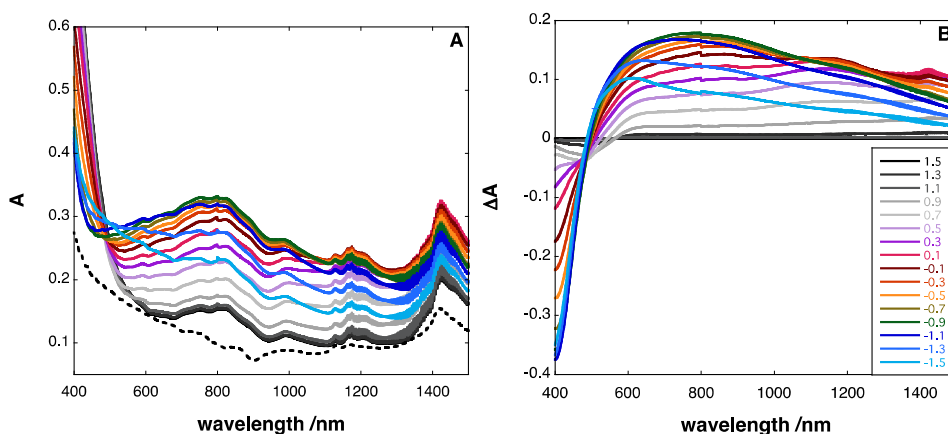
Figure 95: Spectroelectrochemistry in solid state for the vanadium oxide inkjet printed cell on PET-ITO electrodes. **A**) Absorption spectra varying with the applied potential, the dot line is the device without the electrochromic material (blank). **B**) Differential absorption spectra (1.5 V absorption spectrum was used as reference).
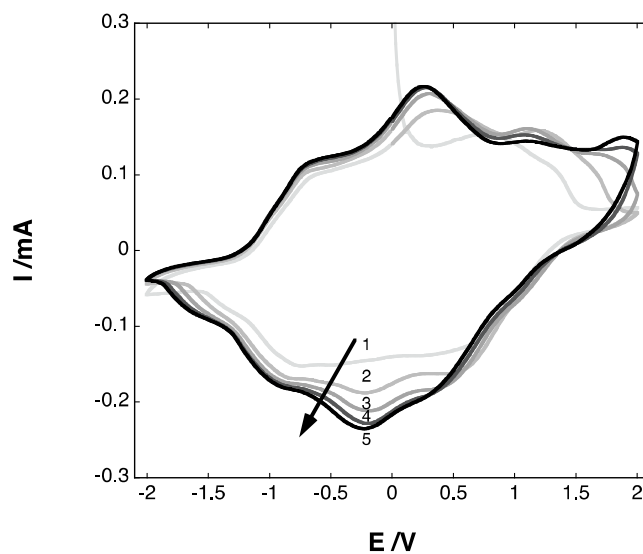
Figure 96: Cyclic Voltammetry of the solid-state electrochromic cell.
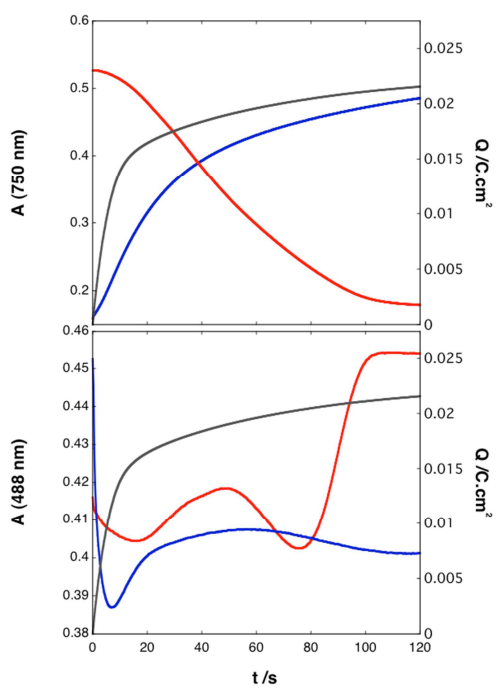
Figure 97: Response time study at 1.5 and -1.5 V. A) Measured at 750 nm. B) Measured at 488 nm. Red lines are the absorption behavior for the oxidation process, blue lines are the absorption behavior for the reduction process and black lines are the charge consumption for the oxidation process.

Lab color space and Cycling

The performance of the solid-state electrochromic cell described above was evaluated by measuring the color coordinates during the switching, its degradation with the number of electrochemical cycles and the coloration efficiency. Figure 98 shows the CIE Lab color coordinates calculated for both liquid-state and solid-state measurements as a function of the applied voltage. This calculation was done from the optical absorption spectra in the visible range (400 to 700 nm), using the Standard Illuminant CIE D65 and using the equations (1 to 4) presented in section 1.2.2.2.

Qualitatively, these results are rather similar to those obtained from absorption spectra since they are interrelated. However one can clearly see that in terms of optical contrast it is *b** (blue/yellow coordinate) that has more significant changes. A more negative value means a blue perception by the eye, which for the liquid state is reached around -0.5 V (vs. SCE) while in the solid-state electrochromic cell (including all parts of the device, namely PET/ITO electrodes and electrolyte layer) it shifts to around -1.1 V. In the second case, between -1.5 and -1.1 V the colors are quite similar.
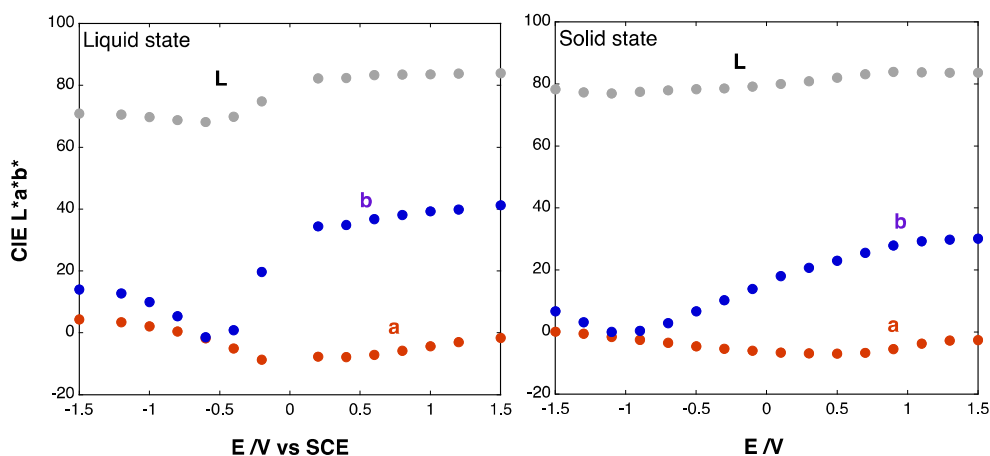
Figure 98: CIE Lab color coordinates calculated for liquid-state (left) and solid-state (right) measurements as a function of the applied voltage (estimated error of 1 CIE L*a*b* a.u.).

To calculate the color coordinates during the electrochromic transition of the solid-state cell, a setup with a digital camera under diffuse light inside a room was used (see experimental section). Afterwards the images were analyzed by calibration with a ColorChecker®, in order to calculate L^*, a^* and b^*. These results were then converted to color contrast values ΔE^* (Figure 99) using the oxidized state as reference (1.5 V) (see section 1.6.1).

The results indicate that after 30 s the available device optical contrast is reached, and therefore this is the practical response time of the device.

111
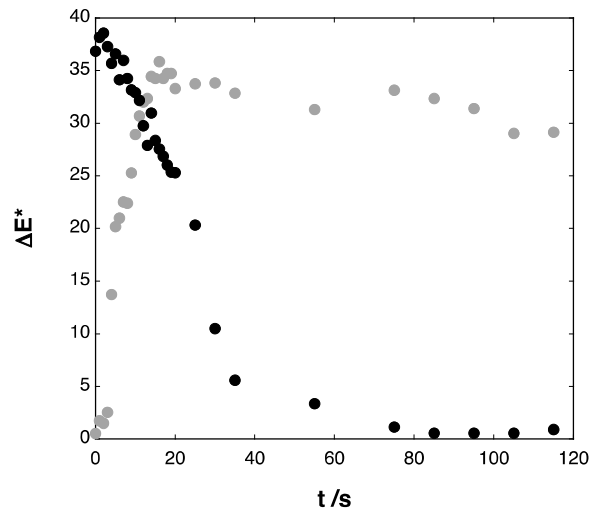
Figure 99: Color contrast values (ΔE*) for the oxidation (black) and reduction processes (grey) (estimated error of 2 ΔE* a.u.).

The device stability was tested by *on/off* cycling, by alternating between the two states of the device at a given voltage and monitoring the performance at 750 (see Figure 100). For the -1.5/+1.5 V cycles the color stability can be measured and is very good after 1000 cycles and rather constant. The stability of the device was also monitored using L*a*b* coordinates, as described in the experimental section and allowing it to perform a long cycling measurement. The device achieved 30000 cycles with 18% of degradation (Figure 101).
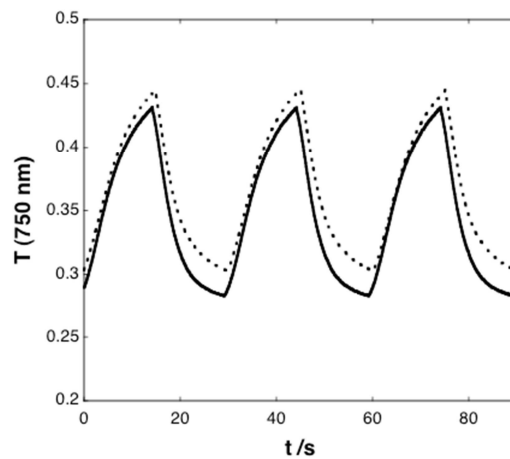
Figure 100: Device stability tested by on/off cycling, by alternating between -1.5 and +1.5 V and monitoring the performance at 750 nm. Black line is the device performance when assembled and dot line is the performance after 1000 cycles.
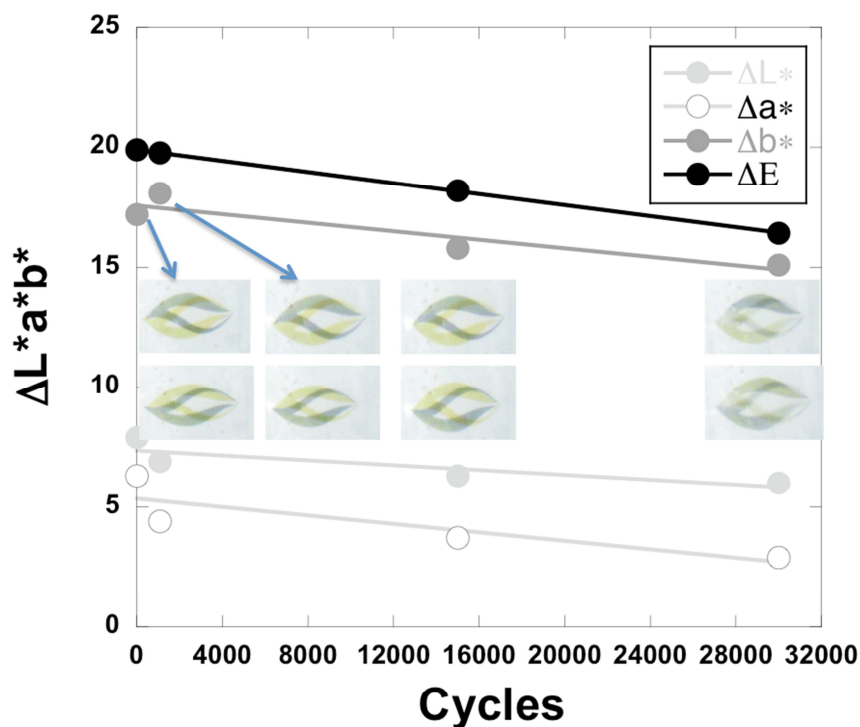
Figure 101: Variation of L*a*b* electrochromic device as a function of the number of cycles. Insert shows images of the device at each cycle (estimated error of 2 ΔL*a*b* a.u.).

Table 27 shows more details about the electrochromic performance of the device. The coloration time τ_c and bleaching time τ_b were measured as the time necessary to obtain 95% of the total optical transmittance contrast at 750 nm from data similar to those shown on Figure 97, as well as the electric current and the so-called coloration efficiency CE at 750 nm. The total charge Q is equal on either coloration or bleaching steps, which is essential for a good long-term cyclability. Coloration efficiency has typical values for vanadium oxide. The switching times, however, are rather long. Those values were taken from changes of the absorption spectra and it is not in accordance with the color contrast changes seen on L*a*b* color coordinates (about 30 s). We think that this result shows that for materials where color transitions do not involve a transparent state, a good color switching time may be reached before the system is stabilized in terms of optical transmittance. Color coordinates indeed give faster switching times, in accordance with the user perception. Transmittance switching times shown on Table 27 are useful because they give an insight of the molecular reaction kinetics. So while switching times are clearly slower than for other materials such as tungsten oxide, vanadium oxide gels still may be used in the future in electrochromic devices that require switching times until about 30 s.

Until now, few electrochromic devices using inkjet printing as deposition technique for the electrochromic layer were reported[210,211]. The results here shown demonstrate that vanadium oxide may also be deposited by inkjet with excellent color contrast and stability. The coloration efficiencies of the present device are similar to those described earlier using deposition techniques such as pulsed spray pyrolysis[212] (CE=13 $cm^2.C^{-1}$, Δ%T around 30%, similar switching times and stability up to 10000 cycles), chemical bath deposition[213] (Δ%T around 20%), sputtering[214] (Δ%T around 40%) or sol-gel based depositions such as spin-coating[215] (CE=20 $cm^2.C^{-1}$). To our knowledge, the best performance with vanadium oxide electrochrome was recently achieved by Scherer *et al*,[216] where an impressive switching time smaller than 1 s and very high CE were obtained on mesoporous film of vanadium oxide (CE=3500 $cm^2.C^{-1}$, Δ%T around 50%, stability up to about 10^2 cycles with 20% degradation). In this case the high porosity of the film greatly enhances Li^+ insertion. Comparing with the literature, the greatest achievement of the results here presented is the possibility to use inexpensive inkjet printing, without annealing, and using flexible PET/ITO electrodes to obtain electrochromic devices with a performance that matches those reported in the literature. Currently the color palette available for electrochromic devices is dramatically expanding due to the use of organic semiconductor polymers.[217,218] This work shows that inorganic metal-oxide nanoparticles also have potentialities, and might be used in the near future in commercial applications.

Table 27: Electric current, transition time between colored and bleached states, coloration efficiency, change in absorbance and in transmittance at 750 nm of a flexible electrochromic device build with the vanadium oxide printed films on PET/ITO using powder A.

Voltage /V	Q /$mC.cm^{-2}$	Δ%T	ΔA	CE /$cm^2.C^{-1}$	τ_c /s	τ_b /s
0.1	0.70	4.1	0.030	42.1	230	230
0.3	2.31	12.4	0.095	41.7	208	196
0.5	4.18	20.4	0.164	40.3	192	170
0.7	6.45	26.3	0.225	36.3	186	166
0.9	9.14	33.0	0.295	33.0	195	150
1.1	11.54	37.1	0.342	30.2	184	118
1.3	13.05	37.8	0.352	27.4	139	92
1.5	22.38	39.6	0.398	16.1	143	103

Some conclusions:

Vanadium oxide gels powders were synthesized using V_2O_5 and hydrogen peroxide as reagents. An inkjet formulation of this gel is proposed by dispersion in water, which was deposited on the surface of flexible and heat sensitive PET/ITO electrode using inkjet printing. Particles of about 64 nm of radius are found

from DLS experiments of the vanadium oxide gel aqueous dispersion and ribbon like structures may be seen on printed films using AFM. It is demonstrated that such vanadium oxide coatings have electrochromic activity with a good color contrast. Spectroelectrochemical measurements evidenced three isosbestic points attributed to the transition between only two different oxidation states (V(V) and V(IV)) that happen in three different phases depending on the applied potential, changing the structure of the crystalline parts and the color observed. The electrochromic cells response time is much faster when calculated using contrast color through CIE Lab color space and slower when calculated using the absorption spectra, pointing out for the necessity of crosschecking the optical performance using both approaches when the samples do not have an uncolored state. The large NIR electrochromism is similar to that observed with tungsten oxide, due to intervalence-transfer interactions, therefore these systems would have applications on devices where NIR transmittance should be controlled (such as intelligent windows).

2.2.4   Devices

In this chapter, the performances of solid-state electrochromic devices built using the electrochromic inks studied in section 2.2.2 are reported. The chapter is divided into two sub-chapters depending on the substrate used as electrode: plastic (PET/ITO) or paper based electrodes.

2.2.4.1   Plastic-based devices

The devices were assembled on PET/ITO substrates with the same design (Figure 102) and the same electrolyte layer which allowed a comparison between the different electrochromes (PEDOT:PSS, P3HT, WO_3, V_2O_5, and PB). The devices had an active area of electrode of 25 cm^2 with a symmetric printed image on both electrodes. The electrolyte used to build these electrochromic devices was a polymer gel electrolyte developed at Ynvisible's laboratory (1st generation electrolyte) described in the experimental section.
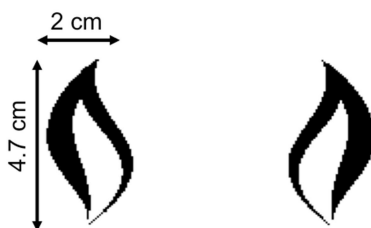
Figure 102: Pattern printed with the electrochromic inks.
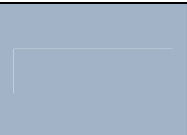
Cyclic voltammetry

The devices were studied using cyclic voltammetry. Potentials of oxidation (E_p^a) and reduction (E_p^c), as well as, current consumption during oxidation (I_p^a) and reduction (I_p^c) of an electrode were determined using this method. Table 28 shows the values of current and potentials of the cyclic voltammetry peaks for the inks developed in section 2.2.2 and now studied on solid-state devices. Figures 103 to 107 show the cyclic voltammograms of the solid-state devices made with a scan rate of 20 mV/s.

The current consumption measured for the different devices is between 10^{-4} and 10^{-5}. As expected, the voltammograms are almost symmetric because one of the electrodes is set as the reference electrode. The colors seen at each peak are also referred in table 28. It can be noticed that the same color transition is seen in solid and liquid electrolyte in PEDOT: PSS, tungsten oxide and PB cases. P3HT presents an oxidized color different in liquid (blue) (Figure 77) or solid electrolyte (green), probably because the reduction occurs only partially. Vanadium oxide shows four colors in a liquid electrolyte (Figure 93) but

116

only three of these colors are seen in solid state (yellow, green and blue) also because of a partial reduction. The color of the solid-state devices can be seen later in this section.

Table 28: Color transition and redox species, potentials of oxidation (E_p^a) and reduction (E_p^c), current consumption during oxidation (I_p^a) and reduction (I_p^c) of all the electrochromic materials tested in solid-state devices (estimated error of 0.01mA and 0.01V).

	Nº. printed layers	I_p^a (mA)	I_p^c (mA)	E_p^a (V)	E_p^c (V)	Redox species Oxidized➔Reduced	
PEDOT PSS	5	0.33	0.35	1.37	1.37		
P3HT	5	0.08	0.08	1.60	-1.60		
WO$_3$	20	0.10	0.11	0.04	-0.10		
V$_2$O$_5$	13	0.11 0.21 0.16	0.17 0.23 0.37	-0.70 0.28 1.20	0.40 -0.20 -0.90		
PB	3	0.07	0.08	0.10	-0.04		

Figure 103: Cyclic voltammograms for PEDOT: PSS solid-state electrochromic device (scan rate of 20 mV/s).
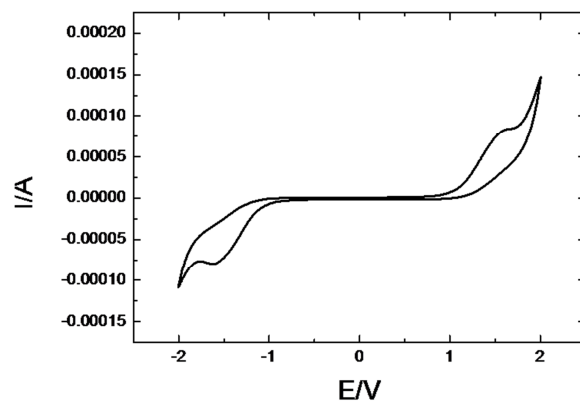
Figure 104: Cyclic voltammograms for P3HT solid-state electrochromic device (scan rate of 20 mV/s).
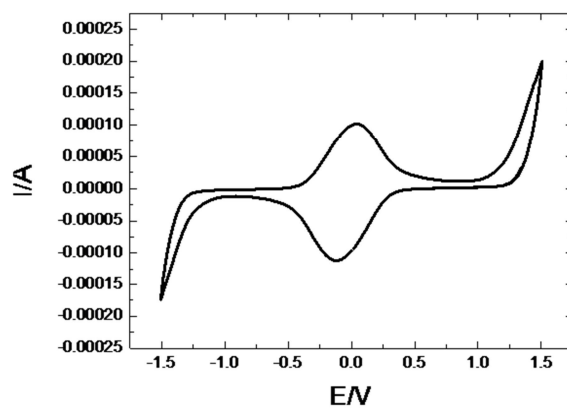
Figure 105: Cyclic voltammograms for WO_3 solid-state electrochromic device (scan rate of 20 mV/s).
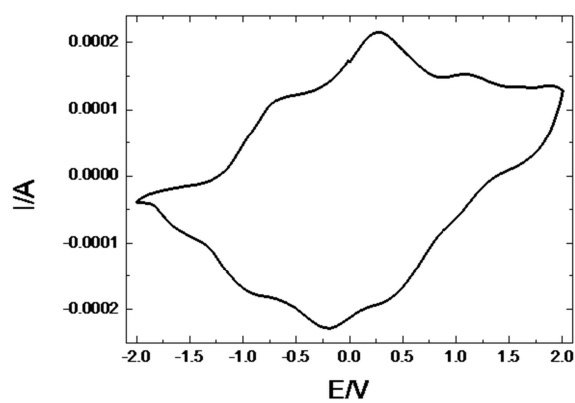
Figure 106: Cyclic voltammograms for V_2O_5 solid-state electrochromic device (scan rate of 20 mV/s).
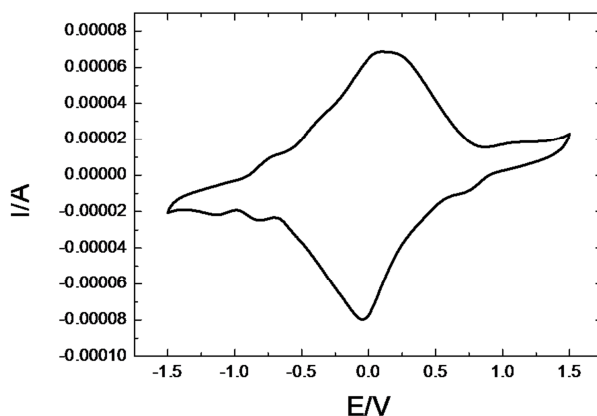
Figure 107: Cyclic voltammograms for PB solid-state electrochromic device (scan rate of 20 mV/s).

Cycling and time response

To compare the performance of the different devices, an applied voltage of 1.5V during 5s was set as the standard experimental method. This standard was slightly readjusted in the case of P3HT (1.5V during 4 minutes) and tungsten oxide (2V for 5s) in order to achieve a maximum color contrast and cyclability. Table 29 shows the results obtained from these experiments: the color contrast (ΔE), the number of cycles performed by each device and the associated degradation, the applied potential and the cycle duration.

Tungsten oxide presents less contrast than the other materials, vanadium oxide and PB have a similar contrast and the higher contrast is obtained for the organic electrochromic materials (PEDOT: PSS and P3HT). The contrast values are strongly dependent on the concentration of the electrochromic material. The number of layers printed for each material was controlled but the amount of electrochromic material (concentration) printed at each layer was not measured. The organic materials inks have more appropriate physical properties to inkjet printing than the inorganic inks (see chapter 2.2.2), which could be also a reason for the large difference in contrast. Although the drop size is always the same (10 pL), some nozzles can fail during the printing when the ink is not within the optimal physical parameters. There is probably more ink in the organic samples than in the inorganic once at each printed layer and, that way, increasing the material concentration and therefore the contrast ratio.

From these results, the main conclusions are that PEDOT: PSS ink achieved the best result with 220000 cycles and only 12.1% of degradation, followed by vanadium oxide and tungsten oxide. P3HT and PB presented the worst performances. It is clearly a question of optimization. PEDOT:PSS is a commercial product, well studied and optimized for electrochromic applications. The presence of PSS in this polymer mixture has the objective of stabilizing and increasing the solubility in water of PEDOT. It must be also very important in the electrochromic process since it needs positive charges to neutralize the SO_3^- group

119

(figure 9). Since the acidic solution was neutralized to produce the ink, a deficiency of H^+ protons was created. These protons are more likely substituted by other ions available in the device. Those ions are most probably Li^+ prevenient from the electrolyte layer, which will enhance the electrochromic effect.

Tungsten oxide and vanadium oxide also presented good results, which is a consequence of all the study and optimization accomplished in this work. The syntheses and powder structures were developed always with the final purpose of a good electrochromic performance.

When comparing the tungsten oxide device performance in this set of experiments with the ones obtained in section 2.2.3.1.1, it can be seen that the degradation is much higher here. A possible explanation is the difference in the size of the electrochromic devices in the two experiments; before the device has a $3cm^2$ area and here it has $25cm^2$. Once the applied potential is the same, it could suggest that for higher active areas, the potential should be increased, or at least, the duration of the applied potential should be higher, to allow the two electrodes to reach a more intense redox state.

Table 29: Number of cycles performed by each device and the associated degradation, response time for the oxidation and reduction at the beginning and at the end of the experiment, the applied potential and the cycle duration as well as the values of ΔL, Δa, Δb and ΔE for all tested inks (estimated error of 0.1 ΔE a.u.).

	Number of cycles	Degradation (ΔE) (%)	ΔE	Applied potential (V)	Cycle duration (s)
PEDOT: PSS	1	12.1	29.7	1.5	10
	220000		26.1		
P3HT	1	34.6	24.6	1.5	480
	49		16.1		
WO₃	1	60.3	12.6	2	10
	12000		5.0		
V₂O₅	1	17.6	19.9	1.5	10
	30000		16.4		
PB	1	60.3	19.6	1.5	10
	360		9.1		

Response times were not calculated but a qualitative evaluation was performed. The fastest response is given by PEDOT: PSS followed by tungsten oxide ink, meaning that the more intense redox state mentioned above would not influence the color perception of the human eye. PB ink time response is very fast and faster than vanadium oxide. The slowest is P3HT ink that takes several minutes to change color.

Devices

Figures 108 to 112 show the two electrodes of the devices inkjet printed for each one of the electrochromic materials tested. With these pictures the print quality can be evaluated, as well as the contrast and the obtained colors. P3HT and V_2O_5 devices present a poorer print quality. These defaults are usually related to the ink rheological properties. In P3HT case, these defaults are due to some missed nozzles. The contrast is satisfactory for all the inks, being clearly stronger for PEDOT: PSS, P3HT and V_2O_5 inks.
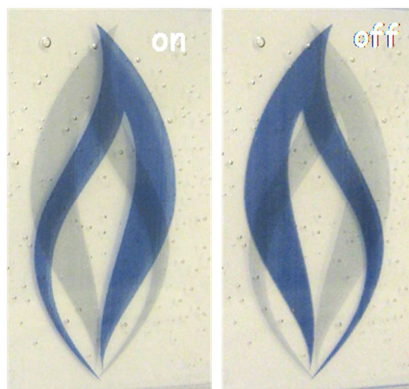
Figure 108: Solid-state electrochromic device obtained with printed PEDOT: PSS ink.

Figure 109: Solid-state electrochromic device obtained with printed P3HT ink.
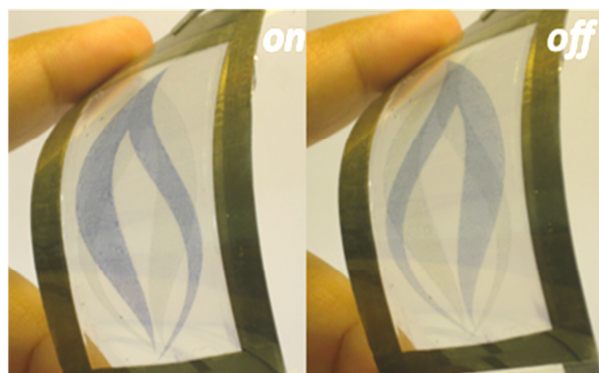
Figure 110: Solid-state electrochromic device obtained with printed WO_3 ink.

Figure 111: Solid-state electrochromic device obtained with printed V_2O_5 ink.
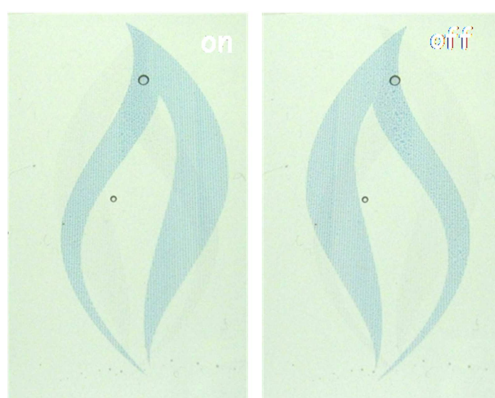
Figure 112: Solid-state electrochromic device obtained with printed PB ink.

2.2.4.2 Paper-based devices

This section is constituted by two different studies. First, a comparison of several different types of papers and also several different configurations but using as electrochromic material only PEDOT:PSS. A second section reports the performance of electrochromic devices built on paper but with the electrochromic inks described in section 2.2.2.

2.2.4.2.1 <u>Types of paper and architectures</u>

Drafting paper, pasteboard paper and glossy coated paper were coated with a conducting IZO thin film as described in complementary work (section 3.3) using DC sputtering. These substrates were tested in several different configurations (paper-paper and paper-PET) using only PEDOT:PSS as electrochromic material. This electrochromic ink was chosen due to its high color contrast and may be printed using screen-printing. The aim of this work is to compare the performance of the different paper substrates into electrochromic devices and select the most promising one for future use. The devices build had an active area of 25 cm^2 with a symmetric pattern (Figure 113) and the electrolyte used was an UV cured electrolyte developed at Ynvisible's laboratory (3rd generation electrolyte) described in the experimental part.
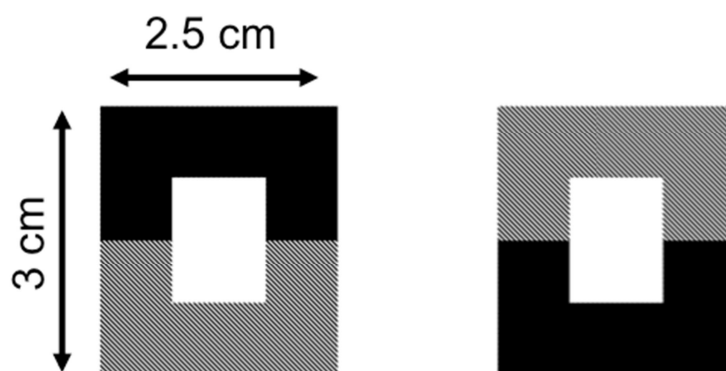
Figure 113: Pattern printed using PEDOT:PSS on the different paper electrodes.

<u>PEDOT:PSS screen-printing</u>

We have selected screen-printing technique to deposit PEDOT:PSS patterns on flexible PET and paper substrates. Screen-printing was chosen because it is a fastest printing technique than inkjet (since it is possible to print all the devices at the same time). The screen-printing equipment used in this study was a manual machine (printable, SAMPAS) and a polyester screen with 140 wires/cm. The electrochromic ink was purchased from Heraeus (PEDOT:PSS Clevios S V3 HV) and two layers were deposited on each pattern in order to achieve the desired contrast on the electrochromic colored state.

<u>Architectures evaluated</u>

The following display architectures were evaluated:

Arch. 1: PET-ITO/PEDOT:PSS/ UV electrolyte / PEDOT:PSS/IZO-drafting paper

Arch. 2: PET-ITO/PEDOT:PSS/ UV electrolyte / PEDOT:PSS/IZO-pasteboard paper

Arch. 3: PET-ITO/PEDOT:PSS/ UV electrolyte / PEDOT:PSS/IZO-glossy coated paper

Arch. 4: Drafting paper-IZO/PEDOT:PSS/ UV electrolyte / PEDOT:PSS/IZO-drafting paper

Arch. 5: Drafting paper -IZO/PEDOT:PSS/ UV electrolyte / PEDOT:PSS/IZO- pasteboard paper

Arch. 6: Drafting paper -IZO/PEDOT:PSS/ UV electrolyte / PEDOT:PSS/IZO- glossy coated paper

<u>Time response and cycling performance</u>

Since the devices are symmetric, it is necessary to apply the same potential (but with different polarities) in each electrode. To compare the performance of the different devices, an applied voltage in a square waveform of 1.5 / -1.5 V, during 5s at each potential was set as the experimental cycling test method. Table 30 lists the color contrast (ΔE), the number of cycles performed by each device and the corresponding degradation.

The best results are obtained for drafting paper both in architectures 1 and 4, in terms of performance and response time. These devices show a degradation of around 22% for 30000 cycles. In general, this experiment shows that using one or two paper electrodes on a device leads to similar results. It is also evident that the best device performance is not obtained with the most conductive paper (pasteboard paper).

These results are not directly comparable with the results obtained in plastic substrate because the printing method used to print the electrochromic material was not the same and the electrolyte is also different.

The response time was not calculated in this experiment but a qualitative evaluation was also done and the results are in accordance with those obtained in the previous section.

Table 30: Color contrast and degradation associated to 30000 cycles performed by the devices seen at both electrodes of each device (architecture 6 only performed 20000 cycles) (estimated error of 0.1 ΔE a.u.)

Architectures	ΔE initial/ ΔE final	ΔE Degradation (%)
1-Drafting paper	32.2 / 25.3	21
1-PET	26.8 / 21.0	22
2-Pasteboard paper	24.7 /10.8	56
2-PET	24.3 / 18.4	24
3-Glossy coated paper	24.5 / 15.5	37
3-PET	26.9 / 11.5	57
4-Drafting paper	25.3 / 19.8	22
5-Drafting paper	24.0 / 12.2	49
5-Pasteboard paper	27.8 / 18.1	35
6-Drafting paper	24.0 / 12.0	50
6-Glossy coated paper	25.0 / 11.1	56

Devices

In this section, only the best results are shown. The following pictures show drafting paper-based devices with architecture 1 (Figure 114). These images show the two different colored electrodes when PEDOT/PSS electrochromic film is in its reduced state. There is no available picture for the device built with architecture 4 characterized in this section. Nevertheless, Figure 115 shows a device with this architecture were the pattern printed was not symmetric.

Figure 114: Images of a working device build with architecture 1 (Drafting paper / PET).

Figure 115: Images of a working device build with architecture 4 (Drafting paper / Drafting paper). This was not the device characterized in this section.

Some conclusions:

The devices built on these paper-based electrodes showed a very good performance with 22% of degradation after 30000 cycles in the best case. It was demonstrated that having one or two paper electrodes in a device would not affect the performance. The architecture chosen to use when PEDOT:PSS is the electrochromic printed material is architecture 4. This choice is based on the excellent color contrast of PEDOT:PSS that can be seen through the drafting paper and also because of the very good performance of such device. To proceed with the study of electrochromic inks printed on paper electrodes, architecture 1 was chosen. Due to the poor color contrast of some electrochromic inks developed in section 2.2.2, it was decided to use architecture 1 to ensure that the color contrast would be seen for all the devices, through PET/ITO.

The present section describes the performance of electrochromic devices built with the electrochromic inks developed in section 2.2.2 on drafting paper electrodes, using architecture 1 described in the last section.

The electrochromic inks were inkjet printed on these paper electrodes. The pattern chosen is represented in Figure 116. The pattern is not symmetric at both electrodes, the devices had an active area of around 16 cm^2 and the electrolyte was an UV cured electrolyte developed at Ynvisible's laboratory (4th generation electrolyte) (see experimental section).
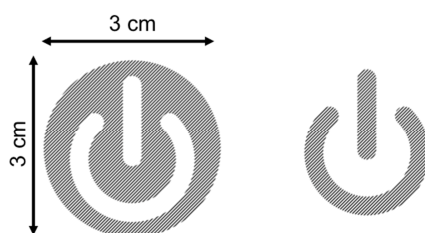
Figure 116: Pattern printed on paper electrodes using different electrochromic inks.

Architectures evaluated

The following displays were evaluated:

Arch 1: PET-ITO/ inkjet printed PEDOT:PSS/ UV electrolyte / inkjet printed PEDOT:PSS/IZO-drafting paper.

Arch 2: PET-ITO/ inkjet printed WO$_3$/ UV electrolyte / inkjet printed WO$_3$/IZO-drafting paper.

Arch 3: PET-ITO/ inkjet printed V$_2$O$_5$/ UV electrolyte / inkjet printed V$_2$O$_5$/IZO-drafting paper.

Arch 4: PET-ITO/ inkjet printed PB/ UV electrolyte / inkjet printed PB/IZO-drafting paper.

Arch 5: PET-ITO/ inkjet printed P3HT/ UV electrolyte / inkjet printed P3HT/IZO-drafting paper.

Cycling, contrast and response time

The experimental setup and the conditions used for the experiment are the same used in section 2.2.4.1 (on PET/ITO electrodes).

Table 31 lists the color contrast, the number of cycles performed by each device and the corresponding degradation.

Response times were not calculated but a qualitative evaluation was performed. The results are also in accordance with the results obtained in section 2.2.4.1. The fastest response is given by PEDOT: PSS

followed by WO$_3$ ink. PB ink time response is very fast and faster than V$_2$O$_5$. The slowest is P3HT ink that takes several minutes to change color.

Since the conductivity of the paper electrodes is higher than in PET/ITO, the color contrast on these electrodes tends to be faster. The paper electrode is not interfering negatively in the response time.

After 700 cycles, the contrast decreases for all the electrochromic devices. This was not an expected result. During these experiments, it was noticed that the pattern selected for the inkjet printed electrochromic layer was influencing drastically the degradation value (in comparison with the experiments described in the previous section). This fact happened because of the disparity on the amount of electrochromic material in both electrodes; the "on" symbol has much less ink then the negative pattern of the symbol. Since each cycle as the same duration for the reduction and the oxidation process (5s), the equilibrium is not reached when the negative pattern is reduced cycle after cycle, leading to a slow loose of performance also cycle after cycle. In conclusion, the degradation that is measured is mostly due to the lack of symmetry between electrodes in terms of electrochromic material concentration and not because of the material degradation itself.

P3HT is not referred to in these results because the device after 700 cycles was already completely degraded.

Table 31: Color contrast (ΔE) at the beginning of the experiment and after 700 cycles and the associated degradation. The measurements were done at both electrodes of each device (Arch. 1 to 4) (estimated error of 0.1 ΔE a.u.)

Architecture	ΔE initial/ ΔE final	ΔE Degradation (%)
7-Drafting paper (PEDOT:PSS)	27.1/23.7	12.5
7-PET (PEDOT:PSS)	26.6/24.5	7.9
8-Drafting paper (WO$_3$)	16.3/15.0	8
8-PET (WO$_3$)	17.9/17.0	5.1
9-Drafting paper (V$_2$O$_5$)	24.5/18.9	22.9
9-PET (V$_2$O$_5$)	33.5/24.5	26.9
10-Drafting paper (PB)	18.8/17.0	9.6
10-PET (PB)	17.6/13.0	26.1

Devices

The following pictures (Figure 117 to 121) show drafting paper-based devices with the architectures described before, using PEDOT:PSS, WO_3, V_2O_5, PB and P3HT respectively as ECMs, when both electrodes are reduced. It can be noticed that, in fact, the contrast is excellent for PEDOT:PSS and V_2O_5, and satisfactory in the case of WO_3, PB and P3HT.

Figure 117: Paper-electrode device with PEDOT:PSS inkjet printed as electrochromic material.

Figure 118: Paper-electrode device with WO_3 inkjet printed as electrochromic material.

Figure 119: Paper-electrode device with V_2O_5 inkjet printed as electrochromic material.

Figure 120: Paper-electrode device with PB inkjet printed as electrochromic material.
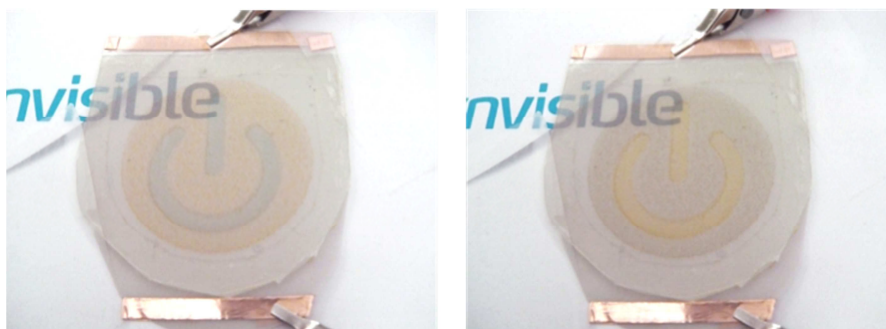
Figure 121: Paper-electrode device with P3HT inkjet printed as electrochromic material.

Some conclusions:

In this work we presented the performance of several electrochromic materials (PEDOT:PSS, WO_3, V_2O_5 and PB) used on electrochromic materials. The electrochromic devices had one paper-based electrode coated with IZO, deposited by DC sputtering as TCO layer and the electrochromic layer was inkjet printed on top of these paper-based electrodes. The performances of the different devices were assessed and it is possible to conclude that all the ECMs exhibited very promising results that can be improved by simply choosing a more symmetric pattern (in terms of concentration of electrochromic ink) on both electrodes.

2.3 Characterization Techniques

2.3.1 Functional materials

Dynamic Light Scattering (DLS)

DLS experiments were performed on a Brookhaven Instruments BI-90, Brookhaven Instruments Corporation, New York, Speed: 1 minute; Accuracy: ±1%; Sample volume: 0.5-3 ml, was used. The mean particle size value and the standard deviation were calculated (size distribution by weight) assuming a Lognormal fit. The diffusion coefficient was measured for different sample concentrations and an extrapolation for infinite dilution was made. The particle sizes were determined using the Stokes-Einstein equation. The samples were previously filtered at 1 µm. This technique allows the determination of diffusion coefficients D, which can be afterwards used to calculate the particle size. Samples with different volume fractions of dispersed phase (ϕ) were measured, allowing determination of D at each sample. It is known that extrapolations to infinite dilution are necessary to avoid interference of the attractive or repulsive forces between particles. This interference can be modeled by:[219]

$$D = D_0\left(1 + \alpha\phi\right) \tag{17}$$

Where D_0 is the diffusion coefficient at infinite dilution and α is the virial coefficient. The virial coefficient provides information on the type of interactions that occur between nanoparticles. For hard spheres or when the interactions are repulsive due to electrostatic forces, α is positive, while when attractive interactions take place the virial coefficient is negative.[219] Stokes-Einstein equation was then applied to calculate the average particle diameter d:

$$d = \frac{k_B T}{3\pi\eta D_0} \tag{18}$$

Where k_B is the Boltzmann constant, T is the absolute temperature (298 K) and η is the solvent viscosity.

Dispersion Analysis

Ink sedimentation velocity and nanoparticle size were determined on different dispersions with a Lumisizer dispersion analyzer (LUM-GmbH, Germany). This apparatus allows acquisition of space- and time-resolved extinction profiles over the sample length. Parallel light (I_0) illuminates the entire sample cell and transmitted light (I) is detected by sensors arranged linearly across the sample from top to bottom. Transmission is converted into extinction coefficient and particle concentration is calculated, therefore allowing the sedimentation velocity to be determined. Centrifugal force is used to accelerate the sedimentation process. The equipment uses an indirect method to determine the nanoparticles size, using the density of the solid and the liquid phases, the liquid's viscosity and the sedimentation velocity, by

applying Stokes Law. Radial positions vs. time were taken in order to calculate the sedimentation velocity for a given angular velocity, which afterwards enables the particle diameter calculation. A plot of u vs. $\omega^2 r/g$ (where g is the gravity acceleration constant) should give a straight line in which the slope is u for earth gravity. This type of measurement relies on Stokes law (for particle diffusion under an acceleration field) and Lambert-Beer law (in order to convert optical transmission to particle concentration). Sedimentation velocity u depends on particle diameter, according to the following equation for diluted samples: [220]

$$u = \frac{1}{18}\frac{\Delta\rho\,d^2}{\eta}\omega^2 r \tag{19}$$

Where $\Delta\rho$ is the density difference between particles and the solvent, ω is the angular velocity and r is the radial position. $\omega^2 r$ represents the centrifugal acceleration experienced by the particles at each radial position. The profiles of optical transmission vs. radial position vs. time are obtained at different rotational speeds, and using Lambert-Beer law, it is possible to determine the sedimentation velocity for each angular velocity. In this work, a normalized optical transmission value was chosen in order to avoid meniscus and bottom cell errors.[221]

Scanning electron microscopy (SEM)

The film surface morphology of the bare substrates and the IZO coated substrates was analyzed by field-emission scanning electron microscopy (FE-SEM) (JEOL JSM7001F), in secondary electron mode, at 10,0 kV.

Atomic force microscopy (AFM)

AFM measurements were made on an Agilent AFM 5500+.

X-Ray Fluorescence (XRF)

XRF measurements were performed in an ArtTAX spectrometer of Intax GmbH, with a molybdenum (Mo) anode, Xflash detector refrigerated by Peltier effect (Sidrift), with a mobile arm. The experimental parameters used were: 40kV of voltage, 300 µA of intensity, for 200 seconds.

Elemental analysis

Elemental analysis was performed in an Elemental Analyzer (Thermo Finnigan-CE Instruments, Italy, model Flash EA 1112 CHNS series).

<u>X-Ray Diffraction (XRD)</u>

XRD measurements were made on a powder X-Ray diffractometer for powders, RIGAKU, model MiniFlex II, 30kV/15mA, with copper X-Ray tubes.

<u>Fourier transform infrared spectroscopy (FTIR)</u>

Infrared analyses were performed on a Nicolet Nexus spectrophotometer. Spectra were obtained in absorbance mode, with a resolution of 8cm^{-1} and 64 scans. Spectra are shown here as acquired, without corrections or any further manipulation, except for baseline correction. The samples consisted of powders grounded with potassium bromide. This powder mixture was then compressed in a mechanical press to form a translucent pellet through which the spectrophotometer infrared light beam passes.

<u>Raman spectroscopy</u>

Raman spectroscopy was made in a Labram 300 JobinYvon spectrometer equipped with a He/Ne laser of 17 mW, operating at 632.8 nm and using the powders.

<u>Differential scanning calorimetry (DSC) and thermogravimetric analysis (TGA)</u>

DSC and TGA analysis were performed on powders with a Netzsch STA 409 PC Luxx. The scan temperature was between 40ºC and 1300ºC and the scan rate used was 10ºC/min.

<u>Transmission electron microscopy (TEM)</u>

Transmission electron microscopy (TEM) images were obtained with a Hitachi H-8100 microscope operating at 200 kV directly on the powder. The images were obtained with a point-to-point resolution of 2.7 Å.

2.3.2   Inks

<u>Surface tension, density and viscosity measurements</u>

Ink surface tension was measured with a KSV Instruments Sigma 70 (Monroe, CT). The DuNoüy ring method was used (R=9.545 mm, r=0.185 mm and l=119.9 mm) and the surface tension obtained value was corrected following the Zuidema-Waters method. The standard glass beaker had a 66 mm diameter and 110 ml maximum volume. The sample volume used was 80-100 ml. Five measurements were

conducted for each sample. Ink viscosity measurements were made with a Brookfield LVT viscometer. Density was measured with a 25 ml pycnometer.

<u>Drop formation and print quality</u>

To see the formation of the drops when it exits the nozzle, the stroboscopic camera of the DMP-2800 was used. This camera allows direct viewing of all the 16 nozzles of the printhead and the faceplate surrounding the nozzles. It therefore allows evaluating the presence of defaults like satellites, tails, misdirected nozzles and non-matched velocities. The print quality was evaluated taking a picture of the printed film with a simple photographic camera. This evaluation is subjective and depends mostly on the final application of the devices. The printing quality is driven towards applications, and therefore the printed films are evaluated mainly by the perception of the human eye.

<u>Reliability</u>

The reliability of the ink can be defined as the percentage of working nozzles after a period of time of continuous printing and also as the percentage of working nozzles after a pause in printing during a certain time. In this work, the printing nozzles were counted at the beginning of the experiments. In the first situation, the printhead was firing for 5 minutes and then the printing nozzles were counted again. In the second case, the printing was interrupted for 1 minute and restarted afterwards without cleaning the printhead and finally the printing nozzles were counted again. The stroboscopic camera of the DMP-2800 was used.

2.3.3 Functional layers

<u>Electrochemical and Spectroelectrochemical measurements</u>

Electrochemical measurements on inkjet printed films were performed in a conventional three-electrode cell. The films deposited on a TCO electrode were the working electrodes (Indium tin oxide (ITO) coated PET (polyethylene terephthalate) with a surface resistivity of 60 Ω/sq was purchased from Sigma-Aldrich and used as received), a platinum wire was used as counter-electrode, a saturated calomel electrode (SCE) was the reference electrode and the supporting electrolyte was acetonitrile with 0.1M of lithium perchlorate (in the case of PEDOT:PSS, tungsten oxide, vanadium oxide and P3HT) or acetonitrile with 0.1M of potassium trifluoromethanesulfonate [222] (in the case of PB). The equipment used was a potentiostat / galvanostat Model 20 Autolab from Eco Chemie BV (Utrecht, The Netherlands). The collection of data was controlled by GPES version 4.9 Eco Chemie BV software. No IR compensation was used. For spectroelectrochemical measurements, the same setup was prepared inside a UV-Vis cuvette that was placed in the spectrophotometer (UV-Vis spectrophotometer Cary 300 Bio) compartment with the film itself perpendicularly positioned to the light beam.

<u>UV-Vis spectroscopy measurements</u>

The optical transmittance measurements were performed using a UV-Vis spectrophotometer Cary 300 Bio in the wavelength range from 380 to 800 nm.

<u>Sheet resistance measurements</u>

Sheet resistance measurements were performed following the method described in IEC Standard 93 (VDE 0303, Part 30). Figure 122 represents this method. On top of deposited conductive thin film, two contacts with 1 cm length, made with a highly conductive tap, were placed 1cm apart from each other. The resistivity of the film is defined by:

$$\rho = R * d * a / b \quad (\Omega.cm) \qquad (20)$$

Where (a) is the length of contacts, (b) is the distance between contacts, (d) is the film thickness and (R) is the resistance measured with a multimeter. When a=b, sheet resistance (Rsq) is calculated using:

$$Rsq = \rho / d \quad (\Omega/sq) \qquad (21)$$
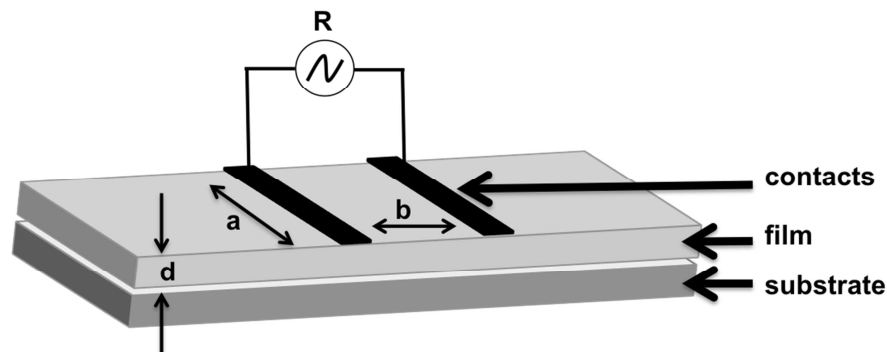
Figure 122: IEC Standard 93 (VDE 0303, Part 30) method for measuring thin films resistivity.

To convert this method into an easiest and fastest way of measuring sheet resistance, a homemade wood box was built. This wood box incorporates two metallic contacts with 5 cm long that were assembled with 5 cm distance between them as shown on Figure 123. The metallic contacts are connected to the terminal of a multimeter to read directly the sheet resistance obtained when those metallic terminals are in contact with a conductive surface. The wood structure is used to ensure a homogeneous and reproducible pressure on the substrates.

136
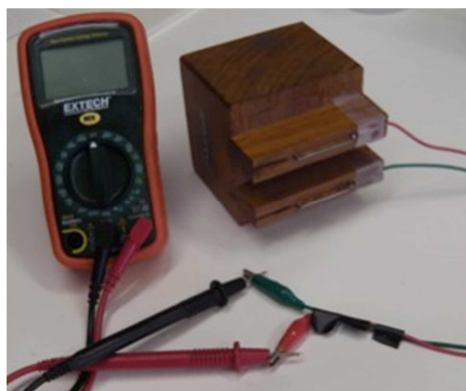
Figure 123: Homemade wood box used to measure sheet resistance following the method IEC Standard 93 (VDE 0303, Part 30).

2.3.4   Electrochromic devices

To evaluate the performance of an electrochromic device, some parameters have to be studied, such as: optical contrast, response time, stability towards cycling tests, electrochromic memory, power consumption and coloration efficiency[41]. The next two experimental setups allow us to determine all these properties.

<u>Electrochemical and Spectroelectrochemical measurements</u>

For the solid-state electrochromic device a two-electrode cell configuration was used. The working electrode and the counter-electrode were both constituted by a layer of printed film on top of the TCO, with the electrolyte layer sandwiched between them, as described above (see Fig. 10). The equipment used was a potentiostat / galvanostat Model 20 Autolab from Eco Chemie BV (Utrecht, The Netherlands). The collection of data was controlled by GPES version 4.9 Eco Chemie BV software. No IR compensation was used.

In-situ UV/Vis absorbance spectra and chronoabsorptometry measurements of the devices were performed using a UV-Vis-NIR spectrophotometer Varian Cary 5000 (spectral range from 220 to 3000 nm). The devices were potentiostatic or potentiodinamically controlled with a potentiostat/galvanostat Model 20 Autolab as described in 2.3.3. The two-electrode cell configuration is the same of 2.3.3. The device was placed in the spectrophotometer compartment perpendicularly to the light beam. The potentiostat/galvanostat applied a square-wave form electric potential (at selected values described below), and the spectrophotometer registered the absorbance at the wavelengths selected for each experiment within the range of the equipment. Stability cycling tests were also performed in the same set-

up. This method was used to determine stability toward cycling, coloration efficiencies, power consumption and response time (see section 1.6).

Stability toward cycling

To perform this measurement, an experimental set-up and analysis algorithm was developed at Ynvisible. A camera, a lamp (to control the luminosity) and a ®ColorChecker (color pattern) were put inside an isolated box. The electrochromic device is placed inside the box with the other elements and connected to a function generator. While the function generator applies a determined potential in a square waveform (changing from positive to negative), the camera is recording, at defined intervals, 150 pictures along Xs, this allows to capture the full cycle sequence (display ON-OFF-ON) oxidation and reduction. This set-up is fully automated and the acquisition interval and period can be programmed. The pictures are then treated with Matlab software (version Matlab R2010b) converting RGB coordinates obtained from the captured images from the electrochromic display into the CIELAB coordinates. The percentage of degradation due to the cycling stress is measured as the variation of the color CIELAB coordinates and the contrast is calculated (see section 1.6.1).

2.4   Experimental details

2.4.1   Conductive materials

<u>Reagents</u>

Ethanol (99.5%, Panreac), indium (III) chloride (98%, Aldrich), tin (II) chloride dihydrate (98%, Aldrich), antimony (III) chloride (99%, Aldrich), ammonium fluoride (98%, Aldrich), methanol (99.8%, Aldrich), ethylene glycol (99%, Alfa-Aesar), citric acid (99.5%, Aldrich), nitric acid (70%, Aldrich), antimony (III) oxide (98%, Aldrich), Ammonium hydroxide (25%, Aldrich) and antimony tin oxide (99.5+%, Aldrich).

<u>Synthesis, deposition and sinterization (Metallic chlorides method)</u>

ITO

A solution of indium chloride (0.37M) in 20 ml of ethanol and a solution of tin chloride dihydrate (0.18M) in 4 ml of ethanol were heated and stirred separately until complete evaporation of the solvent. The collected powders were mixed together in 5 ml ethanol, heated at 80ºC and stirred until half solvent volume evaporates. To reach the viscosity wanted, some water can be added. The films were deposited on glass using inkjet printing. The inkjet printed films were dried at 120ºC for 40 minutes and then sintered at 550ºC for 15 minutes.

ATO

A solution of antimony chloride (0.18M) in 4 ml of ethanol and a solution of tin chloride dihydrate (0.37M) in 20 ml of ethanol were heated and stirred separately until complete evaporation of the solvent. The collected powders were mixed together in 5 ml ethanol, heated at 80ºC and stirred until half solvent volume evaporates. To reach the viscosity wanted, some water can be added. The films were deposited on glass using spin coating (1000 rpm during 10s). The spin-coated films were dried at 120ºC for 40 minutes and then sintered at 550ºC for 15 minutes.

FTO

An aqueous solution of ammonium fluoride 7,5% (w/w) was added to a solution of tin chloride dihydrate (0.44M) in 50 ml of methanol. This solution was heated at 80ºC and stirred until 1/4 of the solvent volume evaporates. The films were deposited on glass using spin coating (1000 rpm during 10s). The spin-coated films were dried at 120ºC for 40 minutes and then sintered at 550ºC for 15 minutes.

<u>Synthesis (Pechini method)</u>

ATO 1

1.7g of $SnCl_2.2H_2O$ were added to 50ml of water under stirring. 1.025g of $SbCl_3$ were added to the solution. After complete dissolution of the powders, 1.5g of citric acid and 0.4ml of ethylene glycol were added. The solution was kept under stirring in a closed vessel during 15 minutes.

ATO 2

2.6g of ethylene glycol and 2.6g of citric acid were mixed under stirring at 65ºC. After complete dissolution of the powder the temperature was raised to 90ºC. 2.1g of tin citrate and 0.2g of antimony citrate were added (the citrates were synthesized using the method described below). HNO_3 was added drop by drop until the two powders were completely dissolved in the solution. The heat was removed and some water was added to adjust the viscosity and the solution was kept under stirring during 15 minutes.

ATO 3

2.86g of ethylene glycol and 2.86g of citric acid were mixed under stirring at 65ºC in 50ml of water. After complete dissolution of the powder the temperature was raised to 90ºC. 2g of tin citrate and 0.05g of antimony citrate were added (the citrates were synthesized using the method described below). HNO_3 was added drop by drop until the two powders were completely dissolved in the solution. The heat was removed and some water was added to adjust the viscosity and the solution was kept under stirring during 15 minutes.

Commercial ATO

1.2g of ethylene glycol and 1.2g of citric acid were mixed under stirring at 65ºC. After complete dissolution of the powder the temperature was raised to 90ºC. 0.5g of commercial antimony tin oxide was added. The heat was removed and some water was added to adjust the viscosity and the solution was kept under stirring during 15 minutes.

Tin citrate

4.2g of $SnCl_2.2H_2O$ were dissolved in an aqueous solution of citric acid (50ml of water and 1.82g of citric acid) under stirring. 60 drops of NH_3 (25%) were added one by one until a white precipitate is obtained. The white powder was collected by filtration and washed several times with water to remove the chlorides. The obtained powder was dried at 70ºC for 24 hours.

Antimony citrate

0.45g of $SbCl_3$ was dissolved in an aqueous solution of citric acid (20ml of water and 1.7g of citric acid) under stirring. 60 drops of NH_3 (25%) were added one by one until a white precipitate is obtained. The

white powder was collected by filtration and washed several times with water to remove the chlorides. The obtained powder was dried at 70ºC for 24 hours.

2.4.2 Electrochromic Materials

2.4.2.1 Tungsten oxide

Reagents

The following reagents were purchased and used without further purification: metallic tungsten (99.9%, Aldrich), hydrogen peroxide (30%, Fluka), tungsten (VI) oxide (99.9%, Fluka),

Synthesis

New

Metallic tungsten was added to hydrogen peroxide (6.8% (w/w) of metallic tungsten in hydrogen peroxide) and allowed to react about three minutes until a clear transparent colorless solution was formed (without aging or heating). This solution was heated (100ºC) under stirring in a closed vessel, giving a yellow solution after 2 hours. A pale yellow precipitate appears after 5 hours under the same conditions. The resulting dry powder (A) was obtained after solvent evaporation.

In addition to the synthesized powder (A) and the commercially available tungsten oxide (B), two more powders were obtained: one in which A was sintered at 550ºC for 1 hour (C) and another powder by dispersing A in water, followed by 1 week of ageing and lyophilisation, in order to obtain the "dry" powder D.

Ink formulation

The obtained tungsten oxide nanoparticles (powder A) were dispersed in water, giving a stable colloidal suspension characterized by sedimentation techniques. The ink dispersion used has a tungsten oxide concentration equal to 1.7 g/dm^3 in water.

2.4.2.2 Vanadium oxide

Reagents

The following reagents were purchased and used without further purification: Vanadium (V) oxide (98+%, Aldrich) and hydrogen peroxide (30%, Fluka).

<u>Synthesis</u>

1.07 g of Vanadium (V) oxide was added to 40 ml of hydrogen peroxide. An exothermic reaction occurs spontaneously giving a brown-red paste. This brown-red paste was allowed to dry on a hot plate at 100ºC for 2 hours. A brown-red powder is obtained (Figure 50).

<u>Ink formulation</u>

The synthesized vanadium oxide powder can be readily suspended on water (2.54 g/dm^3) and filtered at 1µm, giving a very stable colloidal suspension.

2.4.2.3   Poly(3,4-ethylenedioxythiophene) poly(styrenesulfonate)

<u>Reagents</u>

The following reagents were purchased and used without further purification: PEDOT: PSS (1.3 wt% water dispersion, Aldrich), Triton X-100 (Fluka) and sodium hydroxide (>98%, Aldrich).

<u>Ink formulation</u>

The obtained PEDOT:PSS ink was formulated dissolving the copolymer (47.8% w/w) in water (50.2% w/w) and adding 2% w/w of NaOH 1M and 1% (w/w) of triton-X.

2.4.2.4   Poly(3-hexylthiophene)

<u>Reagents</u>

Iron (III) chloride (anhydrous, 98%, Alfa-Aesar), Chloroform (analysis ISO, Carlo Erba), 3-hexylthiophene (99%, Aldrich), methanol (puriss p.a. 99,8%, Aldrich) and chloridric acid (Acs reagent 37%, Aldrich).

<u>Synthesis</u>

This organic electrochromic material was synthesized as referred in the literature[223]. Anhydrous FeCl3 (0.65 g, 4.0 mmol) and CHCl3 (1 mL) were placed in a 25-mL two-necked round-bottom flask. The flask was then filled with nitrogen, and 3-hexylthiophene (0.17 g, 1.0 mmol) was added via a syringe to the suspension. The resulting black mixture was stirred for 24 h under a flow of nitrogen. The reaction mixture was poured into methanol containing 10% concentration of HCl aq. The precipitate was collected by filtration and washed with methanol in a Soxhlet's extractor for 24 h. The resulting dark purple was extracted with CHCl3 in the same apparatus, and the sol- vent was evaporated to give the product. This synthesis was performed by Ana Lúcia Morais from the Chemistry Department of FCT/UNL and the powder was used as received for this work.

Ink formulation

The ink formulation used was: tetrahydrofuran (46.1% w/w), chlorobenzene (52.5% w/w) and P3HT (1.4% w/w) with the physical properties presented in table 11.

2.4.2.5   Prussian blue

Reagents

Potassium trifluoromethanesulfonate (98%, Aldrich), potassium hexacyanoferrate (III) (≥99.0%, Aldrich) and iron (II) sulfate heptahydrate (99%, Aldrich).

Synthesis

This inorganic electrochromic material was synthesized as referred in the literature[224] with some small changes. A 0.05M potassium hexacianoferrate (III) and a 0.01M Iron (II) Sulfate aqueous solutions were prepared. These two solutions were mixed and allowed to react for 24 hours under stirring. The final solution was filtered with a filter membrane of 3000 Da. The resulting powder was washed with water until clear water was obtained. The powder was dried by Lyophilization. This synthesis was performed by Ângela Serrano from Ynvisible and the powder was used as received for this work.

Ink formulation

PB particles were dispersed only in water (1.1%).

2.4.3   Electrolyte

1st generation: a polymer with lithium salt (prepared from a mixture containing a polyethylene oxide-polypropylene oxide copolymer (PEO-PPO). This copolymer has an average molecular weight of 150000 D, and the fraction of PPO is 1% of the weight. The copolymer was dissolved in acetonitrile containing $LiClO_4$. The mass percentages were 24% for the copolymer, 12% for $LiClO_4$ and 64% for acetonitrile) or a solution of lithium perchlorate 0.1M in acetonitrile (or potassium trifluoromethanesulfonate for PB).

3rd generation: the solid-state electrolyte was obtained in one step, by photo polymerization of a solution containing all the components of the final material. The electrolyte formulation is composed by an acrylate based monomer, aprotic solvents, a lithium salt and a photo initiator for the acrylate polymerization reaction. The electrolyte was prepared by dissolving the lithium salt in the solvents under stirring in a

closed flask at room temperature. The solvents were used as received. When the salt was completely dissolved, the monomer was added to the solution and kept under stirring for a few minutes. Then, the flask was protected from the light with an aluminum foil, the photo initiator was added and the mixture was left under stirring. After a few minutes, a homogeneous yellowish solution is obtained.

4th generation: the solid-state electrolyte was obtained in one step, by photo polymerization of a gelled solution containing all the components of the final material. The electrolyte formulation is composed by a polymer based on poly(ethylene oxide) (PEO) containing organic groups which promote cross linking of the polymeric chains, a mixture of aprotic solvents, a lithium salt and a photo initiator. The electrolyte was prepared by dissolving the desired amount of lithium salt in the aprotic solvents under stirring in a closed flask at room temperature. The solvents were used as received. When the salt is completely dissolved, the cross-linkable PEO based polymer powder is added to the solution and the components are homogenized with a spatula. The solution becomes a gel when complete dissolution of the polymer in the solvents occurs. This step takes place by leaving the mixture under mechanic stirring for a few hours until the desired solution viscosity is attained (close to 40 kcp at room temperature). Then, the flask was protected from the light with an aluminum foil, the photo initiator was added and the mixture was left under stirring for a few minutes, until a homogeneous yellowish gel is obtained.

3 Complementary Work: conductive electrodes

For the correct execution of this project, the challenge of building conducting electrodes on heat sensitive substrates, such as paper, is crucial. Since the attempt to obtain these conducting electrodes using sol-gel techniques and sinterization at low temperatures presented a high risk of failure (see section 2.1), other techniques and materials were explored simultaneously, so electrochromic devices could be built on paper and characterized in order to reach one of the goals of this thesis.

Several materials such as gold thin films, silver inks or even carbon fibers incorporated into paper substrates were explored but the results were not satisfactory for electrochromic applications. As explained in the introduction chapter, metals are sensitive to redox processes, so they are not a viable choice for electrochromism. Carbon based approaches have also an important limitation for its application on electrochromic devices, which is the color of the film or of the substrate. These materials are too dark and the visual electrochromic effect is completely or partially lost. The conducting materials identified as the most promising for our applications are still TCO's.

In this chapter, three different TCO depositions were studied: ITO deposition using sputtering at CENTI, IZO (metallic target) deposition using sputtering also at CENTI and IZO (ceramic target) deposition using DC and RF sputtering at INESC.

The most common choice of TCO for optoelectronics applications is, in fact, ITO as a thin film sputtered onto glass[41,225] because it presents a wide band gap, good electrical conductivity and high transmittance; however, ITO must be deposited at high temperatures and then annealed at a temperature above 300ºC for good electrical conductivity, high transmittance and high stability. This annealing temperature causes the ITO films to be crystallized and roughened.[226] The annealing step is also necessary to increase the film density and, therefore, to increase the resistance to H_2O and O_2 penetration and the device lifetime.[227] On the other hand, the use of high temperatures limits the application on flexible substrates like plastic or paper. Nevertheless, CENTI obtained good results depositing ITO on plastic, so it was decided to explore first this material also on paper (section 3.1).

Since the results obtained with ITO were not satisfactory in terms of stability, another TCO material was chosen: IZO (indium oxide doped with zinc oxide), which appears as an attractive alternative to ITO films[226]. IZO also has a wide band gap (>3.5 eV), good electrical conductivity (>10^3 $\Omega^{-1}cm^{-1}$) and a high transmittance (>80%) in the visible region of the spectrum[42]. Amorphous IZO has a better structural and chemical stability at a relatively high temperature compared to ITO.[226] It can be deposited at room temperature without any annealing step and still be a very stable material.[228] It also has a very low roughness, internal stress[229] and a higher elastic modulus than ITO.[230] Indeed, the elasticity of amorphous IZO makes it adequate to be deposited on flexible substrates. IZO is however a recent material and that is

146

the reason why ITO is still mostly used industrially. The sputtering equipment used at CENTI requires preferably metallic targets, so a target with the composition In/Zn 90/10% wt was used (section 3.2). The results were again not satisfactory.

It is known that reactive sputtering (metallic targets) is always more complicate to achieve than non-reactive sputtering (ceramic targets)[42] because of the reduced window of oxygen that can be used to obtain a transparent and conductive film. It is also known that, in principle, sputtering from ceramic targets with zinc oxide is a simple and reliable deposition method. Since ceramic targets are expensive and the sputtering equipment at CENTI demands a very large target, it was decided to continue this study with a smaller sputtering equipment to evaluate this new strategy and to have a proof of concept for further depositions in bigger equipments.

INESC-MN (Microsistemas e Nanotecnologias) has a small sputtering machine that allows depositions both with DC an RF (radio-frequency) sputtering using targets with only 3 inches of diameter (section 3.3).

3.1   ITO deposition by sputtering

ITO was deposited on paper using a sputtering machine available at CENTI – Centre for Nanotechnology and Smart Materials. The target used in the equipment had a size of 50x10 cm and the composition was In_2O_3/SnO_2 90/10% wt with a purity of 99.999%. The experiments were done using preferably drafting paper as substrate.

The following parameters were used and/or optimized. The next sections will demonstrate the influence of these variations, as well as the storage conditions, in the performance of the conducting substrate in terms of sheet resistance and stability:

- Initial pressure: from $2,4 \times 10^{-4}$ to $6,2 \times 10^{-5}$ torr;
- Frequency: 40 kHz;
- Argon: from 60 to 500 sccm;
- Oxygen: without oxygen
- Power: from 500 to 900 Watt;
- Current: depends on the power;
- Tension: depends on the current;
- Deposition time: from 2,5 to 5 minutes.

Initial pressure of deposition

An optimization of the initial pressure regarding the sheet resistance obtained was achieved. The ITO coated substrates were monitored for 22 hours to see the thin film stability. Figure 124 shows the variation of the sheet resistance depending on the initial pressure of deposition used. This initial pressure of deposition is the degree of vacuum that is allowed to reach before the deposition starts and before the introduction of the gases (without insertion argon or oxygen). The measurements of sheet resistance were made after deposition, 15 and 22 hours after deposition. The most promising results were obtained for an initial pressure of 6×10^{-5} torr. However the stability test shows that the thin film is not stable once it started with 1kOhm/sq and 22 hours later, it showed a sheet resistance of 12kOhm/sq.
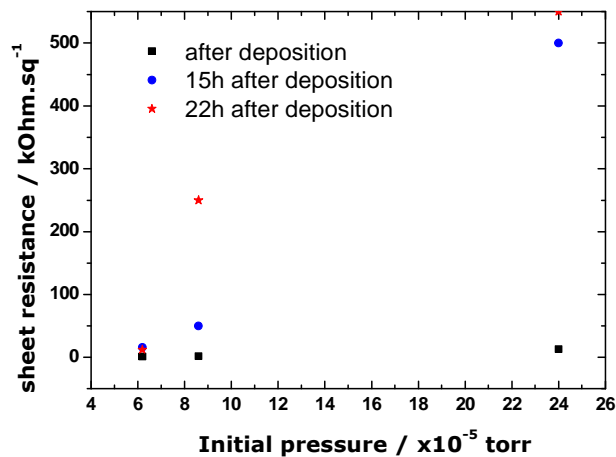
Figure 124: Variation of sheet resistance depending on the initial pressure of deposition used and stability test at 0, 15 and 22 hours after deposition.

Argon

The next step was to determine the relationship between sheet resistance and the amount of argon introduced into the chamber. Figure 125 shows this variation, as well as the stability of the films during time.

The most promising results were obtained for 60 and 70 sccm of argon, but the samples reached 800Ohm/sq 36 hours after deposition, showing that the thin film is not stable. Besides the lack of stability, the deposited films had very strong yellow coloration, not suitable for electrochromic applications.
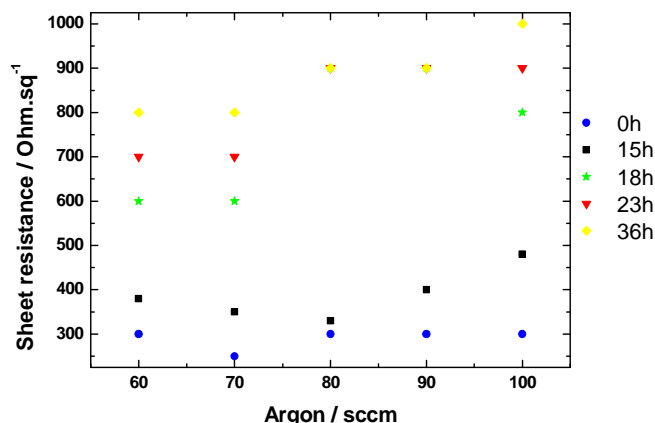
Figure 125: Variation of sheet resistance depending on the amount of argon introduced into the chamber and stability test at 0, 15, 18, 23 and 36 hours after deposition.

Storage after deposition

Because of the lack of stability in the two previous experiments, it was decided to test the storage conditions to see if the atmosphere where the samples were kept was responsible for their degradation. One sample was kept in air; the other was kept under vacuum during the first 15 hours after deposition and then put together with the first sample. Figure 126 shows that vacuum really delays the degradation but when the sample is in contact with air, the degradation starts and 24 hours after deposition the two samples reached the same level of degradation.

Figure 126: Variation of sheet resistance depending on the storage conditions and stability test at 0, 15, 18 and 24 hours after deposition.

149

From these results, we can conclude that the samples should be kept in controlled atmospheres and handled in special conditions, which is not compatible with the simple and inexpensive printing method required for our application.

Power

The power used in the sputtering equipment was varied and the sheet resistance and stability of thin films were assessed with these conditions (Figure 127). The most promising result was obtained for 900W. However, the conducting film is still not stable after deposition and 900W is in the limit of the equipment range. The target started to heat too much and eventually it started to melt.
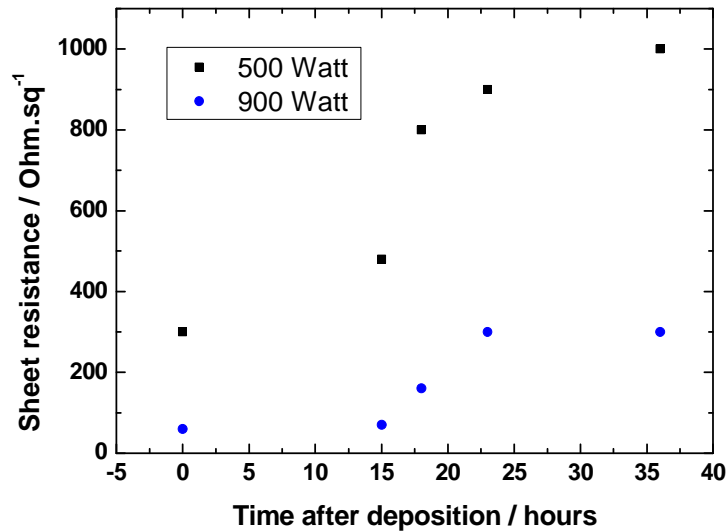
Figure 127: Variation of sheet resistance depending on the power applied and stability test at 0, 15, 18, 24 and 36 hours after deposition.

Deposition time

The next parameter studied was the deposition time. Figure 128 shows that 5 minutes of deposition lead to more conductive and more stable films than 2.5 minutes of deposition, but the thin films are still not stable enough and 36 hours after deposition, the sheet resistance of the film was already three times higher than just after the deposition.
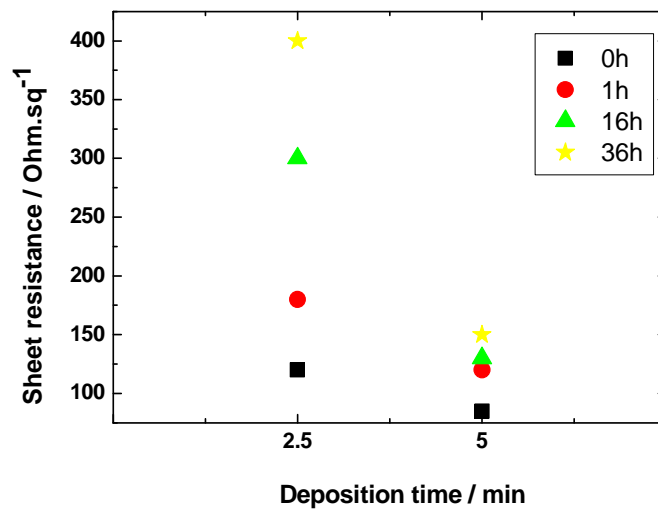
Figure 128: Variation of sheet resistance depending on the deposition time and stability test at 0, 1, 16 and 36 hours after deposition.

<u>Substrates</u>

Figure 129 shows the results obtained for different papers coated with a thin layer of a polymer deposited using PML (Polymer Multilayer) technique before the deposition of the ITO layer. PML is a technique to deposit a monomer under vacuum into a substrate and then the monomer is cured using e-beam technology.
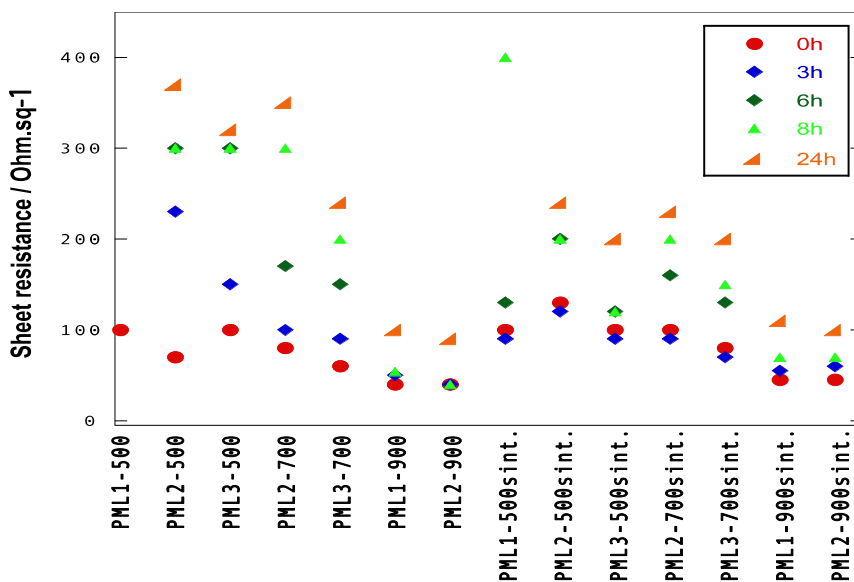
Figure 129: Variation of sheet resistance depending on the coated substrate used and stability test at 0, 3, 6, 8 and 24 hours after deposition.

151

This deposition was done with the rotation of the substrate. Therefore the monomer was deposited and cured continuously into the same substrate until the thickness wanted is achieved. The designation PML1, PML2 and PML3 refer to the thickness of the polymer layer: PML 3 being thicker than the others because the deposition time was longer. The numbers 500, 700 and 900 are referred to the power used to deposit the ITO layer in the presence of 100 sccm of argon. The indication "sint" indicates that the samples were heated at 80ºC for 1 hour (after the deposition of ITO layer).

The best results were obtained again for the samples deposited at 900W of power; with PML1 and PML2 both sintered and not sintered (meaning that the sinterization at this temperature did not improve the sheet resistance or the stability). Some degradation is still viewed after 24 hours.

Figure 130 shows the results obtained for different papers: two different types of drafting paper, drafting paper covered with three different thicknesses of polymer layer (PML1, PML2 and PML3), pasteboard paper and copy paper. The argon flow was reduced to 70 sccm. The best results were obtained with PML1, but again, with some degradation after only 70 hours.
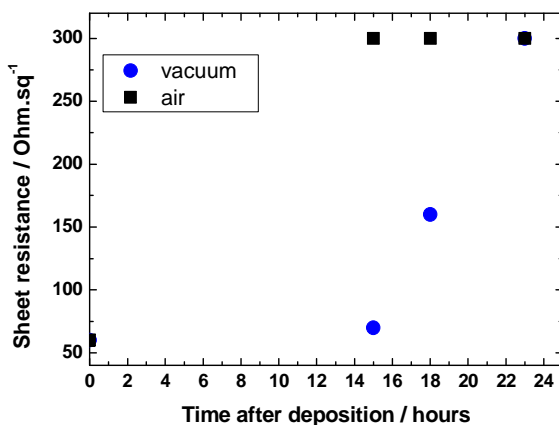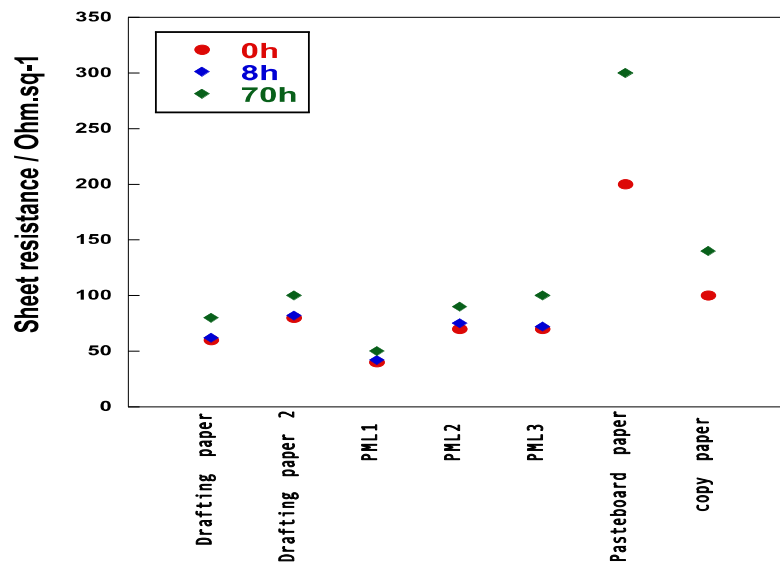

Figure 130: Variation of sheet resistance depending on the substrate used and stability test at 0, 8 and 70 hours after deposition.

It is known from previous experiences at CENTI that these depositions of ITO but on plastic provides very conductive and stable thin film for several months. Obviously, on paper, this is not the case. This fact could be due to the elasticity of paper fibers; ITO being a material that is rather crystalline, tends to reorganize itself after deposition and the fibers of the paper will follow this movement creating cracks on the thin film and, that way, increasing the sheet resistance. Oxygen or moisture must also play an

important role in this degradation because of the results obtained in Figure 124. One explanation could be the fact that the surface of a paper substrate is much more rough than a plastic substrate, meaning that the TCO layer, considering that all the area is covered is also rougher when deposited on paper. Therefore, the area of ITO in contact with air is larger than in plastic and that way promoting the degradation on paper and not on plastic.

3.2   IZO deposition on paper by DC and RF sputtering (metallic target)

The experiments were done using preferably drafting paper as substrate.

The following parameters were used and/or optimized. The next sections will demonstrate the influence of these variations in the performance of the conducting substrate in terms of sheet resistance and stability:

- Initial pressure: in the order of 10^{-5} torr;
- Frequency: 62 kHz:
- Deposition mode: AC and DC;
- Argon: from 150 to 280 sccm;
- Oxygen: from 7 to 15 sccm;
- Power: from 100 to 500 Watt;
- Current: depends on the power;
- Tension: depends on the current;
- Deposition time: from 5 to 12.5 minutes.

Oxygen

Figure 131 shows the variation of sheet resistance in accordance with the amount of oxygen present in the deposition chamber. The substrate was in a static position relatively to the target (deposition mode: AC).

Figure 131: Variation of sheet resistance depending on the oxygen used for the deposition and stability test at 0 and 20 hours after deposition.

154

The best result was obtained for 10 sccm of oxygen, but the obtained thin films are too dark and not stable after only 20 hours after deposition.

The next experiment is to repeat the best results obtained in the previous set of tests in a rotation mode (with 10 sccm of O_2, with AC mode). The transparency increased drastically but one side of the paper substrate was brown. This is due to an equipment problem. The magnetron seems to be heating more at one side of the target and that way producing darker films at that side. Figure 132 shows the conducting substrate obtained with this experiment. The sheet resistance immediately after deposition was 125 Ohm/sq.
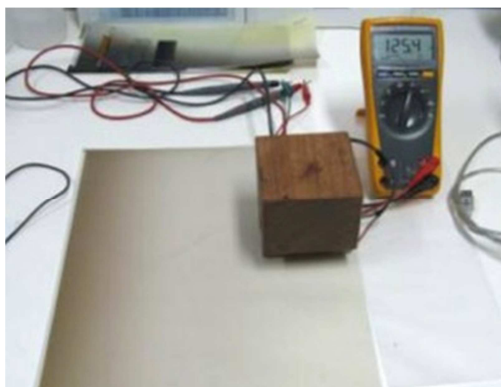
Figure 132: Conducting substrate obtained in rotation, with 10 sccm of O_2 and AC mode.

This conducting paper substrate was then tested using it to build an electrochromic device with PEDOT:PSS as electrochromic material and PET/ITO as the top substrate. Since the conductivity is still not appropriate, the device displayed long switching times (Figure 133).

Figure 133: Electrochromic device build using IZO deposited on drafting paper as down electrode and PEDOT:PSS as electrochromic material.

IZO thin films are more stable than ITO, but they are still not appropriate for electrochromism. AFM measurements were performed to understand the morphology of IZO films (Figure 134). From this image, it seems that the layer of IZO is too thick, since it is expected to see the fibers of the paper below the thin film. This fact could lead to cracks of the film and that way increase the sheet resistance.
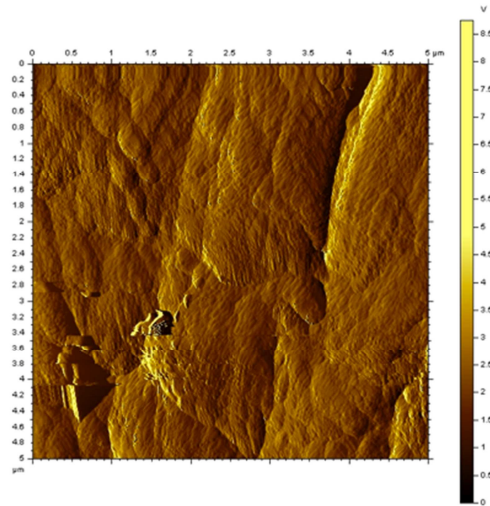
Figure 134: AFM image of IZO layer on drafting paper substrate.

Power

These experiments were prepared with the aim of controlling the film thickness by varying the power used in the deposition. Figure 135 shows the results of sheet resistance obtained for power variations from 100W to 500W in an AC (alternating current) mode, using 10 sccm of oxygen and 265 sccm of argon.
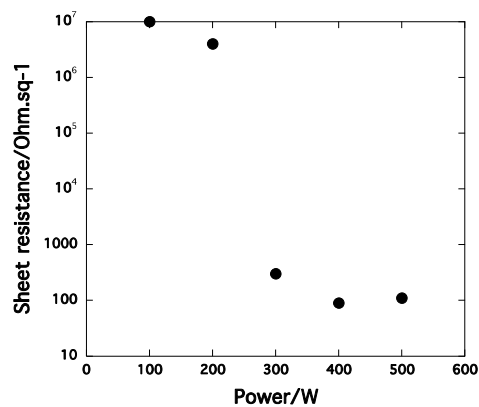
Figure 135: Variation of sheet resistance depending on power used for the deposition.

With 100 and 200W, the films were completely transparent but the sheet resistance was very high. With 300, 400 and 500W the sheet resistance was improved but the films were too dark. These films are still unstable, so apparently, varying the power did not solve the thickness problem. The next step would be to reduce the amount of argon but for that, the depositions have to be made in DC (direct current) mode.

Deposition time

Figure 136 show the results obtained in DC mode with 400W and with several different deposition times using 10 sccm of oxygen and 150 sccm of argon. The best result was obtained for 10 minutes of deposition and seems to be more stable. .
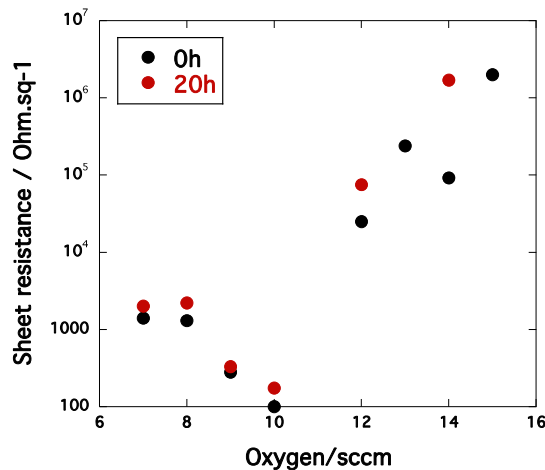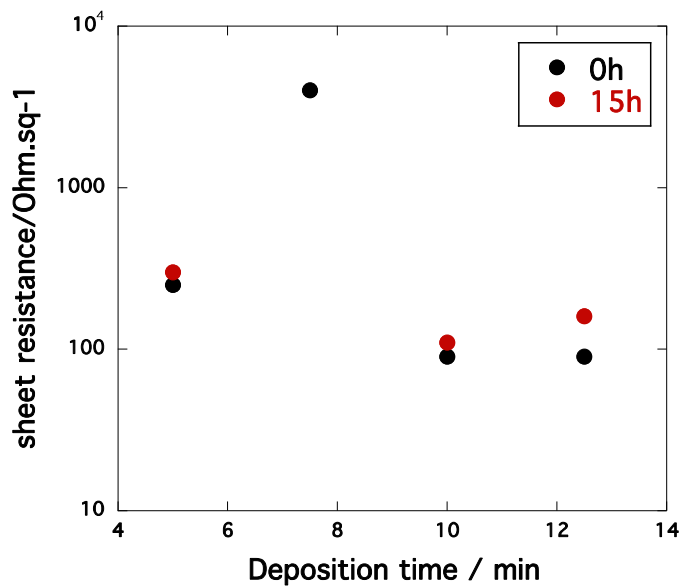

Figure 136: Variation of sheet resistance depending on the deposition time and stability test at 0 and 15 hours after deposition.

From this point, CENTI tried to improve the functionality of the equipment, improving the uniformity of deposition and the cooling of the target, allowing the use of higher power during depositions without melting the target, using for that purpose monopulse depositions. Some preliminary tests were done and the main conclusion is that the films are more stable when deposited at 1000W.

Because of this new approach, another set of experiments was performed varying the amount of oxygen used during the deposition.

Figure 137 shows the results obtained. Depositions with 9 % sccm of O_2 or less (proportion between oxygen and argon, in this case 230 sccm of argon were used for 23 sccm of oxygen), presented black

conductive films. With 10 % of O_2, the film was yellow and presented a sheet resistance of 120 Ohm/sq. With 20, 30 and 40% of O_2, the films were completely transparent but not conductive.
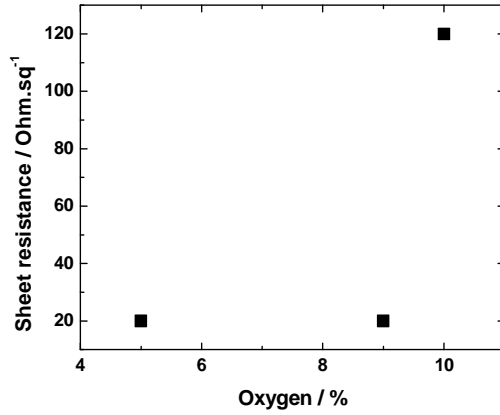
Figure 137: Variation of sheet resistance depending on the oxygen used for the deposition.

Following these results, a new set of experiments was done where the percentage of oxygen was adjusted around 10% (7, 9, 12, 15 and 18%).

The target started to melt again when the deposition with 15% of oxygen was being done, but a good result was obtained for 9% with a light brown film with 20 Ohm/sq of sheet resistance. 18 hours later, the film presented a sheet resistance of 25 Ohm/sq.

It was then decided to reduce the power to prevent further melting of the target and the oxygen percentage was adjusted again for this power. After 15 minutes of deposition, the results obtained are shown in figure 138. The best result was obtained for 7% of oxygen, but the film color is still too brown.
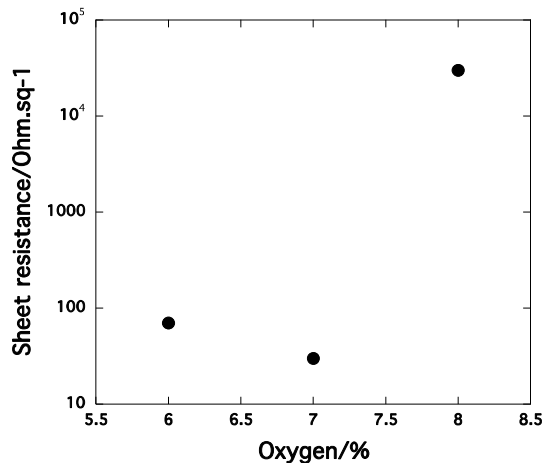
Figure 138: Variation of sheet resistance depending on the oxygen used for depositions at 700W.

Some electrochromic devices were built with IZO films obtained in this last set of experiments (Figure 139). The electrochromic material (PEDOT:PSS) was inkjet printed on top of the IZO layer. The Top substrate used was PET/ITO. The results were encouraging since it showed acceptable contrast and a cycling performance of 50000 cycles with 50% of degradation.
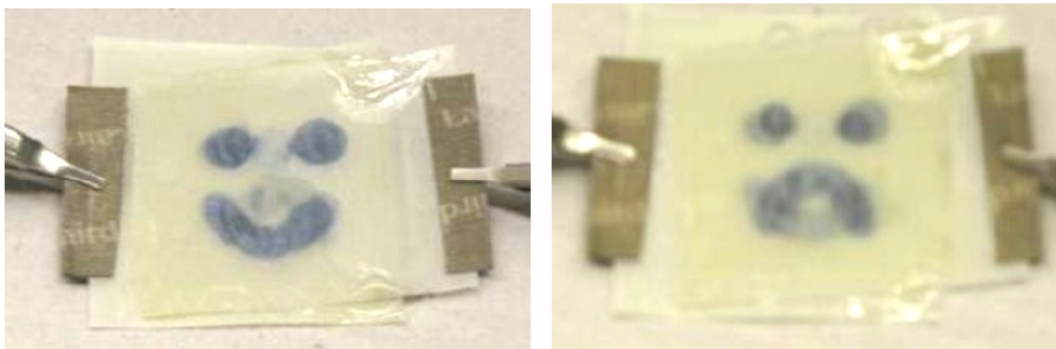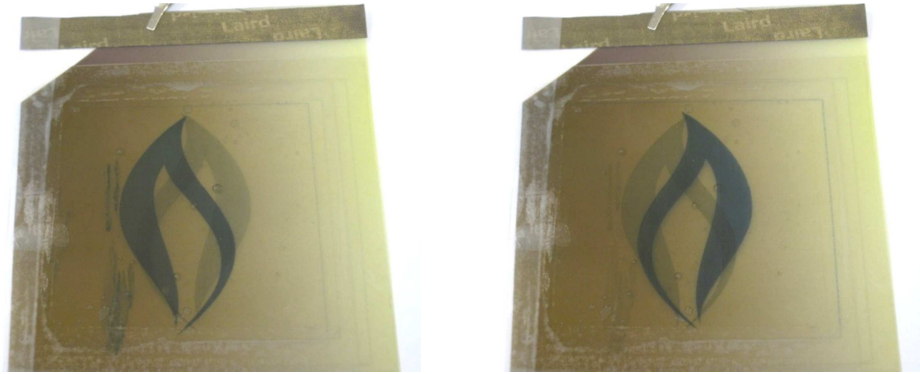

Figure 139: Electrochromic device build using IZO deposited on drafting paper as down electrode and inkjet printed PEDOT:PSS as electrochromic material.

3.3   IZO deposition on paper by DC and RF sputtering (ceramic target)

This section describes depositions into several types of papers of an IZO ceramic target (composition: In_2O_3:ZnO (87:13 wt%)). Since the target is conductive enough, both RF and DC sputtering could be used. Insulating targets require the plasma excitation to be performed by an RF power supply, since with DC excitation no plasma can be ignited. DC power supplies are significantly more cost effective than RF power supplies and, therefore, of these two processes, DC sputtering deposition is the technique most widely used industrially[42]. In this work, the deposition of IZO with an RF power supply was performed to create a "conductive paper", while DC power supply-based depositions were used to prove that the process could be implemented industrially.

Deposition parameters and sheet resistance measurements

The films were deposited on glass and various paper substrates (pasteboard paper, glossy coated paper and drafting paper) at room temperature by RF and DC sputtering from an In_2O_3:ZnO (87:13 wt%) alloy target (99,99% purity, from Testbourne, Ltd) with 7.5 cm diameter and 3 mm thick.

The depositions were made at INESC-MN on an Alcatel SCM450 sputtering system, with a base pressure of ~$1x10^{-7}$ Torr maintained by a rotary and turbo molecular pumps. For RF sputtering, power was varied from 40 to 50 W, and pure Ar plasma was maintained with Ar flow rates from 20 to 50 sccm (standard cc/min). For DC sputtering, oxygen (O_2) gas was also incorporated into the plasma at a flow rate of 0.8 sccm. Power was set to 40 W. The sputter deposition rate was derived from stylus profilometer measurements of film thickness. The typical IZO film thickness ranged from 100 to 200 nm. These thicknesses would require long deposition times (30 min) and substrate cooling (achieved through copper heat sink substrate holder mounted in contact with a water cooled table) is a key factor. Deficient cooling of the substrate would cause film degradation, with a dark signature rather than transparent.

In this section, the method followed to optimize the deposited IZO thin film, in terms of transparency and conductivity, is reported. The deposition parameters used with RF and DC power supplies are described, as well as the results obtained for each experiment and substrate used. Table 32 lists the results for a RF power supply. The shaded cells, in the table, illustrate the parameter changed from one experiment to the next. The sputtering deposition process was optimized based on previous know-how. It is known that, in general, more power will increase the film thickness and, therefore, the conductivity. However, transparency decreases under these conditions (until a certain level, after which the substrate can be damaged). More Ar will increase the conductivity but may degrade the transparency and O_2 will increase the transparency but will decrease the conductivity. On the other hand, a longer deposition time will increase the conductivity, but decrease the transparency. In order to balance the long deposition times,

some stops were made during the process. It is also known that, for RF power supplies with ceramic targets, O_2 is not required during deposition, but for DC power supplies, the target must be conductive enough to be able to start the plasma and some O_2 could be needed, as well[42]. DC power supplies also deposit more material than RF power supplies in the same range of time, using the identical deposition parameters. The RF power supply experimental parameters (power, Ar flow rate, deposition time and stops) are listed in table 32 and were selected based on previous experience employing sputtering technique. Such parameters were adjusted in the present work to obtain an optimized uniform transparent and conductive film, which was achieved with the experiment number 6 conditions. The parameters applied in this experiment (with RF power supply) were used in the deposition by DC sputtering (Table 33). Additionally, a very low oxygen flow was used and the deposition time was kept, to slightly increase the film thickness and conductivity as a result, as explained above. Figure 140 shows the evolution of the IZO sheet resistance with the Ar gas flow for RF deposition (on drafting paper) and DC deposition (on drafting paper, glossy coated paper and pasteboard paper).

Table 32: Deposition parameters tested and results obtained with a RF supply for each experiment. Substrate used: Drafting paper.

Experiment number	Power (W)	Ar (sccm)	Deposition time and stops during deposition (min)	Results		
				Color	Thickness (nm)	Sheet resistance (Ω/sq)
1	50	50	30 min. deposition (15+15) with 3 min. stop	Brown	200	130
2	40	50	30 min. deposition (15+15) with 3 min. stop	Light Brown	140	150
3	40	20	30 min. deposition (15+15) with 3 min. stop	Brown	100	360
4	40	30	30 min. deposition (15+15) with 3 min. stop	Brown	140	130
5	40	40	30 min. deposition (15+15) with 3 min. stop	Light Brown	140	120
6	40	40	30 min. deposition (10x3) with 3 min. stop	Transparent	120	87

Table 33: Deposition parameters used and results obtained with a DC supply for each substrate.

Power (W)	Ar (sccm)	O2 (sccm)	Deposition time and stops during deposition (min)	Substrate	Results		
					Color	Thickness (nm)	Sheet resistance (Ω/sq)
40	40	0.8	30 min. deposition (10x3) with 3 min. stop	Glossy coated paper	Transparent and uniform	180	50
				Pasteboard paper			20
				Drafting paper			30
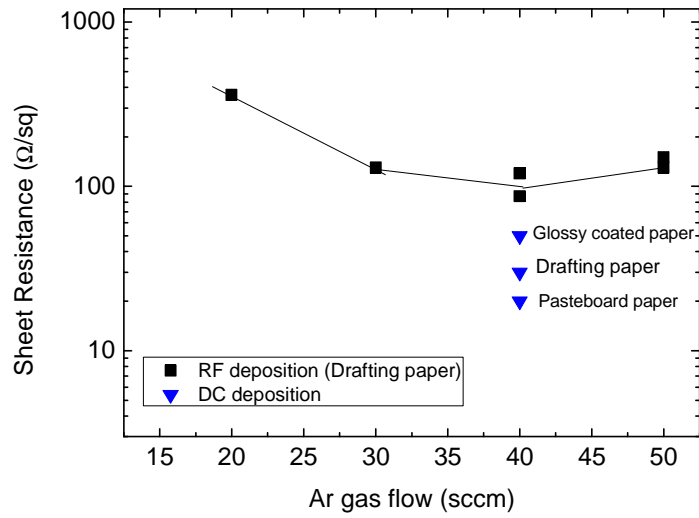
140: IZO sheet resistance versus Ar gas flow for RF deposition (on drafting paper) and DC deposition (on drafting paper, glossy coated paper and pasteboard paper).

UosUV-Vis spectroscopy measurements

The transmittance of the obtained IZO films was measured on glass samples. The deposition parameters used were those detailed in Table 33. A high transmittance of ca. 80% in the visible range was achieved (Figure 141).
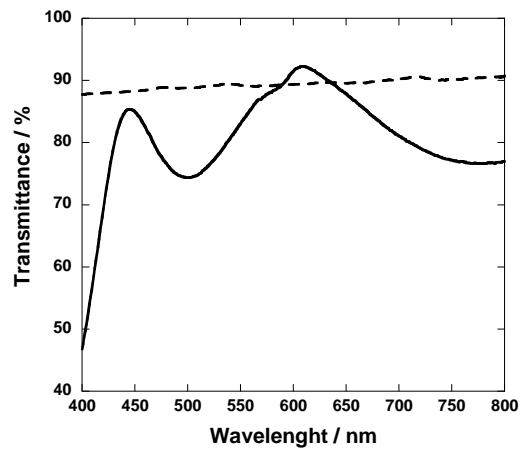
Figure 141: Optical transmittance of IZO film deposited on glass substrate (full line). The dash line is the glass without IZO.

<u>SEM</u>

Figures 142B and 143B clearly show the presence of the IZO thin film on drafting and pasteboard papers, respectively. The surface of the bare drafting paper appears to be relatively smooth in the photomicrograph of Figure 142A. The IZO layer deposited on it (Figure 142B) is rougher, but seems to be continuous. The surface of the bare glossy coated paper (Figure 143A) contains crystallites, which result from a previous surface treatment present already in the as-received samples. These additives are typically used for toughening and whitening this type of paper. The glossy coated paper, after IZO deposition (Figure 143B) exhibits such crystallites completely covered with the IZO grains.
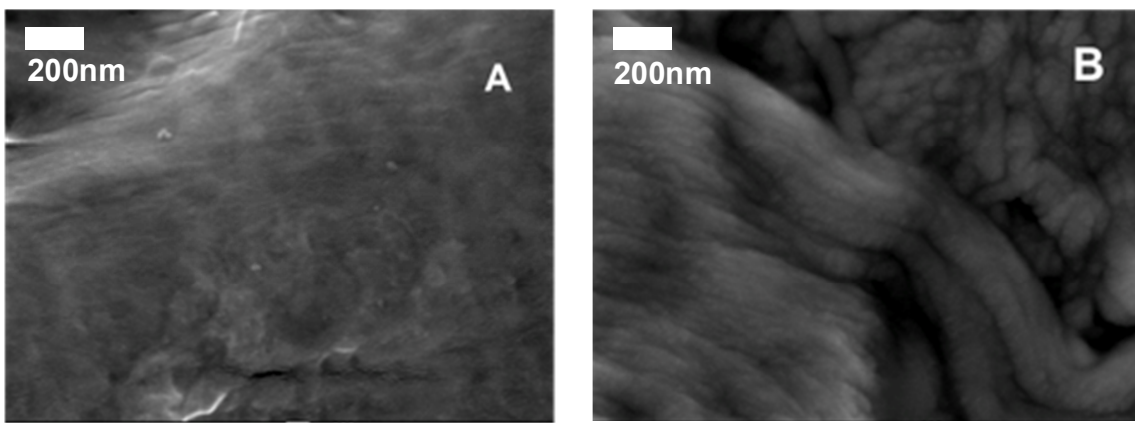
Figure 142: Photomicrograph of (A) bare drafting paper (without IZO) and (B) drafting paper with IZO on the surface. Magnification of 50000X.
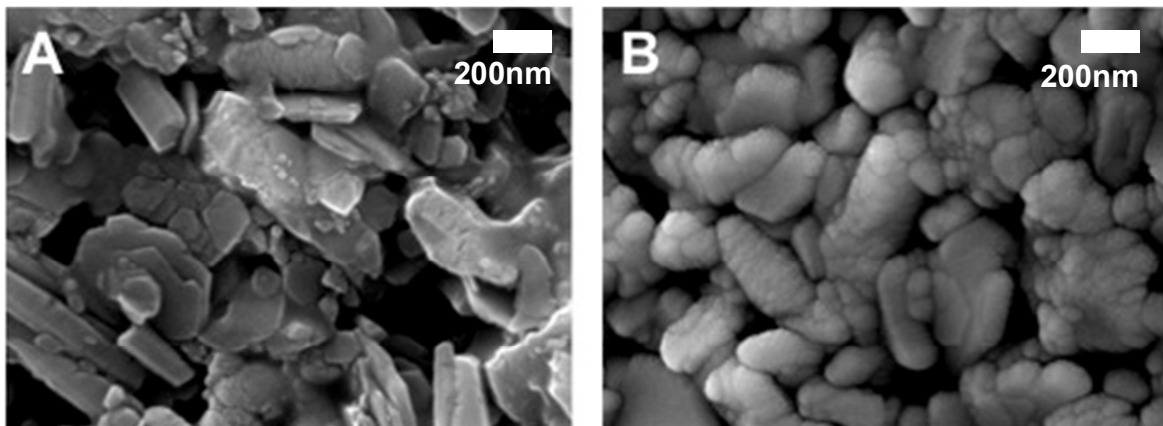
Figure 143: Photomicrograph of (A) pasteboard paper without IZO and (B) pasteboard paper with IZO on the surface. Magnification of 50000X.

Cyclic voltammetry

The cyclic voltammetry was performed using a three-electrode cell configuration, as described above, in a liquid electrolyte (0.1M LiClO$_4$ in acetonitrile). The voltammograms obtained (Figures 144A and 134B) show that all samples, i.e. IZO coated paper and ITO coated PET (PET-ITO) analyzed are stable at positive potentials (up to 2V). However, PET-ITO exhibits a significant increase in current intensity starting at -1.2V, followed by drafting paper and glossy coated paper. Pasteboard paper did not show any current intensity variation. This behavior was observed both for RF and DC sputtering, meaning that there are no significant differences in electrochemical stability depending on the power supplies used.
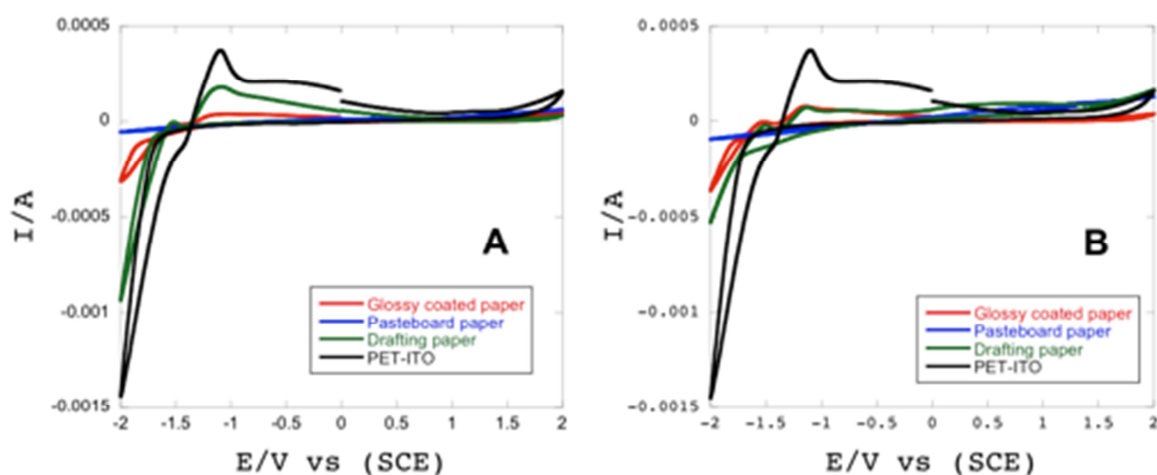
Figure 144: Voltammograms of IZO coated glossy paper, pasteboard paper and drafting paper. Comparison with PET-ITO. – Electrolyte: 0,1M LiClO$_4$ in acetonitrile A) DC sputtering and B) RF sputtering.

Stability measurements

Stability measurements were achieved using a drafting paper based electrode (with IZO deposited by DC sputtering). The paper-electrode was kept, during the time of the experiment, inside a desiccator (with only silica gel) without vacuum, temperature or humidity control. The sheet resistance was determined during 8 months using the method described in section 2.4.1. The maximum value of sheet resistance acceptable for these samples would be 60 Ω/sq, which is the value of the commercial PET/ITO used. There is no minimum value of sheet resistance preferred for this application. A slight increase of the sheet resistance during this period of time was observed (Figure 145). However, it can also be seen that the

error associated with the measurement method itself is high, once the homemade wood box with metallic contacts is removed from the sample between each reading, the next measurement is not performed at the exact same place than the previous one, leading to this error. Nevertheless, it is possible to conclude that the paper electrodes tested presented a good stability over the experiment time.
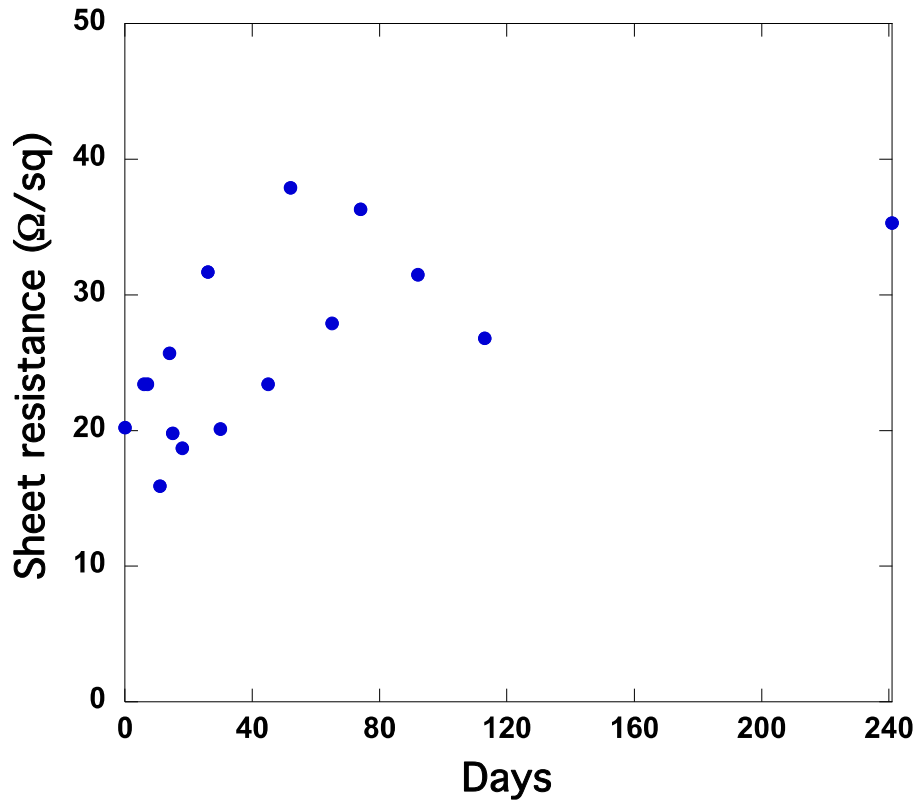
Figure 145: Sheet resistance measured during time on a drafting paper electrode.

In this section we presented the deposition of IZO thin films using RF and DC sputtering on different paper-based substrates with an excellent performance to be used on electrochromic devices. The thin films presented sheet resistances around 30 Ω/sq. with an average transmittance of 80% in the visible part of the spectrum and a stability above 8 months with a slight increase of sheet resistance but still perfectly usable in the suggested application. Being DC sputtering a technique used in industrial environment, it was demonstrated that these results could be implemented in a large-scale production.

Conclusions and future work

Considering electrochromic materials, it is important to have a diverse color palette to work with when building electrochromic devices. In this work, two electrochromic materials, tungsten oxide and vanadium oxide, were extensively studied, which are characterized by colors such as blue, green, yellow and transparent, at different oxidation states. The nanoparticle synthesis methods developed and optimized for these two inorganic materials are simple and cost-effective, thereby making possible their application at the industrial level. In this particular area, further work to be conducted in the future includes synthesizing new electrochromic materials with new colors, using also simple methods.

Regarding tungsten oxide in particular, it would also be interesting to study the ratio crystalline/amorphous domains in the resulting powder and the associated performance when used in electrochromic devices. This would be important as a way to try to improve the color contrast of the material, which is the main issue of the synthesized tungsten oxide at this point.

In the case of vanadium oxide, a comparison between different crystalline states and its impact on the electrochromic performance would also be useful. The toxicity of synthesized vanadium oxide is one of the main problems facing a possible commercialization. Such study should be performed in this particular situation. Despite current knowledge that V_2O_5 is toxic, the material developed in this work is a highly hydrated gel with morphology different from the usual V_2O_5 and the toxicity in this case has not been reported in the literature. Even if this electrochromic material is in fact toxic, the amount of material used in an electrochromic device is diminute and in this particular circumstance, it would be necessary to test the entire device to determine the total level of toxicity.

In the case of tungsten oxide and vanadium oxide, a complete study on the electrochromic device performance depending on the size of the device, the area covered with electrochromic material at each electrode, the symmetry between electrodes when different potentials are applied to the devices, should be carefully analyzed.

Considering ink formulations, a large amount of work still needs to be done for a possible industrialization. The inks were all printed on a Dimatix® materials printer, but to be used in industrial printers more optimizations are needed for a good reliability of printing. Rheological parameters of the inks, such as surface tension, viscosity and density must be adjusted to the printhead chosen, as well as the pH and the stability of the inks. To achieve these goals, new solvents, surfactants and binders have to be tested to ensure that the electrochromic response of the device is not inhibited.

From the results presented in this thesis, it is clear that only PEDOT:PSS is ready for commercialization at this point, followed by vanadium oxide (toxicity issues) and tungsten oxide (color contrast enhancement). To achieve similar statuses as those shown for tungsten oxide and vanadium oxide, PB and P3HT need a complete spectroelectrochemical and morphology study to determine the reasons for the poor electrochromic performances.

Considering the conductive materials study presented in this work, the Pechini method will be followed. It was demonstrated that the average particle size of the synthesized powders is probably the main cause of failure when deposited as thin films, in terms of transparency and conductivity. Two different approaches should be considered: grinding the powder to obtain smaller particles, or changing synthesis parameters, such as temperature and duration of the reaction. In addition, the sinterization step must be substituted by methods available from NovaCentrix or Xenon, to allow their possible use on heat sensitive substrates.

Products and competitiveness study

The device architecture used by Ynvisible (used in this work) and described in section 1.2.1 (Figure 8) is a simple, interesting and viable way to achieve electrochromic devices with full compatibility between electrodes, and allows, at the same time, the creation of fantastic visual effects. These devices present high cyclability due also to the fact that they are programmed to work in an alternate mode, applying alternatively to each electrode a small voltage during a short period of time. This voltage and the duration of the pulse can be adjusted separately at each electrode, giving some attractive effects on the final product. The sealing process is also responsible for such good performance and it was developed at Ynvisible's laboratory, as well as the electrolyte layer, which is also crucial for a good performance of the devices.

Allying the architecture to the design, it is possible to have some remarkable and unique behaviors such as to have two distinct images that commute between each other, and not only one image that appears or disappears, like NTERA[®]'s approach. Figure 146 shows the structure of the devices used by NTERA[®].
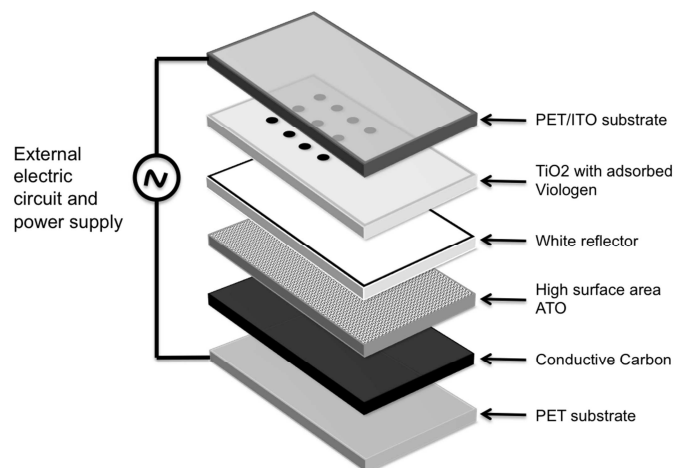
Figure 146: Architecture scheme of solid-state electrochromic devices used by NTERA[®].

The two images can be hidden or "confused" using design effects and not only two images that appears alternatively but that are always perfectly distinguishable like ACREO®'s solution. Figure 147 shows the parallel architecture used by ACREO®. Figure 148 shows a Christmas card used by YDreams Brazil showing two hidden messages in one device only. Figure 149 shows an advertising insert developed for an airline, which is a good example of a "confused" image that is revealed when a button is pushed.
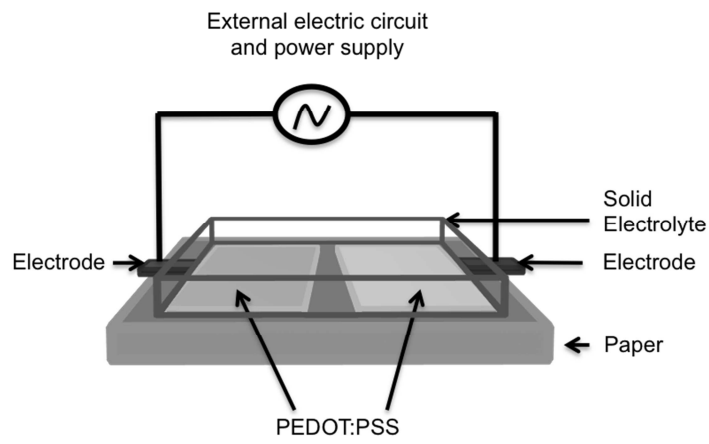
Figure 147: Architecture scheme of solid-state electrochromic devices developed by ACREO®.

Figure 148: Christmas card used by YDreams Brazil using Ynvisible's technology.

Figure 149: advertising insert developed for an airline by Ynvisible.

With Ynvisible's displays it is also possible to have very fast transitions between electrodes, as well as different transition times from one electrode to the other, giving the impression of movement in the resulting image, like a heartbeat or wheel spinning effect, for example.

The transparency is another advantage of Ynvisible's devices in comparison with the main competitors. It is possible to have fully transparent backgrounds, where only the electrochromic material appears and disappears and where a back image can be seen through the electrochromic device.

The production method used by Ynvisible until now is a sheet-to-sheet process where the electrochromic material is screen-printed. The electrolyte layer is deposited using coating techniques and the two electrodes are laminated together. The price calculated for Ynvisible's display raw materials is approximately 5 cents/cm^2. From these 5 cents/cm^2, around 51% is for PET/ITO, 8% is for electrolyte, 6% is for the sealant, 17% is for PEDOT:PSS ink and the remaining 18% is for conductive tape. This value will vary depending on the size of the devices and consequent number of items that can be printed per sheet.

Both NTERA and ACREO use a roll-to-roll process based on printing techniques, meaning that they can print the entire device, layer by layer. Ntera is no longer in operation, so they are no longer direct competitors to Ynvisible, but the materials they used in their architecture are very expensive. ACREO's devices are probably more cost-effective than Ynvisible's technology also because they use PEDOT:PSS both as conductive electrode and as electrochromic material, eliminating the need for PET/ITO, but again, the performances achieved are weaker.

170

ACREO's process is based on flexography with an output of 5 to 20 m/min. The devices work with 3V and the transition speed between images is about 10 s. ACREO's devices are commercialized by Paper Display.

In Figure 150 some products commercialized by Ynvisible available on the website of the company can be seen. Those products reflect the parameters and characteristics described above.

Figure 150: Some examples of products developed and commercialized by Ynvisible

List of Publications

Scientific publications

<u>Papers</u>
1. M.M. Silva, P.C. Barbosa, L.C. Rodrigues, A. Gonçalves, **C. Costa**, E. Fortunato, (2010) "Gelatin in electrochromic devices", Optical Materials 32, 719–722.
2. **C. Costa**, C. Pinheiro, I. D. S. Henriques, C. A. T. Laia "Inkjet Printing of Sol–Gel Synthesized Hydrated Tungsten Oxide Nanoparticles for Flexible Electrochromic Devices" ACS Appl. Mater. Interfaces, 2012, 4 (3), pp 1330–1340.
3. A. Gonçalves, **C. Costa**, S. Pereira, N. Correia, M. M. Silva, P. C. Barbosa, L. C. Rodrigues, I. Henriques, R. Martins and E. Fortunato. "Study of electrochromic devices with nanocomposites polymethacrylate hydroxyethylene resin based electrolyte". Polym. Adv. Technol. 2012, 23 791–795.
4. **C. Costa**, C. Pinheiro, I. Henriques, C. A. T. Laia, "Electrochromic Properties of Inkjet Printed Vanadium Oxide Gel on Flexible PET/ITO Electrodes". ACS Appl. Mater. Interfaces, 2012, 4 (10), pp 5266–5275.
5. L. Gomes, A. Marques, A. Branco, J. Araújo, M. Simões, S. Cardoso, F. Silva, I. Henriques, C.A.T. Laia, **C. Costa**; IZO deposition by RF and DC sputtering on paper and application on flexible electrochromic devices. Submitted to the journal Displays Ref. No.: DISPLA-D-12-00074.
6. **C. Costa**, L. Gomes, J. Ricardo, A. Branco, A. Marques, I. Henriques, C. A. T. Laia, J. Parola, C. Pinheiro, "Inkjet printing of organic and inorganic electrochromic materials and application on flexible and transparent electrochromic displays/indicators". (In preparation)
7. M. Simões, J. Araújo, A. Branco, L. Gomes, **C. Costa**, C. Pinheiro, I. Henriques, A. Marques, "A high performance solid polymeric electrolyte for thin, flexible, transparent electrochromic displays". (In preparation).

<u>Proceedings</u>
1. Fortunato, E., Correia, N., Barquinha, P., **Costa, C.**, Pereira L., Gonçalves G., Martins, R., (2009) "Paper field effect transístor", Proceedings SPIE - Conferences & Publications on Photonics, Optics, & Imaging (Proc. SPIE), Vol. 7217, 72170K.
2. **C. Costa**, C. A. T. Laia, A. J. Parola, L. Gomes, J. Ricardo, A. Branco, A. Marques, I. Henriques, C. Pinheiro, (2012) "Inkjet printing of electrochromic materials on plastic and paper-based electrodes for electrochromic devices", Proceedings LOPE-c.

Patents
1. Portuguese Patent 104.634; **Costa, C**., Senadeera, G. K. R., Fortunato, E., Henriques, I. D. S.
2. Portuguese Patent Application 104.635 Ferreira, I., **Costa, C.**, Fortunato, E., Martins, R., Henriques.
3. Portuguese Patent Application 105.814, **Costa, C**., Pinheiro, C., Henriques, I., Laia, C.
4. Portuguese Provisional Utility Patent Application 106.301**, Costa, C**., Gomes, L., Marques, A., Branco, A., Araújo J., Simões, M.

Bibliography

[2] Peter Andersson; http://www.diva-portal.org/liu/theses/abstract.xsql?dbid=6102; 26-05-2009.

[3] Peter Harrop; http://www.idtechex.com/products/en/articles/00000574.asp; 26-05-2009.

[4] Acreo; http://www.acreo.se/templates/Page_____780.aspx; 26-05-2009.

[5] Idtechex; http://www.idtechex.com/printedelectronicsworld/en/; 26-05-2009.

[6] Idtechex ; http://www.idtechex.com/products/en/articles/00000609.asp; 26-05-2009.

[7] Fantastic Plastic; http://fantasticplastic.org/category/electronic-paper/; 26-05-2009.

[8] Gizmodo; http://gizmodo.com/gadgets/reading-is-fundamental/hp-e%2Bbook-reader-design-fakes-turning-pages-260744.php; 26-05-2009.

[9] Gizmodo; http://gizmodo.com/gadgets/gps-concept/e%2Bpaper%2Bbased-gps-concept-keeps-tourists-on-the-right-track-260278.php; 26-05-2009.

[10] Gizmag; http://www.gizmag.com/go/4821/; 26-05-2009.

[11] Tony Davis; http://www.smh.com.au/news/technology/fastforward-through-the-supermarket-aisles/2005/10/16/1129401145745.html; 26-05-2009.

[12] SPIE; http://spie.org/x17480.xml; 26-05-2009.

[13] Ziljak; http://www.ziljak.hr/tiskarstvo/tiskarstvo08/Radovi08/ZA%20WEB/Epaper180.html; 26-05-2009.

[14] Krause D., Paquet V., Electro-Opt. Systems Design 9 (11), (1977) 54-55.

[15] Svensson J.S.E.M., Granqvist C.G., Proc. Soc. Photo-Opt. Instrum. Eng. 502, (1984) 30-37.

[16] Svensson J.S.E.M., Granqvist C.G., Solar Energy Mater. 12, (1985) 391-402.

[17] Braig A., Meisel T., Dornier-Post 2, (1992) 29-30.

[18] Papaefthimiou S., Leftheriotis G., Yianoulis P., Electrochimica Acta 46 (2001) 2145-2150.

[19] Cui H. N., Costa M. F., Teixeira V., Porqueras I., Bertran E., Surface Science 532-535 (2003) 1127-1131.

[20] Somani P. R., Radhakrishnan S., Materials Chemistry and Physics 77 (2002) 117-133.

[21] Girotto E. M., Paoli M.-A., Braz. J., Chem. Soc. Vol.10, No. 5 (1999) 394-400.

[22] Acreo; www.acreo.se; 26-05-2009.

[23] Erggren et al, United States Patent Application No.: 2007/0076287 A1 (2007).

[24] Ntera; http://www.ntera.com/; 26-05-2009

[25] Pichot et al., United States patent No. US 7,270,880 B2 (2007).

[26] Kaufman G.B., Inorganic Coordination Compounds: Nobel Prize Topics in Chemistry, Heyden, Philadelphia, (1981).

[27] Berzelius J.J., J. Chem. Phys. 16 (1816) 476-488.

[28] Wohler F., Ann. Phys. 2 (1824) 350-358.

[29] Kobosew N., Nekrassow N.I., Z. Elektrochem. 36 (1930) 529-544.

[30] Talmey P., U.S. Patent 2,281,013 (1942).

[31] Brimm E.O., Brantley J.C., Lorenz J.H., Jellinek M.H., J. Am. Chem. Soc. 7.3 (1951) 5427-5432.

[32] Kraus T., Laboratory Report at Balzers AG, Liechtenstein (entry made 30 July 1953), unpublished.

[33] Philips Electronic and Associated Industries Ltd. British Patent 1,302,000 (1973).

[34] Schoot, C. J., Ponjee, J. J., van Dam, H. T., van Doorn, R. A., Bolwijn, P. T., Appl. Phys. Lett., 23 (1973) 64–65.

[35] Short G. D., Thomas L., British Patent 1,310,813 (1973).

[36] Platt, J. R., J. Chem. Phys., 34 (1961) 862–3.

[37] Deb S.K., Appl. Opt. Suppl. 3 (1969) 192-195.

[38] Deb S.K., Philos. Mag. 27 (1973) 801-822.

[39] Mohapatra, S. K., J. Electrochem. Soc., 285 (1978) 284–8.

[40] Granqvist C. G., Handbook of Inorganic Electrochromic Materials, Elsevier (1995).

[41] Monk P. M. S., Mortimer R. J., Rosseinsky D. R., Electrochromism and Electrochromic Devices, Cambridge University Press (2007).

[42] Ginley D.S., Handbook of Transparent conductors, Springer, London (2010).

[43] Mochel J. M., US Patent n.º 2,564,706 (1947).

[44] Zunick M. J., US Patent n.º 2,516,663 (1947).

[45] Lee, D.H. et al, Adv. Mater. 19 (2007) 843-847.

[46] Hong, S. J. et al., IEEE Transactions on Nanotechmology, vol 7 (2) (2008).

[47] Shen, W. et al, Thin Solid Films 483 (2005) 382-387.

[48] Puetz, J., Aegerter, M., Thin Solid Films 516 (2008) 4495-4501.

[49] Cranton W. M., Wilson S. L., Ranson R., Koutsogeorgis D. C., Chi K., Hedgley R., Scott J., Lipiec S., Spiller A., Speakman S., Thin Solid Films, vol. 515 (24) (2007) 8534-8538.

[50] Tadatsugu M., Semicond. Sci. Technol., 20 (2005) S35-S44.

[51] Brinker C. J., Scherer G. W., Sol-gel Science, Academic Press, (1990).

[52] Sakka S., Handbook of Sol-Gel Science and Technology, Vol. I, II and III, Kluwer Academic publishers, (2004).

[53] Livage J., Ganguli D., Solar Energy Materials & Solar Cells, 68 (2001) 365-381.

[54] Ozer N., Lampert C. M., Solar Energy Materials & Solar Cells, 54 (1998) 147-156.

[55] Sandu, C.S., J. sol-gel Sci. And Technol. 28 (2003) 227-234.

[56] Cranton, W. M. et al, Thin Solid Films 515 (2007) 8534-8538.

[57] Tahar, R. B. H., Journal of the European Ceramic Society 25 (2005) 3301-3306.

[58] Aegerter, M. A. et al, J. Sol-gel Sci. Technol. 47 (2008) 203-236.

[59] Puetz, J. et al, Advanced Engineering Materials, 6, No. 9. (2004).

[60] Al-Dahoudi, N., Aegerter, M. A., Thin Solid Films 502 (2006) 193-197.

[61] Kipphan, H.. Handbook of print media: technologies and production methods, Springer (2001).

[62] Johansson, Lundberg & Ryberg "A guide to graphic print production", John Wiley & Sons Inc., Hoboken, New Jersey (2003).

[63] Pneac; http://www.pneac.org/printprocesses/screen/; 13-09-2012

[64] Kipphan, H., Handbook of print media: technologies and production methods, Springer (2001).

[65] Pneac; http://www.pneac.org/printprocesses/gravure/; 13-09-2012

[66] Konica Minolta; http://www.konicaminolta.com/inkjethead/technology/technology.html; 13-09-2012

[67] http://www.imaging.org/ist/resources/tutorials/inkjet.cfm; 13-09-2012

[68] http://en.wikipedia.org/wiki/Inkjet_printer; 15-03-2012.

[69] www.britannica.com/EBchecked/topic/340440/light/258424/Interactions-of-light-with-matter; 13-09-2012

[70] Nassau, K., The physics and chemistry of color. Wiley Interscience: New York, (1983).

[71] Brotherston I.D., Mudigonda D.S.K., Osborn J.M., Belk J., Chen J., Loveday D.C., Boehme J.L., Ferraris J.P., Meeker D.L., Electrochim Acta, vol. 44 (18) (1999) 2993-3004.

[72] Mortimer, R.J., Reynolds, J. R., J. Mater. Chem., 15 (2005) 2226-2233.

[73] Gaupp, C. L.; Welsh, D. M.; Rauh, R. D.; Reynolds, J. R., Chemistry of Materials, 14 (9) (2002) 3964-3970.

[74] NovaCentrix; http://www.novacentrix.com/; 13-09-2012.

[75] XenonCorporation; http://www.xenoncorp.com/; 13-09-2012.

[76] Terrier, C., Chatelon, J. P., Roger, J. A., Berjoan, R., Dubois, C., J. Sol-gel Sci. Tech. 10 (1997) 75-81.

[77] Purushothaman, K. K., Dhanashankar, M., Muralidharan, G., Current Applied Physics, vol.9 (2009) 67-72.

[78] Bernardi M. I. B., Feitosa C. A. C., Paskocimas C. A., Longo E., Paiva-Santos C. O., Ceramics International, vol. 35 (1) (2009) 463-466.

[79] Bernardi M.I.B., Soledade L.E., Santos I.A., Leite E.R., Longo E., Varela J.A., Thin Solid Films 405 (2002) 228–233.

[80] Legnani C., Lima S.A.M., Oliveira H.H.S., Quirino W.G., Machado R., Santos R.M.B., Davolos M.R., Achete C.A., Cremona M., Thin Solid Films 516 (2007) 193–197.

[81] He G., Cai J.H., Ni G., Materials Chemistry and Physics 110 (2008) 110–114.

[82] Zhang J., Gao L., Materials Chemistry and Physics 87 (2004) 10–13.

[83] Zhang J., Gao L., Materials Research Bulletin 39 (2004) 2249–2255.

[84] Faughnan, B. W.; Crandall, R. S.; Heyman, P. M. RCA Rev. 36 (1975) 177-197.

[85] Granqvist, C. G. Sol. Energ. Mat. Sol. C., 60 (2000) 201-262.

[86] Granqvist, C. G.; Green, S.; Niklasson, G. A.; Mlyuka, N. R.; von Kraemer, S.; Georen, P. Thin Solid Films 518 (2010) 3046-3053.

[87] Rauh, R. D. Electrochim. Acta, 44 (1999) 3165-3176.

[88] Niklasson, G. A., Granqvist, C. G. J. Mater. Chem. 17 (2007) 127-156.

[89] Baetens, R., Jelle, B. P., Gustavsen, A. Sol. Energ. Mat. Sol. C. 94 (2010) 87-105.

[90] Crandall, R. S., Faughnan, B. W. Appl. Phys. Lett. 28 (1976) 95-97.

[91] Zeller, H. R., Beyeler, H. U. Appl. Phys. 13 (1977) 231-237.

[92] Hashimoto, S., Matsuoka, H. J. Electrochem. Soc. 138 (1991) 2403-2408.

[93] Batchelor, R. A.; Burdis, M. S.; Siddle, J. R. J. Electrochem. Soc. 143 (1996) 1050-1055.

[94] Lee, S. H., Cheong, H. M., Tracy, C. E., Mascarenhas, A., Czanderna, A. W., Deb, S. K. Appl. Phys. Lett. 75 (1999) 1541-1543.

[95] Monk P. M. S., Critical Reviews in Solid State and Materials Sciences 24 (1999) 193-226.

[96] Lee, S. H., Cheong, H. M., Zhang, J. G., Mascarenhas, A., Benson, D. K., Deb, S. K. Appl. Phys. Lett. 74 (1999) 242-244.

[97] Berggren, L., Azens, A., Niklasson, G. A. J. Appl. Phys. 90 (2001) 1860-1863.

[98] Granqvist, C. G., Avendano, E., Azens, A. Thin Solid Films 442 (2003) 201-211.

[99] Azens, A., Gustavsson, G., Karmhag, R., Granqvist, C. G. Solid State Ionics, 165 (2003) 1-5.

[100] Ho, J. J., Chen, C. Y., Lee, W. J. Electron. Lett. 40 (2004) 510-511.

[101] Kamal, H., Akl, A. A., Abdel-Hady, K. Physica B 349 (2004) 192-205.

[102] Rodrigues, L. C., Barbosa, P. C., Silva, M. M., Smith, M. J., Goncalves, A., Fortunato, E. Opt. Mater. 31 (2009) 1467-1471.

[103] Silva, M. M., Barbosa, P. C., Rodrigues, L. C., Goncalves, A., Costa, C., Fortunato, E. Opt. Mater. 32 (2010) 719-722.

[104] Vemuri, R. S., Bharathi, K. K., Gullapalli, S. K., Ramana, C. V., Acs. Appl. Mater. Inter. 2 (2010) 2623-2628.

[105] Gullapalli, S. K., Vemuri, R. S., Ramana, C. V., Appl. Phys. Lett. 96 (2010) 171903.

[106] Okamoto, H., Ishikawa, A., Kudo, T., Bull. Chem. Soc. Jpn. 62 (1989) 2723-2724.

[107] Judeinstein, P., Livage, J. J. Mater. Chem. 1 (1991) 621-627.

[108] Livage, J., Guzman, G. Solid State Ionics 84 (1996) 205-211.

[109] Lee, K. D. Thin Solid Films 302 (1997) 84-88.

[110] Santato, C., Odziemkowski, M., Ulmann, M., Augustynski, J., J. Am. Chem. Soc., 123 (2001) 10639-10649.

[111] Ozkan, E., Lee, S. H., Liu, P., Tracy, C. E., Tepehan, F. Z., Pitts, J. R., Deb, S. K., Solid State Ionics 149 (2002) 139-146.

[112] Badilescu, S., Ashrit, P. V., Solid State Ionics 158 (2003) 187-197.

[113] Brezesinski, T., Fattakhova-Rohlfing, D., Sallard, S., Antonietti, M., Smarsly, B. M. Small 2 (2006) 1203-1211.

[114] Deepa, M., Srivastava, A. K., Kar, M., Agnihotry, S. A., J. Phys. D. Appl. Phys. 39 (2006) 1885-1893.

[115] Deepa, M., Joshi, A. G., Srivastava, A. K., Shivaprasad, S. M., Agnihotry, S. A., J. Electrochem. Soc. 153 (2006) C365-C376.

[116] Deepa, M., Singh, D. P., Shivaprasad, S. M., Agnihotry, S. A., Curr. Appl. Phys. 7 (2007) 220-229.

[117] Djaoued, Y., Priya, S., Balaji, S., J. Non-Cryst. Solids 354 (2008) 673-679.

[118] Wang, W., Pang, Y., Hodgson, S. N., B. Micropor. Mesopor. Mat. 121 (2009) 121-128.

[119] Balaji, S., Djaoued, Y., Albert, A. S., Bruening, R., Beaudoin, N., Robichaud, J., J. Mater. Chem. 21 (2011) 3940-3948.

[120] Livage J., Ganguli D., Sol. Energy Mater. Sol. Cells 68 (2001) 365–381.

[121] Krings L.H.M., Talen W., Energy Mater. Sol. cells 54(1–4) (1998) 27–37.

[122] Judeinstein P., Livage J., J. Mater. Chem 1(4) (1991) 621–627

[123] Kudo T., Okamoto H., Matsumoto K., Sasaki Y., Inorganica Chimica Acta 111 (1986) L27-L28.

[124] Yamanaka K., Oakamoto H., Kidou H., Kudo T., Japanese Journal of Applied Physics 25 (1986) 1420-1426.

[125] Sharma N., Deepa M., Varshney P., Agnihotry S.A., Journal of Non-Crystalline Solids 306 (2002) 129–137.

[126] Deepa M., Srivastava A. K., Kar M., Agnihotry S. A., Journal of Physics & Applied Physics 39 (2006) 1885-1893.

[127] Biswas P.K., Pramanik N.C., Mahapatra M. K., Ganguli D., Livage J., Materials letters 57 (2003) 4429-4432.

[128] Pecquenard B., Garcia S. C., Livages J., Zavalij P. Y., Whittingham M. S., Thouvenout R., Chemistry of Materials 10 (1998) 1882-1888.

[129] Cronin J. P., Agrawal A., Tarico D. J., Tonazzi J. C. L., Patent US5525264 (1996).

[130] Avellaneda C. O., Dahmouche K., Bulhões L. O. S., Pawlicka A., Journal of Sol-gel Science and Technology, 19 (2000) 447-451.

[131] Huang K., Jia J., Pan Q., Yang F., He D., Physica B 396 (2007) 164-168.

[132] Aegerter M.A., Avellaneda C. O., Pawlicka A., Atik M., Journal of Sol-Gel Science and Technology 8 (1997) 689-696.

[133] Djaoued Y., Priya S., Balaji S., Journal of non-cristalline solids 354 (2008) 673-679.

[134] Badilescu S., Ashrit P. V., Solid State Ionics 8830 (2002) 1-11.

[135] Bessière A., Badot J.C., Certiat M.C., Livage J., Lucas V., Baffier N. Electrochim. Acta 46(13–14) (2001) 2251–2256.

[136] Daniel, M.F., Desbat, B., Lassegues, J. C., Gerand, B., Figlarz, M. J. Solid State Chem. 67 (1987) 235-247.

[137] Baserga, A., Russo, V., Di Fonzo, F., Bailini, A., Cattaneo, D., Casari, C. S., Li Bassi A., Bottani, C. E. Thin Solid Films 515 (2007) 6465-6469.

[138] Parvulescu V.I., Boghosian S., Parvulescu V., Jung S.M., Grange P., J. Catal. 217 (2003) 172.

[139] Huang Z., Zhu Z., Liu Z., Liu Q., J. Catal. 214 (2003) 213.

[140] Zhuiykov S., Wlodarski W., Li Y., Sens. Actuators B 77 (2001) 484.

[141] Passerini S., Tipton A.L., Smyrl W.H., Sol. Energy Mater. Sol. Cells 39 (1995) 167.

[142] Delmas C., Cognac-Auradou H., Cocciantelli J.M., Ménétrier M., Doumerc J.P., Solid State Ionics 69 (1994) 257.

[143] Julien C., Poniatowski H., Lopez C., Escobar-Alarcon M.A., Jarquin J., Mater. Sci. Eng. B 65 (1999) 170.

[144] Rauh, R. D., Cogan, S. F., Solid State Ionics 28-30 (1988) 1707-14.

[145] Ashrit, P. V., Girouard, F. E., Truong, V. V., Solid State Ionics 89 (1996) 65-73.

[146] Livage, J., Coordination Chemistry Reviews 178–180 (1998) 999–1018.

[147] Livage J., J. Phys. 42 (1981) C4 98l-C4 992.

[148] Livage J., Mater. Res. Soc. Syrup. Proc 32 (1984) 125-134.

[149] Livage J., J. Solid State Chem. 64 (1986) 322-330.

[150] Livage J., Chem. Mater. 3 (1991) 578-593.

[151] Livage J., Mater. Res. Soc. Syrup. Proc. 293 (1993) 261-271.

[152] Livage J., M. Henry, C. Sanchez, Prog. Solid State Chem. 18 (1988) 259-341.

[153] Livage J., J. Lemerle, Ann. Rev. Mater. Sci. 12 (1982) 103-122.

[154] Lei, S., Tang, K., Jin Y., Chen C. Nanotechnology, 18 (2007) 175605.

[155] Baddour-Hadjean, R.; Pereira-Ramos, J. P. Chem. Rev. 110 (2010) 1278–1319.

[156] Jin, A., Chen, W., Zhu, Q., Yang, Y., Volkov, V. L., Zakharova, G. S. Solid State Ionics 179 (2008) 1256-1262.

[157] Lee, S., Cheong, H., Seong, M., Liu, P., Tracy, C. E., Mascarenhas, A., Pitts, J. R., Deb, S.K., J. Appl. Phys., 2 (2002) 1893-1897.

[158] Surca, A., Orel, B., Drazic G., Pihlar, B., J. Electrochem. Soc.146 (1999) 232-242.

[159] Sahana, M. B., Sudakar, C., Thapa, C., Lawes, G., Naik, V. M., Baird, R. J., Auner, G. W., Naik, R., Padmanabhan, K. R., Mater. Sci. Eng. B 143 (2007) 42–50.

[160] Wang, Y., Shang, H.M., Chou, T., Cao, G.Z., J. Phys. Chem. B 109 (2005) 11361-11366.

[161] Alonso, B., Livage, J., J. Solid State Chem., 148 (1999) 16-19.

[162] Vivier,V., Farcy, J., Pereira-Ramos, J. P., Electrochim. Acta, 44 (5) (1998) 831-839.

[163] Moon, J., Grau, J.E., Knezevic, V., Cima, M. J., Sachs, E. M., Journal of the American Ceramic Society 85 (4) (2002) 755-762.

[164] Gans, B. J., Duineveld, P. C., Schubert, U. S., Advanced Materials 3 (2004) 203-213.

[165] Tuladhar T.R., Mackley M. R., Journal of Non-Newtonian Fluid Mechanics 148 (2008) 97-108.

[166] Lin S.P., Reitz R. D., Annual Review of Fluid Mechanics 30 (1998) 85-105.

[167] Chretien M. N., Chopra N., Heuft M., Kazmaier P., US Patent 2009288517 (2009).

[168] Oriakhi C. O., Rengaswamy S., Farr I., US patent 7641728 (2010).

[169] Calvert P., Chemistry of Materials 13 (2001) 3299-3305.

[170] Avellaneda C. O., Materials Science and Engineering B 138 (2007) 123-127.

[171] Dimatix Materials Printer, User Manual

[172] Werblan L., Rotowska A., Minc S., Electrochimica Acta 16 (1971) 41-59.

[173] Hush, N. S., Annals of the New York Academy of Sciences 1006 (2003) 1–20.

[174] Akamatu, H., Inokuchi, H. Matsunaga, Y., Nature 173 (4395) (1954) 168.

[175] McNeill, R., Weiss, D.E.; Willis, D., Australian Journal of Chemistry 18 (4) (1965) 477.

[176] Shirakawa, H., Edwin J.L., MacDiarmid, A. G., Chiang, C. K., Heeger, A. J., Journal of the Chemical Society, Chemical Communications (16) (1977) 578.

[177] Scholz, F., Conducting Polymers: A New Era in Electrochemistry. Monographs in Electrochemistry, Springer, (2008).

[178] Friend R. H., Gymer R. W., Holmes A. B., Burroughes J. H., Marks R. N., Taliani C., Bradley D. D. C., Dos Santos D. A., Brédas J. L., Lögdlund M., Salaneck W. R., Nature 397 (1999) 121–128.

[179] Bayer AG, Eur. Patent 440957 (1991).

[180] Agfa Gevaert, Eur. Patent 564911 (1993).

[181] Jonas, F. Macromol. Symp. 100 (1995) 169.

[182] Jonas, F. Synthetic metals 85, (1997) 1397.

[183] Gustafsson J. C., Solid State Ionics 69 (1994) 145.

[184] Kumar, A., Reynolds, J. R., Macromolecules 29 (1996) 7629.

[185] Groenendaal L., Jonas F., Freitag D., Pielartzik H., Reynolds J. R., Advanced Materials 12 (7) (2000) 481–494.

[186] Hou J., Chen T. L., Zhang S., Huo L., Sista S., Yang Y., Macromolecules 42 (2009) 9217–9219.

[187] Shin H., Kim Y., Bhuvana T., Lee J., Yang X., Park C., Kim E., Acs Appl. Mater. Inter. vol. 4 (1) (2012) 185-191.

[188] Ware, M., Cyanotype. In The history, science and art of photographic printing in Prussian Blue, Science Museum, London, (1999) 21-37.

[189] Batten, S. R.; Neville, S. M.; Turner, D. R., Coordination polymers design, analysis and application. The Royal Society of Chemistry: Cambridge, (2009).

[190] Gotoh, A.; Uchida, H.; Ishizaki, M.; Satoh, T.; Kaga, S.; Okamoto, S.; Ohta, M.; Sakamoto, M.; Kawamoto, T.; Tanaka, H.; Tokumoto, M.; Hara, S.; Shiozaki, H.; Yamada, M.; Miyake, M.; Kurihara, M., Nanotechnology 18 (34) (2007) 6.

[191] Neff V. D., Journal of the Electrochemical Society 125 (6) (1978) 886-887.

[192] Mortimer R. J., Reynolds J. R., J. Mater. Chem. 15 (2005) 2226-2233.

[193] Pecquenard, B., Lecacheux, H., Garcia, S. C., Livage, J. Journal of Sol-gel Science and Technology 13 (1998) 923-927.

[194] Green, M., Smith, W. C., Weiner, J. Thin Solid Films 38 (1976) 89-100.

[195] Zhang, J. G., Benson, D. K., Tracey, C. E., Deb, S. K., Czanderna, A. W., Bechinger, C. J., Electrochem. Soc. 144 (1997) 2022-2026.

[196] Zhang, L., Goto, K. S., Proc. Electrochem. Soc. 90-2 (1990) 23-29.

[197] Faughnan, B. W., Crandall, R. S., Display Devices, Springer-Verlag: Berlin, (1980).

[198] Ingram, M. D., Duffy, J. A., Monk, P. M. S., J. Electroanal. Chem. 380 (1995) 77-82.

[199] Bessiere, A., Marcel, C., Morcrette, M., Tarascon, J. M., Lucas, V., Viana, B., Baffier, N., J. Appl. Phys. 91 (2002) 1589-1594.

[200] Niklasson, G. A., Berggren, L., Larsson, A. L., Sol. Energ. Mat. Sol. C. 84, (2004) 315-328.

[201] Ederth, J., Hoel, A., Niklasson, G. A., Granqvist, C. G., J. Appl. Phys. 96 (2004) 5722-5726.

[202] Balaji S., Djaoued Y., Albert A. S., Ferguson R. Z., Bruning R., Chemistry of Materials 21 (2009) 1381-1389.

[203] Azuma, R., Baillot, Y., Behringer, R., Feiner, S., Julier, S., MacIntyre, B., IEEE Comput. Graph. 21 (2001) 34-47.

[204] Lee, J. D., Concise Inorganic chemistry, Chapman & Hall: England, (1996).

[205] Anaissi, F. J., Demets, G. J. F., Toma, H. E., Electrochem. Commun. 1 (1999) 332-335.

[206] Talledo, A., Granqvist, C. G., J. Appl. Phys. 77 (9) (1995) 4655-4666.

[207] Bay N.T.B., Tien P.M., Badilescu S., Djaoued Y., Bader G., Girouard F.E., Truong V.V., Nguyen L.Q., J. Appl. Phys. 80 (12) (1996) 7041-7045.

[208] Cogan, S. F., Nguyen, N. M., Perrotti, S. J., Rauh, R. H., J. Appl. Phys. 66 (1989) 1333-1337.

[209] Livage, J. Solid State Ionics 86-88 (1996) 935-942.

[210] Andersson, P., Forchheimer, R., Tehrani P., Berggren, M., Adv. Funct. Mater. 17 (2007) 3074-3082.

[211] Costa, C., Pinheiro, C., Henriques, I., Laia, C. A. T., ACS Appl. Mater. Interfaces 4 (2012) 1330–1340.

[212] Patil, C. E., Tarwal, N. L., Shinde, P. S., Deshmukh, H. P., Patil, P. S., J. Phys. D: Appl. Phys. 42 (2009) 025404.

[213] Najdoski, M., Koleva, V., Demiri S., Mater. Res. Bull. 47 (2012) 737–743.

[214] Lin, Y. S., Tsai, C. W., Surf. Coat. Tech. 202 (2008) 5641–5645.

[215] Wang, Z. C., Chen, J. F., Hu, X. F., Thin Solid Films 375 (2000) 238-241.

[216] Scherer, M. R. J., Cunha, P. M. S., Scherman, O. A., Steiner, U., Adv. Mater. 24 (2012) 1217–1221.

[217] Beaujuge, P. M., Reynolds, J. R., Chem. Rev. 110 (2010) 268-320.

[218] Amb, C. M., Dyer, A. L., Reynolds, J. R., Chem. Mater. 23 (2011) 397-415.

[219] Laia, C. A. T., López-Cornejo, P., Costa, S. M. B., D'Oliveira, J., Martinho, J. M. G., Langmuir 14 (1998) 3531-3537.

[220] Petzold, G., Goltzsche, C., Mende, M., Schwarz, S., Jaeger, W., Journal of Applied Polymer Science 114 (2009) 696-704.

[221] Detloff, T., Sobisch, T., Lerche, D., Powder Technology 174 (2007) 50-55.

[222] Oi, T., Ann. Rev. Mater. Sci. 16 (1986) 185-201.

[223] Amou, O., Shirato, H., Journal of Polymer Science: Part A: Polymer Chemistry 37 (1999) 1943 – 1948.

[224] DeLongchamp, D. M., Hammond, P. T., Chem. Mater. 16 (2004) 4799-4805.

[225] Teixeira V., Cui H.N., Meng L.J., Fortunato E., Martins R., Thin Solid Films 420 (2002) 70-75.

[226] Kim, J. H., Moon, J. Y., Kim, H., Lee, H. S., Journal of the Korean Physical Society 55 (2009) 1931-1935.

[227] Lee, W. J., Fang, Y. K., Ho, J. J., Chen, C. Y., Chiou, L. H., Wang, S. J., Dai, F., Hsieh, T., Tsai, R. Y., Huang, D., Ho, F. C., Solid-State Electronics 46 (2002) 477–480.

[228] Martins R., Ferreira I., Fortunato E., Phys. Status Solidi RRL 5, No. 9 (2011) 332 – 335.

[229] Sasabayashi, T., Ito, N., Nishimura, E., Kon, M., Song, P. K., Utsumi, K., Kaijo, A., Shigesato, Y., Thin Solid Films 445 (2) (2003) 219-223.

[230] Zeng, K., Zhu, F., Hu, J., Shen, L., Zhang, K., Gong, H., Thin Solid Films 443 (1-2) (2003) 60-65.